Curriculum Vitae (not exceeding two pages)
Prof Xie George Xu, Ph.D.,
University of Science and Technology of China (USTC) , PR China (Email: xgxu@ustc.edu.cn)

Education

- B.S., Applied Physics, Xidan University (Xi'An, China)
- Ph.D., Nuclear Engineering (Health/Medical Physics focus), Texas A&M University (College Station, Texas, USA)

Career (abbreviated version)

1995-2014 Assistant, Associate, Full, and Hood Endowed Chair Professor, Nuclear Engineering and Biomedical Engineering, **Rensselaer Polytechnic Institute (RPI)** (Troy, New York, USA)
2009 -2010 Visiting Professor, **Harvard Medical School/ Massachusetts General Hospital (MGH)** (Boston, MA, USA)
2009-present Co-founder and president, **Virtual Phantoms, Inc** (Albany, New York, USA)
2014-present Distinguished Professor, College of Nuclear Science and Technology, **University of Science and Technology of China (USTC)** (Hefei, China)
2017-present Co-founder, **Wisdom Tech, Inc** (Hefei, China)
2021-present Department of **Radiation Oncology of the First Affiliated Hospital**, USTC
2021-present Director, **Institute of Nuclear Medical Physics**, USTC

Education of Graduate Students Prof. Xu has mentored nearly 100 Ph.D. and M.S. students at RPI (Troy, New York, USA) and USTC (Hefei, China). These include most notably: Dr. PF Caracappa (Director of Radiation Safety, Columbia University), Dr. B Wang (Prof and Chief of Radiation Physics, Yale University Hospital), Dr. B Bednarz (Associate Prof of Medical Physics, University of Wisconsin-Madison), Dr. C Shi (Associate Attending, Memorial Sloan Kettering Cancer Center), E TC Chao (Associate Prof, RadOncology, Chang Gung University Hospital, Taiwan), Dr. TT Zhang, Lead Engineer, Imaging & Clinical Applications, GE Healthcare), Dr. B Han, Associate Prof, RadOncology, Stanford University), Dr. AP Ding (Dept of Radiology, Duke University), Dr. M Mille (Staff Scientist, National Cancer Institute/CIRMS president), Dr. L Su, Associate Prof, RadOncology, Johns Hopkins University), Dr. YM Gao (Medical Physics resident, Radiology, Memorial Sloan Kettering Cancer Center), Dr. H Lin (Assistant Professor, RadOncology, UCSF).

Research Interests (1) Computational Phantoms. Techniques for advanced human phantoms that significantly improved the accuracy of radiation protection dosimetry (VIP-Man, RPI-Pregnant Female, RPI-Adult Male and Female, RPI-Obese Patients, as well as a set of deformable phantoms mimicking walking workers). The paper about the VIP-Man phantom is one of the most cited papers in the field of radiation phantoms. (2) Patient dose from Computed Tomography (CT) "Cloud" SaaS technologies to accurately track organ doses from CT for patients of various ages and sizes. This research has led to a commercial software package called VirtualDose for CT which was accessed more than 35-million times in the year of 2021 by users worldwide, making this software the most widely used clinical tool for CT organ dose assessment. (3) Non-target secondary cancer after radiotherapy Review article and TG reports on dosimetry studies this particular topic. (4) Management of respiration during external-beam treatment Earliest studies using 4D Monte Carlo simulation and finite-element modeling techniques. (5) Real-time GPU-based Parallel Monte Carlo computing ARCHER — a coupled photon, electron and proton Monte Carlo radiation transport package for dose verification and treatment planning. 6) AI-based automatic multi-organ segmentation of CT and PET/CT images. (7) Nanotube-based Brachytherapy Devices

Professional Services (abbreviated version)

American Association of Physicists in Medicine (AAPM): Vice Chair, Therapy Physics, Radiation Safety Subcommittee (2005 –2009); Imaging Physics, Radiation Prot Subcommittee (2005 –2008); Therapy Physics, Imaging for Treatment Planning Subcommittee (2006 –2009); Therapy Physics, Dosi & Treatment Planning Subcommittee (2019 – present); Task Group #136 "Hazards due to Induced Radioactivity Produced by Radiotherapy Accelerators" (2006 –2008); Task Group # 158 "Measurements and Monte Carlo Calculations of Whole-Body Organ Doses from External Beam Radiotherapy" (2007-2011); Task Group #180 "Modeling and Accounting for the Imaging Guidance Radiation Doses to Radiotherapy Patients in Treatment Planning" (2008 -2015); Medical Physics Journal - Associate Editor (2013 - 2015); Senior Associate Editor (2016 – present).

Council on Ionizing Radiation Measurements and Standards (CIRMS): President 1999-2000 (National priorities in radiation measurements and standardization for the U.S. governmental agencies and private-sector industry through "Needs Reports" and annual meetings and workshops at the National Institute of Standards and Technology (NIST) in four sub-committee areas: 1) Medical Applications; 2) Radiation Protect; 3) Industrial Applications and 4) Homeland Security.
Consortium of Computational Human Phantoms (CCHP): Co-founder and Steering Committee Chair (2009 - present) International Workshop on Computational Phantoms for Radiation Protection, Imaging and Radiotherapy (Beijing 2011, Zurich 2013, Seoul 2015, Annapolis, MD 2017, Munich 2019).
National Council of Radiation Protection and Measurements (NCRP): Council Member (2008-2026)**;** Member of Scientific Committee (1-17) "Second Cancers and Cardiopulmonary Effects After Radiotherapy." (
Chinese Medical Physics Society: Conference Chairman, 1st (2015), 2nd (2016) and 3rd (2017) *International Forum on Radiation Medical Physics - Critical Issues in R&D, Clinical Practice, and Education for Proton and Heavy-ion Radiotherapy*, paving the way for rapid advancement of the field in China (20 proton hospitals planned, 3 of which have started clinical testing, 30 university programs are taking shape).
International Organization of Medical Physics: Webinar Speaker: New Tools of Phantoms, Monte Carlo Calculations, and AI for Medical Physics Applications (Oct 2021) – 700 worldwide participants
IUPESM WC2012 Organizer for Symposium on "Visible Human Projects in the United States, Korea and China and applications to radiation dosimetry" (Beijing 2012); WC 2022 Organizer for Symposium on "Organ Doses from Diagnostic and Therapeutic Procedures: Necessity and Feasibility" (Singapore 2022).

Publications (https://inmp.ustc.edu.cn/2021/0908/c25802a521946/page.htm)
Prof. Xu has authored/co-authored 2 books, 200+ peer-reviewed journal papers, 400+ conference abstracts, 150+ invited plenary/seminar presentations, 10+ industrial/commercial software packages.
[5 attached]: (Corresponding author in bold and students with *)

1. **Xu XG**, Chao TC*, Bozkurt A*. VIP-Man: An image-based whole-body adult male model constructed from color photographs of the Visible Human Project for multi-particle Monte Carlo calculations. Health Phys., 78(5):476-486 (2000). **One of the most cited papers in "computational phantoms"**
2. **Xu XG**. An exponential growth of computational phantom research in radiation protection, imaging, and radiotherapy: a review of the fifty-year history. Phys. Med. Biol. 59: R233–R302 (2014). **Top-10 most-downloaded paper in PMB in 2014**
3. Ding A*, Gao Y*, Liu H , Caracappa PF, Long DJ*, Bolch WE, Liu Bob, **Xu XG**. VirtualDose: A New CT Dose Reporting Software for Adult and Pediatric Patients. Phys. Med. Biol. 60(14):5601-5625 (2015). **100+ pieces of media coverage**
4. Adam DP*, Liu T*, Caracappa PF, Bednarz BP, **Xu XG**. New capabilities of the Monte Carlo dose engine ARCHER-RT: clinical validation of the Varian TrueBeam machine for VMAT external beam radiotherapy. Med Phys doi.org/10.1002/mp.14143 (2020).
5. Peng Z*, Fang X*, Yan P, Shan H, Liu T*, Pei X, Wang G, Liu B, Kalra M, **Xu XG**. A Method of Rapid Quantification of Patient-Specific Organ Dose for CT Using Coupled Deep Multi-Organ Segmentation Algorithms and GPU-accelerated Monte Carlo Dose Computing. Med Phys doi: 10.1002/mp.14131 (2020).

Awards/Honors:

- National Science Foundation / **Faculty Early Career Development (CAREER) Award** (1999)
- American Association of Physicists in Medicine (AAPM) - **Fellow** (2009)
- American Nuclear Society - **Fellow** (2012)
- Health Physics Society- **Fellow** (2013)
- Council on Ionizing Rad Measurement and Standards (CIRMS) – **R S Caswell Award for Distinguished Achievements** (2015)
- Health Physics Society - **Distinguished Scientific Achievement Award**, (2018)
- the American Association of Physicists in Medicine (AAPM) - **Edith H. Quimby Award for Lifetime Achievement in Medical Physics** (2020)
- American Nuclear Society - **Arthur Holly Compton Award in Education** (2020)
- American Nuclear Society - Radiation Protection and Shielding Div **Rockwell Lifetime Achievement Award** (2020)
- American Institute for Medical and Biological Engineering - **Fellow** (2021)
- North American Chinese Medical Physicists Association (NACMPA) - **Hall of Fame** (2021)

Summary of Significant Contributions (One-page)

Scholarship Prof. Xu is a world authority and one of the foremost researchers in "**Digital Human / Computational Human Phantoms**" that has extremely broad applications in medical physics and biomedical engineering. He has made exceptional contributions to the scientific literature of radiation dosimetry and clinical practice involving radiotherapy and medical imaging, as well as protection of workers and members of the public. Prof. Xu is an extremely productive writer (**2 books, 200+ peer-reviewed journal papers, 400+ conference abstracts, 150+ invited plenary/seminar presentations, 10 industrial/commercial software packages**). He has served as a PI for research grants totaling **US$20M**. He is internationally known as a pioneer and one of the first to propose and demonstrate the concept of "**Digital Human**" that enables the integration of modern medical images and simulation technologies with tissue materials that are radiological, electrical, thermal, chemical, mechanical, or biological (**Xu et al 2000 – one of the most cited papers in the field of human phantom modeling**). In a review article on the history of computational phantoms (**Xu 2014**), Prof. Xu theorized, for the first time, that there were only three distinct methods or generations: (1) Stylized phantoms that are based on quadratic equations; (2) Voxel phantoms that are based on tomographic images; (3) BREP phantoms that are in the form of Non-Uniform Rational B-Splines (NURBS) or polygonal meshes efficient for clinical studies involving organ motions. He noted observation that computational phantoms from the past 60 years followed a surprising pattern of exponential growth. **Prof. Xu's scientific vision and insight allowed me to act as an effective and influential leader of the research community.**

Professional Leadership Within the AAPM, Prof. Xu has served on a number of committees and task groups covering **patient safety, imaging dose, treatment planning, dosimetry, and secondary non-target doses, shielding, and radiation measurements**. For 20 years, he has been serving on the editorial boards of several leading journals (**Physics in Medicine and Biology, Med Physics, Rad Protection Dosimetry**). A Fellow of **AAPM, ANS, HPS and AIMBE**, he was elected the **President (1999-2000) of the Council on Ionizing Radiation Measurements and Standards (CIRMS)**. In 2008, he was elected to a 6-year term (and was re-elected in 2014 and in 2020) as a member of the **National Council of Radiation Protection and Measurements (NCRP)**. For 20 years, he has organized the **International Workshop on Computational Phantoms for Radiation Protection, Imaging and Radiotherapy** and served as the editor of **"Handbook of Anatomical Models for Radiation Dosimetry"** involving 60 authors from 13 countries. His recent roles in China ─ a rapidly advancing country short of both radiotherapy technologies and qualified medical physicists ─ include serving as organizer for the 1st (2015), 2nd (2016) and 3rd (2017) **International Forum on Critical Issues in R&D, Clinical Practice, and Education for Proton and Heavy-ion Radiotherapy in China** ", paving the way for rapid advancement of the field in China. Prof. Xu is a frequent international speaker including **IOMP webinar and IUPESM WC on Medical Physics and Biomedical Engineering**.

Education of Graduate Students Prof. Xu has mentored nearly 100 Ph.D and M.S. students at RPI (Troy, New York, USA) and USTC (Hefei, China) who are currently working as medical/health physicists or engineers in leading medical centers/organizations in the USA such as Columbia University, Yale University Hospital, University of Wisconsin-Madison, Memorial Sloan Kettering Cancer Center, Chang Gung University Hospital, GE Healthcare, Stanford University, Duke University, National Cancer Institute, Johns Hopkins, UCSF, MGH.

Clinical Commercial Products Prof. Xu is the co-founder of two start-up companies that serve the medical physics community: (1) **Virtual Phantoms Inc** (Albany, New York) commercializes VirtualDose™ (For tracking patient organ doses from CT and interventional radiology procedures. In 2021, the SaaS website has registered 35-million applications worldwide making it the most widely used tool of its kind). (2) **Wisdom Technologies, Inc** commercializes DeepViewer (an AI-based automatic multi-organ segmentation tool for radiation therapy), ArcherQA (An independent dose-check software tool for radiation treatment), and DeepPlan (A treatment planning system (TPS) for photons and protons – undergoing clinical testing).

In summary, in the history of "medical physics" and "biomedical engineering", it is rare for a single person to be so productive and successful in all these four areas (research, professional leadership, education, and clinical commercial product development) making significant impact on the clinical practice in the USA, China and beyond. For his exceptional dedication and achievements, Prof. Xu has been recognized by numerous professional awards.

Paper

VIP-MAN: AN IMAGE-BASED WHOLE-BODY ADULT MALE MODEL CONSTRUCTED FROM COLOR PHOTOGRAPHS OF THE VISIBLE HUMAN PROJECT FOR MULTI-PARTICLE MONTE CARLO CALCULATIONS

X. G. Xu,*† T. C. Chao,* and A. Bozkurt*

Abstract—**Human anatomical models have been indispensable to radiation protection dosimetry using Monte Carlo calculations. Existing MIRD-based mathematical models are easy to compute and standardize, but they are simplified and crude compared to human anatomy. This article describes the development of an image-based whole-body model, called VIP-Man, using transversal color photographic images obtained from the National Library of Medicine's Visible Human Project for Monte Carlo organ dose calculations involving photons, electron, neutrons, and protons. As the first of a series of papers on dose calculations based on VIP-Man, this article provides detailed information about how to construct an image-based model, as well as how to adopt it into well-tested Monte Carlo codes, EGS4, MCNP4B, and MCNPX.**
Health Phys. 78(5):476–486; 2000

Key words: Monte Carlo; modeling, dose assessment; imaging; dose, internal

INTRODUCTION

DOSE ASSESSMENT in health physics (radiation protection) relies largely on a few sets of basic organ dosimetric quantities. For example, the fluence-to-dose-equivalent conversion factors are the basis for facility shielding design and for calculating dose to a worker/patient exposed to radiation external to the body (ICRU 1998). For assessing dose equivalent to target organs due to radionuclides internally deposited in the source organ(s) following an accidental intake or a nuclear medicine procedure, the specific absorbed fractions (SAFs) or the specific effective energies (SEEs) are used (Snyder et al. 1978; ICRP 1979, 1990). The whole-body risk can then be assessed by using ICRP methodologies for effective dose or effective dose equivalent (ICRP 1990; U.S. NRC 1991). The conversion factors and SAFs have been pre-determined using human anatomical models and Monte Carlo calculations. The computational procedures involve careful specification of the human body and the irradiation conditions. Radiation transport and energy deposition in the body are taken care of by a Monte Carlo code. It is apparent that the accuracy of these quantities (and others derived from them) depends upon the body modeling, radiation environment modeling, and the Monte Carlo treatment. Over the years, health physics dosimetry has been incrementally improved by adopting more realistic body models and better Monte Carlo techniques. This article is about the latest effort to revolutionize the way the models are developed and adopted for Monte Carlo calculations.

Existing mathematical models

Early models representing the human body were mostly homogeneous slabs, cylinders, and spheres. The first heterogeneous anthropomorphic model was devised at Oak Ridge National Laboratory for the Medical Internal Radiation Dose (MIRD) Committee of The Society of Nuclear Medicine (Snyder et al. 1969, 1978). This model, known as MIRD Phantom, was based on the concept of the "Reference Man" for radiation protection purposes, although it was recognized that variation among individuals could be significant (ICRP 1975). Reference Man was originally defined as being a 20–30-y-old Caucasian, weighing 70 kg and 170 cm in height. The original MIRD phantom was analytically described in three principal sections: an elliptical cylinder representing the arm, torso, and hips; a truncated elliptical cone representing the legs and feet; and an elliptical cylinder representing the head and neck. The mathematical descriptions of the organs were formulated based on descriptive and schematic materials from general anatomy references. The goal was to make the mathematical equations simple, thus minimizing computation time (Snyder et al. 1978; ICRP 1987, 1996). More than 40 organs and tissues were specified, with basically three media of distinct densities: bone, soft tissue, and lung. Later improvements at Oak Ridge National Laboratory

* Nuclear Engineering and Engineering Physics Programs, NES Building, Tibbits Avenue, Rensselaer Polytechnic Institute, Troy, NY 12180; † Medical Physics Division, Department of Radiation Oncology, Albany Medical College, 47 New Scotland Avenue, Albany, NY 12208.

For correspondence or reprints contact: X. G. Xu, Nuclear Engineering and Engineering Physics Programs, NES Building, Tibbits Avenue, Rensselaer Polytechnic Institute, Troy, NY 12180, or email at xug2@rpi.edu.

(*Manuscript received* 9 *December* 1999; *accepted* 13 *January* 2000)

0017-9078/00/0

have led to a "family" of models having both sexes at various ages (Cristy and Eckerman 1987). Others have developed similar models known as the "Adam" and "Eva" (Kramer et al. 1982). One of the most recent improvements is a newly revised head and brain model (Bouchet et al. 1996). These MIRD-based models have served practically as the "standard" to the health physics community. Fig. 1 shows exterior and cut-away views of the mathematical models. Several groups of researchers worldwide have used these MIRD-based mathematical models extensively, with different Monte Carlo computer codes, to calculate internal and external organ doses for a variety of health physics applications involving photon, electron, neutron, and proton sources. For a comprehensive listing of papers and discussions, the readers are referred to ICRU Report 48 (1992) and ICRP Publication 74 (1996). For more than two decades, MIRD-based mathematical models allowed the radiation protection community to gain important insights into the distribution of organ doses that were difficult or impossible to study with physical phantoms.

It is clear, however, that the human anatomy is too complex to be realistically modeled with a limited set of equations. As such, many anatomical details in the mathematical models had to be compromised. In spite of the effort to develop more complicated mathematical models, they remain simplified and crude. For instance, the skeleton in the MIRD mathematical model does not resemble a human, and the radiosensitive red bone marrow is not represented. Many researchers have begun to realize that today's computers are so powerful that it is technically *no longer* necessary to limit the geometry representation to overly simplified shapes. The medical community had already started using advanced imaging techniques, such as Computed Tomography (CT) and Magnetic Resonance Imaging (MRI), to study patient-specific anatomy. These new technologies suggest new types of body models for health physics dosimetry that are image-based and realistic.

Image-based models

3-D medical imaging techniques, such as CT and MRI, have advanced remarkably, allowing us to easily visualize the internal structures of the body and to store the images in versatile digital formats. In the past few years, the radiotherapy community (e.g., the Peregrine Project) has begun to use Monte Carlo techniques with patient CT images for clinical treatment dose optimization (Hartmann Siantar et al. 1997). Compared to the medical community, however, health physicists face at least the following unique and intractable technical challenges: 1) Whole-body models are needed for most health physics applications, but medical images are taken only for a portion of the body (CT procedures expose the patients to intense x rays and MRI is time-consuming); 2) A large amount of internal organs/tissues have to be identified and segmented for organ dose calculations in health physics, while, in radiotherapy, only the tumor volume needs to be specified; 3) The size of a whole-body model can be potentially too big for computers and Monte Carlo codes to handle; and 4) Health physics dosimetry involves photons, electrons, neutrons, and protons, but the majority of the clinical radiotherapy procedures involve only photon/electron beams or seeds (a few centers also involve neutron or proton beams).

Because of these issues, only a few groups have successfully constructed image-based whole-body models (e.g., Zubal et al. 1994; Jones 1997; Hickman and Firpo 1997; Petoussi-Henβ and Zankl 1998). However, these models have some of the following shortcomings:

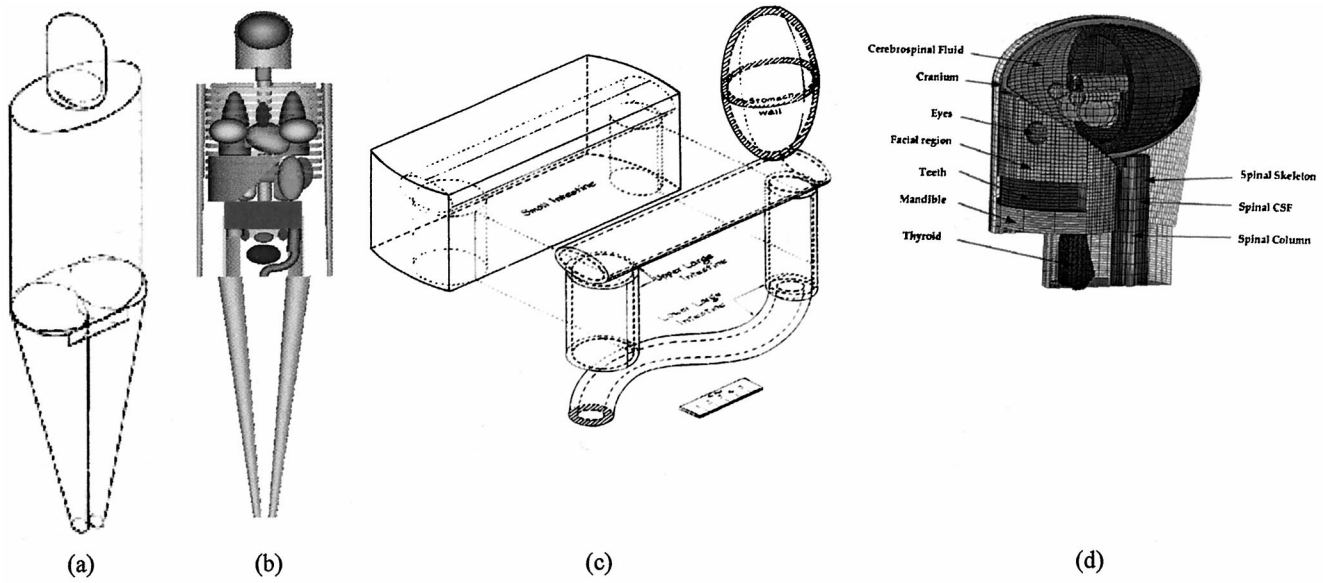

Fig. 1. MIRD-based mathematical adult male model showing (a) exterior view; (b) skeleton and internal organs; (c) detailed GI track; and (d) a recently revised MIRD head and brain model.

1) Not good enough resolutions for small anatomical structures; 2) Not whole body; or 3) No segmentation done. So far all calculations have been only related to photons, and there are practically no results on electron, proton, or neutron sources.

Monte Carlo methods

Analytical calculations for the transport of the radiation through media can be performed only in very simple geometries and under severe approximations. Monte Carlo method, which is based on the first principles, provides the only practical way of performing accurate calculations of 3-D dose distributions from particle interactions in a complex target such as the human body. The earliest use of a Monte Carlo simulation technique was around 1873 (Hammersley and Handscomb 1964). The real development and application of the technique, however, stemmed from work on the atomic bomb during World War II by von Neumann, Ulam, and Fermi. Neumann coined the term "Monte Carlo" to reflect the idea that a conceptual roulette wheel could be employed to select the random nuclear processes. Today, a computer-generated random number between 0 and 1 is used for this purpose. The random number determines which interaction will occur by comparing probabilities (i.e., cross sections) of each interaction. The process is repeated and a particle is tracked in the target until it deposits all its energy or escapes. When a large number of particles (usually several million) are studied this way, the results accurately predict the physical processes that may be experimentally determined. Validation of a code must be done before the code may be used for calculations.

The widespread acceptance of computational models in radiation dosimetry was made possible by the availability of well-validated and maintained Monte Carlo codes and very fast personal computers since the late 1980's. Among all the Monte Carlo codes, there are four general purpose codes that have been widely used in the United States and elsewhere: **1) EGS4**, originally developed at Stanford Linear Accelerator Center, is well known for its detailed physics treatment involving electron-gamma showers (Nelson et al. 1985). Electron transport algorithms, such as the PRESTA, make EGS4 one of the most sophisticated and efficient photon/electron codes ever developed; **2) MCNP**, originated from Los Alamos National Laboratory, has the capability to transport photons, neutrons, and in the recent version 4B, also the electrons (Hendricks 1997). MCNP4B has a generalized input capability allowing a user to model a variety of source and detector conditions without having to modify the source code itself. The "lattice structure" feature facilitates the definition of repeated "cells." However, MCNP is not as efficient as EGS4 in tracking particles in a target that has a very large amount of divided regions; **3) LAHET** is a code for the transport and interaction of nucleons, pions, muons, light ions, and anti-nucleons in complex geometry (Prael and Lichtenstein 1989). The code handles geometry input and the tracking of the particles the same way as MCNP. For neutron interactions above a cutoff energy (20 MeV), the code uses Bertini and Isabel intranuclear cascade models to describe the nuclear interactions mechanism. If the energy falls below the cutoff, the particle transport needs to be performed by the models in MCNP, which are based on ENDF/B cross section libraries; **4) MCNPX**, released in 1999, is a newly merged code that combines the theoretical models of the LAHET Code System with the general features of the MCNP to provide a fully-coupled treatment of the transport problem (Hughes et al. 1997). The code, which is currently only available for UNIX platform, expands the capabilities of MCNP by increasing the set of transportable particles (such as protons). Experience with the beta version shows that MCNPX promises to be a very versatile Monte Carlo code. Together, these codes represent the state-of-the-art in terms of the radiation physics cross-section data and physical models involving photons, electrons, neutrons, and protons. E-mail groups focused on these codes include EGS4-L@mailbox.slac.stanford.edu, mcnp-forum@lanl.gov, and lcs-forum@lanl.gov.

The next section of the article details the development of a new image-based whole-body model from images obtained from National Library of Medicine's Visible Human Project and the procedures to adopt the model into EGS4, MCNP4B, and MCNPX.

MATERIALS AND METHODS

Original images

The quality of original image data for constructing a whole-body model is crucial. At an early stage of our project, several unique sets of whole-body CT/MR/color photographic images from the National Library of Medicine's (NLM) Visible Human Project (VHP) became available (http://www.nlm.nih.gov/research/visible). The ambitious goal of the VHP, which was conceived in 1988 and initiated in 1991, was to build the most detailed digital image library about the anatomies of an adult male and an adult female. VHP is the result of a recommendation from the visionary NLM Board of Regents who foresaw an increasing demand for electronically represented images in clinical medicine and biomedical research (NLM 1990; Ackerman 1995).

Cadavers that were considered "normal" and representative of a large population were evaluated. The donated body of a recently executed 38-y-old male from Texas was the first specimen to be selected for VHP. Later, a 58-y-old female cadaver was also obtained. To ensure the applicability, it was decided that the image data needed to be documented in several common formats used by radiologists and other physicians. Eventually, four modalities were used: traditional x rays and CT scans to optimally visualize bone, MRI for soft tissue, and color photographs for definitive resolution. The color photographs, which had the finest resolution, were used to provide a standard for comparison. Fig. 2 shows the Visible Human Male data set consisting of MRI, CT and color anatomical photographs.

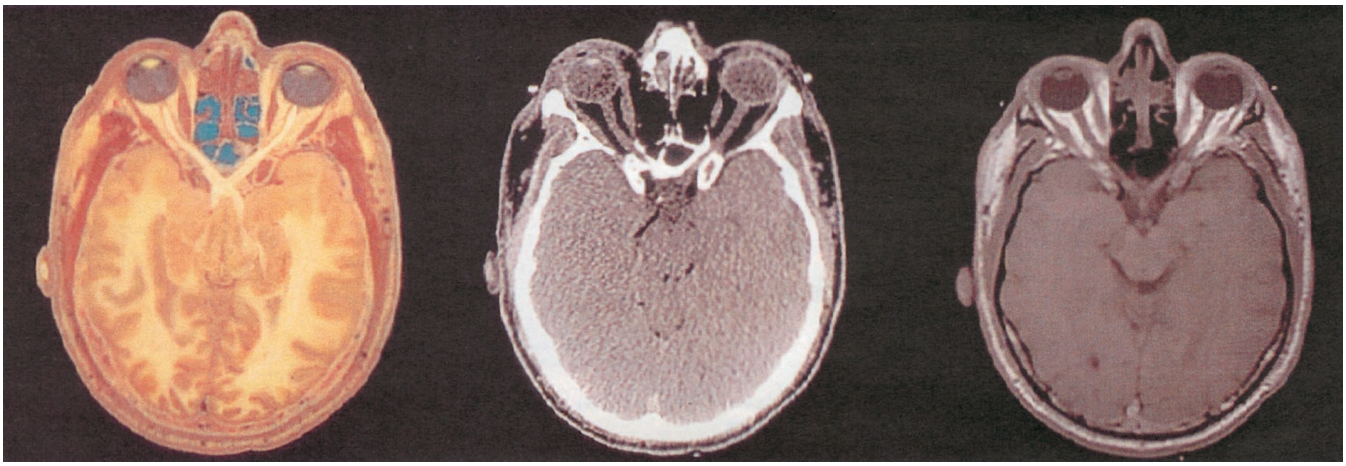

Fig. 2. Images from the Visible Human Project: (Left) Transversal color photography at 2,048 × 1,216 pixel resolution; (Middle) CT images at 512 × 512 pixel resolution; and (Right) MR images at 256 × 256 pixel resolution.

Generally, image format consists of many pixels (picture elements), as shown in Fig. 3, each representing a tissue volume in a 2-D plane. The 3-D volume of the tissue is called a voxel (volume element), and it is determined by multiplying the pixel size by the thickness of an image slice (Bushong 1997). Unlike mathematical whole-body models, an image-based model (also called voxel or tomographic model) contains a huge number of

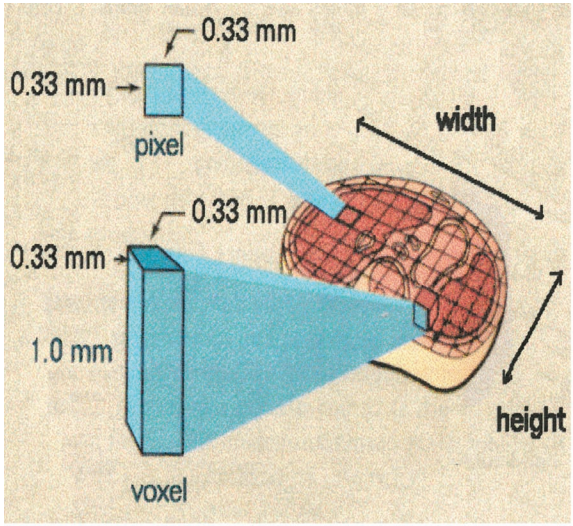

(a)

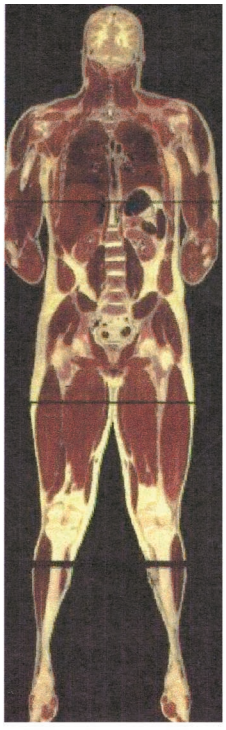

(b)

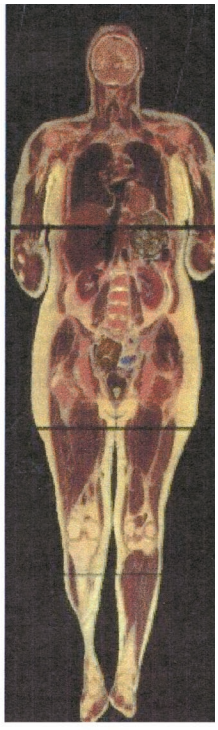

(c)

Fig. 3. (a) Illustration of a pixel and a voxel. A whole-body model is made of a huge number of tiny voxels; (b) Original Visible Man obtained from a 38-y-old male cadaver, 186 cm in height and 90 kg in weight. The pixel resolution is 0.33 mm × 0.33 mm at slice thickness of 1 mm. The whole-body image contains 2,048 × 1,216 × 1,871 = 4.7 billion voxels; (c) Original images of the Visible Woman from a 59-y-old female cadaver, 167 cm in height and 72 kg in weight. The pixel resolution is 0.33 mm × 0.33 mm at slice thickness of 0.33 mm. The whole-body image contains 2,048 × 1,216 × 1,871 × 3 = 14.1 billion voxels.

tiny cubes grouped to represent each anatomical structure. Transversal MRI images of the head and neck and longitudinal sections of the rest of the body were obtained at 4 mm intervals. The MRI images are 256 pixel × 256 pixel resolution. Each pixel has 12 bits of gray tone resolution. The voxel size for MRI data (torso portion) set is 1.88 mm × 1.88 mm × 4 mm. The CT data consists of transversal CT scans of the entire body taken at 1-mm intervals at a resolution of 512 pixels × 512 pixels where each pixel is made up of 12 bits of gray tone. The voxel size for the CT data set (torso portion) is 0.94 mm × 0.94 mm × 1 mm. The transversal anatomical photographs for both male and female cadavers are 2,048 pixels by 1,216 pixels where each pixel is defined by 24 bits of color. The anatomical photographs are at 1-mm-thick slices for the male cadaver and 0.33 mm for the female. There are a total of 1,871 slices CT and anatomical photographs (male), respectively. The transversal anatomical images were obtained by photographing the top surface of the body block after removal of (by shaving) each successive millimeter (0.33 mm for the female) by a cryomacrotome. This color photographic data set for whole-body has a voxel size of 0.33 mm × 0.33 mm × 1 mm for the male (0.33 mm × 0.33 mm × 0.33 mm for the female). Fig. 3 also shows the coronal views constructed from the transverse color images. Since the first public debut on 28 November 1994, VHP images have been available in the public domain (www.nlm.nih.gov/research/visible/). Since then, computer engineers and anatomists, working together, have devoted unprecedented effort to classifying and visualizing the data sets. The Visible Human Male is by far the most complete computerized database of the human body ever assembled (Spitzer and Whitlock 1998). Called "the greatest contribution to anatomy since Vesalius's 1543 publication of De Humani Corporis Fabrica," the VHP data sets are the seeds for a growing medical revolution. Today, scientists worldwide for biomedical sciences and engineering applications are utilizing this national resource for anatomical information (NLM 1998). Based primarily on the color photographic images, a model called *Vi*sible *P*hotographic *Man*, or VIP-Man, has been constructed at Rensselaer for radiation transport studies.

Steps to construct whole-body model

In addition to adopting original VHP images, three more steps had to be completed to construct the VIP-Man: 1) Identify and segment the organs or tissues from the original images; 2) Assign physical properties to organs or tissues; and 3) Implement the anatomical data into a Monte Carlo code. These steps are discussed in detail as follows:

1. The original color photographs for the male had been identified and segmented mostly by manual procedures to yield up to 1,400 structures (Spitzer and Whitlock 1998). Organs or tissues adopted to construct VIP-Man include adrenals, bladder, esophagus, gall bladder, stomach mucosa, heart muscle, kidneys, large intestine, liver, lungs, pancreas, prostate, skeletal components, skin, small intestine, spleen, stomach, testes, thymus, thyroid, etc. Additional automatic and manual imaging processing and segmentation were performed by this group to obtain gray matter, white matter, teeth, skull CSF, stomach mucosa, male breast, eye lenses, and red bone marrow. Traditional image processing techniques were employed to identify tissues based on color separation (for example, redness for red bone marrow). GI track mucosa was realistically represented, except for stomach, where one voxel layer on the inner surface of the wall was used. The male breasts were created by defining a region of skin and soft tissue with appropriate weight. The final list covers "critical" organs or tissues that have been assigned "tissue weighting factors" (ICRP 1990; U.S. NRC 1991). Other organs or tissues are included because of their potential roles in biomedical engineering applications. Once an organ or tissue has been segmented, the associated voxels could be arbitrarily colored for visualization. Fig. 4 shows the images before and after the segmentation, as well as the whole-body 3-D distribution of the red bone marrow. In the mathematical model, the skeleton is not realistic and the red bone marrow is not represented. As a result, the dose to the red bone marrow had always been derived from the dose to the bone assuming each of the bones has a uniform marrow distribution (Reece et al. 1994; Xu et al. 1995; Xu and Reece 1996; Reece and Xu 1997). The only radiosensitive tissue that is not available in VIP-Man is the "bone surface," which is defined as the tissue lining the medullary cavity of a bone (ICRP 1975). At an estimated thickness of 0.01 mm, bone surface will have to be based on images of resolution better than a few microns. Fig. 5 presents views of the 3-D VIP-Man.
2. For engineering applications, organs or tissues of interest have to be related to appropriate physical properties. For radiation protection purposes, the average tissue compositions and densities recommended in ICRP 23 were used to tag each voxel in VIP-Man (ICRP 1975). This step allows the radiation interaction cross section library in a Monte Carlo code to be linked to each voxel for radiation transport simulations. Table 1 compares the organ masses of VIP-Man with the Reference Man by ICRP 23 (1975) and mathematical adult male model by Cristy and Eckerman (1987), all using very similar densities. At more than 103 kg, VIP-Man is fatty, having nearly 30 kg more in fat than the Reference Man. The major organs seem to have much more similar masses than the Reference Man. The body had a slight increase in body volume after it was frozen, causing the weight also to increase. The height of VIP-Man is 186 cm, slightly taller than the Reference Man, which has been recently modified to be 174 cm in height and 73 kg in mass (ICRP 1995). The major organs have fairly similar masses. Technically, VIP-Man can be easily re-scaled by a user if necessary, so that the height and total weight agree even better with the Reference

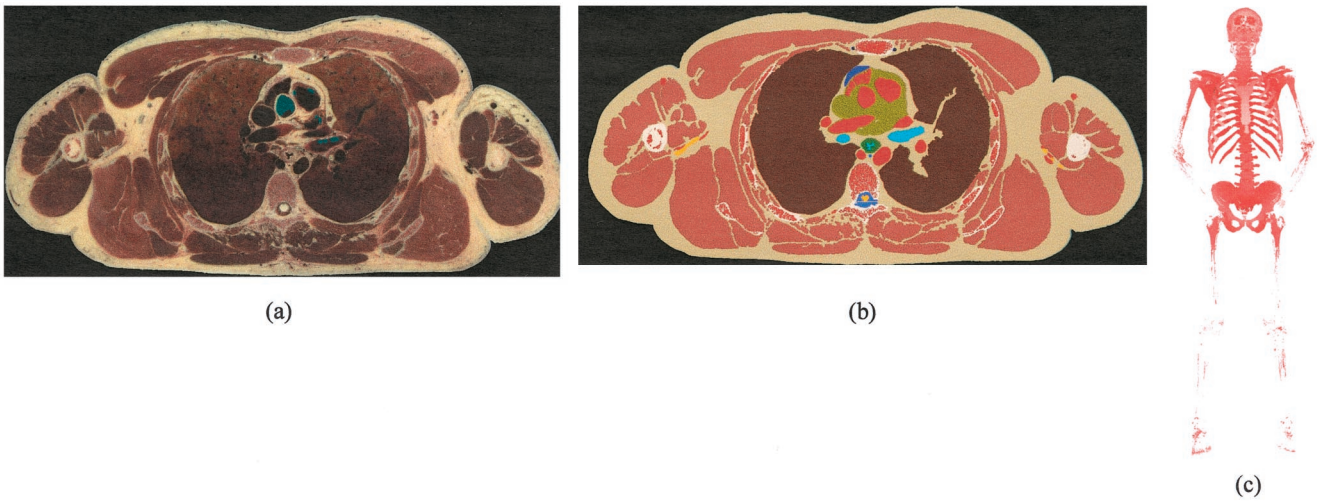

Fig. 4. (a) Original transversal color photograph image (slice No. 1400) at chest level; (b) The same slice after segmentation and classification containing only important organs and tissues; (c) 3-D whole body red bone marrow distribution.

Man. Table 2 lists the mass distributions of red bone marrow and skeleton in VIP-Man in comparison with ICRP 70 Reference Man values (ICRP 1995). As can be seen from Table 2, the mass distribution as segmented for VIP-Man, based on a 38-y-old man, is in remarkable agreement with the ICRP 70 values which were clinically obtained for similar age groups of patients. Table 3 expands the head portion by listing all the tissues that have been included in VIP-Man in comparison with a recently revised MIRD Head/Brain model (Bouchet et al. 1996). There are some noticeable differences in masses, which inevitably will contribute to differences in calculated S-values for internal sources (Snyder et al. 1975; Xu et al. 1999).[‡]

3. Computers have a limited amount of random accessible memory (RAM). Although today's technologies are much more advanced than a few years ago, the maximum "useable" RAM for a typical PC is often less than 1 GB, seemingly less than the size of VIP-Man containing a total of about 3.7 billion voxels and additional coding. A significant amount of effort was required to reduce the memory burden by using an innovative look-up table (LUT) algorithm. The LUT algorithm was successfully implemented in EGS4, allowing the computer to store only key anatomical and physical data; the details are unfolded from specific tables when needed. The memory saving with the LUT algorithm in VIP-Man/EGS4 is about a factor of 20. On a 450-MHz Pentium II PC of 512 MB RAM, VIP-Man/EGS4 can be run at the original 0.33 mm × 0.33 mm × 1 mm voxel size. This makes VIP-Man/EGS4 the finest model ever developed for Monte Carlo calculations. MCNP and MCNPX, on the other hand, were designed to be general-purpose codes; therefore, their default code options had to be changed to optimize memory. These improvements, however, were not enough, and as a result, the voxel size of VIP-Man/MCNP/X had to be compromised to 4 mm × 4 mm × 4 mm (or about 6 million voxels for the whole body) in order to run it on the same PC. Others have reportedly been able to handle a head model of 65 million voxels in MCNP4A using the ASCI Blue Mountain supercomputer (over 6,000 Parallel CPUs from SGI) at Los Alamos National Laboratory.[§‖] Therefore, the original voxel size at 0.33 mm seems to be out of reach for a foreseeable time. Although the resolution for VIP-Man/MCNP/X is limited by the current computer technologies, VIP-Man/MCNP/X is the first whole-body model ever constructed for neutron and proton dose calculations. Although the current running time is more than 10 h due to the size of data, the detailed physics treatments in EGS4, MCNP4B, and MCNPX were not compromised in any way. All of our calculations are being performed on PCs operated under a Linux environment, which is a complete operating system that is similar but not identical to UNIX. The parallel virtual machine (pvm) in Linux enabled us to use multiple CPUs for very time-consuming tasks. Compilers, such as g77, had to be used in EGS4 to

[‡] Xu, X. G.; Chao, T. C.; Bozkurt A.; Eckerman, K. F. Voxel-based adult male model using color photographic images from VHP. Invited Presentation at International Workshop on the Development of Human Anatomical Models. Oak Ridge, Tennesseee. September 28–30, 1999.

[§] Grooley, J. Voxelized model for MCNP. Private e-mail. 24 May 1999.

[‖] McKinney, G. W. Voxelized model for MCNP. Private e-mail. 24 May 1999.

Table 1. Comparison of organ masses for VIP-Man, MIRD Mathematical Phantom, and ICRP 23 Reference Man.[a]

Organs/tissues	VIP-Man (g)	MIRD (g)	ICRP 23 (g)
Adrenals	8.3	16.3	14.0
Bladder (wall)	41.4	47.6	45.0
Bladder (urine)	43.2	211.0	102.0
Brain + nerve	1,574.0	1,420.0	1,429.0
Breast (male)	33.6	403.0	26.0
CSF	265.1	—	121.0
Esophagus (wall)	38.9	—	40.0
Esophagus (lumen)	26.8	—	—
Esophagus (mucosa)	3.5	—	—
Fat	36,326.6	—	17,200.0
Gall bladder (wall)	12.0	10.5	10.0
Gall bladder (bile)	21.0	55.7	60.0
Heart muscle	398.7	316.0	330.0
Kidneys	335.4	299.0	310.0
Lens of eyes	0.54	—	0.4
Liver	1,937.9	1,910.0	1,800.0
Lower large intestine (wall)	290.8	167.0	160.0
Lower large intestine (lumen)	324.2	143.0	135.0
Lower large intestine (mucosa)	35.8	—	—
Lungs	910.5	1,000.0	1,000.0
Muscle	43,002.6	—	28,000.0
Pancreas	82.9	94.3	100.0
Prostate	18.9	—	16.0
Skeleton+RBM	11,244.6	10,000.0	10,000.0
Skin	2,253.4	3,010.0	2,600.0
Small intestine	1,291.8	1,100.0	1,040.0
Spleen	244.0	183.0	180.0
Stomach (wall)	159.5	158.0	150.0
Stomach (content)	324.5	260.0	250.0
Stomach (mucosa)	13.7	—	—
Testes	21 (1)	39.1	35.0
Thymus	11.2	20.9	20.0
Thyroid	27.6	20.7	20.0
Upper large intestine (wall)	461.1	220.0	160.0
Upper large intestine (lumen)	905.7	232.0	135.0
Upper large intestine (mucosa)	63.4	—	—
Other	1,688.0	51,887.7	4,382.0
Total	104,277.2	73,224.8	70,000.0

[a] Reference Man values are from ICRP 23 (1975) and the MIRD model values from Cristy and Eckerman (1987).

accommodate the large integral format.[¶] Since both EGS4 and MCNP4B transport photons and electrons, we were able to "validate" the modeling and Monte Carlo coding by making sure both codes give the same results for VIP-Man (at identical voxel sizes at 4 mm × 4 mm × 4 mm resolution). Fig. 6 compares organ doses from 1-MeV parallel photon beams at anterior-posterior (AP) direction. The calculations took about 50 h for 10-million photons in MCNP and about 25 h for 25-million photons in EGS4. Both codes tracked electrons by different transport algorithms with carefully optimized electron step settings. Results indicated remarkable agreement within the statistical uncertainty between EGS4 and MCNP. More information about benchmarking will be published in a later article.

CONCLUSION

An adult male whole-body model, VIP-Man, has been constructed from the color photographic images of the famous Visible Human Project. VIP-Man has been adopted into the state-of-the-art Monte Carlo codes, EGS4, MCNP, and MCNPX for radiation transport studies and organ dose calculations involving photons, electrons, neutrons, and protons. To date, VIP-Man represents the world's finest and most complete human anatomical model, containing small tissues, such as skin, GI track mucosa, eye lenses, and red bone marrow, which were not (or not as realistically) represented in the MIRD-based mathematical models and other image-based models. This is also the first time that an image-based whole-body model was adopted for Monte Carlo calculations involving electrons, neutrons, and protons. These advances are significant in that we now are able to investigate subtle dose variations in relatively small structures from various charged particles. The new capability in multiple particle transport not only provides needed health physics dosimetric data but also opens doors for applications in radiotherapy. Compared to MIRD-based mathematical models, VIP-Man is realistic and contains much more anatomical information. The detailed procedure for constructing the image-based models presented in this article should help allow readers to develop their own models in the future.

[¶] Chao, T. C.; Bozkurt, A.; Xu, X. G. Development and validation of a specialized Monte Carlo code for voxelized whole body model from very large segmented images. In preparation.

Table 2. Comparison of skeleton and red bone marrow mass distributions from VIP-Man and ICRP 70 (1995) Reference Man.

	Red bone marrow		Skeleton (w/marrow)	
Bone structure	VIP-Man (g)	ICRP 70 Ref. Man (g)	VIP-Man (g)	ICRP 70 Ref. Man (g)
Cranium	48.21	88.92	876.43	1,239.00
Mandible	2.00	9.36	89.14	126.00
Scapulae	46.43	32.76	319.24	378.00
Clavicles	13.41	9.36	102.68	84.00
Sternum	43.13	36.27	117.00	126.00
Ribs	160.80	188.37	728.34	735.00
Cervical vertebrae	22.87	45.63	155.85	
Thoracic vertebrae	145.06	188.37	563.28	1,995.00
Lumbar vertebrae	135.09	143.91	470.22	
Sacrum	110.07	115.83	303.16	
Innominate	315.93	204.75	1,071.43	1,113.00
Femora	41.37	78.39	2,027.67	1,606.50
Tibiae	0.78	—	1,376.93	1,186.50
Other foot	2.01	—	768.96	661.50
Humeri	37.09	26.91	647.61	556.50
Radii and Ulane	2.08	—	379.68	378.00
Other hand bone	1.11	—	244.64	241.50
Other	1.14	1.17	21.01	73.50
Total	1,128.57	1,170.00	10,263.27	10,500.00

Table 3. Comparison of tissues in the head/brain for VIP-Man and recently revised MIRD model (Bouchet 1996).

	VIP-Man			Revised MIRD head/brain Model		
Tissue/organ	Mass (g)	Volume (cm^3)	Density ($g\ cm^{-3}$)	Mass (g)	Volume (cm^3)	Density ($g\ cm^{-3}$)
Caudate nuclei	8.95	8.60	1.04	10.50	10.10	1.04
Cerebellum	122.69	117.97	1.04	139.10	133.75	1.04
Cerebral cortex	681.37	656.11	1.04	622.40	598.46	1.04
Cranial CSF	97.75	94.90	1.03	56.90	54.71	1.04
Cranium	841.44	568.54	1.48	364.60	260.43	1.40
Eyes	14.91	14.48	1.03	15.20	14.62	1.04
Lentiform nuclei	13.41	12.53	1.07	19.40	18.65	1.04
Mandible	86.22	58.26	1.48	170.50	121.79	1.40
Teeth	40.51	19.29	2.10	31.20	22.29	1.40
Thalami	8.07	7.76	1.04	15.70	15.10	1.04
Thyroid	27.56	26.25	1.05	19.90	19.13	1.04
White matter	440.49	422.21	1.04	639.20	614.62	1.04
Lateral ventricle	7.08	6.87	1.03	20.10	19.33	1.04
Corpus callosum	16.92	16.27	1.04	—	—	—
Pons and middle cerebellar peduncle	24.57	23.62	1.04	—	—	—
Fronix	2.22	2.14	1.04	—	—	—
Optic chiasma	0.33	0.32	1.04	—	—	—
Vestibulocochlear	0.07	0.06	1.04	—	—	—
Optic nerve	1.75	1.68	1.04	—	—	—
Lens of eyes	0.54	0.49	1.10	—	—	—

It is perhaps important to note that there are Monte Carlo photon transport codes that lack the capability of transporting electrons. In these codes, secondary electrons from photon interactions have to be assumed to deposit their energies at the interaction sites (i.e., kerma approximation) (ICRP 1996). Kerma approximation is valid only when charged particle equilibrium is established, for example, in a large volume of tissue for mean absorbed dose calculations (Attix 1986). Therefore, high energy photons incident on relatively shallow tissues described by tiny voxels (such as skin, eye lenses or gonads) or at a boundary of tissues having different densities (e.g., bone and lung) would be problematic without tracking secondary electrons. In the case of neutron transport, kerma approximation (i.e., without tracking the recoil protons) should also be practiced with care. This is an important issue that should be kept in mind when comparing dose results obtained from different Monte Carlo codes. A standard procedure for comparing Monte Carlo calculations should also be developed, taking into account of the voxelized small geometries.

VIP-Man is being used to evaluate and compare some of

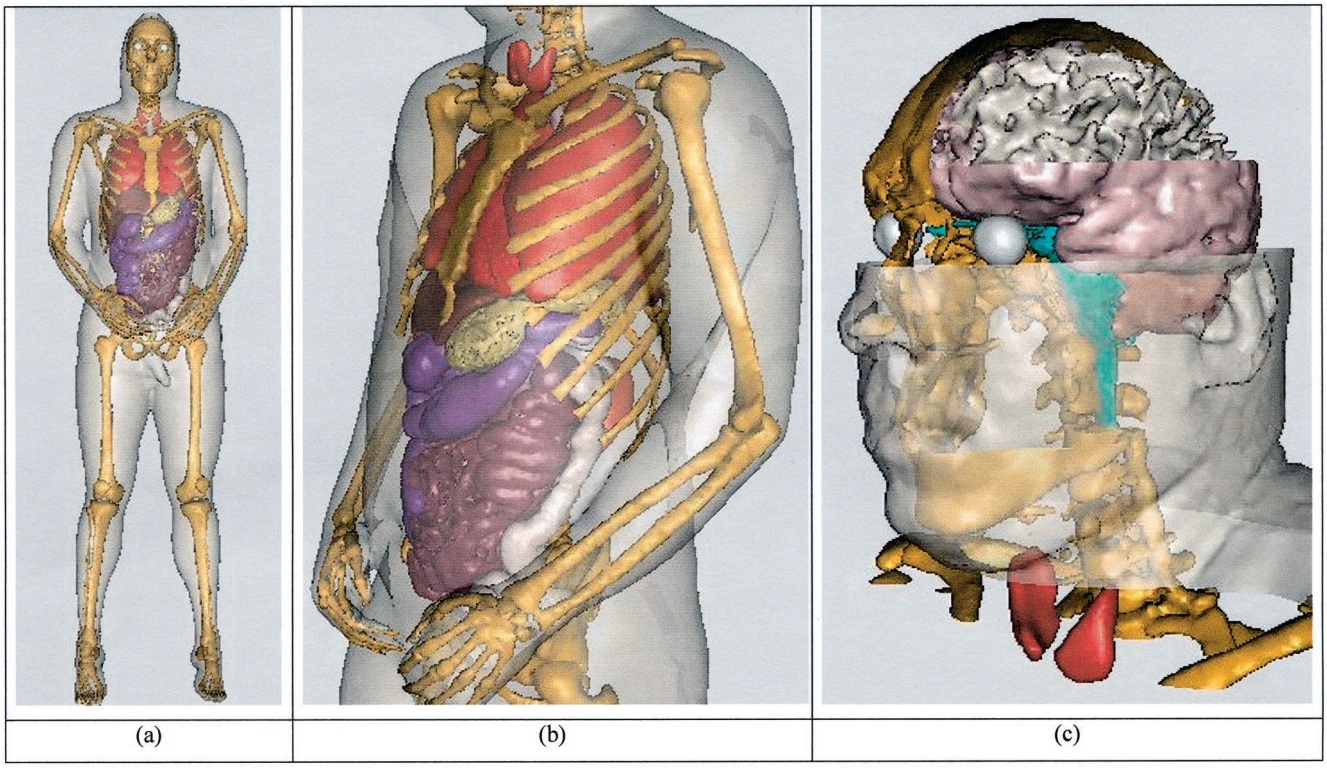

Fig. 5. VIP-Man in 3-D views showing (a) whole-body skin and skeletal structure; (b) details of internal organs with lungs in red, stomach in gold, upper large intestine in purple, kidney in red, liver in maroon, lower large intestine in brown, etc.; (c) details of the head and brain containing skull in gold, white matter in white, gray matter in gray, nerve in blue, spinal cord in gold, thyroid in red, and skin in white, etc. Visualization Toolkit was used in the surface rendering of the voxelized images (Schroeder et al. 1997).

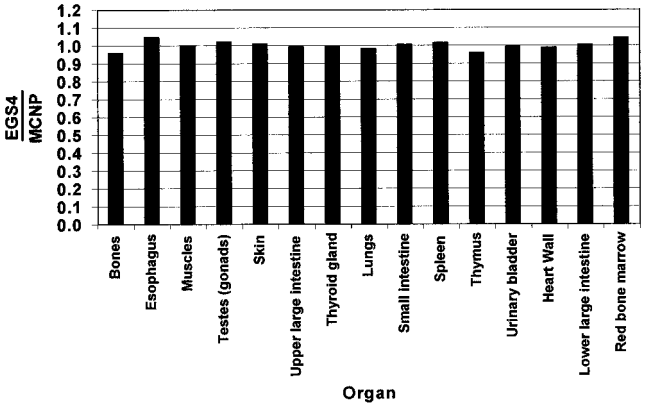

Fig. 6. Comparison of organ doses for VIP-Man using EGS4 and MCNP4B for 1-MeV parallel photon beams at AP direction.

the most important dosimetric quantities for external and internal sources under standard irradiation conditions that have been studied in the past with other models. For more information about this project, please contact the authors or visit http://www.rpi.edu/dept/radsafe/public_html/. Copies of papers and presentations about VIP-Man are also available from the Web site. A series of papers, with interested collaborators, are expected to document all these studies, including results for doses to some of the never-before-modeled organs or tissues. Meanwhile, it should be noted that well-defined MIRD models, although not realistic, have the advantage of being relatively easy to adopt for Monte Carlo calculation and for standardization. This kind of model, however, can be made more anatomically accurate by adopting the data available from VIP-Man and other image-based models. At the present time, it is urgent to fully understand the dosimetric differences between the two types of models. For the purposes of setting radiation protection standards, it may be possible to eventually bridge these two types of models, leading to a new generation of hybrid "standard" model(s) that will be acceptable to the radiation protection community. Such a new generation of models for radiation protection should be realistic enough to accurately represent major radiosensitive tissues and organs, and flexible enough to represent different populations by scaling. Computers are going to be so powerful that very complex models can be handled without a problem. No matter what will happen, however, it is certain that health physics dosimetry will be more realistic and accurate because of these image-based models and the state-of-the-art Monte Carlo techniques. It is anticipated that, for situations involving high occupational radiation exposures (for example, when people travel to the space station on a

daily basis in the future), person-specific dosimetry can be done using images (such as MRI) coupled with rapid segmentation tools and well established Monte Carlo procedures.

VIP-Man also has wide applications in clinical radiotherapy, where highly precise treatment plans have to be verified and optimized with a standard patient dosimetric model (Aldridge et al. 1999). Fundamentally, VIP-Man is digital and it can be easily adopted for applications beyond radiation transport by coupling with physical properties that are electrical, thermal, chemical, mechanical, or biological. When these become technically possible in the future, the reality of "virtual digital human" for every citizen in the "digital society" will be within reach.

Acknowledgments—The authors would like to thank many organizations and individuals who helped make this project possible, particularly, the National Science Foundation/Biomedical Engineering Program for a Faculty Early Career Development Award (BES-9875532), the National Library of Medicine for the Visible Human images, Keith Eckerman at Oak Ridge National Laboratory for his insightful discussions during the planning and execution of the project, and the Monte Carlo Transport Methods Group at Los Alamos National Laboratory for their technical inputs on MCNP and MCNPX.

REFERENCES

Ackerman, M. J. Accessing the visible human project. D-lib Magazine: The magazine of the digital library forum. 1995. http://www.dlib.org/dlib/october95/10ackerman.html.

Aldridge, J. S.; Rechwerdt, P. J.; Rockie, T. R. A proposal for a standard electronic anthropomorphic phantom for radiotherapy. Med. Phys. 26:1901–1903; 1999.

Attix, F. H. Introduction to radiological physics and radiation dosimetry. New York: John Wiley & Sons; 1986.

Bouchet, L. G.; Bolch, W. E.; Weber, D. A.; Atkins, H. L.; Poston, J. W. Sr. A revised dosimetric model of the adult head and brain. J. Nucl. Med. 37:1226–1236; 1996.

Bushong, S. C. Radiological science for technologists. New York: Mosby-Year Book; 1997.

Cristy, M.; Eckerman, K. F. Specific absorbed fractions of energy at various ages from internal photon sources. Oak Ridge, TN: Oak Ridge National Laboratory; Report No. ORNL/TM-8381/V1; 1987.

Hammersley, J. M.; Handscomb, D. C. Monte Carlo methods. London: Methuen; 1964.

Hartmann Siantar, C. L.; Bergstrom, P. M.; Chandler, W. P.; Chase, L.; Cox, L. J.; Daly, T. P.; Garrett, D.; Hornstein, S. M.; House, R. K.; Moses, E. I.; Patterson, R. W.; Rathkopf, J. A.; Schach von Wittenau, A. Lawrence Livermore National Laboratory's PEREGRINE Project. Livermore, CA: LLNL; Report No. UCRL-JC-126732; 1997.

Hendricks, J. S. MCNP4B, LANL memorandum. Los Alamos, MN: Los Alamos National Laboratory; 1997.

Hickman, D. P.; Firpo, M. Magnetic resonance image phantom. Livermore, CA: Lawrence Livermore National Laboratory; UCRL-MA-118455; 1997.

Hughes, H. G.; Prael, R. E.; Little, R. C. MCNPX—The LAHET/MCNP Code Merger. Los Alamos, NM: Los Alamos National Laboratory; XTM-RN(U) 97-012; 1997.

ICRP. Report of the task group on Reference Man. Oxford: Pergamon Press; ICRP Publication 23; 1975.

ICRP. Limits for intake of radionuclides by workers. Oxford: Pergamon Press; ICRP Publication 30; 1979.

ICRP. Data for use in protection against external radiation. Oxford: Pergamon Press; ICRP Publication 51; 1987.

ICRP. Recommendations of the International Commission on Radiological Protection. Oxford: Pergamon Press; ICRP Publication 60; 1990.

ICRP. Basic anatomical and physiological data for use in radiological protection: the skeleton. Oxford: Pergamon Press; Ann. ICRP 25(2), ICRP Publication 70; 1995.

ICRP. Conversion coefficients for use in radiological protection against external radiation. Oxford: Pergamon Press; ICRP Publication 74; 1996.

ICRU. Phantoms and computational models in therapy, diagnosis and protection. Bethesda, MD: International Commission on Radiation Units and Measurements; ICRU Report 48; 1992.

ICRU. Conversion coefficients for use in radiological protection against external radiation. Bethesda, MD: International Commission on Radiation Units and Measurements; ICRU Report 57; 1998.

Jones, D. G. A realistic anthropomorphic phantom for calculating organ doses arising from external photon irradiation. Radiat. Prot. Dosim. 72:21–29; 1997.

Kramer, R.; Zankl, M.; Williams, G.; Drexler, G. The calculation of dose from external photon exposures using reference human phantoms and Monte-Carlo methods, Part 1: The male (ADAM) and female (EVA) adult mathematical phantoms. Munchen: Gesellschaft fur Strahlen-und Umweltforschung mbH; GSF Bericht S-885; 1982.

National Library of Medicine, U.S. Board of Regents. Electronic imaging: Report of the Board of Regents. Bethesda, MD: National Library of Medicine; NIH Publication 90-2197; 1990.

National Library of Medicine. Proceedings of the Second Visible Human Project Conference, October 1–2. Bethesda, MD: National Library of Medicine; 1998.

Nelson, W. R.; Hirayama, H.; Rogers, D. W. O. The EGS4 code system. Stanford, CA: Stanford Linear Accelerator Center; SLAC-265-UC-32; 1985.

Petoussi-Henβ, N.; Zankl, M. Voxel anthropomorphic models as a tool for internal dosimetry. Radiat. Prot. Dosim. 79:415–418; 1998.

Prael, R. E.; Lichtenstein, H. User guide to LCS: The LAHET code system. Los Alamos, NM: Los Alamos National Laboratory; LA-UR-893014; 1989.

Reece, W. D.; Poston, J. W.; Xu, X. G. Determining the effective dose equivalent for external photons: Calculational results for beam and point-sources. Radiat. Prot. Dosim. 55:5–21; 1994.

Reece, W. D.; Xu, X. G. Determining effective dose equivalent for external photon radiation: Assessing effective dose equivalent from personal dosemeter readings. Radiat. Prot. Dosim. 69:167–178; 1997.

Schroeder, W.; Martin, K.; Lorensen, B. The visualization toolkit—An object-oriented approach to 3D graphics. New Jersey: Prentice Hall; 1997.

Snyder, W. S.; Ford, M. R.; Warner, G. G.; Fisher H. L., Jr. Estimates of absorbed fractions for monoenergetic photon source uniformly distributed in various organs of a heterogeneous phantom. Medical Internal Radiation Dose Committee (MIRD) Pamphlet No. 5, Supplement No. 3. J. Nuclear Med. 10. New York: Society of Nuclear Medicine; 1969.

Snyder, W. S.; Ford, M. R.; Warner, G. G.; Watson, S. B. "S," absorbed dose per unit cumulated activity for selected radionuclides and organs. New York, NY: The Society of Nuclear Medicine; Medical Internal Radiation Dose Committee (MIRD) Pamphlet No. 11; 1975.

Snyder, W. S.; Ford, M. R.; Warner, G. G.; Fisher H. L., Jr. Estimates of absorbed fractions for monoenergetic photon source uniformly distributed in various organs of a heterogeneous phantom. New York, NY: The Society of Nuclear Medicine; Medical Internal Radiation Dose Committee (MIRD) Pamphlet No. 5, Revised; 1978.

Spitzer, V. M.; Whitlock, D. G. Atlas of the visible human male. Sudbury, MA: Jones and Bartlett Publishers; 1998.

U.S. Nuclear Regulatory Commission. Title 10 Part 20 of the Code of Federal Regulations: Standards for protection against radiation. Washington, DC: U.S. NRC; 1991.

Xu, X. G.; Chao, T. C.; Bozkurt, A.; Eckerman, K. F. Development of realistic body models for organ dose calculations. Health Phys. S76:S160; 1999.

Xu, X. G.; Reece, W. D. Sex-specific tissue weighting factors for effective dose equivalent calculations. Health Phys. 70:81–86; 1996.

Xu, X. G.; Reece, W. D.; Poston, J. W. A study of the angular dependence problem in effective dose equivalent assessment. Health Phys. 68:214–224; 1995.

Zubal, I. G.; Harrel, C. R.; Smith, E. O.; Rattner, Z.; Gindi, G.; Hoffer, P. B. Computerized three-dimensional segmented human anatomy. Med. Phys. 21:299–302; 1994.

■ ■

IOP Publishing | Institute of Physics and Engineering in Medicine Physics in Medicine & Biology

Phys. Med. Biol. **59** (2014) R233–R302 doi:10.1088/0031-9155/59/18/R233

Topical Reviews

An exponential growth of computational phantom research in radiation protection, imaging, and radiotherapy: a review of the fifty-year history

X George Xu

Rensselaer Polytechnic Institute Troy, New York, USA

Received , revised
Accepted for publication 7 July 2014
Published 21 August 2014

Abstract

Radiation dose calculation using models of the human anatomy has been a subject of great interest to radiation protection, medical imaging, and radiotherapy. However, early pioneers of this field did not foresee the exponential growth of research activity as observed today. This review article walks the reader through the history of the research and development in this field of study which started some 50 years ago. This review identifies a clear progression of computational phantom complexity which can be denoted by three distinct generations. The first generation of stylized phantoms, representing a grouping of less than dozen models, was initially developed in the 1960s at Oak Ridge National Laboratory to calculate internal doses from nuclear medicine procedures. Despite their anatomical simplicity, these computational phantoms were the best tools available at the time for internal/external dosimetry, image evaluation, and treatment dose evaluations. A second generation of a large number of voxelized phantoms arose rapidly in the late 1980s as a result of the increased availability of tomographic medical imaging and computers. Surprisingly, the last decade saw the emergence of the third generation of phantoms which are based on advanced geometries called boundary representation (BREP) in the form of Non-Uniform Rational B-Splines (NURBS) or polygonal meshes. This new class of phantoms now consists of over 287 models including those used for non-ionizing radiation applications. This review article aims to provide the reader with a general understanding of how the field of computational phantoms came about and the technical challenges it faced at different times. This goal is achieved by defining basic geometry modeling techniques and by analyzing selected phantoms in terms of geometrical features and dosimetric problems to be solved. The rich historical information is summarized in four tables that are aided by highlights in the text on how some of the most well-known phantoms were developed and used in practice. Some of the information covered in this

review has not been previously reported, for example, the CAM and CAF phantoms developed in 1970s for space radiation applications. The author also clarifies confusion about 'population-average' prospective dosimetry needed for radiological protection under the current ICRP radiation protection system and 'individualized' retrospective dosimetry often performed for medical physics studies. To illustrate the impact of computational phantoms, a section of this article is devoted to examples from the author's own research group. Finally the author explains an unexpected finding during the course of preparing for this article that the phantoms from the past 50 years followed a pattern of exponential growth. The review ends on a brief discussion of future research needs (a supplementary file '3DPhantoms.pdf' to figure 15 is available for download that will allow a reader to interactively visualize the phantoms in 3D).

S Online supplementary data available from stacks.iop.org/Phys.Med.Biol./59/R233/mmedia

(Some figures may appear in colour only in the online journal)

1. Introduction

For more than 50 years, radiation dose assessment using computational models of the human anatomy has been a subject of great interest to the fields of radiation protection, medical imaging, and radiotherapy. Health physicists often need to understand how radiation interacts with the human body so that they can ensure the safety of workers and members of the public in accordance with complicated regulatory requirements. In diagnostic radiology and nuclear medicine, the imaging process—involving x-ray and gamma-ray photons powerful enough to traverse bodily tissues—must be optimized to achieve necessary image quality while minimizing potentially harmful radiobiological effects. Radiation therapy aims to deposit a lethal dose to the tumor—which may be subjected to organ motion—using focused external beams of x-ray and gamma-ray photons, electrons, protons, and heavy ions, or using internal sources that are less penetrating, while sparing healthy tissues from toxicity and secondary cancer. The anatomical modeling techniques evolved over time and new phantoms would emerge, as expected. However, the early pioneers of this field did not foresee the exponential growth of research activity that this review article has uncovered.

Radiation dosimetry is a basic science that has to do with the determination of the amount and distribution pattern of ionizing energy deposited in the object of interest. Accurate radiation dosimetry in the human body is quite challenging for several reasons: (1) exposure scenarios are diverse, often including complex and unique geometrical relationships between the source and human body; (2) an exposure can involve multiple radiation types, each of which transverse the human body and interact with tissues according to different radiation physics principles; (3) the human body consists of a very large number of anatomical structures that are heterogeneous in density and composition sometimes under in the influence of organ motion. For instance, cardiac and respiratory motion can result in complex 3-dimensional (3D) and 4-dimensional (4D) dose distribution patterns that must be accounted for during medical imaging or radiotherapy. This last point underscores the importance of anatomical models in radiation dosimetry because dose inside a living person cannot usually be directly measured. Instead, one must use computational or physical anatomical models to estimate the dose delivered to a worker or patient exposed to ionizing radiation. The accuracy of the dose estimate critically depends on how well the anatomical models account for the specific

geometry and radiation attenuation properties of each individual—a quite daunting task in light of the fact that every person has a unique body shape and size.

It has been known for a long time that dose inside the body can be derived using either a physical phantom or a computational phantom that mimics human anatomical features. Historically, the term *phantom* was used in the radiological science literature to mean a physical device that mimics the human body. In the radiation protection community, phantom has also been used to refer to a mathematically defined *anatomical model* instead of a physiologically based model such as a respiration or blood flow model. In this review article, 'computational phantom' and 'physical phantom' are used to avoid confusion.

Physical phantoms are made of solid materials which are radiologically equivalent to human tissues. Because the human body consists mostly of water, homogenized water or plastic phantoms are widely used for the calibration of radiation detectors and treatment systems. The simpler designs of these phantoms are useful for routine measurements where standardization between laboratories or hospitals is of critical importance (DeWerd and Kissick 2014). Another use of such homogeneous phantoms is to calibrate calculations by measuring the power output from a specific radiation-emitting machine. In contrast, anthropomorphic phantoms are more realistic and better represent the complex heterogeneity of the human body; they often consist of several tissue-equivalent materials that are molded into shapes of organs or bones to represent part or all of the body. For the ease of placing tiny radiation dosimeters, some of the physical phantoms for dose measurements come in slices with cavities in locations that match with organs of interest.

The approach of using such anthropomorphic physical phantoms for organ dose measurements can be expensive and time-consuming due to necessary experimental and radiation safety procedures. Furthermore, commercially available physical phantoms only come in a limited number of body sizes and do not fully reflect the diversity of the human population. Luckily, the advent of first-generation computers and Monte Carlo simulation methods originally designed for nuclear weapons research demonstrated the feasibility to calculate organ doses using computational phantoms. Such computational phantoms include extensive details of the exterior and interior features of the human body such as the shape, volume, and mass of radiosensitive organs. Coupled with information for tissue density and chemical composition, a computational phantom allows a researcher to simulate radiation interactions and energy deposition patterns in the body accurately. Although experimental work involving a whole-body physical phantom is still needed to verify the calculations especially when involving complex irradiation conditions, the computational approach is, in general, advantageous compared with the experimental approach in versatility, efficiency, precision, and safety. Furthermore, internally distributed radiation sources are best handled by the computational approach.

Since the 1960s, the development and application of computational phantoms have evolved into a specialized field of research that is integral to radiation protection, medical imaging, and radiotherapy. For non-ionizing radiation, similar computational phantoms have been developed over the years to study the biological effects caused by the heat produced by radiofrequency-emitting devices such as electric power lines and wireless cellular-phones. In the twenty years after the first computational phantom was developed in the 1960s, less than two dozen computational phantoms were developed and used by a small group of people in national laboratories who had access to computers. Computational phantoms became widely adopted in the 1980s with the advent of personal computers. By then, medical imaging had made it possible to visualize the anatomy in 3D. An international research community soon took shape and, over the years, several workshops were held to disseminate research ideas, facilitate collaboration, and develop roadmap for the future.

In 1996, Peter Dimbylow organized the first workshop on voxelized computational phantoms at the National Board of Radiological Protection (now Health Protection Agency) in the United Kingdom (Dimbylow 1996). In 2000, Keith Eckerman hosted a similar workshop at Oak Ridge National Laboratory in the United States (Eckerman 2000). The interest about computational phantoms was so widespread in the mid of 2000s that many colleagues decided to form the Consortium of Computational Human Phantoms (CCHP) during a dinner meeting at the Monte Carlo 2005 Topical Meeting, American Nuclear Society, Chattanooga, TN, April 17–21, 2005 (http://www.virtualphantoms.org). Under the umbrella of CCHP, George Xu and Keith Eckerman published the *Handbook of Anatomical Models for Radiation Dosimetry* in 2009 involved 64 authors from 13 countries (Xu and Eckerman 2010). In 2011, George Xu and Junli Li organized a workshop under the name of 'The 3rd International Workshop on Computational Phantoms for Radiation Protection, Imaging and Radiotherapy,' in Beijing, China (http://www.virtualphantoms.org/3rdWorkshopInBeijing.html). The Beijing Workshop was the first time that researchers from both ionizing and non-ionizing radiation communities attended. In Beijing, it was decided that the workshop would be held every other year. The 4th workshop (http://cp2013.org/) was then hosted by Niels Kuster of the Foundation for Research on Information Technologies in Society (IT'IS) in Zurich, Switzerland, May 20–22, 2013. At the Zurich workshop, it was decided to hold the next workshop in Seoul, Korea in 2015.

By 2009, approximately 121 computational phantoms had already been reported in the literature for studies involving ionizing and non-ionizing radiation (Xu and Eckerman 2010). Such a large number of computational phantoms was somewhat surprising at the time, given the fact that less than a dozen existed prior to the 1980s. Most of these phantoms were reported during the late 1980s and early 1990s due to the increased availability of advanced medical imaging technologies such as x-ray computed tomography (CT) and magnetic resonance imaging (MRI). It also became clear that organ surfaces could be defined in a variety of solid geometry modeling techniques including those we were familiar with, such as quadric equations and voxels, but also advanced geometries such as B-Splines, Non-Uniform Rational B-Splines (NURBS), and polygonal meshes. In the recent workshops, a number of questions were on people's minds:

- What are the fundamental challenges in phantom related research?
- Why did the computational phantoms evolve the way they did?
- Will the number of computational phantom stop increasing at some point of time?
- What are the differences between 'population-average' prospective dosimetry needed for radiological protection under the current ICRP radiation protection system and 'individualized' retrospective dosimetry often performed for medical physics studies?
- Is the concept of 'Reference Man' in radiation protection obsolete?
- What are future research directions?

Answers to these questions, and many others, require an appreciation of the rationales and methods responsible for some of the most important computational phantoms. Through a review about when and how various computational phantoms came about in the last 50 years, this article also attempts to learn insight into where this field of study may be heading in the future.

This article is organized into the following sections: (1) Introduction, (2) Solid-geometry modeling methods: CSG and BREP, (3) Monte Carlo Codes used with Computational Phantoms, (4) The Evolution of Computational Phantoms, (5) Physical Phantoms, (6) Examples of Computational Phantom Applications at RPI, (7) Discussion, and (8) Conclusion.

2. Solid-geometry modeling methods: CSG and BREP

It is essential to understand the geometrical shapes—the building blocks—of computational phantoms. The construction of a computational phantom must consider multiple factors such as anatomy, radiosensitivity of specific organs/tissues, computational efficiency, and geometrical compatibility with the Monte Carlo code that carries out the radiation transport calculation. As a first step, a phantom must be generated by explicitly defining the surfaces of an organ in which radiation interactions and energy depositions occur. The computer graphics community has dealt extensively with solid-geometry modeling for computer-aided-design (CAD). Two general modeling methods have been widely used: (1) constructive solid geometry (CSG) and (2) boundary representation (BREP) (Leyton 2001, Stroud 2006). The topology—spatial location and relationship of the surfaces—is fundamentally different for these two methods.

CSG allows the modeler to create a solid object using Boolean operators (or the equivalent) to combine very simple shapes called primitives. Examples of these primitives include cuboids, cylinders, prisms, pyramids, spheres, cones and ellipsoids—surfaces that are easily described by quadric equations. CSG representations are easy to adopt and can yield good results when the objects are relatively simple in shape.

Modern CAD software systems, however, are based on the more powerful BREP methods. There are two types of information in BREP: topological and geometric. Topological information provides the relationships among vertices, edges, and faces. In addition to connectivity, topological information also includes orientation of edges and faces. In advanced BREP-based CAD, the exterior of an object can be defined as NURBS, which afford very smooth surfaces. The faces can alternatively be represented as polygons whose vertices are defined by a set of coordinate values x, y and z. A polygon mesh or unstructured grid is a collection of vertices and polygons that define the geometric shape of a polyhedral object in CAD. In principle, NURBS and polygonal meshes are interchangeable BREP data structures; however, unlike the CSG representation, BREP is much more flexible because a richer set of operation tools are available (e.g. extrusion, chamfering, blending, drafting, shelling, and tweaking). These features allow BREP-based models to include very complex anatomical features. Furthermore, the BREP technique is ideally suited for surface deformation—an operation necessary for the adjustment of organ size and for organ motion simulations and for changing the posture of phantoms to better simulate how humans interact with their environment.

For example, the left lung can be represented in the CSG method by 'half an ellipsoid with a section removed' (Cristy and Eckerman 1987). The cut-out section, which is not specified by the original authors, can be defined by a Boolean operation subtracting one ellipsoid (B) from the other (A) to create the left lung, as described below:

$$A\text{: } \left(\frac{X-8.5}{5}\right)^2+\left(\frac{Y}{7.5}\right)^2+\left(\frac{Z-43.5}{24}\right)^2 \le 1\ ,\ Z \ge 43.5$$

$$B\text{: } \left(\frac{X-2.5}{5}\right)^2+\left(\frac{Y}{7.5}\right)^2+\left(\frac{Z-43.5}{24}\right)^2 \ge 1\ ,\ \textit{if}\ y<0$$

In figure 1(a) and (b), the 3D shapes of the left lung before and after the Boolean operation are illustrated. These surface equations are computationally efficient and are accepted by nearly all Monte Carlo codes. When using a Monte Carlo code, the geometry of the left lung is often further simplified by replacing the ellipsoid B with several planes. This type of phantoms is commonly referred to as 'stylized' or 'mathematical' phantoms. However, even with complicated and carefully designed Boolean operations, phantoms based on quadric surfaces

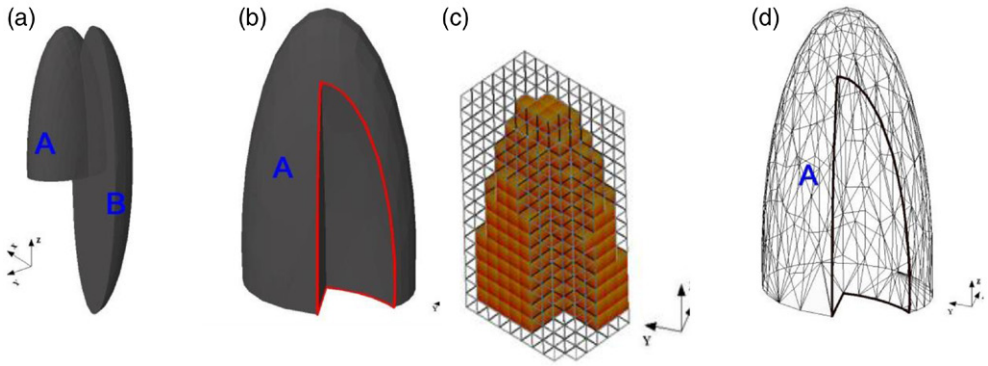

Figure 1. A model of the left lung defined by different modeling methods. (*a*) The CSG-type modeling before the Boolean operation (subtraction) is performed involving two ellipsoids A and B. (*b*) After the subtraction of B from A. (*c*) A voxel representation of the lung. (*d*) A BREP-type of modeling of the same lung using polygon mesh.

are not anatomically accurate. The true shape of a human lung is more amorphous and cannot be described by a simple ellipsoid.

Using voxels as a CSG modeling technique, figure 1(*c*) defines the left lung as an assembly of 3D cuboids. Medical image data can be converted to voxel geometry that provides a direct way of realistically describing the human anatomy. The geometry of a voxel is very easy for existing Monte Carlo codes to handle. On the other hand, each tomographic image slice needs to be treated by a 'segmentation' process, which assigns each pixel to an organ or tissue of interest such as the lung, bone, or skin using a unique identification number. It can take a significant amount of time to prepare a voxel-based phantom because there is no automatic segmentation algorithm that works on all organs. Furthermore, a voxel phantom is based on images for one subject, therefore lacking the anatomical variability associated with organ size, shape, and location that are important in the current paradigm for radiation protection dosimetry. Furthermore, CT images do not generally distinguish between soft tissues well and are typically not whole-body images. Finally, the boundary of an organ is defined by uneven steps instead of a smooth surface, as shown in figure 1(*c*). As a result, the anatomical fidelity depends on the voxel size, especially for thin and small tissues such as the skin, eye lens, ribs, and bone marrow. An adjustment to the organ shape will likely involve all underlying voxels, which is computationally inefficient. These types of computational human body models are commonly referred to as 'voxel' or 'tomographic' phantoms.

The lung can also be defined by the advanced BREP modeling techniques involving NURBS or polygon mesh surfaces. The most common technique to create a BREP-based phantom involves the surface contour extraction of each organ from a tomographic image dataset using a commercial software package, followed by the integration of individual organs into a whole body assembly. In essence, the contours convert the voxels into NURBS or mesh surfaces that are smooth and anatomically realistic. These phantoms are commonly referred to as 'NURBS,' 'mesh' or 'BREP' phantoms. A misleading name for this type of phantom is 'hybrid' which does not specify what two formats are actually used. Figure 1(*d*) shows the triangular meshes of a left lung, which was derived from high-resolution tomographic images.

3. Monte carlo codes used with computational phantoms

Computational phantoms must be coupled with Monte Carlo codes that simulate radiation transport inside the human body for the purposes of determining the patterns of radiation interaction and energy deposition. Most health and medical physics applications employ photons and electrons with energies up to 20 MeV and protons up to 300 MeV. Health physics dosimetry, however, also considers neutron sources in nuclear reactors and particles with energies in the TeV range in high energy physics research or space radiation environment. Each type of radiation interacts with matter differently. For example, photons (x-rays or gamma-rays) deposit energy primarily via photoelectric effect, Compton scattering, and pair production processes (Attix 1986). The probability of a photon interaction occurring within an organ or tissue is determined by 'cross sections' that are associated with the energy, the tissue electron density, and the tissue chemical composition. Mathematically, the differential cross section per electron for a photon undergoing the Compton scattering at angle φ per unit solid angle Ω is analytically determined by using the Klein-Nishina Equation (Attix 1986)

$$\frac{d\sigma}{d\Omega_\phi} = \frac{r_0^2}{2}\left(\frac{hv'}{hv}\right)^2\left(\frac{hv}{hv'} + \frac{hv'}{hv} - \sin^2\phi\right) \tag{2}$$

where r_o is the classical electron radius, and *hv* and *hv'* are photon energies before and after the scattering, respectively. Extensive photon cross-section libraries have been developed for these purposes (Hubbell 1969, Storm and Israel 1970).

In general, Boltzmann radiation transport problems described by various differential, integral, and integro-differential equations can be solved by numerical computational methods including finite difference, finite element, discrete ordinates, and Monte Carlo. However, only the Monte Carlo methods are able to account for all aspects of particle interactions within 3D heterogeneous media such as the human body. Monte Carlo methods, which are based on statistical simulations, have a long history, but the real application to radiation transport simulations and the associated software development arose from nuclear weapons research at Los Alamos National Laboratory during World War II (Hammersley and Handscomb 1964).

In a Monte Carlo code, random numbers are used to determine the distance and fate of a particle by comparing interaction probabilities for every geometrical region of interest. This rather tedious process is repeated for an extremely large number of particles (nowadays often exceeding 1 billion), and each particle is tracked in the 3D anatomical model until all its energy is absorbed or the particle escapes from the transport geometry. The inherent statistical uncertainty can be controlled to be less than 1%, which is often more precise than an experimental result performed in a physical phantom using a dosimeter (for quantities such as the absorbed dose). Experiments with physical phantoms are often still needed, however, to validate the Monte Carlo calculations. This creates a peculiar situation where it is not immediately clear whether the direct measurement in a simplistic physical phantom or the Monte Carlo calculation involving a more realistic compuational phantom provides the more accurate dose estimate. One reason for the rise in popularity of the Monte Carlo methods for dose estimation is the improvement in computer affordability and computing power over the last 30 years. The development of major Monte Carlo code packages is supported by national labs as well as by the user community at large. As a result, Monte Carlo codes are used today for many applications in nuclear engineering, health physics, and medical physics.

Most production Monte Carlo codes were originally developed for nuclear engineering and high energy physics research. Although these codes have been vigorously validated for radiation physics, the software packages are often difficult to use without extensive experience. Nearly all existing Monte Carlo codes can handle CSG shapes including the voxels. In

the 1990s, some of these codes had trouble handling the very large numbers of voxels required for simulations involving whole-body computational phantoms (e.q., MCNP would limit the voxels to less than 25 millions).

There are many comprehensive reviews or introductory articles about the Monte Carlo methods for health physics and medical physics (Raeside 1976, Turner *et al* 1985, Andreo 1991, Zaidi 1999, Zaidi and Sgouros 2003, Rogers 2006). Some of the public-domain, general-purpose Monte Carlo codes used for radiation dose calculations include: EGS (NRC 2013), FLUKA (Battistoni *et al* 2007), GEANT4 (Allison *et al* 2006), MCNP (Brown 2003), MCNPX (Pelowitz 2005), MCNP6 (Goorley *et al* 2013), and PENELOPE (Salvat *et al* 2003). Specific codes for radiation therapy have also been developed (Rogers 2006).

4. The evolution of computational phantoms

Previously published reviews on the historical development of computational phantoms have focused on a certain time period or a particular phantom type (Caon 2004, Zaidi and Xu 2007, Eckerman *et al* 2010, Zaidi and Tsui 2009). These reviews did not explicitly classify phantom modeling techniques, and since the time of their publication, many new phantoms have been developed using the BREP methods. An understanding of the modeling techniques and when the research community predominantly adopted each technique provides important insight into future directions. Based on chronological and technical information in the literature, this review article divides computational phantoms into three generations: (1) Stylized phantoms that are based on quadratic equations (1960s to 2000s); (2) Voxel phantoms that are based on tomographic images (1980s to present); (3) BREP phantoms that are based on advanced primitives and are deformable (2000s to present). Figure 2 contrasts these phantom generations in terms of their geometric sophistication.

4.1. Stylized Phantoms (1960s to 2000s)

The first-generation computational phantoms were developed for the purpose of better assessing organ doses from internally deposited radioactive materials for workers and patients (Eckerman *et al* 2010). Some of the earliest dose assessment techniques were developed in the first third of the 20th century primarily for use with interstitial radiation sources such as radium. According to Loevinger (1965a, 1965b, 1969), the dosimetry of radioactive materials distributed in the body had been under consideration as early as the 1920s. Quimby has provided an excellent historical review of the early development of radiation dosimetry in nuclear medicine (Quimby 1970). The early techniques were adaptations of methods used for external dose assessment with assumptions and corrections applied to account for the different types of radiation used (NCRP 1985). However, rather than being able to measure the exposure or the absorbed dose, an internal dose assessment required a calculation.

Internal dose calculations were performed during early days using the formulation presented by Marinelli and his colleagues in the 1940s (Marinelli 1942, Marinelli *et al* 1948). These equations considered only the absorbed dose from beta-emitting radionuclides (classified as non-penetrating radiation) and from gamma-rays (penetrating radiation) emitted in the decay of these radiation sources.

In 1959, the International Commission on Radiological Protection (ICRP) used very simple models for the internal dosimetry calculations associated with the Report of ICRP Committee II (ICRP 1959). In these calculations, each organ of the body was represented as a sphere with an 'effective radius.' The radionuclide of interest was assumed to be located at the center

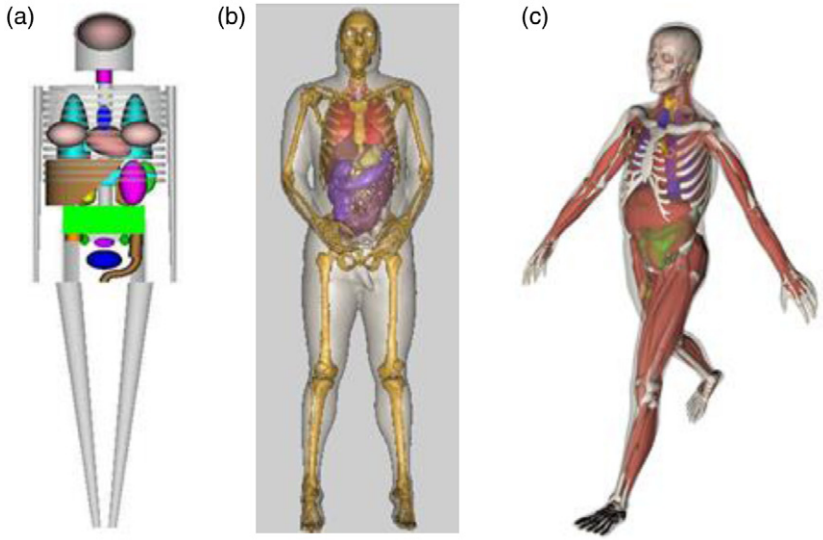

Figure 2. Three phantom generations: (1) Stylized phantom; (2) Voxel phantom (but displayed in smooth surfaces); (3) BREP phantom.

of the sphere and the 'effective absorbed energy' was calculated for each organ. Corrections were made for the photon energy lost from the sphere. In this approach, the total body was represented as a 30 cm radius sphere. It is also interesting to note that the 30 cm radius sphere was used for an organ designated as 'muscle' as well as for the small intestine and the entire gastrointestinal tract.

At the time, these approaches provided reasonably accurate estimates of the dose from a distributed radionuclide. However, most dosimetrists and researchers hoped for improved techniques and more accurate dosimetry estimates as technology developed. There was also a need for dose calculations for a number of new radionuclides introduced into nuclear medicine and more was known regarding the distribution and retention of these radionuclides in specific organs. Of course, the next step was to attempt to model individual organs of the body and ultimately the entire human body in a realistic manner. With the increase in the size and speed of computers, some progress occurred during the late 1950s and through the 1960s, eventually leading to the first-generation of stylized anthropomorphic phantoms.

Table 1 summarizes some of the most important and unique stylized phantoms developed since 1960s. This generation of stylized phantoms originated from work performed at Oak Ridge National Laboratory (ORNL) by Fisher and Snyder in the 1960s (Fisher and Snyder 1966, Fisher and Snyder 1967). Using CSG modeling techniques involving shapes such as elliptical cylinders and cones, they developed the so-called Fisher-Snyer adult phantom. The adult phantom was assumed to be standing erect with the arms at the sides of the body. Three specific regions were defined; the head and neck, the trunk including the arms, and the legs. The head and neck were represented by a 14 cm × 20 cm elliptical cylinder with a height of 24 cm. The trunk and arms were modeled as a larger elliptical cylinder, 20 cm × 40 cm with a height of 70 cm. The legs below the buttocks were modeled as a truncated elliptical cone with a height of 80 cm. Regions of little dosimetric importance were not included, e.g. the hands, feet, ears, nose, etc The composition of the phantom was assumed to be tissue distributed homogeneously throughout. No attempt was made to model the lungs or skeleton or to

Table 1. Alphabetical listing of developers of stylized computational phantoms including information on the phantom names, phantom data types, the anatomical features modeled, the human subjects they mimic, whether they were designed for ionizing or non-ionizing radiation applications, and literature references.

Developers	Phantom Names	Data Types	Human Subjects	Anatomical Features	Ionizing (I) orNon-ionizing radiation (N)	References
Bhaba Atomic Research Centre, India	BARC WBC Phantoms (4 phantoms)	Quadric equations	Indian Adult Male	Phantoms representing the BOMAB phantoms BARC Reference Phantom and a scaled version of the ICRP Reference phantom	I	Bhati *et al* (2012)
Catholic University of Pusan, Bugok	Korean Male	Quadric equations	Korean Male	MIRD type phantom with outer body and internal organs modified according to reference values from the Korean Ministry of Science and Technology	I	Kim *et al* (2010)
GSF, Germany	ADAM and EVA	Quadric equations	Caucasian adult male and female	Gender-specific phantoms revised from the ORNL MIRD-5 Phantom for external dose assessment. Several minor anatomical changes including the breast size.	I	Kramer *et al* (1982)
Hanyang University, Korea	KMIRD	Quadric equations	Korean adult male	Outer body and internal organs of the ORNL adult male phantom modified according to Korean anthropometric data.	I	Park *et al* (2006)
ITN, Portugal	ITN WBC Phantom	Quadric equations	Caucasian adult male	A mathematical simulation of the reference male BOMAB phantom.	I	Bento *et al* (2012)
Johns Hopkins University, USA(formerly with the University of North Carolina)	MCAT	Quadric equations	Caucasian adult male	3D and 4D cardiac torso phantom with gated patient organ motion information for imaging applications.	I	Pretorius *et al* (1997), Tsui *et al* (1993,1994)
Key Laboratory of Particle & Radiation Imaging, Beijing	CMP	Quadric equations	Chinese adult male	An anthropomorphic phantom constructed from the Reference Asian Man and the Chinese Reference Man	I	Qiu *et al* (2008)
NASA, USA	CAM	Quadric equations	Caucasian adult male	A standing U.S. air force adult male representing 50th-percentile height and weight. More than 1000 geometric surfaces and 2450 solid regions.	I	Billings and Yucker (1973)

ORNL, USA	Fisher-Snyder Phantom (MIRD-5) and others(6 phantoms)	Quadric equations	Caucasian newborn,1-, 5-, 10-, 15-year-old and the adult	The first anthropomorphic phantom representing a hermaphrodite adult for internal dosimetry. Organ masses, body weight and body height correspond to 50^{th}-percentile data recommended in ICRP 23. Later, age-specific phantoms were developed by others.	I	Fisher and Snyder (1966), Fisher and Snyder (1967)
	Pediatric Phantoms	Quadric equations	Caucasian newborn, 1-year, 5-year, 10-year, and 150-year old	Individual phantoms based on the literature for each age.	I	Deus and Poston (1976), Hwang *et al* (1976), Jones *et al* (1976)
	Cristy-Eckerman Family Phantoms (6 phantoms)	Quadric equations	Caucasian adult	Based on MIRD-5 Phantom and others from ORNL, including a 15-year male/female phantom	I	Cristy (1980), Cristy and Eckerman (1987)
	Pregnant Women (3 phantoms)	Quadric equations	Caucasian pregnant women at three, six and nine months of gestation	The stylized adult female was modified by adding uterine contents including the fetus, fetal skeleton and placenta at three different gestational stages.	I	Stabin *et al* (1995)
Nagoya Institute of Technology, Japan	Japanese Infants (2 phantoms)	Quadric equations	Japanese 3-year-old child	Infant represented by a homogenous spherical model, and an ellipsoidal model with three separate muscle tissues.	N	Hirata *et al* (2008)
Radiation Protection Bureau, Canada	Mathematical Models of the Embryo and Fetus (4 phantoms)	Quadric equations	Caucasian pregnant women at 8, 13, 26,38 weeks of gestation	Phantoms include an embryo and fetus at different gestational periods not included in the ORNL Pregnant Women Phantoms. Designed for dosimetry studies involving commercial flights.	I	Chen (2004)

define the locations of specific organs in the phantom. Approximately 120 sub-regions were defined in the phantom, which were used to assign approximate values of the absorbed doses to organs located within specific regions. In some cases, absorbed dose estimates for large organs required the evaluation of the doses deposited in several of these regions. Even though the original phantom was designed for use with internally- deposited radionuclides, Snyder saw many other applications. For instance, Snyder used the phantom to study the distribution of dose in the body from external, point sources of gamma-rays (Snyder 1967). He studied four photon energies (0.07, 0.15, 0.5 and 1.0 MeV) and four different source locations at distances of one and two meters from the center of the phantom.

Fisher and Snyder also developed the 'similitude' children phantoms which were scaled-down versions of the adult with added assumption that the entire body was a homogenous tissue (i.e. the lungs and skeleton were ignored) (see discussion by Eckerman *et al* 2010). These phantoms represented children of 0 (newborn), 1, 5, 10, and 15 years of age. These early phantom designs had outer dimensions representing the average height, surface area, and body mass of a children within each particular age group. These phantoms became known as the 'similitude phantoms' because of their resemblance to children. This approach had its limitations because children, in general, are not just 'little adults.' However, at the time, these phantoms helped answer a real need in the nuclear medicine community (Kereiakes *et al* 1965).

In 1969, Snyder and his colleagues reported the first heterogeneous phantom that became known as the 'MIRD-5 Phantom,' a named derived from the Medical Internal Radiation Dosimetry (MIRD) Committee of the Society of Nuclear Medicine which adopted the phantom (Snyder *et al* 1969). This phantom was composed of a skeleton, a pair of lungs, and the remainder (soft tissue). The representation of internal organs in this mathematical phantom was crude, as the simple equations captured only the most general description of the position and geometry of each organ. The original model was intended to represent a healthy 'average' adult male, the so-called Reference Man, as defined by the International Commission on Radiological Protection (ICRP). The characteristics of the Reference Man were the result of an extensive review of medical and other scientific literature on the European and North American populations (ICRP 1975). The Reference Man was defined as a 20- to 30-year-old Caucasian, 70 kg in weight and 170 cm in height (the height was later changed to 174 cm). In 1978, Snyder *et al* (1978) published an elaborative set of specific absorbed fractions using an improved version of their heterogeneous phantom which contained more than 20 organs and more detailed anatomical features.

The limitations associated with the approach of applying a set of scaling factors to the adult phantom to create age-dependent similitude phantoms were clear. Significant efforts were undertaken at ORNL during the mid-1970s to develop individual pediatric phantoms based upon a careful review of the existing literature for each particular age group. This effort produced the next generation of mathematical stylized phantoms that, although they appeared to be modeled after the adult, were designed independently. Three 'individual phantoms' were designed by Hwang *et al* (1976). This set consisted of the newborn, the 1-year old, and 5-year old models. A separate effort was undertaken by Jones *et al* (1976) for the 15-year old model, and Deus and Poston (Deus and Poston 1976) undertook the design of a 10-year old model after the other four designs were complete. The development of the 10-year old was significantly different from those for the other four ages. In fact, this design was intended to point the way to the next generation of more realistic phantoms (see discussion by Eckerman *et al* (2009)). Even though the design was completed and used for a limited number of dose calculations, it was not popular because of the very complex geometry and, after Poston left ORNL, alternative approaches were developed.

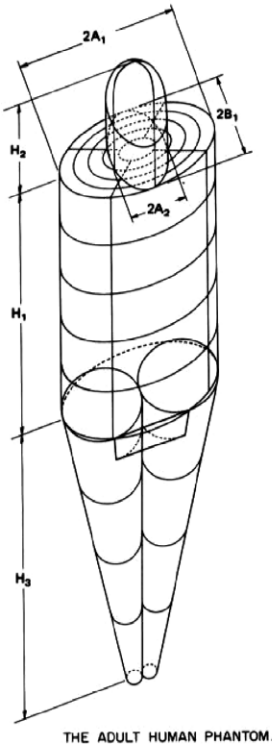

ORNL-DWG. 74-9373

PHANTOM DIMENSIONS AND DOSE REGIONS

Age (yr)	Weight (kg)	H_1 (cm)	H_2 (cm)	H_3 (cm)	A_1 (cm)	B_1 (cm)	A_2 (cm)
0	3.148	23	13	16	5.5	5	4.5
1	9.112	33	16	28.8	8	7	6.5
5	18.12	45	20	46	11	7.5	6.5
10	30.57	54	22	64	14	8	6.5
15	53.95	65	23	78	18	9	7
Adult	69.88	70	24	80	20	10	7

Figure 3. The adult male phantom and its dimensions. Similar descriptions and diagrams were purposely followed in a series of ORNL technical reports by Snyder *et al* (1978), Cristy (1980), and Cristy and Eckerman (1987).

Building upon previous work, Cristy reported the development of a new series of stylized phantoms in 1980 and then with Eckerman in 1987 in the report ORNL/TM-8381 (Cristy 1980, Cristy and Eckerman 1987). This series of 'family' of phantoms consisted of an adult male, a newborn, and individuals of ages 1, 5, 10 and 15 (also representing an adult female with additional anatomical features). As shown in figure 3, each phantom consists of three major sections: (1) an elliptical cylinder representing the trunk and arms; (2) two truncated circular cones representing the legs and feet; and (3) a circular cylinder on which sets an elliptical cylinder capped by half an ellipsoid representing the neck and head. Attached to the legs section is a small region with a planar front surface to contain the testes. The female phantom included two ellipsoids attached to the trunk to represent breasts (not shown in figure 3). The arms are embedded in the trunk, and minor appendages such as fingers, feet, chin, and nose are omitted.

Drawings depicting the external features of all the family phantoms are shown in figure 4. The pediatric phantoms were designed to form a developmentally consistent family with the existing Snyder adult phantom. The exterior of each phantom has approximately the form of the human body; but, as in their adult phantom, there has been no attempt to model for realistic details because these were presumed to have only small effect on the scattering of photons. Similarly, the description of the interior organs, while approximately correct as to size, shape, position, composition and density, are simplified to provide formulas which could be easily modeled on the computers available at the time. Figure 5 shows a schematic view of the principal organs.

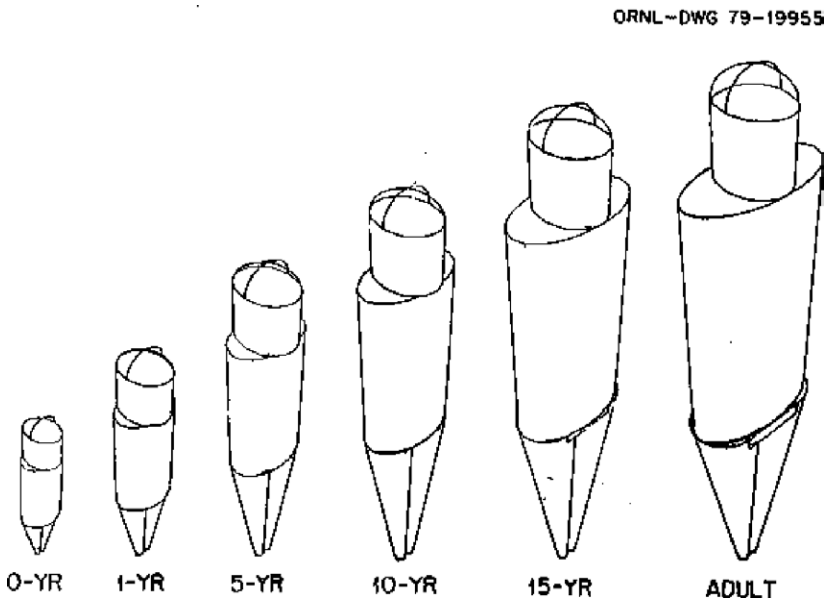

Figure 4. External views of the age-specific phantom phantoms representing an adult male and children at 15-year old (adult female), 10-year old, 5-year old, 1-year old, and 0-year old (newborn) (From Cristy and Eckerman 1987). When used for an adult female, the 15-year old phantom has breasts appropriate for a reference adult female, which are not shown.

4.1.1. Pregnant Woman Phantoms. In 1995, Stabin and his colleagues at ORNL adapted the adult female phantom in this family to represent a pregnant woman at the end of each trimester of pregnancy (Stabin *et al* 1995). This set of three stylized pregnant female phantoms were used for various internal nuclear medicine applications. Figure 6 shows a drawing of the cross sectional view of the uterine region at 9-months in the pregnant female phantom series by Stabin *et al* (1995).

4.1.2. GSF Gender-specific ADAM and EVA Phantoms. In parallel with the efforts at ORNL by Cristy and Eckerman to revise the MIRD-5 Phantom, a group at GSF—National Research Center for Environment and Health in Germany (now known as HZM—the German Research Center for Environmental Health) used the anatomical descriptions of the hermaphrodite MIRD-5 phantom to develop a pair of gender-specific adult phantoms later known as the ADAM and EVA for external dosimetry studies (Kramer *et al* 1982). The EVA phantom was derived by scaling down all relevant volumes of the MIRD-5 phantom with the total whole body mass ratio of 0.83 that was based on the analysis of ICRP reference organ masses. Then, the female organ masses were modified to create space for neighboring organs. Finally, sex-specific organ such as testes, ovaries, uterus and breasts were introduced into the appropriate phantom to yield ADAM and EVA, respectively. The chin was introduced by removing a section of the neck to created a more realistic external irradiation geometry for the thyroid. The female breasts were represented by two ellipsoid sections attached to the trunk of EVA. There are a number of minor anatomical differences, such as breast sizes, from those reported by Cristy and Eckerman (Kramer *et al* 1982, Cristy and Eckerman 1987).

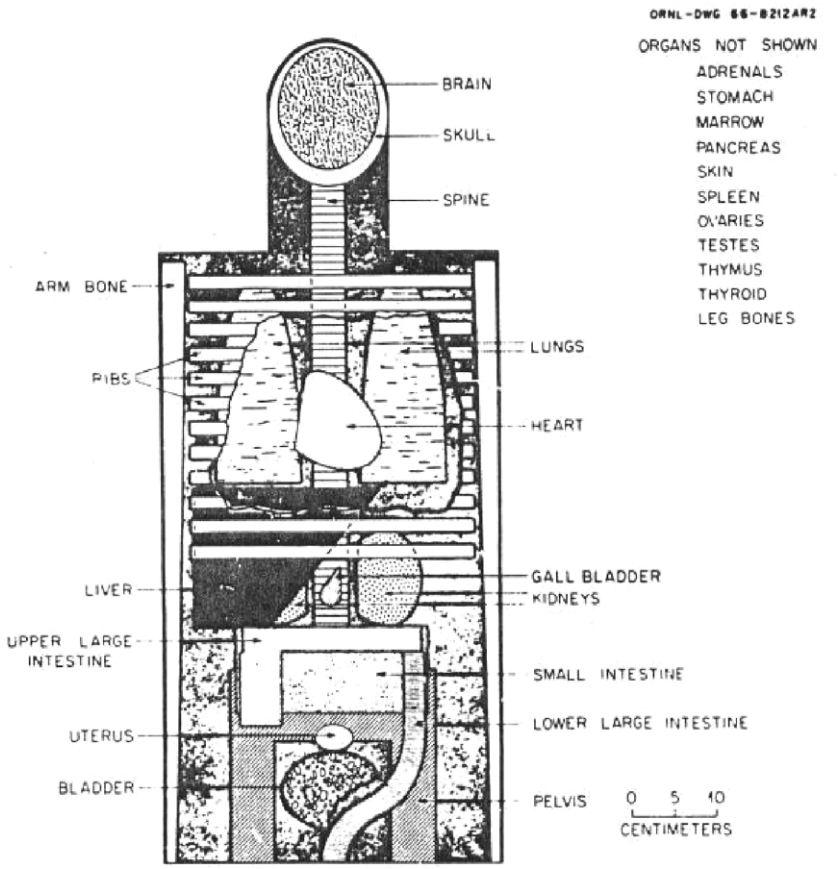

Figure 5. Anterior view of the principal organs in the head and trunk of the adult phantom developed by Snyder *et al* (1978). Although the heart and head have been modified, this schematic illustrates the crude nature of the geometric modeling by today's standards. At the time, however, this was important work that represented the state of the science.

4.1.3. CAM and CAF Phantoms for Space Radiation Dosimetry. The Computational Anatomical Man (CAM) and CAF (Computerized Anatomical Female) phantoms, developed by Billings and Yucker in 1973 for the National Aeronautics and Space Administration (NASA), demonstrated a very different and aggressive approach in stylized modeling because the phantoms reportedly consisted of 1100 unique geometric surfaces and 2450 solid regions (Billings and Yucker 1973). According to the authors, internal body geometries such as organs, voids, bones, and bone marrow were explicitly modeled using CSG modeling techniques. A computer program called CAMERA was also developed for performing analyses with the CAM and CAF phantoms. The authors state that 'extremely detailed geometrical model of the human anatomy, the most detailed yet prepared, has been developed for use in investigations dealing with exposure of astronauts to the natural space radiation environment'. According to the authors, the model was equally applicable to investigations dealing with exposure of humans to radiation associated with nuclear weapon and nuclear power system environments as well as medical applications such as radiotherapy and radiography (Billings and Yucker 1973). Indeed the surface geometry was so detailed that one may wonder how this

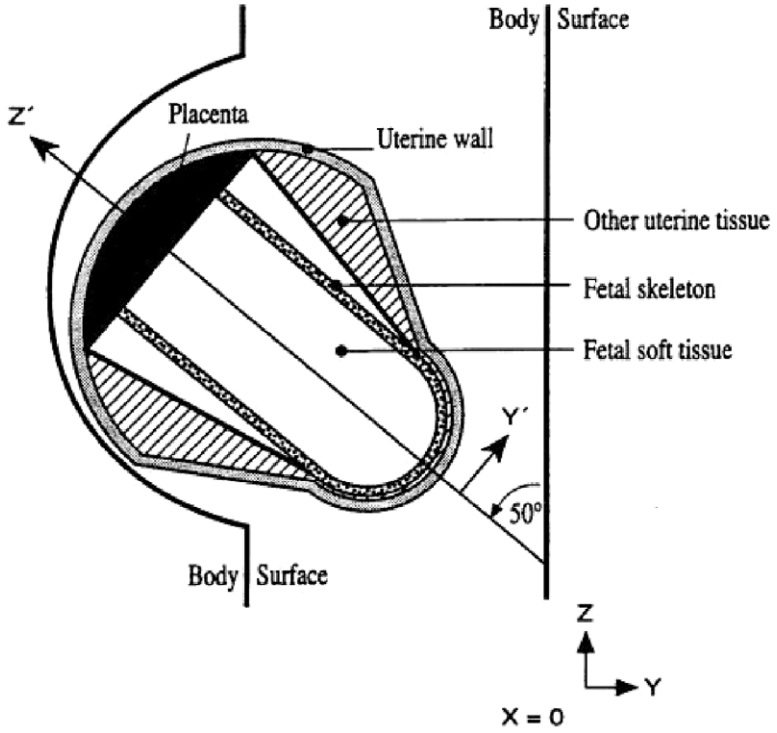

Figure 6. Diagram of the uterus of the 9-month gestation model in the Stabin *et al* (1995) pregnant female phantom series.

was possible using computers in the 1970s. Unfortunately, the CAM and CAF phantoms were never adopted for applications outside the aerospace industry and very little information about the work was accessible by the radiation dosimetry community until Tom Jordan who worked for years for NASA as a contractor recently released some of the images (CMPWG 2013). It is interesting to note one unique exterior anatomical feature of these phantoms: the arms are seperated from the trunk, unlike the MIRD-5 phantom and its successors developed around the same time. Two images of the CAM phantom are shown in figure 7.

4.1.4. MIRD Committee Work. Since the publication of the stylized dosimetry model of Snyder *et al* in MIRD Pamphlet 5 Revised (Snyder *et al* 1978), SNM's MIRD Committee has refined several internal organs to support the development of radiopharmaceutical tracers and therapeutic nuclear medicine. Modifications to the MIRD stylized model have been published as MIRD Pamphlets, which include equations of the new geometries, tabulated absorbed fractions of energy for monoenergetic photons and electrons, and tabulated radionuclide S-values. In 1999, the MIRD Committee adopted 6 new age-specific models of the head and brain for a newborn, 1-year old, 5-year old, 10-year old, 15-year old (also representing the average adult female), and adult male (Bouchet *et al* 1999). Similar to previous stylized models, simplistic geometrical shapes were used to represent the different regions of the head and brain, with volumes derived from published reference masses and shapes from analysis of MRI images. Later, the MIRD Committee also adopted an age-dependent series of stylized kidney models that are used widely in therapy nuclear medicine for renal toxicity predictions (Bouchet *et al* 2003).

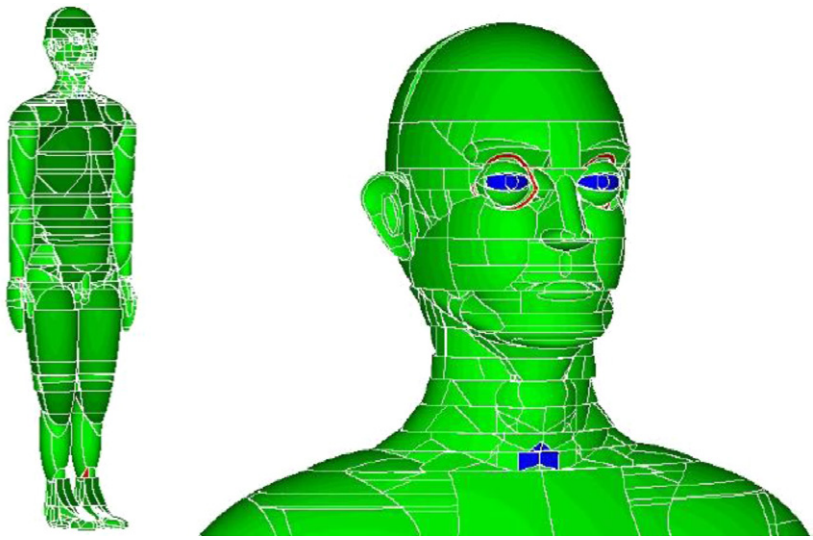

Figure 7. The CAM phantom. (Left) The whole body view showing arms separated from the trunk. (Right) The close-up view of the facial details (Reproduced with permission from the American Nuclear Society's (ANS) Computational Medical Physics Working Group (http://cmpwg.ans.org)).

4.1.5. MCAT Phantom for SPECT and PET Imaging. The stylized modeling technique was also adopted by one group for medical applications. The Mathematical Cardiac Torso (MCAT) phantom, which includes the major thoracic structures and organs, was developed by a research group led by Benjamin Tsui (currently with Johns Hopkins University) at the University of North Carolina for use in nuclear medicine imaging research, specifically single-photon emission computed tomography (SPECT) and positron emission tomography (PET) (Tsui *et al* 1993, Tsui *et al* 1994, Pretorius *et al* 1997). The same group, especially Paul Segars (who was a Ph.D. student of Tsui at the time), later developed more advanced phantoms that are discussed later in this article.

4.1.6. Other Stylized Phantom Works. Table 1 also lists several additional efforts related to stylized phantoms. In the early 1990s, it was clear that the research community no longer favored stylized phantom modeling methods. However, several groups continued to develop stylized phantoms for particular methods. Two groups developed computational phantoms of an embryo and fetus for space radiation dosimetry (Chen 2004) and an adult representing the Korean population (Park *et al* 2006). A group at the Nagoya Institute of Technology developed two new stylized phantoms of a 9-month old Japanese infant (Hirata *et al* 2008). Around the same time, researchers at Tsinghua University in Beijing created a new mathematical phantom named the Chinese Mathematical Phantom (CMP) using anatomical data for the Reference Asian Man and the Chinese Reference Man (Qiu *et al* 2008). A new MIRD phantom based on reference data for the standard Korean male was developed at the Catholic University in Pusan, Bugok (Kim *et al* 2010a). This latter phantom was used to model a patient implanted with ^{192}Ir for brachytherapy treatment of prostate cancer. Bento *et al* (2011) at the Nuclear and Technological Institute (ITN) in Portugal also developed a new mathematical phantom to simulate the reference male BOMAB phantom. This phantom was used to simulate the detection of internal sources of radiation with a whole body counter (WBC). A series of four

Table 2. Alphabetical listing of developers of voxel computational phantoms including information on the phantom names, phantom data types, the anatomical features modeled, the human subjects they mimic, whether they were designed for ionizing or non-ionizing radiation applications, and literature references.

Developers	Phantom Names	Data Types	Human Subjects	Anatomical Features	Ionizing (I) or Non-ionizing radiation (N)	References
Austrian Institute of Technology, Austria	MATSIM head MATSIM torso	CT	International Space Station Astronaut	Based on the MATROSHKA RANDO phantom	I	Beck *et al* (2011)
Brooks Air Force Base, USA	Visible Man	Color photos	Caucasian 39-year old male cadaver	Visible Human Project. More than 40 tissues were identified.	N	Mason *et al* (2000), Wang *et al* (2004)
Chang Gung University, Taiwan	Taiwanese Adult	CT	30 Taiwanese adults	Whole body phantom (152 cm, 50 kg, Female)	I	Tung *et al* (2011)
China Institute for Radiation Protection, China	CNMAN	Color Photos	Chinese adult male cadaver	Chinese Visible Human Project	I	Zhang *et al* (2007a)
Darmstadt University of Technology, Germany	HUGO	Color photos	Caucasian 39-year old male cadaver	Visible Human Project. A total of 32 tissues were identified.	N	Gjonaj *et al* (2002)
ENEA, Italy	NUDEL	CT	Caucasian Male	Based on a reconditioned physical phantom named AMOS	I	Ferrari (2010)
FCS Department, Italy	DAM	MRI	34-year old male volunteer	Dielectric anatomical phantom.	N	Mazzurana *et al* (2003)
Federal University of Pernambuco, Brazil	MAX	CT	Caucasian adult male patient	Based on VOXTISS8 phantom and adjusted to ICRP-89 Reference Man.	I	Kramer *et al* (2003)
	FAX	CT	Caucasian adult female patient	Images of the trunk, the neck and the lower part of the head were from CT scan of a 37-year-old female. Images of the legs and feet were from CT scan of a 62-year-old woman. The head and arms were from MAX phantom.	I	Kramer *et al* (2004)

	MAX06 and FAX06	CT	Caucasian adult male and female patient	Extension of MAX and FAX phantoms by adding more details in the skeleton to better match the ICRP-89 Reference Man values.	I	Kramer *et al* (2006)
Flinders University, Australia	ADELAIDE	CT	Caucasian 14-year old female patient	Torso phantom, without head and arms.	I	Caon *et al* (1999), Caon *et al* (2000)
Graz University of Technology, Austria	SILVY	MRI, CT	Caucasian pregnant woman patient at 30 weeks gestation	Trunk was based on MR images of a pregnant women and on modified CT images of a woman in the 30th week of pregnancy developed by RPI. The brain and spinal cord were from NORMAN and fitted into SILVY.	N	Cech *et al* (2007), Cech *et al* (2008)
GSF-National Research Center for Environment and Health, Germany	BABY	CT	Caucasian 8-week old female cadaver	57 cm in height and weighed 4.2 kg.	I	Williams *et al* (1986), Zankl *et al* (1988)
	CHILD	CT	Caucasian 7-year old female leukemia patient	115 cm in height and weighed 21.7 kg.	I	Williams *et al* (1986), Zankl *et al* (1988)
	DONNA	CT	Caucasian 40-year old female patient	Whole body phantom (176 cm, 79 kg)	I	Fill *et al* (2004), Petoussi *et al* (2002)
	FRANK	CT	Caucasian 48-year old male patient	Head and torso	I	Petoussi *et al* (2002)
	HELGA	CT	Caucasian 26-year old female patient	From mid-thigh upwards	I	Fill *et al* (2004), Petoussi *et al* (2002)
	IRENE	CT	Caucasian 32-year old female patient	Whole body phantom (163 cm, 51 kg)	I	Fill *et al* (2004), Zankl *et al* (2002
	GOLEM	CT	Caucasian 38-year old male patient	The weight and height are similar to those of ICRP 23 reference man.	I	Zankl *et al* (2002)

Table 2. (Continued)

Developers	Phantom Names	Data Types	Human Subjects	Anatomical Features	Ionizing (I) or Non-ionizing radiation (N)	References
	GODWIN	CT	Caucasian 38-year old male patient	Modification of Golem phantom to agree with the ICRP 89 reference values.	I	Zankl *et al* (2005)
	VISIBLE HUMAN	CT	Caucasian 39-year old male cadaver	Head to knee. CT data from the Visible Human Project.	I	Zankl *et al* (2002)
	LAURA	CT	Caucasian 43-year old female patient	167 cm height and a weight of 59 kg.	I	Zankl *et al* (2005)
	KLARA	CT	Caucasian 43-year old female patient	The modification of Laura to agree with ICRP 89 reference values.	I	Zankl *et al* (2005)
	KATJA	MRI	Caucasian pregnant woman patient in her 24th week of pregnancy	A woman in her 24th week of pregnancy. Based on the modified REGINA phantom and patient MRI images of the abdominal and pelvic regions.	I	Becker *et al* (2007)
	REGINA (ICRP Reference Phantom)	CT	Caucasian 43-year-old female patient	An adjusted LAURA phantom according to ICRP 89 reference values.	I	ICRP (2007), Schlattl *et al* (2007)
	REX (ICRP Reference Phantom)	CT	Caucasian 38-year-old male leukemia patient	An adjusted GOLEM phantom according ICRP 89 reference values	I	ICRP (2007), Schlattl *et al* (2007)
Hanyang University, South Korea	KORMAN	MRI	Korean 30-year-old healthy male	Korean male of average height and weight.	I	Lee *et al* (2004)
	KORWOMAN	MRI	Korean 35-year-old female	Korean female of average height and weight. Legs were modeled from the Visible Human Project data.	I	Lee *et al* (2005)
	KTMAN-1	MRI	Korean 25-year-old male volunteer	Korean Typical Man (172 cm, 65 kg, without arms)	I	Lee *et al* (2006a)
	KTMAN-2	PET and CT	Korean 35-year-old male volunteer	Korean Typical Man-2 (172 cm, 68 kg)	I	Lee *et al* (2006a)
	HDRK-Man	Color photos	Korean 33-year-old adult male cadaver	High-Definition Reference Korean Male phantom from the Visible Korean Human data.	I	Choi *et al* (2006), Kim *et al* (2008)

Health Protection Agency, UK (formerly National Radiological Protection Board)	NORMAN	MRI	Caucasian adult male	Normalized man. Only 10 sets of ribs rather the traditional 12.	N, I	Dimbylow (1996), Dimbylow (1997), Jones (1997)
	NAOMI	MRI	Caucasian healthy adult female volunteer	Weight and height were scaled to the values by ICRP 89.	N	Dimbylow (2005a,2005b)
	NORMAN-05	MRI	Caucasian adult male	Based on NORMAN with new tissues recommended by ICRP.	I	Ferrari and Gualdrini (2005)
	Pregnant female, hybrid phantoms (4 phantoms)	Quadric equations and MRI	Pregnant woman at 8, 13, 26, 38 weeks of gestation	Based on NAOMI and Chen's stylized fetal phantoms	N	Dimbylow (2006)
Huazhong University of Science and Technology, China	VCH	Color Photos	Chinese adult male cadaver	Visible Chinese Human Project	I	Zhang *et al* (2008a, 2008b, 2008c)
	VCH-FA	VCH phantom	Chinese female astronauts	Based on cryosection images, the VCH phantom was constructed via NURBS so the models could deform to match the body parameters of Chinese female astronauts.	I	Sun *et al* (2013)
Institut National de la Santé et de la Recherché Médicale (INSERM), France	WBPM (4 Phantoms)	CT	27-year-old male, 52-year-old-female, two 3-year-old-boys	4 phantoms of different age and gender for radiotherapy treatment. Based on CT images of 4 volunteers	I	Alziar *et al* (2009)
Institut de Radioprotection et de Sûreté Nucléaire (IRSN), France	Personalized Voxel Phantom	CT	Hispanic Male	Male victim of a radiological accident in South America	I	Courageot *et al* (2011)
Japan Atomic Energy Agency (JAEA), Japan	OTOKO	CT	Japanese adult male volunteer	Japanese adult male voxel phantom (170 cm, 65 kg)	I	Saito *et al* (2001)
	JM	CT	Japanese 54-year-old male volunteer	Japanese adult male voxel phantom using a CT scan in supine posture	I	Sato *et al* (2007a)
	JM2	CT	Japanese 54-year-old male volunteer	The male subject recruited for the construction of JM was selected to obtain CT scan in upright posture.	I	Sato *et al* (2007b)
	ONAGO	CT	Japanese adult female Volunteer	Japanese adult female phantom (162 cm, 57 kg)	I	Saito *et al* (2008)
	JF	CT	Japanese adult female volunteer	Japanese adult female phantom (152 cm, 44 kg)	I	Sato *et al* (2009)

Table 2. (Continued)

Developers	Phantom Names	Data Types	Human Subjects	Anatomical Features	Ionizing (I) or Non-ionizing radiation (N)	References
Korea Atomic Energy Research Institute, South Korea	Photographic voxel phantom	Color Photos	Korean adult volunteers	A phantom was constructed from photographic images of subjects. Phantoms were modeled as homogenous	N	Kim *et al* (2010b)
National Institute of Information and Communications Technology (NIICT), Japan	TARO	MRI	Japanese 22-year-old male volunteer	Adult male phantom (171.4 cm, 65.0 kg) representing average anatomical values of Japanese 18-year-old male	N, I	Lee *et al* (2006c)
	HANAKO	MRI	Japanese 22-year-old female volunteer	Adult female phantom (159.1 cm, 52.6 kg) representing average anatomical values of Japanese 30-year-old female.	N, I	Lee *et al* (2006c), Nagaoka *et al* (2004)
	Pregnant woman	MRI	Japanese 26-week-pregnant woman volunteer	Based on the HANAKO phantom and the abdominal phantom of a 26-week pregnant woman.	N	Nagaoka *et al* (2006, 2007)
	Deformed Children (3 phantoms)	MRI/ FFD	Japanese 3-, 5-, and 7-year children	Transformed from the TARO phantom into children models using the FFD algorithm.	N	Nagaoka *et al* (2008)
Oak Ridge National Laboratory (ORNL), USA	VOXMAT	CT and quadric equations	Caucasian adult male	Voxelized head and torso phantom with stylized arms and legs.	I	Akkurt (2008)
Rensselaer Polytechnic Institute (RPI), USA	VIP-Man	Color photos	Caucasian 39-year-old male cadaver	High resolution images from Visible Human Project	I	Xu *et al* (2000)
	Pregnant Woman	CT	30-week pregnant woman patient	A pregnant woman phantom covering the abdominal region	I	Shi and Xu (2004)
	RANDO CT Phantom	CT	Adult male	A whole-body model of the RANDO physical phantom	I	Wang *et al* (2004)
Tsinghua University, China	CVP	MRI	Chinese adult male volunteer	Chinese Voxel Phantom (170 cm, 70 kg).	I	Li *et al* (2009), Zeng *et al* (2006)
University Hospitals of Leuven, Belgium	Phantom 1	MRI	33-week old stillborn male baby cadaver	Baby phantom (50 cm, 1.91 kg)	I	Smans *et al* (2008)

	Phantom 2	CT	22-week old stillborn male baby cadavers	Baby phantom (30.4 cm, 0.59 kg)	I	Smans *et al* (2008)
University of Florida, USA	UF 2 month	CT	Caucasian 6-month old male cadaver	A voxel phantom equivalent to a 2 month old male newborn, representing a critically ill child.	I	Nipper *et al* (2002)
	UF Newborn	CT	Caucasian 6-day old female newborn cadaver	A normal 6-day female newborn phantom; The lungs were created using CT images of a 1-month old patient and the adrenal glands created using CT images of a 2-month old male patient.	I	Nipper *et al* (2002)
	UF Series A (5 phantoms)	CT	9-month, 11-, and 14-year old males; 4- and 8-year old females patients	UF pediatric phantom series without arms and legs.	I	Lee *et al* (2005)
	UF Series B (5 phantoms)	CT	9-month, 11-, and 14-year males; 4- and 8-year female patients	Based on the UF Series A phantoms with arms and legs from CT images of a healthy Korean adult attached. The organ masses were adjusted to ICRP 89 reference values.	I	Lee *et al* (2006b)
University of Houston, USA	10 Year Old Boy	CT	10-year old male	Pediatric phantom developed for craniospinal proton irradiation.	I	Taddei *et al* (2009)
University of Karlsruhe, Germany	MEET Man	Color photos	Caucasian 38-year-old adult male cadaver	Models for simulation of Electromagnetic, Elastomechanic and Thermic behavior of Man, developed from the Visible Human Project.	N, I	Doerfel and Heide (2007), Sachse *et al* (1997)
University of Utah, USA	Anatomically based model	MRI	Caucasian adult male volunteer	Anatomic phantom. The outer parts of the arms are missing.	N	Tinniswood *et al* (1998)
Vanderbilt University, USA	Gibbs Phantoms	Radiography	Caucasian representative female cadaver	Phantom includes head, trunk and proximal extremities developed from x-ray images	I	Pujol and Gibbs (1982), Gibbs *et al* (1987, 1984)
Yale University, USA	Zubal	CT	Caucasian adult male patient	Head and torso	I	Zubal *et al* (1994)
	MANTIS-SUE3-6	CT	Caucasian adult male patient	Arms and legs from the Visible Human Project were attached to the Zubal phantom	N	Dawson *et al* (1997)
	VOXTISS8	CT	Caucasian adult male patient	Arms and legs were attached to the Zubal phantom and the arms were straightened along the phantom side	I	Sjögreen *et al* (2001)

mathematical phantoms were developed at the Bhaba Atomic Research Centre in India to simulate the calibration of whole body monitoring systems for internal radionuclide contamination using BOMAB phantoms (Bhati *et al* 2012). More recently, Gardumi *et al* converted MIRD-type mathematical phantoms to NURBS before voxelizing them to investigate the so-called 'voxel effect' which arises because of the stairstepped approximation of smooth surfaces with cubic voxels (Gardumi *et al* 2013).

For nearly 50 years since the first stylized phantom was reported, these anatomically simplified phantoms have been used as the *de facto* 'standard' representations of the ICRP 'Reference Man' methodology which is based on 'population-average' 50th-percentile anatomical parameters specified in ICRP-23 (ICRP 1975) and ICRP-89 (ICRP 2002a). Applications of stylized phantoms have eventually included many aspects of radiation protection, radionuclide therapy, and medical imaging (ICRU 1992). In addition, national and international bodies have adopted organ dose estimates derived from these stylized phantoms in guidelines and regulations related to industrial and medical uses of ionizing radiation.

Although stylized phantoms made it possible to carry out Monte Carlo computations during times when computers were much less powerful, the original developers recognized the obvious shortcomings. Human anatomy is too complex to be realistically modeled with a limited set of surface equations. Many anatomical details in these models were compromised that sometimes led to inaccurate results. For example, when such phantoms were applied to nuclear medicine procedures where precise dosimetry is necessary, the calculated average organ and marrow doses did not produced strong correlations with observed marrow toxicity (Lim *et al* 1997). Most nuclear medicine physicians consequently tend to administer lower-than-optimal amounts of radioactivity to avoid toxicity. For CT dose reporting, most existing commercial software systems were based on the stylized patient models that are known to cause very large errors for low-energy x-rays (Gu *et al* 2008a). Similar stylized models have also been used to derive dose-response relationships for Japanese atomic bomb survivors and for medical patients in epidemiological studies. In the external-beam radiotherapy community, a stylized homogenous phantom was used by the Radiation Epidemiology Branch of the National Cancer Institute (NCI) in studies related to assessing secondary organ doses of theraputically irradiated patients (Stovall *et al* 1989). By the late 1980s, a few groups of researchers began to seek new ways to develop anatomically realistic phantoms. The underlying motivation was the belief was that new anatomically realistic phantoms would not only take advantage of improvements in computer modeling technology, but would ultimately lead to improved estimates for assessing the risks of patients or workers exposed to radiation.

4.2. Voxel Phantoms (1980s to Present)

The development of anatomically realistic models was desirable but impossible until early 1980s when powerful computer and tomographic imaging technologies became available. With the advent of medical imaging techniques such as CT and MRI, researchers could, for the first time, visualize the internal structures of the body in 3D and store the images in versatile digital formats. These advantages brought about the exciting and prolific era of the so-called voxel or tomographic phantoms. Table 2 summarizes a total of 84 phantoms that were constructed, typically from one of three types of tomographic images: CT and MR images of live subjects, and cross-sectional photographs of cadavers. In two previously published review articles, a total of 21 voxel phantoms was reported by Caon (2004) and 38 by Zaidi and Xu (2007). The notable increase in the number of phantom due to a more exhaustive literature search, recent developments, and the inclusion of phantoms developed for use solely in non-ionizing radiation applications.

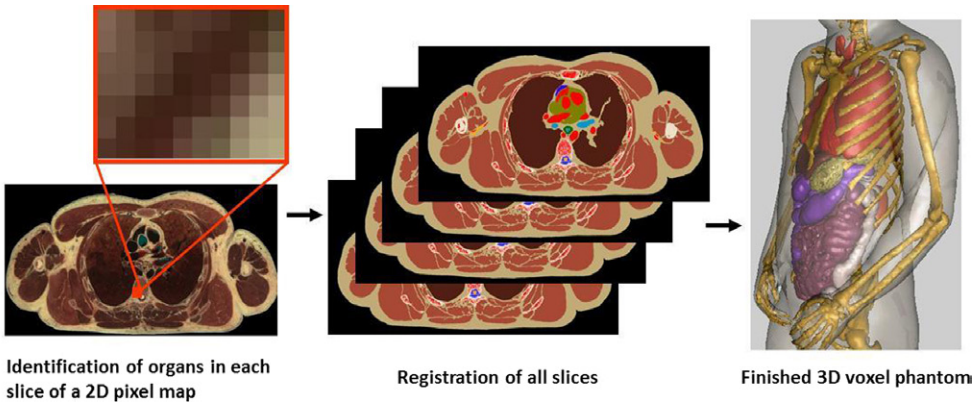

Figure 8. Steps to create a voxel phantom using the Visible Human cadaver image dataset as an example.

In terms of solid-geometry modeling techniques, a cubic voxel—one of the basic CSG primatives—is simply a 3D representation of a pixel; however, compared with the medical applications such as radiation treatment planning, the task of developing reference human phantoms presented some unique and intractable challenges: (1) to construct a whole-body phantom, image slices should ideally cover the entire body—a process not normally carried out in rountine medical examinations because of the need to minimize x-ray exposures or the lengthy time required for MRI procedures; (2) a large amount of internal organs/tissues must be identified and segmented for organ dose calculations, whereas, in radiotherapy, only the tumor volume and adjacent regions are routinely outlined; (3) the image data size of a whole-body model, especially when high-resolution images are used, can be potentially too great for a computer to handle; and (4) a standardized patient phantom is often used to study diverse radiation types such as photons, electrons, neutrons, and protons, thus requiring considerable Monte Carlo simulation capabilities.

In terms of the developmental process, tomographic phantoms are fundamentally different from the stylized ones. A tomographic image data set is composed of many slices, each displaying a 2-dimensional (2D) pixel map of the anatomy. The 3D volume of a voxel is measured by multiplying the pixel size by the thickness of an image slice. Unlike stylized phantoms, which are based on quadric surface equations, a voxel phantom contains a huge number of tiny cubes grouped to represent various anatomical structures. However, both quadric surface equations and cubic voxels belong to the same class of CGS geometries.

The creation of a tomographic phantom involves four general steps: (1) acquire a set of tomographic images (e.g. CT, MR, or anatomical photography) that cover the entire volume of the body; (2) identify (or segment) organs or tissues of interest (e.g. lungs, liver, skin, etc) from the original image slice by assigning every pixel with an identification number; (3) specify the density (e.g. soft tissue, hard bone, air, etc) and chemical composition of organs or tissues; and (4) Register the segmented image slices into a 3D volume that can be used for 3D visualization (for checking anatomical structures) and for Monte Carlo calculations. Figure 8 illsutrates these steps using the VIP-Man phantom (Xu *et al* 2000).

The earliest effort to create an image-based phantom for radiation dosimetry is believed to have been reported by S. Julian Gibbs, a radiology professor at Vanderbilt University (Pujol and Gibbs 1982, Gibbs *et al* 1984, Gibbs *et al* 1987). In these pioneering studies, Gibbs and her co-workers explored the use of 2D x-ray images as the basis to form an anatomically

realistic model of the patient. They used this information in Monte Carlo calculations to assess doses received by patients who underwent dental radiologic procedures.

Zankl and her colleagues at the GSF, Germany decided in the late 1980s to use 3D CT imaging on healthy volunteers and patients to develop what eventually became a family of 12 voxel phantoms: BABY, CHILD, DONNA, FRANK, HELGA, IRENE, GOLEM, GODWIN, VISIBLE HUMAN, LAURA, KLARA, and KATJA (Williams *et al* 1986, Zankl *et al* 1988, Smith *et al* 2000, Petoussi-Henss *et al* 2002, Zankl *et al* 2002, Fill *et al* 2004, Becker *et al* 2007, Zankl *et al* 2005). The adult male phantoms were developed first, followed by the adult female, pediatric, and pregnant-woman phantoms.

In its annual report for 2002, ICRP (2002b) states: '*An important issue for Committee 2 is the substitution of an anatomically realistic voxel phantom, obtained digitally in magnetic resonance tomography and/or computed tomography, for the MIRD phantom which is a mathematical representation of a human body*.' The ICRP Committee 2 has a task group on Dose Calculations (DOCAL) that was directly responsible for the development of a set of standard voxel phantoms. DOCAL is made of active researchers as members and consultants on internal and external dosimetry. The GOLEM and LAURA phantoms later underwent significant revision by the group led by Zankl at GSF, to yield the REX and REGINA phantoms which were released to the public as the ICRP adult Reference Male and Reference Female shown in figure 9 (ICRP 2009, Schlattl *et al* 2007). Interestingly, ICRP did not endorse the first-generation stylized phantoms. Figure 9 shows the ICRP adult Reference Male and Female phantoms (ICRP 2009).

Several processes were considered to develop the ICRP reference phantoms: (1) CT image datasets of individuals close to the Reference Man and Woman (height and weight) were needed, (2) the datasets were segmented, (3) the body heights were adjusted to reference values by scaling the voxels, (4) the skeletal masses were adjusted to the reference values, and (5) individual organs were adjusted to reference values by adding and subtracting voxels. These processes were extremely time-consuming as the voxel data format is difficult to deform, unlike more advanced BREP geometries. While the ICRP reference phantoms filled a blank in the standardization of phantom-based radiation protection dosimetry, these phantoms had a relatively large slice thickness (up to 8 mm) compared to many phantoms reported later. At these voxel sizes, small organs cannot be realistically defined and the skin and walled organs reportedly contain small holes. To address this problem, A Korean group Yeom *et al* (2013) recently developed a polygon-surface version of the ICRP Reference Male by converting voxels to polygon-surfaces.

In 1994, Zubal *et al* (1994) from Yale University published a head-torso model called VoxelMan, which was developed from CT images. The original phantom was used for optimizing nuclear medicine imaging. Improvements to the original phantom were made with an MRI scan data of a human brain. This phantom is commonly known as the 'Zubal Phantom' and registered users can freely download the original data from the internet. Two early users later revised the original data to report what are known as the MANTISSUE3-6 and VOXTISS8 phantoms by attaching arms and legs in two different positions to the original torso phantom (Dawson *et al* 1997, Sjögreen *et al* 2001). Adopting this publically available data, Kramer *et al* from Brazil developed an adult male phantom named MAX (Male Adult voXel) in 2003 (Kramer *et al* 2003) and later an adult female phantom named FAX in 2004 (Kramer *et al* 2004), both adjusted in accordance with ICRP-89 reference body height and organ masses. Kramer *et al* revised the skeletons (cortical bone, spongiosa, medullary yellow bone marrow, and cartilage) of MAX and FAX in 2006 to improve their compatibility with the latest ICRP-103 recommendations. These revised phantoms are known as MAX06 and FAX06. The work by Kramer *et al* is one of the earliest efforts to create a ICRP-89 compatible voxel phantoms for radiation protection dosimetry.

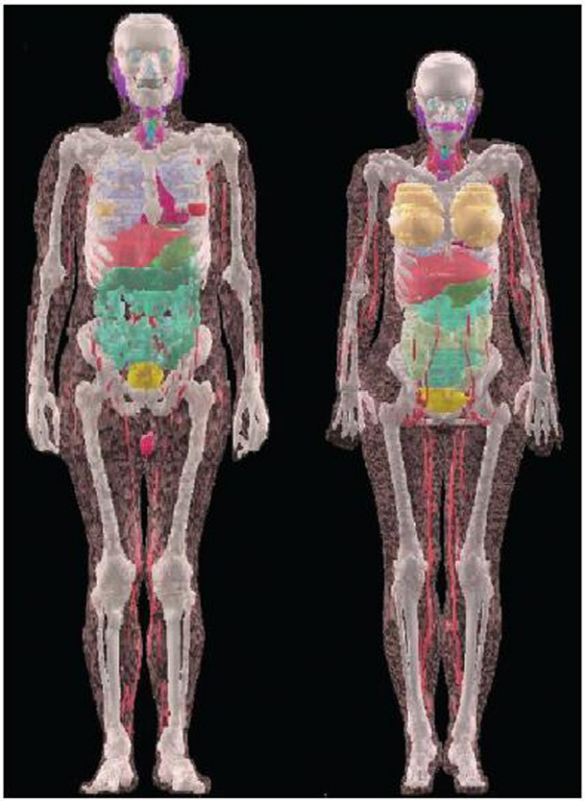

Figure 9. ICRP adult Reference Male and Female that are based on earlier work at the GSF (ICRP 2009), reproduced with permission from Taylor and Francis.

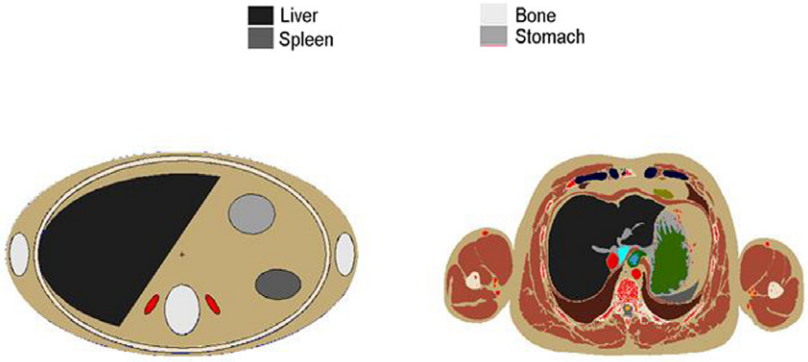

Figure 10. Comparison of stylized adult phantom (left) and VIP-Man phantom (reproduced with permission from Taylor and Francis, Xu *et al* 2000) (right) showing profound differences in anatomical detail. Such anatomical differences were believed effect the accuracy of radiation dose estimates.

In 1996, Dimbylow from the National Radiological Protection Board (NRPB) (now known as the Health Protection Agency) in the United Kingdom reported the development of an adult male phantom known as NORMAN from MR images (Dimbylow 1996). NORMAN,

which has a body height similar to the ICRP Reference Man, was first used by Dimbylow in a finite-element simulation code to determine the specific energy absorption rate from exposures to non-ionizing electromagnetic fields (Dimbylow 1997). In 1997, his colleague Jones adopted NORMAN to estimate organ doses from external and internal photon sources (Jones 1997). In 2005, Dimbylow developed an adult female phantom, NAOMI, also from MRI scans (Dimbylow 2005a). The phantom was rescaled to a height of 1.63 m and a mass of 60 kg, the dimensions of the ICRP Reference Woman. However, to date, the NAOMI phantom has been used only in non-ionizing radiation calculations. In 2005, a revised version of the NORMAN phantom, called NORMAN-5, was created by Ferrari & Gualdrini from ENEA-ION Istituto di Radioprotezione in Italy to derive external photon dose data (Ferrari and Gualdrini 2005). One year later, Dimbylow merged the NAOMI with the stylized fetal phantoms developed by Chen from Canada to create a series of hybrid phantoms for pregnant women (Dimbylow 2006). The process of adjusting two types of geometrical information was reported to be cumbersome.

In 1999, Caon *et al* from Flinders University in Australia reported a torso phantom named ADELAIDE created from CT images of a 14-year old girl (Caon *et al* 1999, Caon *et al* 2000). This phantom was interesting because, for some time, it was the only set of voxel data for a non-adult, and at the time, their studies likely provided the most reliable CT dose estimates for this patient group. Caon later reviewed his and other researchers' experiences on voxel phantoms (Caon 2004).

The VIP-Man (Visible Photographic Man) voxel phantom was reported in 2000 by Xu and two of his students at Rensselaer Polytechnic Institute (RPI) in the U.S. (Xu *et al* 2000). VIP-Man was the first phantom based on cross-sectional color photographic images of a cadaver — a 39-year-old male through the National Library of Medicine's famous Visible Human Project (VHP). The color transversal photos digitally captured at the 0.33 mm x 0.33 mm pixel resolution and each photograph was taken after the removal (by shaving) of each successive 1 mm layer of the frozen cadaver by a cryomacrotome (Xu *et al* 2000). Although the original images were segmented to yield more than 1400 organs and tissues for the purposes of teaching anatomy (Spitzer and Whitlock 1998), only approximately 80 organs and tissues were adopted at RPI for radiation dosimetry purposes. Ultra-fine and color image analysis allowed the RPI group to explicitly segment a number of small and radiosensitive tissues including the stomach mucosa, skin, and red bone marrow. Given the extremely small voxel size, the VIP-Man phantom consists of more than 3.7 billion voxels—the most of any phantom reported at the time. The finalized VIP-Man phantom was unique because it represented an individual with a heavy body mass of 103 kg. Keith Eckerman from ORNL, who headed the ICRP DOCAL Committee at that time, encouraged this effort at RPI because VIP-Man could serve as an interesting variation from the ICRP reference value. However, because the phantom was developed from a cadaver, the lungs of the VIP-Man are deflated and smaller than might normally be expected for a living, breathing individual. Figure 10 is an image that highlights the anatomical differences between the stylized and the voxelized VIP-Man. The VIP-Man was used for a large number of studies in health and medical physics which are discussed on more detail later in this article. It is worth noting that VISIBLE HUMAN developed at GSF was based on CT images at 2–4 mm resolution of the same individual before the body was frozen. The RPI group later also reported a pregnant patient phantom using CT images of a 30-week pregnant female and compared internal dose data with those derived from a stylized phantom (Shi and Xu 2004; Shi *et al* 2008).

Realizing the need for additional phantoms representing children of various ages, Bolch and colleagues from the University of Florida (UF) developed a series of pediatric voxel phantoms that appeared between 2002 and 2006, representing children with ages ranging from newborn to 15 years old (Nipper *et al* 2002, Lee *et al* 2005, Lee *et al* 2006b). This approach

was later extended to two groups (Groups A and B) of phantoms. Group A is composed of male and female voxel phantoms of a newborn, a 1-year old, a 5-year old, a 10-year old, and a 15-year old for whom the phantom stature, total weight, and individual organ masses are within 1% of ICRP-89 reference values. Group B phantoms are constructed by scaling the Group A phantoms up and down to yield phantom at each 1-year age interval, from newborn to 15-years old. The intent of the UF pediatric series was to provide a reference library of phantoms that could be matched to individual patients for age-specific organ dose assessment.

Two Japanese groups were noted in table 2 for their independent efforts to develop voxel phantoms since 2001. Saito *et al* (2001) from the Japanese Atomic Energy Research Institute (JAERI) developed an adult male model named Otoko (the first Asian phantom) and an adult female phantom named Onago. More recently, Sato *et al* developed the JM, JM2, and JF phantoms which have a refined vertical slice thickness (Sato *et al* 2007a, 2007b, Saito *et al* 2008). These phantoms were used mainly for radiation dosimetry applications in Japan were influenced by earlier projects at the GSF. The other group, Nagaoka *et al*, from the National Institute of Information and Communications Technology (NIICT) in Japan reported an adult male model, named TARO, and an adult female model, named HANAKO, developed from MR images for radio-frequency electromagnetic-field studies (Nagaoka *et al* 2004). Later Nagaoka *et al* (2008) would use a free-form deformation (FFD) to change the exterior features of the adult male phantom to develop Deformed Children phantoms of 3-, 5- and 7-year olds. The authors reported that it was difficult to develop these phantoms with the FFD algorithm and the internal organs are not adjusted to age-dependent values. The Otoko phantom was recently used in a study to calculate dose conversion coefficients for the Japanese population (Takahashi *et al* 2011).

Several Korean phantoms have been developed by researchers at Hanyang University in Korea from various image sources: Korean Man (KORMAN), Korean Typical MAN-1 (KTMAN-1), Korean Typical Man-2 (KTMAN-2), High-Definition Reference Korean (HDRK), and Korean WOMAN (KORWOMAN). The HDRK phantom was based on sectioned color photographs of an adult male cadaver that has high image resolution (Choi *et al* 2006, Kim *et al* 2008). The KTMAN-2 phantom has been used by Lee *et al* (2011) to measure the effects of selective collimation in cephalography. Kim *et al* (2010b) from the Korea Atomic Energy Institute have developed a series of voxel phantoms of different body shapes in order to better calculate counting efficiencies for whole-body counters instead of using physical BOMAB phantom that has a fixed size.

Zhang *et al* (2010) summarized three Chinese voxel phantoms developed by three separate groups in China: Chinese Man (CNMAN) produced from color photographs of a cadaver by the China Institute for Radiation Protection (Zhang *et al* 2007a), Visible Chinese Human (VCH) produced from a different set of cadaver color photographs by the Huazhong University of Science and Technology (HUST) (Zhang *et al* 2007b, Zhang *et al* 2008a, 2008b), and Chinese Voxel Phantom (CVP) produced from MRI images by Tsinghua University (Zeng *et al* 2006, Li *et al* 2009). The lead developer of the CNMAN phantom, Binquan Zhang, served as a visiting scholar at RPI during 2007–2008. The Chinese government undertook the Chinese version of the Visible Human Project through the so-called Xiang Shan Conference in early 2000s that resulted in multiple cadaver image datasets, some with a slice thickness as fine as 0.1 mm. Figure 11 depicts the VCH phantom which is based on extremely high-resolution cadaver images (Zhang *et al* 2008 b). The HUST group also reported a rat model (Xie *et al* 2010). Recently, Sun *et al* (2013) adopted NURBS to construct the VCH-F Astronaut (VCH-FA) phantom for dose calculations in the space radiation environment, incorporating statistical body characteristics of Chinese female astronauts as well as ICRP reference organ mass data. Tung *et al* (2011) from the Chang Gung University of Taiwan developed a voxel phantom of the Reference Taiwanese Adult using CT images from thirty Taiwanese adults.

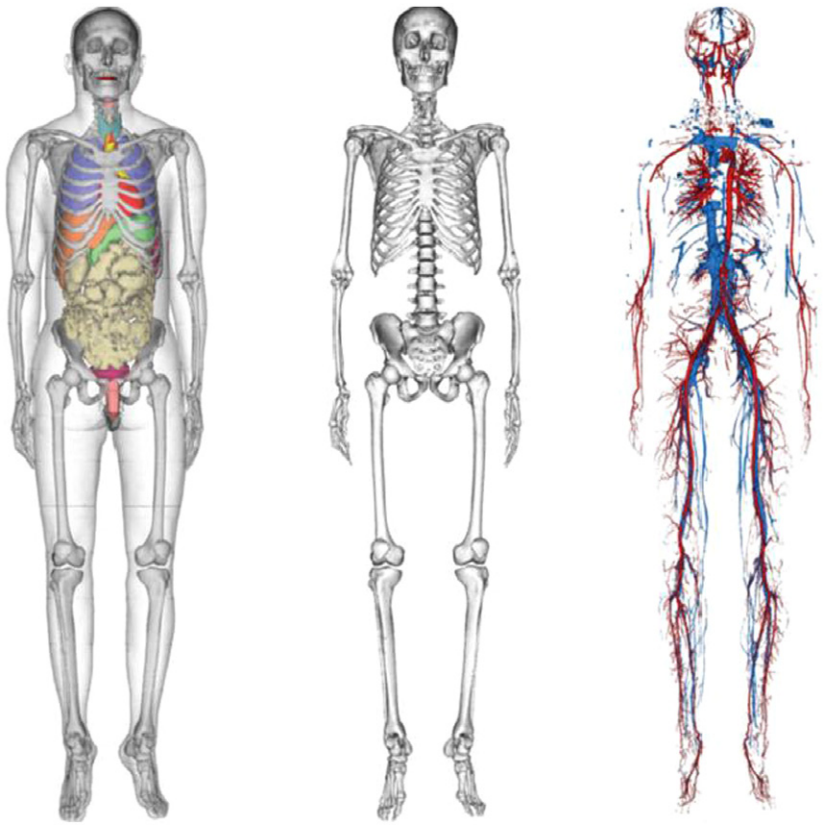

Figure 11. One of the Chinese phantoms—VCH phantom showing (left) internal organs, (middle) whole-body skeleton, and (right) vascular system (reproduced with permission from Zhang *et al* 2008b Wolters Kluwer Health).

A voxel phantom named NUDEL (NUmerical moDEL) was developed by Ferrari in Italy (2010) for use in radiation protection studies. A computational phantom was constructed from CT data of the plastic physical AMOS (Anthropomorphic MOdel for dosimetric Studies) phantom. Dose calculations for several types of nuclide exposure were run in MCNPX code and were compared to experimentally measured values with the physical AMOS phantom. The calculations were also compared to values obtained from the NORMAN-05, GOLEM, DONNA, VOXELMAN, VIP-MAN, REX, and REGINA voxel phantoms.

A radiological accident that occurred in South America in 2009 prompted the construction of a personalized voxel phantom to numerically calculate the dose the victim received. Courageot *et al* (2011) of the Institute for Radiological Protection and Nuclear Safety (IRSN) converted CT scans into a voxel phantom using the Simulation of External Source Accident with Medical Images (SESAME) tool. Courageot *et al* (2010) reported the Simulation of External Source Accident with Medical Images (SESAME) tool that allows the use of NURBS to model a victim's morphology and posture.

Researchers at the French National Institute of Health and Medical Research (INSERM), a public institute focused on biomedical research, designed a series of virtual whole-body patient models (WBPM) for usage in radiotherapy (Alziar *et al* 2009). They used CT data and the software tools IMAgo and ISOgray to model the phantoms. The phantoms accommodate

different radiotherapy treatment positions, genders, and age groups. Alziar *et al* (2009) developed a software tool to take patient data and adjust the phantom's anatomy in order to better match that of a specific individual.

Members of the MATSIM Project (MATROSHKA Simulation) at the Austrian Institute of Technology coordinated research to numerically simulate the effects of irradiation under reference radiation fields in outer space (Beck *et al* 2011). They created a two part voxel phantom using the FLUKA Monte Carlo code and CT images from a physical RANDO phantom. The voxel phantom was split into the MATSIM torso and head. The results of the simulations were within one standard deviation of experimental values. Taddei *et al* (2009) at the M.D. Anderson Cancer Center developed a voxel phantom in MCNPX code to assess the radiation does to pediatric patients receiving craniospinal irradiation with proton beams. An Iranian and Japanese team (Mofrad *et al* 2010) developed a race-specified voxelized organ, specifically a Japanese male liver that contains statistical parameters, for nuclear medicine and internal dosimetry purposes. Patni *et al* (2011) of the Bhabha Atomic Research Centre in India published dose conversion coefficients obtained from the ICRP adult voxel phantoms. In 2008, Akkurt *et al* (2008) from ORNL reported their work involving a hybrid of voxel and stylized geometries.

4.3. BREP phantoms (2000s to present)

The past decade has seen a surprising surge in BREP phantom development. The number of such phantoms is increasingly each month. A non-inclusive list of 10 groups, reporting a total of 183 BREP-based phantoms, are summarized in table 3.

4.3.1. Work at UCSU, JHU, and Duke. Segars and Tsui (2009) summarized their work in a book chapter. Paul Segars's Ph.D. thesis at the University of North Carolina was the first publication that systematically described the anatomical modeling using the NURBS-based techniques (Segars 2001). The well-known NCAT phantom was developed from the Visible Human CT image data set and the 3D anatomy was later extended into the 4th dimension to model cardiac and respiratory motions. The beating heart model of the 4D NCAT was based on 4D tagged MRI data from a real patient. The 4D NCAT phantom offers a vast improvement over the stylized MCAT phantom—a stylized version experimented on earlier by the same group—with more realistic models of the anatomy and the cardiac system, and the respiratory motion (Segars and Tsui 2010). The 4D NCAT has gained a widespread use particularly in nuclear medicine imaging research for evaluating and improving myocardial SPECT imaging. The conceptual design of the NCAT phantom also served as basis for the development of a 4D digital mouse phantom named MOBY (Segars *et al* 2004, Segars and Tsui 2007, Segars *et al* 2009). Figure 12 shows the original MIRD phantom together with MCAT, NCAT, XCAT, MOBY and ROBY phantoms provided by Paul Segars.

Figure 13 shows the 4D Extended Cardiac-torso (XCAT) phantom family recently developed as the next version of the 4D NCAT provided by Paul Segars. The XCAT phantom family includes whole-body male and female anatomies based on the high-resolution Visible Male and Female anatomical datasets. In addition to the basic anatomy, the cardiac and respiratory motions were also updated in the XCAT phantom. The series includes 47 phantoms based on of the XCAT phantom representing the cardiac and repiratory motions of multiple patients. The XCAT phantom was mapped to patient CT data to produce the series, Segars ran simulations of PET, SPECT, and CT to demonstrate the applicability of the phantoms. Mishra *et al* used a modified XCAT phantom to evaluate 3D fluoroscopic image generation from a single planar treatment image (Mishra *et al* 2013). Then Segars *et al* (2013)

Table 3. Alphabetical listing of developers of BREP computational phantoms including information on the phantom names, phantom data types, the anatomical features modeled, the human subjects they mimic, whether they were designed for ionizing or non-ionizing radiation applications, and literature references.

Developers	Phantom Names	Data Types	Human Subjects	Anatomical Features	Ionizing (I) or Non-ionizing radiation (N)	References
Duke University, USA	NCAT	NURBS	Caucasian 39-year-old male and 59-year-old female	NURBS-based Cardiac Torso phantom including organs from the Visible Human Project CT data of the male and female. Gated MRI dataset of a normal patient and 3D angiogram data are used for motion modeling.	I	Segars (2001)
	XCAT (47 phantoms)	NURBS	Caucasian 39-year-old male and 59-year-old female	4D eXtended Cardiac Torso phantom based on the NCAT, including more detailed and realistic anatomy and physiology.	I	Fung *et al* (2011)
	XCAT Library	NURBS	58 (35 male and 23 female) anatomically variable phantoms	extend the XCAT beyond reference anatomies by developing a series of anatomically variable 4D XCAT adult phantoms	I	Segars *et al* (2013)
	MOBY	NURBS	16-week-old male C57bl/6 mouse	Mouse phantom from MR images	I	Segars and Tsui (2007), Segars *et al* (2004)
Federal University of Pernambuco, Brazil	FASH and MASH	Polygon meshes	Anatomical atlases and models	Adult male and female phantoms based off of anatomical atlases and models. Organ masses were adjusted to ICRP89 reference values.	I	Cassola *et al* (2010) Kramer *et al* (2010)
	FASH and MASH series (18 phantoms)	Polygon meshes	Anatomical atlases and models	Male and Female phantoms for the 10^{th}, 50^{th}, and 90^{th} mass and height percentiles from the ICRP89 reference values.	I	Cassola *et al* (2011)
	5 and 10 year old Reference Males and Females	Polygon meshes	Anatomical Atlases and models	Produced by the same methodology as FASH and MASH. No patient images were used.	I	de Melo Lima *et al* (2011)
Hanyang University, Korea	PSRK-Man	Polygon meshes	Korean Male	Polygon mesh phantom based on the VKH-MAN. Simulations can be run without voxelization	I	Kim *et al* (2011)
Institut de Radioprotection et de Sûreté Nucléaire (IRSN), France	Thoracic Female Torsos (34 Phantoms)	Polygon meshes and NURBS	ICRP Reference Female Computational Phantom	34 phantoms of varying girth, cup size, breast tissue, and internal organ volume modified off of the ICRP Reference Female Computational Phantom	I	Farah *et al* (2010a) Farah *et al* (2011)

	Adult Male Whole Body (25 phantoms)	Polygon meshes and NURBS	CAESAR database	25 whole body male phantoms representing Caucasians of various body types.	I	Broggio *et al* (2011)
Foundation for Research on Information Technologies in Society (IT'IS), Switzerland	The Virtual Family (4 phantoms)	Polygon meshes	Caucasian volunteers of different gender and ages	Duke: 34-year-old male (174 cm,70 kg) Ella: 26-year-old female (160 cm,58 kg) Billie: 11-year-old female (148 cm,34 kg) Thelonious: 6-year-old male (107 cm,17 kg)	N	Christ *et al* (2010)
	The Virtual Classroom (4 phantoms)	Polygon meshes	Caucasian volunteers of different gender and ages	Roberta: 5-year-old female (109 cm, 17.8 kg) Dizzy: 8-year-old male (140 cm, 26 kg) Eartha: 8-year-old female (136 cm, 30.7 kg) Louis 14-year-old male (169 cm, 50.4 kg)	N	IT'IS (2011)
	Fats		Caucasian volunteers of different gender and ages	37-year-old male (182 cm, 120 kg)	N	IT'IS (2011)
	Glen		Caucasian volunteers of different gender and ages	84-year-old male (173 cm, 65 kg)	N	IT'IS (2011)
John Hopkins University, USA	Pediatric XCAT phantoms (24 phantoms)	NURBS	Caucasian 39-year-old male and 59-year-old female	Used large deformation diffeomorphic metric mapping to adjust the XCAT phantom to math pediatric reference data	I	Tward *et al* (2011)
Rensselaer Polytechnic Institute (RPI), USA	4D VIP-Man Chest	NURBS	Caucasian 39-year-old male cadaver	Organ surfaces were extracted from the VIP-Man phantom and then extended to 4D by adding the respiration of the NCAT phantom.	I	Xu and Shi (2005), Zhang *et al* (2008c)
	RPI-Pregnant Females (3-, 6- and 9-month)	Polygon meshes	3-, 6-, and 9- month pregnant female	Based on a mixture of anatomical data. Organs of the mother and fetus were adjusted to match ICRP-89 references	I	Xu *et al* (2007)
	RPI-AM and RPI-AF (2 phantoms)	Polygon meshes	Adult Male and Female	Based on mesh anatomical models that are adjusted to match with ICRP-89 references. Software supports deformation and posture change.	I	Zhang (2009), Na *et al* (2010)
	Adult deformable Female breast phantoms (8 phantoms)	Polygon meshes	Adult deformable female breast phantoms	Deformable phantoms based on the RPI-AF phantom. Modified according to ICRP reference data.	I	Hegenbart *et al* (2008)

Table 3. (Continued).

Developers	Phantom Names	Data Types	Human Subjects	Anatomical Features	Ionizing (I) or Non-ionizing radiation (N)	References
	Obese Phantoms (10 phantoms)	Polygon meshes		Based on population surveys for class 1, 2, and 3 obese patients.	I	Ding *et al* (2012)
University of Florida, USA	UFH-NURBS phantoms (4 phantoms)	NURBS	Caucasian 6-day-old female newborn cadaver, 14-year male patient and two 14-year female patients.	UF Hybrid NURBS based on previous voxel phantoms, add 16 sites of lymphatic nodes in 8 hybrid phantoms.	I	Lee *et al* (2007, 2008, 2013)
	UFH-NURBS fetal phantoms (18 phantoms)	NURBS	11 week and 21.5 week fetal specimens	18 fetal phantoms of varying age and weight with detailed soft tissue organs and developing skeletons.	I	Maynard *et al* (2011)
University of Houston, USA	Pregnant Female (9 phantoms)	BREP/STL formatted CAD	A pregnant woman in the 34th gestational week and a non-pregnant female	Nine phantoms of limited organs covering 1- to 9-month pregnant females from MRI of a non-pregnant female and pregnant woman.	N	Wu *et al* (2006)
Vanderbilt University, USA	adult and pediatric phantom series (7 phantoms)	NURBS	Caucasian adult male and female, newborn, 1-, 5-, 10- and 15-year-old	Derived from the NCAT phantom with organ and body masses adjusted to match ICRP-89 references.	I	Stabin *et al* (2008)

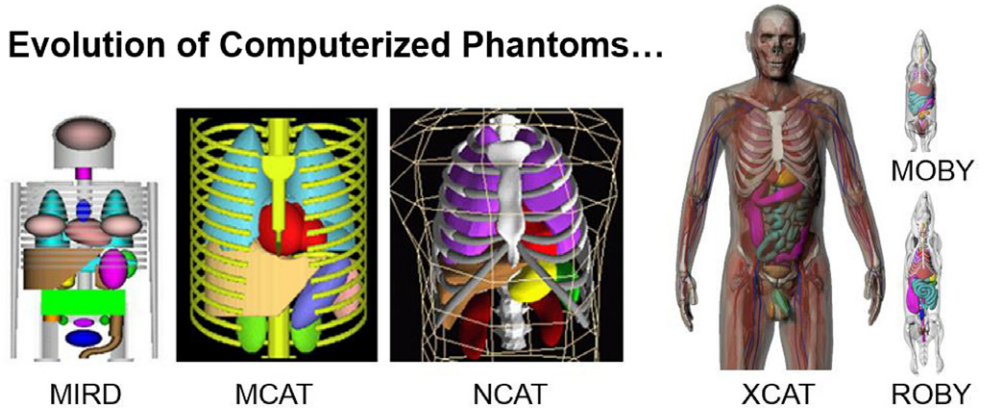

Figure 12. Original MIRD phantom is shown with MCAT, NCAT, XCAT, MOBY and ROBY phantoms (Courtesy of Paul Segars).

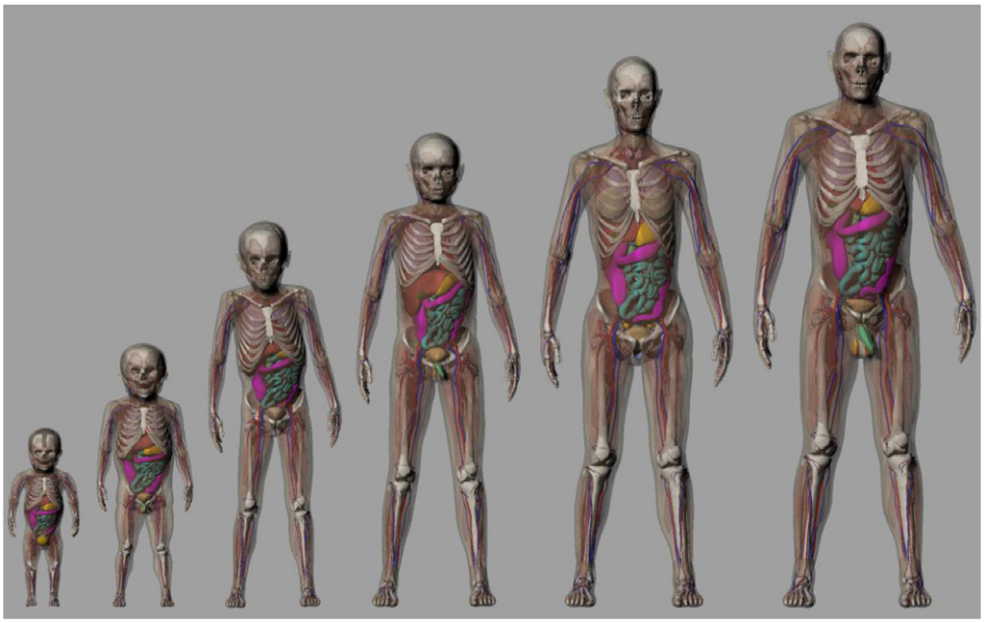

Figure 13. A portion of the XCAT Phantom Family representing ages between newborn and 12 years-old. The phantoms can be adjusted to patient-specific information (Courtesy of Paul Segars).

extended the XCAT beyond these reference anatomies to a library of 35 male and 23 female 4D computational phantoms by developing a series of anatomically variable 4D XCAT adult phantoms for imaging research. The NCAT and XCAT phantoms have been used by other research groups to simulate radiation dose from radiography (Tabary *et al* 2009, Niu *et al* 2010) and radiotherapy (McGurk *et al* 2010). A research group constructed a version of the XCAT heart to enhance the range of cardiac disorders that can be studied using the phantom (Veress *et al* 2011). Tward *et al* (2011) developed a series of pediatric phantoms from a base

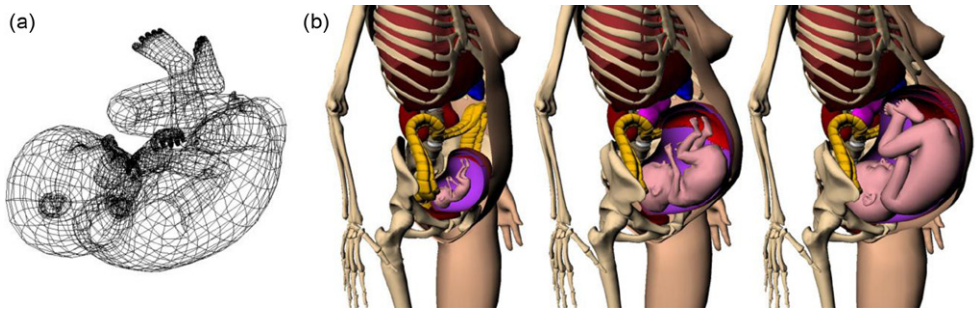

Figure 14. RPI-P phantoms for pregnant women. (*a*) BREP-type geometry of a 9-month old fetus in mesh format. (*b*) The mother and fetus after assembly showing the 3-, 6- and 9-month gestational periods (from left to right).

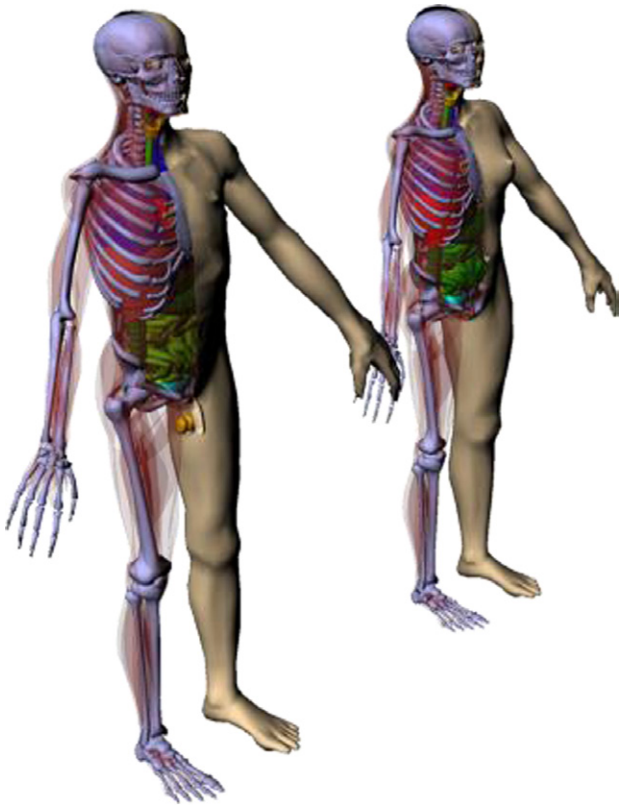

Figure 15. The triangle mesh based RPI Adult Male and Adult Female phantoms (a supplementary file '3DPhantoms.pdf' (stacks.iop.org/Phys.Med.Biol./59/R233/mmedia) to this figure is available for download that will allow a reader to interactively visualize the phantoms in 3D).

adult XCAT phantom. An algorithm to modify the XCAT phantom was developed and used to generate 24 male pediatric patients with 8 organs each.

4.3.2. Work at RPI. In 2005, the research group led by Xu at RPI used the VIP-Man phantom to simulate respiratory motions by adopting the gated respiratory motion data of the NCAT

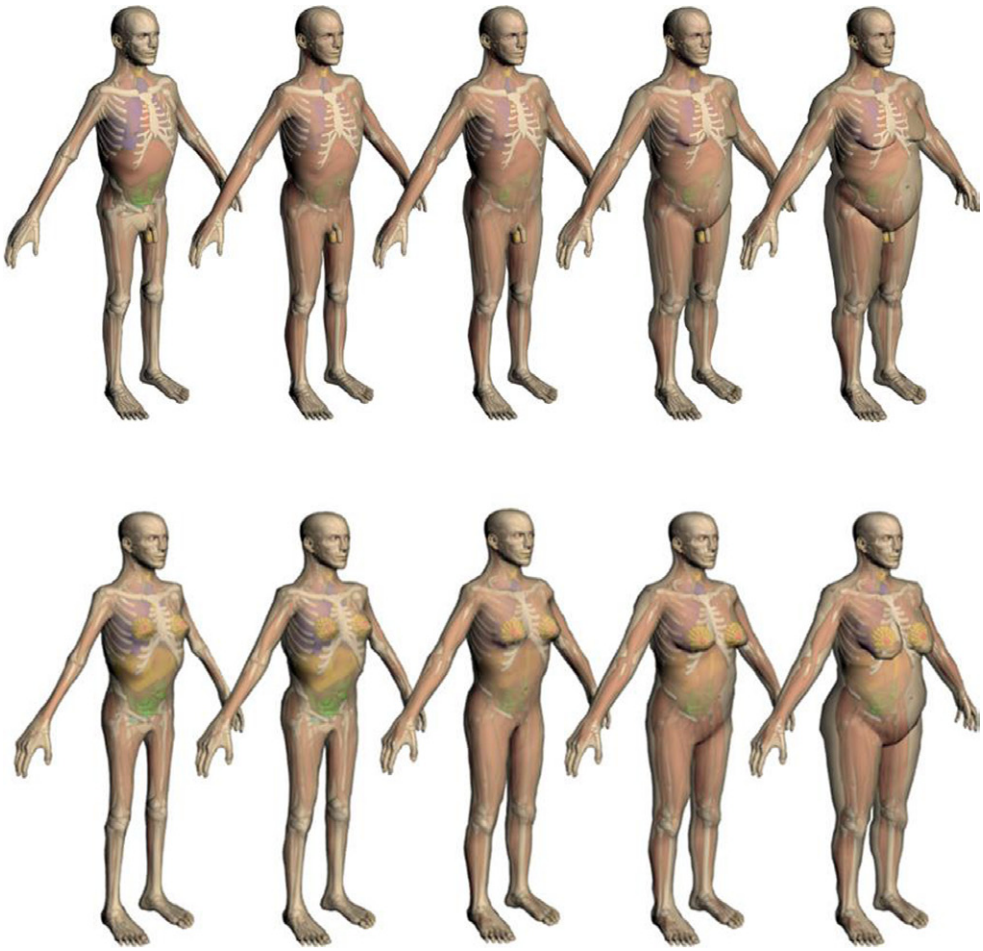

Figure 16. The RPI Adult Male (top) and Adult Female (bottom) phantoms representing the 5th, 25th, 50th, 75th, and 95th weight percentiles (from left to right) (reproduced with permission from Institute of Physics Publishing, Na *et al* 2010).

phantom (Xu and Shi 2005). The 4D VIP-Man Chest phantom was used to study external-beam treatment planning for a lung cancer patient (Zhang *et al* 2008c).

From 2005 to 2007, using the BREP modeling technique, Xu *et al* from RPI reported a set of phantoms at the end of three gestational periods of 3, 6 and 9 months—called RPI-P3, RPI-P6 and RPI-P9 (Xu *et al* 2007). Unlike the stylized models and the voxel models, these BREP-based models were found to be more flexible. These features allow BREP models to realistically change the size and shape for geometrically complex organs. Figure 14 shows the polygonal mesh model of the 9-month old fetus. Organs in the un-pregnant female are also individually adjusted to the ICRP-89 values and then deformed to allow for the fetus to be inserted using reference information and the help from an experienced anatomist.

Continuing their BREP technique involving triangular meshes, the RPI group reported in 2008 the development of a pair of phantoms called RPI Adult Male and Adult Female (Zhang *et al* 2009b). Shown in figure 15, this pair of adult phantoms was carefully adjusted to match the ICRP-89 reference values for more than 70 organs and 45 bones (including cortical bone,

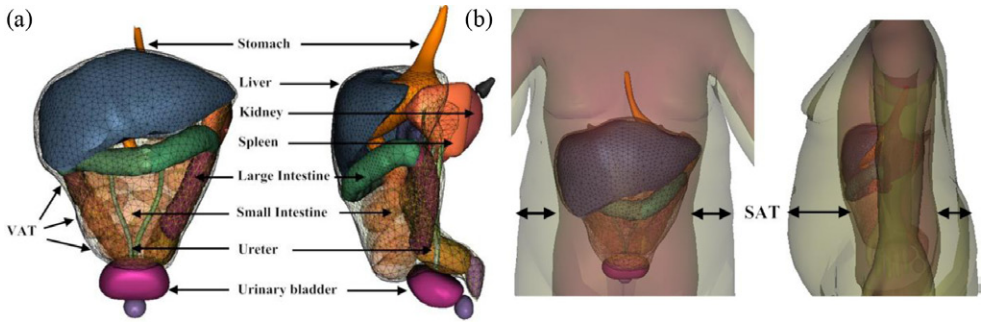

Figure 17. Illustration of the method to develop overweight and obese individuals by adding adipose tissues: (*a*) abdominal organs (surface rendering mode) and VAT (wire-frame rendering mode) which surrounds the abdominal organs, (*b*) SAT layer beneath the skin, defined as the region between the body surface and internal body cavity.

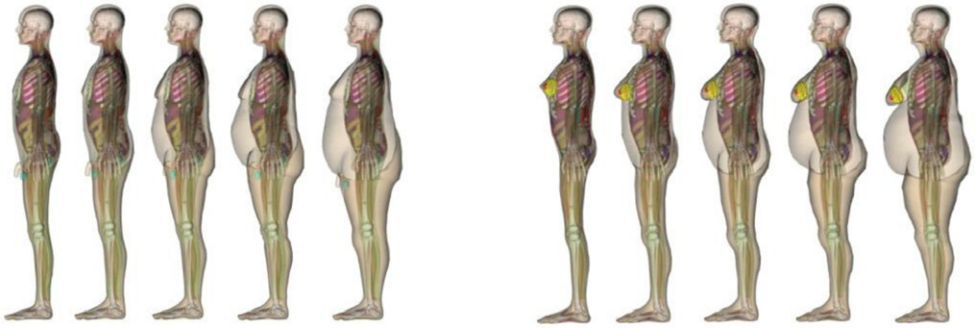

Figure 18. Phantoms for overweight and obese individuals. (Left) males, and (right) females. The phantoms have the same height (1.76 m for the male and 1.63 m for the female) but differ in weight. From left to right, the weight classifications are, normal-weight, overweight, obese level-I, obese level-II and morbidly obese (reproduced with permission from Institute of Physics Publishing, Ding *et al* 2012).

spongiosa, and cavities) as well as muscles. Several software algorithms were systematically developed to automate the deformation and organ overlap detection that were based entirely on about 126 sets of triangle meshes (Download a supplementary file '3DPhantoms.pdf' to this figure to interactively visualize the phantoms in 3D). In a subsequent work, as shown in figure 16, the RPI Adult Male and Adult Female phantoms were extended into weight-specific phantoms representing the 5th, 25th, 50th, 75th, and 95th weight percentiles (Na *et al* 2010).

The RPI Adult Female phantom was used to create phantoms of female workers with different breast sizes for the purpose of studying the effect of this parameter on the lung counting of internally deposited radionuclides (Hegenbart *et al* 2008). This was one of the first efforts to perform the so-called 'virtual calibration' for bioassay measurement of internally deposited radionuclides in workers. Existing physical phantoms for this purpose come in a limited number of body sizes. In comparison, computational methods detector efficiency calculation provide a more convenient means of for determining the internal radioactivity content in people across a spectrum of different body shapes and sizes.

Using the same BREP deformable modeling methods, Ding *et al* (2012) modified the RPI Adult Male and Female phantoms to produce 10 phantoms representing overweight and obese

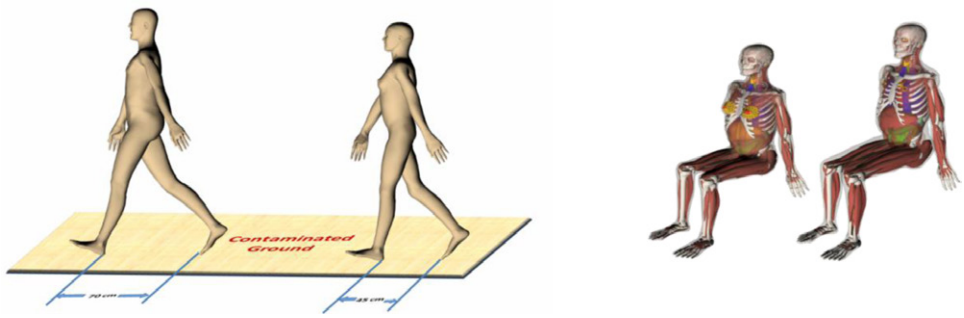

Figure 19. (Left) Walking adult male and adult female phantoms on contaminated ground with a step size of 70 cm and 45 cm, respectively. (Right) Sitting phantoms on a floor above nuclear medicine clinic.

individuals with a Body Mass Indices from 26 to 48. These phantoms consist of more than 100 deformable organs defined in the mesh-geometry format. Two main classes of adipose tissue in the human body were considered: (1) subcutaneous adipose tissue (SAT) located beneath the skin and (2) visceral adipose tissue (VAT) which surrounds the abdominal organs as illustrated in figure 17.

Figure 18 shows 3D views of the RPI BMI-adjustable male and female phantoms. As the first ever set of phantoms for overweight individuals, these phantoms were applied in an interesting study of radiation dose received by patients undergoing CT examinations (Ding *et al* 2012).

Posture-specific phantom is relatively rare, but is important to more realistically model how people interact with radiation in real-world environments. Han *et al* (2010) reported a pair of walking phantoms to represent individuals walking on a contaminated ground. Using the same method, Su *et al* (2012) then changed the posture of these phantoms to sitting. These are some of the earliest effort to design posture-specific phantoms, but the deformation was based on simple and unrealistic postures, as depicted in figure 19.

To improve the posture-specific phantoms reported earlier at RPI, Vazquez *et al* (2014a, 2014b) developed two phantoms, called CHAD, with adjusted postures defined by a motion capture system. They applied the phantoms to simulate unique human postures found in a criticality accident that took place in 1997 in Sarov, Russia (Vazquez *et al* 2014a) and then a criticality accident at a JCO facility in Tokai-mura, Japan (2014b). Figure 20 shows the process to use motion capture to create a realistic sequence of worker movements.

4.3.3. Work at the University of Florida. In a series of papers, the UF group led by Wesley Bolch reported their work on 'hybrid' family phantoms of both genders and children at various ages (Lee *et al* 2007, 2008, 2010; Bolch *et al* 2010). They created the BREP phantom series, called UFH-NURBS phantoms using the following steps. First, they segmented patient-specific CT image data from which they then generated polygonal meshes. These meshes were then converted to the NURBS format using commercial software. They then extracted several contours from the polygonal meshes and generated the NURBS surfaces by a software tool called 'lofting'. It was then in the NURBS geometrical domain they carried out organ adjustment to match the ICRP-89 reference values. In the final step, the NURBS–based phantoms were voxelized so that they could be implemented in Monte Carlo calculations. However, in order to voxelize the smooth NURBS models, they transferred the NURBS

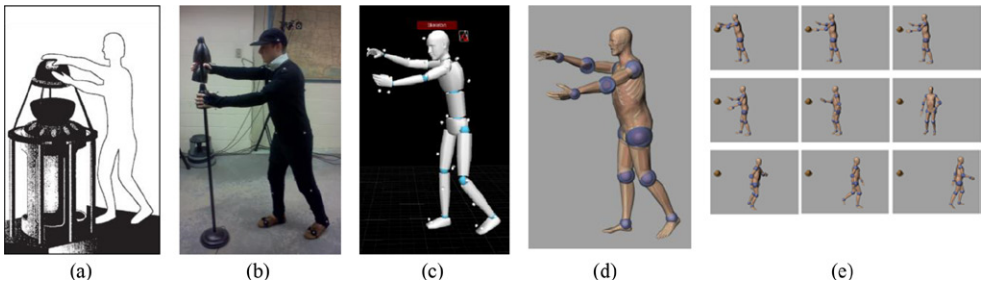

Figure 20. Motion capture technology was used to develop realistic posture sequence for a criticality accident. (*a*) A worker was exposed to criticality excursion and died 66 h later. (*b*) An actor reconstructs the postures using motion capture. (*c*) The postures are recorded sequentially. (*d*) The CHAD phantom recreates the same sequential postures. (*e*) A total of 9 postures used for Monte Carlo dose calculations.

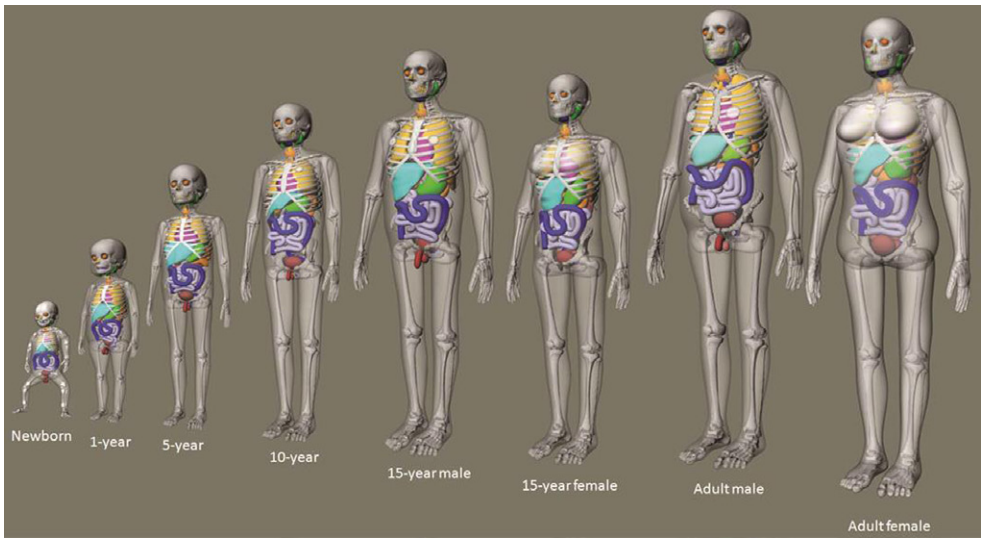

Figure 21. UF family phantoms developed from the BREP methods (reproduced with permission from Springer, Bolch *et al* 2010).

surfaces back to the polygonal meshes. In September 2008, ICRP established that its future reference phantoms for pediatric individuals would be based upon the UF series of hybrid phantoms. Recently, Geyer *et al* (2014) summarized their family phantoms and application to CT dose calculations at the Zurich workshop. Figure 21 shows the UF family phantoms developed using BREP methods (Bolch *et al* 2010).

In 2011, the UF group (Maynard *et al* 2011) reported a family of NURBS based fetal phantoms. The phantoms were based on CT and MR images of fetus specimens of various ages between 10 and 30 weeks and were modified to conform to reference values. Tissues and organs were segmented using the modeling software 3D-DOCTOR and turned into polygon mesh surfaces. The models were then imported into Rhinoceros® 3D modeling software to incorporate NURBS surfaces and correctly orient the models.

One important contribution to the literature by the UF group is in the area of bone marrow dosimetry. For radiation protection purposes, photon or neutron dose response functions can

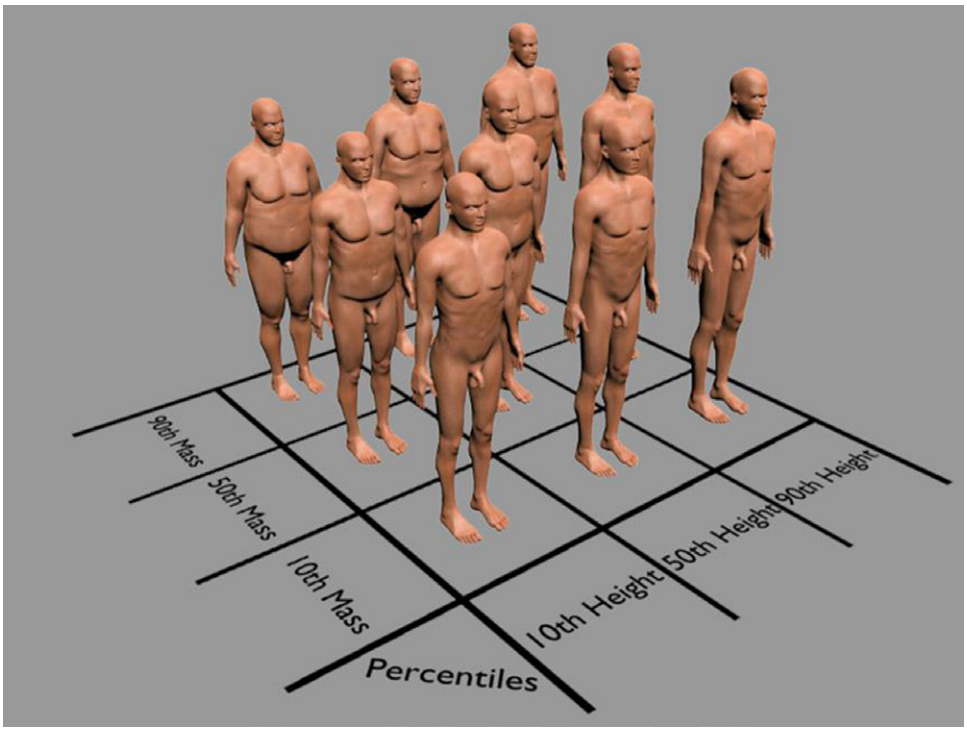

Figure 22. The anthropomorphic MASH phantom organized by weight and height percentiles (reproduced with permission from Institute of Physics Publishing, Cassola *et al* 2011)

be used to report active marrow and endosteum dose by tallying photon or neutron fluence in spongiosa regions of the skeleton (Eckerman 1985). With anatomically realistic phantoms developed at UF, Johnson *et al* (2011) reported information to use the 3-factor method as an alternative to the dose response function for photon skeletal dose. The approach was also applied to neutrons by Bahadori *et al* (2011b)

The UF phantoms have seen wide use. The UF hybrid adult male phantom was used in a study by Johnson *et al* (2009) to calculate the effects of patient size on dose conversion coefficients. A model of electron dosimetry on infants based on the UF hybrid newborn phantom and an earlier developed skeleton tissue model (Pafundi *et al* 2009) was released by Pafundi *et al* (2010) from the UF. Hough *et al* (2011) released a model for skeletal based electron dosimetry in the ICRP reference male. CT scans of a cadaver were implemented in the Rhinoceros® 3D software to modify the UF hybrid male reference phantom to include segmented skeletal tissue. Dimbylow *et al* (2010) published a study that used the UF's newborn NURBS based voxel phantom to calculate SAR for exposure to electromagnetic fields in the 20 MHz to 6 GHz region. Bahadori *et al* (2011a) from the UF released a publication studying dose estimates from space radiation on astronauts. They modeled the astronauts by adapting the UF family of hybrid phantoms to the 5th, 50th, and 95th percentiles for 40 year old American Males and 40 year old Japanese females. Recently, a group led by Zaidi has used the UF phantoms for a number of nuclear medicine dose calculations (Xie *et al* 2013, Xie and Zaidi 2014).

4.3.4. Work at Vanderbilt University. The Vanderbilt group led by Michael Stabin, in collaboration with Segars from Duke University, reported a 'family' of adult and pediatric phantoms

by adapting the NURBS-based NCAT adult male and female phantoms (Stabin *et al* 2008, 2012). ICRP-89 reference body and organ values were used to adjust NURBS surfaces. The authors state several advantages of this approach: (1) NURBS-based phantoms can be developed much more quickly than working with voxels and manually segmenting individual patient image data sets; (2) The phantoms have a higher level of internal consistency; and (3) The phantoms are complete from head to toe, thus avoiding the problem of missing organs in some of the medical images. It should be noted that the groups at RPI, UF, and Vanderbilt (and Duke) developed these BREP phantoms as part of the joint Virtual Patients Project funded by the National Cancer Institute as well as other individual projects.

4.3.5. Work at the Federal University of Pernambuco. Led by Richard Kramer, a group at the Federal University of Pernambuco (UFPE) in Brazil has been active in developing BREP phantoms. Cassola *et al* (2010) reported two phantoms based on polygon mesh surfaces. The phantoms, FASH (Female Adult meSH) and MASH (Male Adult meSH), were constructed using software, including Blender, ImageJ, Binvox, and MakeHuman. The researchers based their phantoms on anatomical models and atlases, and showed that whole-body CT scans are unnecessary for phantom design. The organ masses were based on the values recommended for the male and female reference adult outlined in ICRP-89. Cassola compared FASH and MASH to the RPI-AF and RPI-AM phantoms and noted significant differences in anatomy. The UFPE group (Kramer *et al* 2010) made a series of calculations on the FASH and MASH phantoms. Large differences were observed compared to calculations done on the RPI-AM and RPI -AF mesh phantoms. Cassola *et al* (2011) continued the work on the FASH and MASH phantoms and published a library of 18 phantoms in 2011. The phantoms were adjusted based on reference values for the 10th, 50th, and 90th height and mass percentiles for Caucasian members of each gender. The reference values were obtained from the PeopleSize software package, which obtained the values from over 100 publications in North America, Asia, Australia, and Europe. In 2011, the group published 5 and 10 year old pediatric phantoms based on the same methodology that created FASH and MASH (Lima 2011). The phantoms were developed with polygon mesh surfaces in the modeling programs BLENDER and MAKEHUMAN and were edited in the programs DIP (Digital Imaging Processing) and QtVoxel. The researchers used ICRP data for the 5- and 10-year old reference children. Figure 22 shows the MASH phantoms organized by weight and height at the 10th, 50th, and 90th percentiles (Cassola *et al* 2011)

4.3.6. Work at IRSN. The group at IRSN developed a series of female torso phantoms in the Rhinoceros® 3D modeling software (Farah *et al* 2010a). A thoracic torso phantom was produced from mesh surfaces and NURBS, and was based on reference data from the ICRP adult female reference computational phantom. A series of 34 phantoms of differing girth, cup size, breast tissue composition, and internal organ volumes were created from the base phantom. They used the phantoms to ascertain the morphological dependence of counting efficiency curves from *in vivo* lung monitoring of workers (Farah *et al* 2010b). In 2011 they released a thoracic male phantom and a mesh equivalent to the physical Livermore phantom for the purposes of simulating *in vivo* measurements (Farah *et al* 2011). The phantoms were modeled with mesh and NURBS geometries. Data from CT and MRI scans were used to delineate organs. The data was then imported to Rhinoceros® 3D, where it was assembled into the two phantoms. Simulations of the two phantoms yielded comparable data to those done with voxel phantoms. The phantoms will be the basis for a new library of phantoms in a future study. A separate project at the IRSN produced a library of 25 whole body male phantoms in 2011 (Broggio *et al* 2011). The phantoms were produced from data in the CAESAR database,

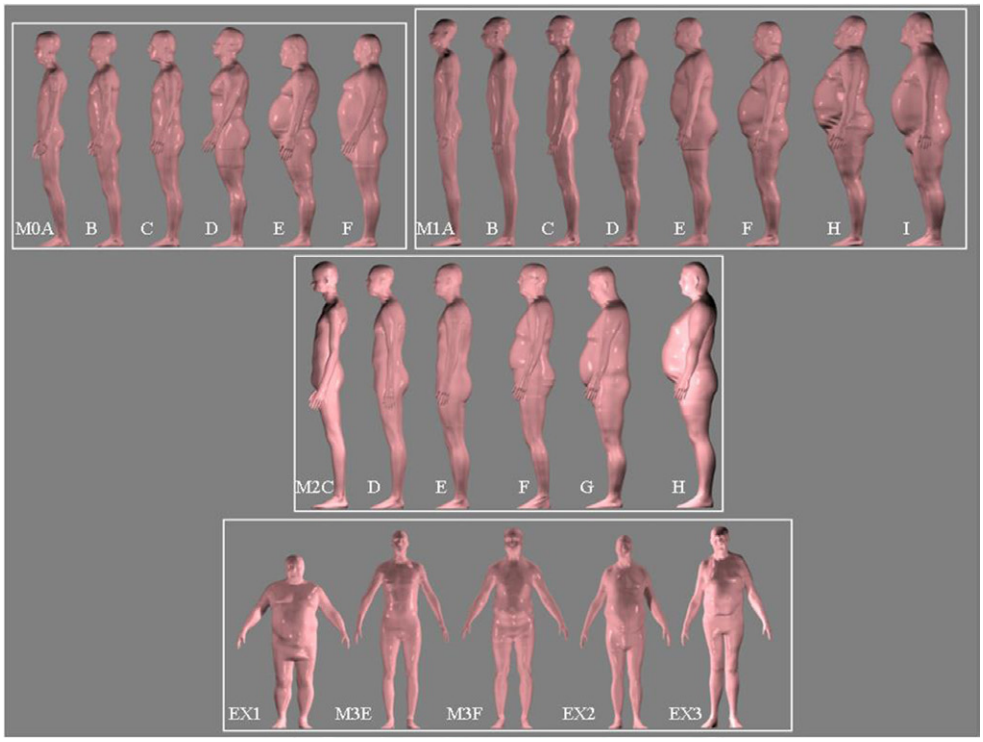

Figure 23. Male phantoms of different body types based on the CAESAR database (reproduced with permission from Institute of Physics Publishing, Broggio *et al* 2011).

a compilation of male and female 3D models constructed from full body optical imaging. A total of 22 male Caucasian optical models were used as the basis for the phantoms. The phantom's organs were constructed from ICRP reference data and added to the optical models. The phantoms possess a total of 109 segmented organs. The phantoms occupy a range of different body types, organ masses, and organ volumes. Figure 23 are the IRSN male phantoms with different body types from the CAESAR database, a compilation of surface models from full body optical images (Broggio *et al* 2011). Later, Moignier *et al* (2013) reported hybrid computational phantoms for retrospective heart dosimetry after breast radiation therapy.

4.4. Non-ionizing radiation applications

Although not the focus of this article, voxel phantoms have also been used for non-ionizing radiation applications are listed in table 2. Most of this work was neglected in the previous review articles by Caon (2004) and by Zaidi and Xu (2007), although the methods and approaches to phantom design are very similar. In fact, some phantoms, such as the NORMAN phantom, have been used for both ionizing and non-ionizing radiation applications. Table 2 clearly specifies whether the voxel phantoms that have been used for non-ionizing applications: the Visible Man from the VHP color photographs by the Brooks Air Force (Mason *et al* 2000, Wang *et al* 2004), the DAM adult male phantom from MR images by a group in Italy (Mazzurana *et al* 2003), the SILVY 30-week pregnant woman phantom from hybrid CT (originally obtained by RPI) and MR images by the Graz University of Technology, Austria (Cech

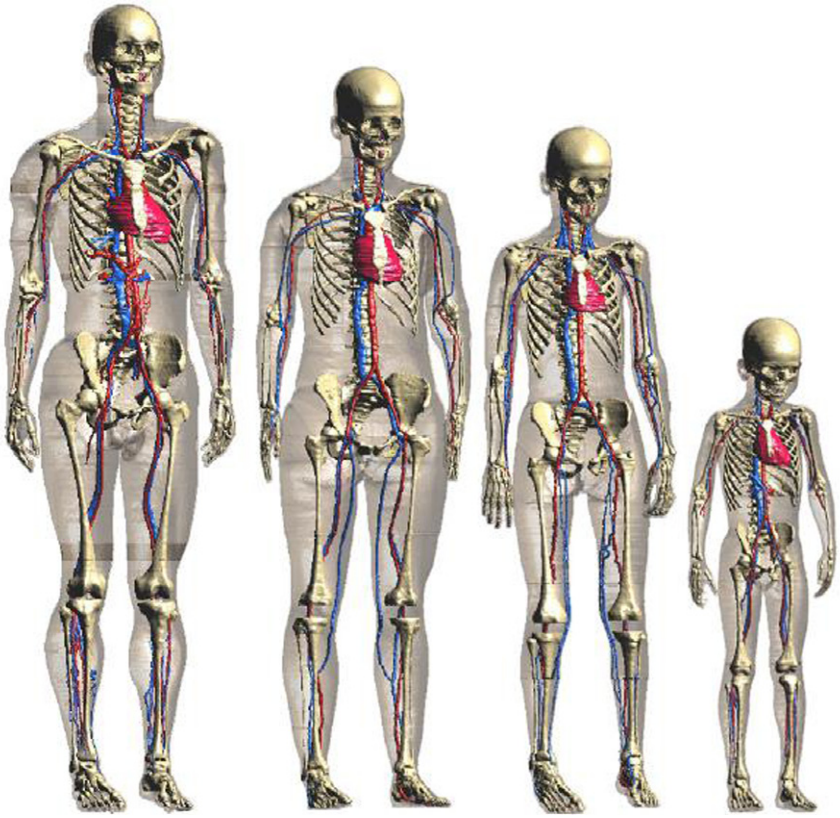

Figure 24. The Virtual Family: Duke, Ella, Billie, Thelonious (from left to right) by IT'IS (reproduced with permission from Institute of Physics Publishing Christ, *et al* 2010).

et al 2007, Cech *et al* 2008), the MEET Man from VHP color photographs by University of Karlsruhe, Germany (Sachse *et al* 1997, Doerfel and Heide 2007), and the Anatomically Based Model from MR images by University of Utah (Tinniswood *et al* 1998).

Findlay and Dimbylow (2009) reported the specific absorption rate (SAR) for exposure to electromagnetic fields using the NORMAN phantom. Findlay and Dimbylow (2010) continued their work on SAR measurements and conducted a study of SAR in children due to Wi-Fi. He rescaled the sitting posture NORMAN phantom so that it matched ICRP reference values for a 10 year old child. The effects of electromagnetic fields from Wi-Fi devices operating at 2.4 and 5 GHz were modeled using a FDTD method.

Uusitupa *et al* (2010) measured SAR in the 300 to 5000 MHz region utilizing 15 voxel phantoms, including NORMAN, the Japan MALE/FEMALE, the VHP Male, and the VF series. The simulations were run with FDTD code on a HP supercluster at the Helsinki University of Technology in Finland. This study modeled the effects of different postures, human body models, and incoming direction of the electromagnetic field.

4.4.1. Work at IT'IS. Christ *et al* (2010) and Gosselin *et al* (2014) report the Virtual Family—a series of BREP-based phantoms developed for electromagnetic exposure calculations by the Foundation for Research on Information Technologies in Society (IT'IS). As shown in figure 24, the Virtual Family consists of a 34-year old adult male, 26-year old adult female, 11-year old girl, and a 6-year old boy (Christ *et al* 2010). MRI images from volunteers were

analyzed and segmented into 80 different tissues and organs using the imaging processing software iSEG. The boundaries between the tissues and organs were then remodeled using the software tool Amira. The Virtual Family is a part of the larger Virtual Population project at IT'IS. The Virtual Population project has developed 6 additional anatomic models using the same methods that were used with the Virtual Family (Gosselin 2014). The additional models consist of the Virtual Classroom, a series of four child models, and two individually developed models: an obese 37-year old male model, and an aged 84-year old male model.

The second to last item in table 3 is a series of 9 phantoms representing a pregnant female in each gestational month developed by a group led by Ji Chen from the University of Houston in collaboration with Wolfgang Kaine of the U.S. Food Drug Administration (FDA) (who was previously with IT'IS) for studying the effects of radiofrequencies emitted from various electronic devices (Wu *et al* 2006). These phantoms only include a limited number of organs such as the body, placenta, embryonic fluid, bladder, bone, fetus and the uterus. They used patient-specific MRI images and CAD software to specify the organ shapes.

Researchers do not consider the heart models in current phantoms to have enough clinical details. Gu *et al* (2011) of the Center for Devices and Radiological Health (CDRH) developed a series of high resolution heart phantoms for the purposes of accurate dosimetric calculations. The computational heart models were generated through a nearly automated algorithm created by the researchers that will allow the creation of new heart phantoms. The heart phantoms were inserted into the mesh based Virtual Family of phantoms for simulation. Aubert *et al* (2013) also built new hybrid computational phantoms (HCPs) with an inserted detailed heart model. The use of a detailed heart model eliminates the problem of identifying the coronaries on the patient's CT.

4.4.2. Work at Hanyang University. Current permutations of hybrid phantoms must be voxelized so that they may be used in Monte Carlo dose calculations. Voxelizing a BREP phantom reintroduces the majority of the limitations of the voxel phantoms. Researchers at Hanyang University in Korea have converted the voxel phantom VKH-Man into a polygon surface phantom using 3D-DOCTOR and directly implemented the phantom into Geant4 code in order to circumvent this limitation (Kim *et al* 2011). Calculational speed and accuracy on their new phantom, PSRK-Man (Polygon Surface Reference Korean Man) have been compared to the HDRK-Man phantom, which was also based on VKH-Man. The PSRK-Man phantom has overcome many of the limitations of a voxel phantom; however, the calculation speed for the phantom is 70–150 times slower than for its voxel counterpart HDRK-Man. The speed was significantly improved later when this group developed a method to calculate polygon-mesh geometry in GEANT4 code directly (Han *et al* 2013).

5. Physical Phantoms

Table 4 summarizes selected physical phantoms that are often used to benchmark calculations performed on computational phantoms. These phantoms are typically used for three different applications: external radiation dosimetry, internal radiation dosimetry, and imaging quality assurance. For external radiation dosimetry, a physical phantom is designed so that small thermoluminescent dosimeters (TLDs) (or ion chambers or solid-state detectors) can be inserted in different locations of the phantom to measure doses from external irradiation. Examples of this type of phantom include the RANDO® phantom by the Phantom Laboratory and the ATOM® phantom by the CIRS Inc., which contain tissue equivalent slices that have anatomical maps and cavities for organ dose measurements (Alderson *et al* 1962, CIRS 2013, Phantom Laboratory 2013). Phantoms for calibrating radiobioassay detectors or nuclear

Table 4. Alphabetical listing of developers of physical phantoms including information on the phantom names, phantom data types, the anatomical features modeled, the human subjects they mimic, whether they were designed for ionizing or non-ionizing radiation applications, and literature references.

Developers	Phantom Names	Anatomical Features	Human Subjects	Ionizing (I) or Non-ionizing radiation (N)	References
Alderson Research Laboratories (acquired by the Phantom Laboratory), USA	RANDO®	Lungs, soft tissue and breasts are included; Natural human skeletons were used.	Caucasian adult male and female	I	Alderson *et al* (1962) Phantom Laboratory (2013))
Computerized Imaging |Reference Systems, Inc. (CIRS), USA	ATOM®	Bone, lung and soft tissue are included. Standard phantom includes head, torso, upper femur and genitalia. Legs and arms are included with the newborn and 1 year pediatric phantoms. Breasts can be added.	Caucasian newborn, 1-, 5-, and 10-year-old children, adult male and female	I	CIRS (2013)
	3D Sectional Torso Phantom	Removable lungs, heart, liver, pancreas, kidney and spleen are included.	Caucasian adult male torso	I	CIRS (2013)
Kyoto Kagaku Co. LTD, Japan	PBU-50	The skeleton, lungs, liver, mediastinum and kidney models are embedded in soft tissue substitute.	Japanese adult male	I	Kyoto Kagaku (2013)
	CTU-41	One-piece anthropomorphic torso phantom with anatomical structures.	Japanese adult male	I	Kyoto Kagaku (2013)
	Chest phantom N1 'lungman'	The inner components consists of mediastinum, pulmonary vasculature and an abdomen block	Japanese	I	Kyoto Kagaku (2013)
Lawrence Livermore National Laboratory (LLNL), USA	LLNL (commercially available through Radiology Support Devices)	Removable organs such as the lungs, heart, liver, kidneys, spleen, tracheo-bronchial lymph nodes are included. Chest plates simulate different chest wall thicknesses. The first generation of LLNL phantom contains a real human male rib cage.	Caucasian adult male	I	Griffith *et al* (1978)

Radiation Health Research Institute of Korea Hydro and Nuclear Power, South Korea	Typical Korean Male	Based on CT images of a human subject. The phantom contains bone, lungs and soft tissue without arms and legs. The rapid prototyping and manufacturing technique were used.	Korean adult male	I	Kim *et al* 2006
Radiation Protection Bureau, Canada	BOMAB phantom family	Each phantom is composed of 10 elliptical containers representing head, neck, chest, gut, arm, thigh, and calf.	Canada 5- and 10-year-old, reference man, reference woman, 5 and 95 percentile men	I	Kramer *et al* (1991)
University of Florida, USA	MIRD stylized Newborn	Based on stylized computational phantom.	Newborn	I	Tresser and Hintenlang (1999)
	UF 1-year old	CT images	1-year-old child	I	Tresser and Hintenlang (1999)
	UF Adult Male	CT images	Adult male		Tresser and Hintenlang (1999)
	UF Newborn physical phantom	Based on UF Newborn voxel phantom including soft tissue, bone and lungs.	Newborn cadaver	I	Jones *et al* (2006), Staton *et al* (2006)

medicine imaging equipment are designed to contain either removable organs that are doped with long-lived radioactive materials or hollow body regions that are filled with short-lived radioactive liquids. These designs allow the phantoms to mimic internally contaminated individuals. The physical torso phantom by Lawrence Livermore National Laboratory (LLNL) and the Bottle Manikin Absorption (BOMAB) phantom family by the Radiation Protection Bureau, Canada are important examples of radiobioassay calibration phantoms. There are many phantoms that are used for medical image quality assurance purposes. Most of these phantoms, such as the NEMA image quality phantom, cover only partial body and some are anatomically very simple. Table 4 lists examples of several such phantoms by the CIRS and Kyoto Kagaku Co. that are used for image analysis. With anatomically realistic computational phantoms, the UF group led by David Hintenlang has fabricated several physical phantoms representing a newborn, 1-year old, and adult male (Hintenlang *et al* 2010). Rapid prototyping processes were also used to quickly produce physical phantoms from patient-specific data (Mille and Xu 2008). A detailed review of physical phantoms can be found in a newly released book edited by DeWerd and Kissick (2014).

6. Examples of computational phantom applications by students at RPI

A potential benefit of this review article is the opportunity to illustrate how computational phantoms have been used for radiation dosimetry. For expedience, projects carried out by my students at RPI since 2000 are used as examples here. The topics cover health physics, diagnostic imaging and radiotherapy. Collaborative projects involving non-radiation related research such as surgical planning is not included (Jin *et al* 2005).

6.1. Health Physics

Health physics dosimetry typically involves organ dose and effective dose quantities for external and internal sources under standard irradiation conditions. The VIP-Man model was used to compare dosimetry data from VIP-Man — a large sized individual of 40 years old — with other voxel phantoms including the ICRP Computational Phantoms. Details of these studies have been reported for different radiation types including photons (Chao *et al* 2001a, Xu *et al* 2005), electrons (Chao and Xu 2001, Chao *et al* 2001b), neutrons (Bozkurt *et al* 2000, Bozkurt *et al* 2001) and protons (Bozkurt and Xu 2004).

6.1.1. External Photon Dosimetry. Using the VIP-Man phantom, Chao *et al* reported a new set of conversion coefficients from kerma free-in-air to absorbed dose and kerma free-in-air to 'effective VIP-Man dose' for external monoenergetic photon beams from 10 keV to 10 MeV (Chao *et al* 2001a, and a later correction by Chao *et al* (2003)). This study noted that kerma approximation, which assumes secondary electrons from photon interactions deposit their energies at an interaction site, could lead to potential uncertainty for high-energy photons incident on shallow tissues (such as breast, skin, eye lenses, or gonads). The study concluded that the size of the model, kerma approximation, and the anatomical difference were three main factors in causing dosimetric discrepancies. These comparisons also suggested possible ways to improve the stylized models. For example, the stomach is situated too close to the left side of the body when compared to VIP-Man.

Han *et al* (2010) used the walking phantoms to calculate environmental exposures involving parallel and isotropic planar sources of ^{137}Cs and ^{60}Co with concentrations of 30 kBq m^{-2}. For the parallel plane source case, the organ doses were found to be up to 78% greater for

walking phantoms than those for the stationary phantoms with legs together. The dose difference is due to that fact that widely open legs during walking provide less shielding to several organs, especially the kidneys, ovaries, and liver, from parallel sources on the ground. The effective doses of the walking phantoms were on average 15% higher than standing phantoms. On the other hand, when isotropic surface contamination sources were considered, no significant dose difference was observed between phantoms with different postures. This study demonstrated the feasible to use deformable phantoms to represent realistic postures for organ dose calculations in environmental dosimetry studies. Similar findings were reported by Su *et al* (2012) for sitting phantoms above a nuclear medicine clinic where positron emission tomography (PET) imaging is used.

6.1.2. External Electron Dosimetry. Chao *et al* (2001b) presented organ doses from the VIP-Man phantom from external electron beams using EGS4-VLSI Monte Carlo code and compared data with those reported for the ADAM phantom using MCNP4 code by Schultz and Zoetelief (1996), a hermaphrodite mathematical model using FLUKA by Ferrari *et al* (1997), and the MIRD-5 mathematical model using EGS4 by Katagiri *et al* (2000). These comparisons suggested, that at least for electron dosimetry, a single standard body model does a poor job in representing individuals of diverse anatomy. The study further concluded that a large number of voxel phantoms would need to be investigated before the degree of dose variation is understood.

6.1.3. External Neutron Dosimetry. Using the VIP-Man phantom, Bozkurt and his co-authors reported a new set of fluence-to-absorbed dose and fluence-to-effective dose conversion coefficients calculated for both low-energy (10^{-9} - 20 MeV) and high-energy (20 - 10000 MeV) neutrons (Bozkurt *et al* 2000, Bozkurt *et al* 2001). The absorbed dose for 24 major organs and effective dose results based on the realistic VIP-Man were presented and compared with those based on the simplified MIRD-based phantoms reported in literature. The authors noted discrepancies between the doses calculated on the two phantoms and concluded that several factors may have contributed to the discrepancies. The differences in anatomical models, which cause approximately a 10% difference in effective dose, are because the VIP-Man is heavier and taller and how the Monte Carlo codes treat the transport of high-energy particles, including the use of evaluated data and theoretical models.

6.1.4. External Proton Dosimetry. Bozkurt and Xu (2004) applied the VIP-Man phantom to calculate fluence-to-absorbed dose and fluence-to-effective dose conversion coefficients under high-energy proton environment. The absorbed dose results were presented for 24 major organs of VIP-Man, and the calculated data were compared with those based on mathematical phantoms reported in literature. Some discrepancies in organ dose and effective dose, within 40%, were observed due to the use of different transport models employed by different Monte Carlo codes. Taranenko and Xu (2009) used the RPI-P phantom series to calculate conversion coefficients for fetuses from whole body irradiation with monoenergetic proton beams. The simulation was run in MCNPX for 12 different source energies ranging from 100 MeV to 100 GeV, and for 6 different configurations.

6.1.5. External Dosimetry for Red Bone Marrow. Caracappa and co-workers used two sets of Visible Human images for the identical anatomy to gain insight to the external dose to the red bone marrow, which is the most radiosensitive tissue (Caracappa *et al* 2009). A Monte Carlo computational model was constructed in this study from the CT images of the Visible Human Project, and compared to the VIP-Man phantom derived from color photographs of the same individual (Xu *et al* 2000). These two data sets for the same individual offered interesting information that

was not previously available. Dose to the red bone marrow was calculated for the CT model using the uniform mixture assumptions and using the cellularity factors adopted by ICRP to test the previous assumptions and evaluate the accuracy of the computed dose to the red bone marrow in Monte Carlo simulations. Based on the newly developed algorithms, three dosimetry applications were investigated and tested. Broad beam photon irradiation in occupational exposure results in similar doses for high energies, but differences as great as 40% for low energies. An electron total-body irradiation procedure for treating skin cancer was also studied, with a 39% difference in red bone marrow dose between the existing method and the proposed revised method. These results demonstrate the advantage of the new algorithms by accounting for marrow cellularity and distribution various bone sites in the anatomical and dosimetry models.

6.1.6. Internal Electron Dosimetry. Based on the VIP-Man phantom, Chao and Xu calculated complete sets of specific absorbed fractions for internal electron emitters (Chao and Xu 2001). This was also the first report of internal electron data for walled organs such as the esophagus, lower large intestine, stomach, and upper large intestine. Although electrons are considered as weakly penetrating radiation and researchers have usually ignored the dose to organs other than the source organ, results from this study show that doses to neighbor organs and nearby organs can be too great to be neglected. This study provided convincing evidence that internal electrons do affect organs beyond the source organ.

6.1.7. Internal Photons Dosimetry for GI tract. In this study, the VIP-Man phantom was used to calculate SAFs for the gastrointestinal (GI) tract (Xu *et al* 2005). SAFs for sources in GI tract have been previously studied based on stylized phantoms. Using the VIP-Man phantom, the authors compared SAFs for stomach wall from VIP-Man to those previously published by Cristy and Eckerman for photon sources in the stomach content. The stylized models have been widely utilized by the nuclear medicine dosimetry community. However, SAFs derived from this phantom can have considerable uncertainties when compared to the realistic VIP-Man under certain conditions. This study clearly demonstrated the advantage of the VIP-Man phantom whose small voxel size allows the dosimetry to be performed on small tissues structures such as the mucosal layer in the GI tract.

6.1.8. Dynamic phantoms for criticality accident dose reconstruction. Using the CHAD phantoms developed motion-capture data, Vazquez *et al* (2014a, 2014b) simulated how workers were fatally exposed to extremely high levels of radiation. Implementation of the emergent techniques produced more accurate and more detailed dose estimates for the workers than were reported in previous studies. In Vazquez *et al* (2014b), a total-body dose of 6.43 and 26.38 Gy was estimated for the two workers, who assumed a crouching and a standing posture, respectively. Additionally, organ-specific dose estimates were determined, including a 7.93 Gy dose to the thyroid and 6.11 Gy dose to the stomach for the crouching worker and a 41.71 Gy dose to the liver and a 37.26 Gy dose to the stomach for the standing worker. Implications for the medical prognosis of the workers are discussed, and the results of this study were found to correlate better with the patient outcome than previous estimates, suggesting potential future applications of such methods for improved epidemiological studies involving next-generation computational phantom tools.

6.2. Radiological Imaging

6.2.1. Organ doses from SPECT and PET brain imaging. To estimate internal dosimetry for brain imaging, a head and brain portion of the VIP-Man was used to implement into the Monte

Carlo code, EGS4-VLSI (Chao and Xu 2004). Fifteen sub-regions were modeled including caudate nucleus, cerebellum, cerebral cortex, cerebral white matter, corpus callosum, eyes, lateral ventricles, lenses, lentiform nucleus, optic chiasm, optic nerve, pons and middle cerebellar peduncle, skull CSF, thalamus, and thyroid. S-values were calculated for the most important sources and targets encountered in SPECT and PET brain imaging. These results were then compared to those from the stylized head/brain model recommended by the MIRD (Bouchet *et al* 1996). Although heavier individuals (e.g. VIP-Man) will usually receive lower radiation doses, the stylized head/brain model underestimates the S-values by 15% on average for a patient similar to the VIP-Man model. More tomographic head/brain models are needed in order to compare various brain sizes and anatomical variations. Before such an inter-comparison is performed, the results presented in this paper are useful for patients who are similar to VIP-Man in body size or weight.

6.2.2. Organ doses from x-ray Radiographs. VIP-Man was used by Mark Winslow, a Ph.D. student at RPI, in collaboration with Walter Huda from University of Syracuse, to calculate values of energy imparted (ε) and effective dose (E) for monoenergetic photons (30–150 keV) in radiographic examinations. Energy deposition in the organs and tissues of the human phantom were obtained using Monte Carlo simulations. These monoenergetic E/ε values can generate values of E/ε for any x-ray spectrum and can be used to convert values of energy imparted into effective dose for patients undergoing common head and body radiological examinations (Winslow *et al* 2004). Later, in his doctoral research, Mark Winslow, in collaboration with Birsen Yazici of RPI, also studied the image quality by analyzing approximately 2000 simulated chest x-ray images for the VIP-Man using the ROC/AUC analysis (Son *et al* 2006, Winslow *et al* 2005).

6.2.3. Organ Dose from CT. Gu *et al* (2009) used the RPI Pregnant Female phantoms to run dose calculations for multi detector CT (MDCT) scans. The MDCT scanner and the phantoms were implemented in MCNPX code. The dose profiles showed that there was little risk to the patient or the fetus from the MDCT scans. Ding *et al* (2012) developed 10 obese phantoms for the purpose of optimizing image quality and CT dose in obese patients. It was found that calculated dose for obese patients differed significantly from the dose calculated for normal weight phantoms.

6.3. Radiotherapy

6.3.1. Adjoint Monte Carlo method for external-beam prostate radiation treatment. The abdominal portion of the VIP-Man model was used in the doctoral research by Brian Wang, a Ph.D student at RPI, to develop and demonstrate an Adjoint Monte Carlo (AMC) method for optimizing the external beam directions in the so-called 3D Conformal Radiation Treatment of prostate cancer (Wang *et al* 2005a). The AMC method had been widely used in nuclear reactor physics research but was never demonstrated for treatment planning in realistic 3D patient anatomy. With the VIP-Man model, which was already implemented in the MCNP code with multi-group adjoint cross-sections, it was possible to test the theory in clinically relevant scenarios. This work was in collaboration with Moshe Goldstein, a nuclear engineer from Israel who first proposed the possibility during a sabbatical at ORNL, and Narayan Sahoo, who was a clinical therapeutic physicist at Albany Medical Center at the time. In this application, the adjoint fluxes for the prostate (PTV) and the rectum and bladder (OARs) in the VIP-Man phantom were calculated on a spherical surface of approximately 1-m radius, centered at the center of gravity of PTV (Wang *et al* 2005a).

An 'importance' ratio, defined as the PTV dose divided by the weighted OAR doses, was calculated for each of the available beamlets to select the best beam angles. Finally, the doses in PTV and OAR were calculated using the forward Monte Carlo method. This study demonstrated the feasibility of the AMC method in optimizing external beam directions based on anatomical information in a 3D and realistic patient anatomy. The study also identified issues to be further addressed before this method could become clinically useful (Wang *et al* 2005b).

6.3.2. Non-target organ doses from proton radiation treatments. In a separate study, doctoral student Brian Wang, worked with Harald Paganetti of Massachusetts General Hospital to adopt the VIP-Man phantom to assess organ doses and the associated risk for developing secondary cancer after proton radiation treatment (Jiang *et al* 2005).

6.3.3. Respiration management in IGRT. After graduating from RPI, Chengyu Shi worked with RPI doctoral student Juying Zhang, to apply the respiration-simulating 4D VIP-Man phantom for Image-Guide Radiotherapy (IGRT) of lung cancer (Zhang *et al* 2008c). To extend the geometry-based modeling to physics-based modeling, Eom *et al* (2010) introduced the use of finite element analysis to develop patient-specific phantoms that simulate respiratory motions in a predictive manner.

6.3.4. Brachytherapy dosimetry. Using the RPI Adult Female phantom, graduate student Matt Mille collaborated with Mark Rivard of Tufts University (Mille *et al* 2010) to simulate patients undergoing balloon brachytherapy of the breast. Monte Carlo simulations were performed to compare doses from treatments involving ^{192}Ir or electronic sources using Monte Carlo simulations. This work helped demonstrate that the recently developed miniature x-ray sources may offer a more optimal treatment for the patient because of the lower radiation doses received by organs and tissues far from the treatment site.

6.3.5. Imaging doses in IGRT for Radiotherapy. Mr. Jianwei Gu and workers used the VIP-Man phantom to calculate organ doses from image-guided radiation treatment (IGRT) (Gu *et al* 2008b). Two imaging procedures were considered: kV Cone Beam CT and MV Cone Beam CT. The results indicate that thyroid received the highest dose in head and neck scans for both kV and MV CBCT, and the bladder receives the highest dose in prostate scan for both kV and MV CBCT. The effective doses for H&N scan and for prostate scan are at the same level in both kV CBCT and MV CBCT. This study provided a method to compute organ doses and effective dose that are useful in treatment planning and risk assessment. A second study performed calculations on the prostate, simulating kV CBCT and MDCT (Ding *et al* 2010). The calculations indicated that the imaging dose from standard IGRT procedures is high enough to warrant modifications to the procedure.

6.3.6. Proton Radiography. In his Ph.D. work, Bin Han collaborated with George Chen from MGH to use Monte Carlo simulations to evaluate the performance of a time-resolved proton range telescope (TRRT) (Han *et al* 2011). This was done by tracking 230 MeV protons as they passed through position detectors, a patient 4DCT phantom, and scintillation detectors. The proton water equivalent length (WEL) was deduced using a reconstruction algorithm that incorporated the linear proton track to improve image quality, and three patients' 4DCT images were used to measure WEL variations and tumor motions. The results from the simulations showed that the tumor trajectories from the WEL map agreed with direct 4DCT measurements within one millimeter.

7. Discussion

It is possible that tables 1–3 do not include all phantoms ever reported in the literature. The grouping of these phantoms into three types may not be always accurate since it was done using author supplied descriptions. Nevertheless, these tables allow us to plot and analyze the trends, as plotted in figure 25. It can be observed that, interestingly, only a total of 38 stylized phantoms were reported in the 50 years since the phantom was first developed in the 1960s. The work on stylized phantoms peaked in the 1980s with the publication of the so-called Cristy and Eckerman stylized family phantoms (Cristy and Eckerman 1987) which were widely adopted as the de facto standard in radiation protection dosimetry. The 2nd generation voxel phantoms surfaced in the late 1980s and gradually reached the peak in the middle of 2000s with a total of 85 voxel phantoms as of 2014. In comparison, the BREP phantoms did not emerge until early 2000s and, out of the total of 287 BREP phantoms as of 2014, the majority were reported within the past several years. When data for three phantom types were shown together in figure 25, a surprising pattern of exponential growth in research activity becomes apparent. Given the fact that the radiation protection dosimetry community relied on a dozen stylized phantoms for decades, one might have probably predicted a similar trend for voxel or BREP phantoms. In this case, we are wrong about the phantoms as we are often wrong about the general trend for technology, according to Ray Kurzweil, the author of the best-seller 'The Singularity Is Near: When Humans Transcend Biology.'

An important question is: why computational phantoms have evolved the way they did? Mathematical formulations of organs and tissues of the body used in the dosimetry of internally distributed radionuclides existed as early as the 1940s, although the first anthropomorphic phantom was not reported until the 1960s. In the 1970s and 1980s, the sophistication of these stylized phantoms was increased significantly. This evolution began with the specification of a single organ mass, followed by the use of simple shapes to simulate organs or the entire body of an adult human. The desire to model the entire body of the 'Reference Man' and to specify the location, shape, volume and mass of organs in the body as realistically as possible has remained the same to this day. The climax for stylized phantoms was reached in the 1980s when the gender- and age-specific family phantoms were systematically documented (Cristy and Eckerman 1987) and widely adopted for various studies in internal and external radiation dosimetry, as well as in medical imaging and radiotherapy. By that time, Monte Carlo codes and personal computers had become accessible to a large number of researchers. I did my PhD research at Texas A&M University using two dozen PCs with Intel 486 processors and MCNP Version 3 (Reece *et al* 1994, Xu *et al* 1995, Xu *et al* 1996, Reece and Xu 1997).

The research on stylized human models at ORNL up to the 1980s played an essential role in the history of computational phantoms. The sex-specific adult phantoms at GSF in the early 1980s were revisions of the MIRD-5 phantom originally developed at ORNL. Major extensions in the 1990s, on the pregnant women and brain/head models, were also closely tied to the earlier work at ORNL. The direct involvement of ORNL's scientists in the Society of Nuclear Medicine (SNM)'s MIRD Committee facilitated the necessary standardization process. It is clear that close collaborations between leading developers were a key factor contributing to the success of first-generation computational phantoms. Not all phantoms of this generation enjoyed the same recognition in the history, however. In fact, CAM and CAF phantoms were practically unknown to people outside the NASA community for decades. The early 1990s marks the beginning of an exciting new era of voxel phantoms. With easy access to rapidly advancing computers and medical imaging technologies, computational phantom research was no longer dominated by a few groups.

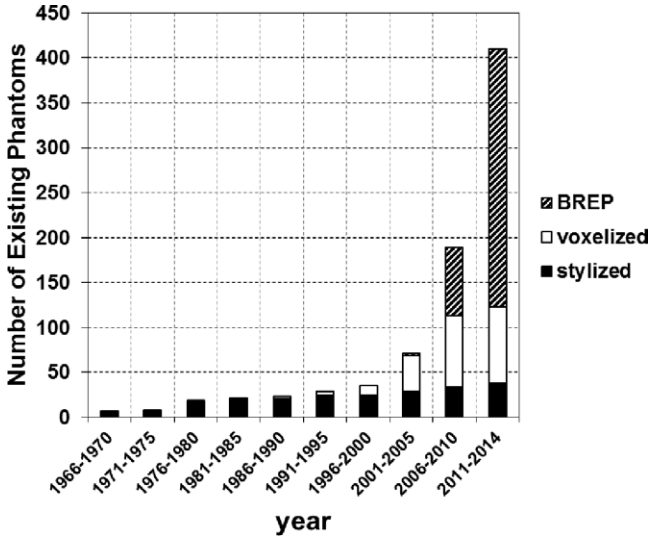

Figure 25. The number of phantoms in existence since 1966, showing a somewhat surprising exponential growth due to the rapid increase in voxel and BREP phantoms in recent decades (note: once a phantom is reported in the literature, it is counted in subsequent years when plotting this figure).

The shift from stylized phantoms to voxel phantoms in the late 1980s was initially motivated by the desire to improve upon anatomical realism. The advent of modern computers and medical imaging fueled the researcher-initiated efforts. During the 1990s, however, it was unclear to the research community what roles voxel phantoms would play. If voxel phantoms were to replace stylized phantoms as the standard in radiation protection, how much improvement in dose estimates should be expected? There were already strong indications that the methods used in voxel phantoms were not ideal, as observed by Caon (2004) and Zaidi and Xu (2007). For example, the segmentation of original images into organs and tissues often required a laborious and tedious manual process, requiring months or years to complete. Some of the voxel phantoms were based on relatively large image slice thickness, thus the anatomical accuracy of such phantoms was inevitably compromised. Even today, there is no consensus as to what constitutes a faithful segmentation procedure in creating these whole-body voxel phantoms because the process often required assumption about the anatomy during the image analysis. Certain organs in the stomach and GI tract have poor image contrast and, as a result, the segmentation is nearly impossible in CT without the use of contrast agent. Then, there is also a question of how small the voxel size should be. While voxels at 2 mm x 2 mm x 2 mm seem to do a good job representing most organs, they are not fine enough for some small and radiosensitive organs to be delineated. For this reason, the skin of most existing voxel phantoms is defined artificially as the outermost voxel layer in a phantom. The segmentation of two radiosensitive tissues—the red bone marrow and bone surface that are explicitly recommended for radiation protection dose calculations—is especially difficult. Consequently, doses to the red bone marrow and bone surface are always calculated using algorithms involving other parts of the bone. It is worth noting that phantoms based on cadaver images provided an opportunity to segment the red bone marrow explicitly. For example, Xu *et al* (2000) reported for the first time the whole-body red bone marrow distribution by harvesting color pixels of 0.33 mm x 0.33 mm resolution. Later the method was adopted in the development of several cadaver-based phantoms (Zhang *et al* 2010).

The lack of standardized procedures contributed to the current situation that although many phantoms and dosimetry data are reported, the accuracy may be impossible to compare. Voxel phantoms were realistic in depicting the anatomy, but they are also tied to a specific individual (thus conceivably not representative for a large group of people). The degree of anatomical differences between two equally realistic voxel phantoms surprised many developers who were used to the idea that a single radiation protection phantom could represent the average population. The 'Reference Man' methodology required a computational phantom to match the 50th percentile values in terms of body height and weight for a specific gender and age group. From the literature review, it was found that many developers later rushed to revise the original voxel phantoms by adjusting the organ sizes in the original image data to match with the ICRP-89 recommended anatomical data. In doing so, these voxel phantoms in fact lost their individual realism — a shortcoming that was associated previously with the stylized phantoms.

It is important to note the differences between 'population-averaged' prospective dosimetry needed for radiological protection under the current ICRP radiation protection system and 'individualized' retrospective dosimetry needed for accident dose reconstruction, medical dose tracking, or epidemiological study[1]. The ICRP system assumes that the workers and members of the public are adequately protected as long as the organ doses and effective doses estimated for the Reference Man — a hypothetical gender-averaged adult person whose relevant anatomical and physiological parameters are at the 50th percentile of the population defined by ICRP 89 — are kept below the ICRP dose limits. In other words, the ICRP system of radiological protection does not require the assessment of the 'real dose' to every exposed person. To follow ICRP recommendations for radiation protection dosimetry, one would need to (1) assess external exposures (e.g. by measuring quantities that can be related to a physical quantity such as fluence) and internal intakes (e.g. by performing bioassay for the amount of radioactivity inside the body) and then (2) convert these quantifies using ICRP reference dose coefficients (e.g. effective dose per fluence or per Bq inhaled) to yield estimates of organ dose or effective dose (ICRP 2007). Similarly, the use of a personnel dosimeter would require the comparison of the 'deep dose equivalent' measured at 1-cm in tissue equivalent materials with 'effective dose'. These dose coefficients, but design, should be calculated using only ICRP Computational Phantoms (e.g. 50th percentile reference phantoms) and reference biokinetic models (ICRP 2009). This means that non-reference phantoms reported in this review article should not be used to assign values of effective dose according to the design of the ICRP radiation protection system. So what is the usage of these phantoms reported in this article? To ICRP, these non-reference phantoms only helped to understand potential uncertainties in using the ICRP Computational Phantoms as the standard models. However, when the effective dose to the Reference Worker is deemed to be high compared to the dose limits such as in the case of an accident or in the case of assessing the dose-response functions during an epidemiological study, one should be encouraged to assess the actual and true organ doses to the exposed individual. At this point, any individual-specific computational phantoms representing an individual of both genders at different ages, heights, and weights can and should be used. Similarly, the ICRP radiation protection system does not apply to medical radiation exposures. A good example is the need to report CT doses to patients who are not subjected to the ICRP occupational dose limits. In that and other potential medical dosimetry applications, the researcher is no longer obligated to restrict their calculation to ICRP Computational Phantoms or reference biokinetic models. In fact, non-reference families of phantoms have been used for CT dose reporting (see www.virtualphantoms.com). Therefore, many voxel

[1] This paragraph about the distinction between ICRP 'population-averaged' prospective dosimetry and 'individualized' retrospective dosimetry is based on extensive discussion with Prof Wesley Bolch.

and BREP phantoms covered in this article are ideally suited for this type of 'individualized' retrospective applications that benefit from person-specific information in the calculations.

Looking into the future, is it necessary or feasible to bring about a change in the ICRP radiation protection concept described above? If so, how should the research community participate? The BREP phantoms have demonstrated the feasibility to develop new-generation phantoms that represent a much broader range of individuals in terms of body height and weight, as well as organ topology—features that were impossible even 10 years ago. So, should we move beyond the 'Reference Man' paradigm even for radiation protection purposes? Why cannot we adopt a method that quantifies 'uncertainty' in every dose calculation using a range of phantoms? There is no doubt that we are at crossroads now, perhaps as we were 20 years ago when voxel phantoms were about to emerge. The diversity of computational human phantoms developed by various groups within the community reflects the true variations amongst people and, ultimately, the true underlying uncertainty in radiation dose estimates.

This review also revealed a human factor that we do not normally see in the scientific discourse. In the history of voxel phantom development, Zubal was one of the first to share the original image data freely with other users based on a mutual agreement. Heated debate continued for some time at workshops regarding the intellectual property associated with phantoms that are revised by phantom users. It is often a technical necessity for a researcher to name a phantom created by him or her. However, it is not clear who should own such a copyright because each of the four steps of developing a phantom can be carried out by a different group. One scenario is when the original images were acquired and segmented by one individual and a different individual performed additional image processing and modification before implementing the data into a specific Monte Carlo code. Such changes produce a practically unique phantom, and proper naming is often useful for research purposes, even though individuals involved in the process do not seem to always agree upon the ownership of such a product. Some have chosen not to share phantoms partially due to this concern. Others are afraid that sharing may cost an advantage in research in a time when too many voxel phantoms exist.

The history of computational phantom development has shown that it is the need for applications, not the need for policy-making, that determines the course of technological advancement. The need for simulating organ motions for cardiac imaging, for example, resulted in the developments of MCAT phantom by Tsui *et al* (2004) using quadric and superquadric surface equations as well as more recently the NCAT models by Segars (2001) using the NURBS technology. Xu and Shi (2005) adopted 'the geometry-based' respiration algorithm in the NCAT phantom for radiation treatment. Later Eom *et al* (2010) developed a 'physics-based' respiration-simulating 4D phantoms for the need to understand and 'predict' the effects of respiration on radiation treatment. Using the same approach, Lee *et al* (2007) developed the size-adjustable pediatric models. The BREP-based pregnant females by Xu *et al* (2007) and those by Stabin *et al* (2008) are also examples of application-driven research that will likely continue to dominate the research horizon in the future.

As shown in figure 25, the BREP-based phantoms are clearly going to be the future. NURBS geometries are flexible and computationally efficient, but fine details may be lost on certain organs that have complex topology. On the other hand, polygonal models can be used to create very smooth surfaces with impressive anatomical detail by paying the price of having too many vertices. Geometrical modeling of the human body is a challenge for that it consists of organ surfaces of complex and unique shapes. For cardiac and respiratory motions at the frequency range of 10–100 cycles per second, the mesh models may still be acceptable. However, previous work has also shown that the NURBS primitives were easy to

adopt for both real-time and non-real-time applications. Therefore, the specific strategy will likely be based on the applications and user preference. Regardless of the specific BREP data structure, there is currently an urgent need for application-based software that can streamline the process.

Looking forward, the following issues should be addressed by the research community in the next 5–10 years:

(1) Intercomparison of ICRP-89 compatible phantoms. More than a dozen groups worldwide have developed anatomically realistic and ICRP-89 compatible phantoms. However, organ locations and shapes differ from phantom to phantom. In particular, the dosimetric differences between these phantoms — some of which represent Asian populations instead of Caucasians —and the ICRP Reference Computational Phantoms are not well understood. What is needed is a systematic intercomparison of these phantoms and quantification of dosimetric differences related to variations in organ topology.

(2) A shift away from the Reference Man-based paradigm in radiation protection. Research on radiation protection phantoms has been influenced by the 'Reference Man' paradigm. This approach required a computational phantom to match the 50^{th} percentile population-average values in terms of body height and weight. However, anatomical variations associated with body size and organ shape can cause as much as 100% difference in the estimated organ doses. So the use of ICRP Reference Computational Phantoms carries a very large uncertainty. Future radiation protection systems may require this uncertainty to be quantified and reduced (say, to a level of 30% or less). To achieve that future goal, a shift away from the ICRP 'Reference Man' methodology must take place by expanding the 50^{th}-percentile phantoms into a much larger set of phantoms ranging from the 10^{th} percentile to the 90^{th} percentile, as well as people who are overweight, in each of the gender and age groups. Anthropometric data from population surveys can be used to evaluate trends in body and organ distributions. Both body weight index and trunk height can be used to match a specific individual with this expanded library of reference phantoms. Such phantoms are already used today for retrospective patient dose tracking and accidental dose reconstruction. It is anticipated that ICRP will begin to consider adopting such phantoms for prospective dosimetry in the future.

(3) Physics-based methods for deformation modeling. Motion-simulating 4D computational phantoms will play an increasingly vital role in the understanding and management of organ motion in radiotherapy and medical imaging. Work has been done to model cardiac and respiratory motions using BREP-based methods. These phantoms contain patient-specific imaging data such as 4D CT and therefore provide a realistic simulation of the motion. A limitation to these models is that they provide only one realization of the motion, specifically that observed in the patient images. They do not have the ability to realistically predict motion variations that may occur inside the same individual. To model variations in motion, one would require accurate handling of the interactions at the organ interfaces. Finite element analysis methods have the advantage of being physics-based and can be used in single- and multiple-organ deformable registration. Furthermore, internal dose models are currently based on a static 3D lung anatomy. Phantoms that account for aerodynamic flow of radioactive particulates in various parts of a deformable respiratory system will be developed in the next decade.

(4) Monte Carlo simulations with advanced geometries. Monte Carlo codes for radiation transport simulations were originally designed for nuclear engineering and high-energy physics applications. Although these codes contain excellent radiation physics algorithms, they

suffer from poor software engineering design and are only able to handle simple geometries. These deficiencies have resulted in three problems that compromise current efforts in phantom research: (1) The implementation of various anatomically complex phantoms in these codes requires cumbersome manual processes. (2) Currently the NURBS-based or mesh-based phantoms must be converted to voxels before using with Monte Carlo programs (but a few groups have begun to address this issue as discussed earlier in this article). (3) Existing Monte Carlo codes are unable to handle a 'moving' target such as the dynamic heart or lung. Research to convert an object defined in CAD software to those acceptable by a Monte Carlo code has been on-going in the nuclear engineering community for years. Future research is needed to develop new and computationally efficient ray-tracing algorithms that can directly process NURBS- and mesh-based geometric objects for Monte Carlo radiation transport calculations. Open-source Monte Carlo codes will be widely adopted in the next decade. With new technologies such as cloud-computing and hardware accelerated Monte Carlo methods involving the GPUs and coprocessors, one expects that dose calculation involving a whole-body voxel and BREP phantom can be carried out in seconds in the near future (for examples, see our own work by Liu *et al* (2014) and Su *et al* (2014)). Such near-real-time Monte Carlo methods will likely further increase the rate of computational phantom research toward the 4th generation of 'patient-specific' phantoms.

8. Conclusion

A paper which appeared in 2000 on the VIP-Man phantom predicted that the advantages afforded by both the voxels and BREP-type of surface geometries would be eventually combined (Xu *et al* 2000):

'*For the purposes of setting radiation protection standards, it may be possible to eventually bridge these two types of models, leading to a new generation of hybrid 'standard' model(s) that will be acceptable to the radiation protection community. Such a new generation of models for radiation protection should be realistic enough to accurately represent major radiosensitive tissues and organs, and flexible enough to represent different populations by scaling. Computers are going to be so powerful that very complex models can be handled without a problem*.'

These so-called 'hybrid' computational phantoms were indeed realized in less than a decade as shown in figure 25. In the next 10 years and beyond, advances in computational phantom research will be once again exponential. Increasingly personalized whole-body computational phantoms will be developed and applied for various clinical applications. Such phantoms will contain deformable anatomies that are physics-based and are, therefore, biomechanically realistic in depicting real-time and multi-organ deformation associated with cardiac and respiratory motions. These phantoms will also possess physiological and functional information of the human body at the organ and cellular levels obtained from multiple scanners. Breakthroughs in computational radiobiology, in the context of cancer radiotherapy, are expected to bring a new horizon to the personalized radiation medicine by understanding and harnessing the massive power of genomic data. At the same time, the power of computers will reach the exascale by the end of 2020s owing to highly efficient hardware designs (such as NVIDIA GPUs and INTEL coprocessors), thus making real-time Monte Carlo calculations for next-generation computational phantoms possible. The 50-year history reviewed in this article shows clearly that coordinated and cooperative efforts among radiological engineers, computer scientists, biologists, and clinicians will always be the key to the success of future research endeavors.

Acknowledgments

This article benefitted from discussions in the past decade with many colleagues, especially Keith Eckerman, John Poston, Dan Reece, Wes Bolch, Mike Stabin, Randy Brill, Paul Segars, Ben Tsui, Harald Paganetti, Mike McNitt-Gray, George Zubal, Maria Zankl, Nina Petoussi-Henss, Richard Kramer, Qian Liu, Junli Li, Chan Kim, and Habib Zaidi. This article adopted several chapters of the *Handbook of Anatomical Models For Radiation Dosimetry* for which I was a co-editor. RPI research activities highlighted in the article were based on the following Ph D or M S projects (the year of graduation indicated): Ahmet Bozkurt (2000), TC Ephraim Chao (2001), Chengyu Shi (2004), Mark Winslow, (2005), Brian Wang (2005), Peter Caracappa (2006), Bryan Bednarz (2008), Juying Zhang (2009), Yong Hum Na (2009), Jianwei Gu (2010), Bin Han (2011), Aiping Ding (2012), Matthew Mille (2013), and Justin Vazquez (2013). Grants Funding for these projects include: National Science Foundation (BES-9875532), National Library of Medicine (R03LM007964, R01LM009362, and R01LM009362-03S1), National Cancer Institute (R01CA116743 and R42CA115122), National Institute of Biomedical Imaging and Bioengineering (R42EB010404), and National Institute of Standards and Technology (70NANB9H9198). Several RPI students and postdoc researchers helped me with the preparation and submission of this article: Xining Du, Michael Pinkert, Ashley Rhodes, Tianyu Liu, Haikuan Liu, and Matthew Mille.

References

Akkurt H, Bekar K B, and Eckerman K F 2008 VOXMAT: phantom model with combination of voxel and mathematical geometry *Health Phys*. **95** S100

Alderson S W, Lanzl L H, Rollins M and Spira J 1962 An instrumented phantom system for analog computation of treatment plans *Am. J. Roentgenol. Radium. Ther. Nucl. Med*. **87** 185–95

Allison J *et al* 2006 Geant4 developments and applications *IEEE Trans. Nucl. Sci*. **53** 270–8

Alziar I *et al* 2009 Individual radiation therapy patient whole-body phantoms for peripheral dose evaluations: method and specific software *Phys. Med. Biol*. **54** N375–83

Andreo P 1991 Monte Carlo techniques in medical radiation physics *Phys. Med. Biol*. **36** 861–920

Attix F H 1986 *Introduction to Radiological Physics and Radiation Dosimetry* (New York: John Wiley & Sons)

Bahadori A A, Johnson P B, Jokisch D W, Eckerman K F, and Bolch W E 2011a Response functions for computing absorbed dose to skeletal tissues from neutron irradiation *Phys. Med. Biol*. **56** 6873–97

Bahadori A A, Van Baalen M, Shavers M R, Dodge C, Semones E J and Bolch W E 2011b The effect of anatomical modeling on space radiation dose estimates: a comparison of doses for NASA phantoms and the 5th, 50th, and 95th percentile male and female astronauts *Phys. Med. Biol*. **56** 1671–94

Battistoni G, Cerutti F, Fassò A, Ferrari A, Muraroi S, Ranft J, Roesler S and Sala P R 2007 The FLUKA code: description and benchmarking *AIP Conf. Proc*. **896** 31-49

Beck P *et al* 2011 MATSIM: development of a voxel model of the MATROSHKA astronaut dosimetric phantom *IEEE Trans. Nuc. Sci*. **58** 1921–6

Becker J, Zankl M and Petoussi-Henss N 2007 A software tool for modification of human voxel models used for application in radiation protection *Phys. Med. Biol*. **52** N195–205

Bento J, Barros S, Teles P, Neves M, Gonçalves I, Corisco J and Vaz P 2011 Monte Carlo simulation of the movement and detection efficiency of a whole-body counting system using a BOMAB phantom *Radiat. Prot. Dosimetry* **148** 403–13

Bhati S, Patni H K, Ghare V P, Singh I S and Nadar M Y 2012 Monte Carlo calculations for efficiency calibration of a whole-body monitor using BOMAB phantoms of different sizes *Radiat. Prot. Dosim.* **148** 414–9

Billings M P and Yucker W R 1973 *The Computerized Anatomical Man (CAM) model NASA CR-134043* (Houston, TX: National Aeronautics and Space Administration)

Bolch W, Lee C, Wayson M, Johnson P 2010 Hybrid computational phantoms for medical dose reconstruction *Radiat. Environ. Biophys.* **49** 155–68

Bouchet L G, Bolch W E, Weber D A, Atkins H L, Poston J W Sr 1996 A revised dosimetric model of the adult head and brain *J. Nucl. Med*. **37** 1226–36

Bouchet L G, Bolch W E, Weber D A, Atkins H L and Poston J W Sr 1999 MIRD Pamphlet No. 15: radionuclide S values in a revised dosimetric model of the adult head and brain *J. Nucl. Med*. **40** 62S–101S

Bouchet L G, Bolch W E, Blanco H P, Rajon D A, Clairand I, Sgouros G, and Wessels BW 2003 MIRD Pamphlet No. 19: absorbed fractions and radionuclide S values for six age-dependent multi-region models of the kidney *J. Nucl. Med.* **44** 1113–47

Bozkurt A, Chao T C and Xu X G 2000 Fluence-to-dose conversion coefficients from monoenergetic neutron beams below 20 MeV based on the VIP-Man anatomical model *Phys. Med. Biol*. **45** 3059-79.

Bozkurt A, Chao T C and Xu X G 2001 Fluence-to-dose conversion coefficients based on the VIP-Man anatomical model and MCNPX code for monoenergetic neutrons above 20 MeV *Health Phys*. **81** 184–202

Bozkurt A and Xu X G 2004 Fluence-to-dose conversion coefficients for monoenergetic proton beams based on the VIP-Man anatomical model *Radiat. Prot. Dosimetry* **112** 219–35

Broggio D, Beurrier J, Bremaud M, Desbrée A, Farah J, Huet C and Franck D 2011 Construction of an extended library of adult male 3D models: rationale and results *Phys. Med. Biol*. **56** 7659–92

Brown F B (ed) 2003 MCNP—A general Monte Carlo N-Particle transport code, *version 5 Report LA-UR-03-1987* (Los Alamos, NM: Los Alamos National Laboratory)

Caon M, Bibbo G and Pattison J 1999 An EGS4-ready tomographic computational model of a 14-year-old female torso for calculating organ doses from CT examinations *Phys. Med. Biol*. **44** 2213–25

Caon M, Bibbo G and Pattison J 2000 Monte Carlo calculated effective dose to teenage girls from computed tomography examinations *Radiat. Prot. Dosim.* **90** 445–8

Caon M 2004 Voxel-based computational models of real human anatomy: a review *Radiat. Environ. Biophys*. **42** 229–35

Caracappa P F 2006 Development and evaluation of a new algorithm for determining radiation dose to the red bone marrow *Ph D Dissertation* Rensselaer Polytechnic Institute

Caracappa P F, Chao T C E and Xu X G 2009 A study of predicted bone marrow distribution on calculated marrow dose from external radiation exposures using two sets of image data for the same individual *Health Phys*. **96** 661–74

Cassola V F, Lima V J M, Kramer R and Khoury H J 2010 FASH and MASH: female and male adult human phantoms based on polygon mesh surfaces: I. Development of the anatomy *Phys. Med. Biol*. **55** 133–62

Cassola V F, Milian F M, Kramer R, de Oliveira Lira C A B and Khoury H J 2011 Standing adult human phantoms based on 10th, 50th and 90th mass and height percentiles of male and female Caucasian populations *Phys. Med. Biol*. **56** 3749–72

CCHP 2005 Tomographic models for radiation protection dosimetry session the Monte Carlo method: versatility unbounded in a dynamic computing world *World Proc. of the Monte Carlo 2005 Topical Meeting on CD-ROM* (*Chattanooga, TN*, *17–21 April 2005*) (LaGrange: American Nuclear Society)

Cech R, Leitgeb N and Pediaditis M 2008 Current densities in a pregnant woman model induced by simultaneous ELF electric and magnetic field exposure *Phys. Med. Biol*. **53** 177–86

Cech R, Leitgeb N and Pediaditis M 2007 Fetal exposure to low frequency electric and magnetic fields *Phys. Med. Biol*. **52** 879–88

Chao T C, Bozkurt A and Xu X G 2001a Conversion coefficients based on the VIP-Man anatomical model and EGS4-VLSI code for external monoenergetic photons from 10 keV to 10 MeV *Health Phys*. **81** 163–83

Chao T C, Bozkurt A, Xu X G 2001b Organ dose conversion coefficients for 0.1–10 MeV electrons calculated for the VIP-Man tomographic model *Health Phys*. **81** 203–14

Chao T C and Xu X G 2001 Specific absorbed fractions from the image-based VIP-Man body model and EGS4-VLSI Monte Carlo code: internal electron emitters *Phys. Med. Biol*. **46** 901–27

Chao T C, Bozkurt A, and Xu X G 2003 Conversion coefficients based on the VIP-Man anatomical model and EGS4-VLSI code for external monoenergetic photons from 10 keV to 10 MeV *Health Phys*. **84** 390

Chao T C and Xu X G 2004 S-values calculated from a tomographic head/brain model for brain imaging *Phys. Med. Biol*. **49** 4971–84

Chen J 2004 Mathematical models of the embryo and fetus for use in radiological protection *Health Phys*. **86** 285–95

Choi S H, Lee C-S, Cho S K, Chung M S, Na S H and Kim C H 2006 Construction of a high-definition 'Reference Korean' voxel phantom for organ and tissue radiation dose calculation *IFMBE Proc*. **14** 4204–7

Christ A *et al* 2010 The Virtual Family—development of surface-based anatomical models of two adults and two children for dosimetric simulations *Phys. Med. Biol*. **55** N23–38

CIRS 2013 *Tissue Simulation and Phantom Technology* www.cirsinc.com

CMPWG 2013 *Phantoms* http://cmpwg.ans.org/phantoms/camera.pdf

Courageot E, Huet C, Clairand I, Bottollier-Depois J F and Gourmelon P 2011 Numerical dosimetric reconstruction of a radiological accident in South America in April 2009 *Radiat. Prot. Dosimetry* **144** 540–2

Courageot E, Sayah R and Huet C 2010 Development of modified voxel phantoms for the numerical dosimetric reconstruction of radiological accidents involving external sources: implementation in SESAME tool *Phys. Med. Biol*. **55** N231-41

Cristy M 1980 Mathematical phantoms representing children of various ages for use in estimates of internal dose *U S Nuclear Regulatory Commission Report NUREG/CR-1159* (Oak Ridge, TN: Oak Ridge National Laboratory) http://web.ornl.gov/info/reports/1980/3445605812234.pdf

Cristy M and Eckerman K F 1987 Specific absorbed fractions of energy at various ages from internal photon sources I: methods *Oak Ridge National Laboratory Report ORNL/TM-8381/V1* (Oak Ridge, TN: Oak Ridge National Laboratory) http://ordose.ornl.gov/documents/tm8381V1.pdf

Dawson T W, Caputa K and Stuchly M A 1997 A comparison of 60 Hz uniform magnetic and electric induction in the human body *Phys. Med. Biol*. **42** 2319–29

Deus S F and Poston J W 1976 The development of a mathematical phantom representing a 10-year-old for use in internal dose calculations *Proc. of the Symp. on Radiopharmaceutical Dosimetry HEW Publication 76–8044* (Rockville, MD: U S Food and Drug Administration)

DeWerd L A and Kissick M 2014 *The Phantoms of Medical and Health Physics* (Berlin: Springer)

Dimbylow P J 1996 The development of realistic voxel phantoms for electromagnetic field dosimetry *Proc. Workshop on Voxel Phantom Development* (*Chilton, UK*)

Dimbylow P J 1997 FDTD calculations of the whole-body averaged SAR in an anatomically realistic voxel model of the human body from 1 MHz to 1 GHz *Phys. Med. Biol*. **42** 479–90

Dimbylow P 2005a Development of the female voxel phantom, NAOMI, and its application to calculations of induced current densities and electric fields from applied low frequency magnetic and electric fields *Phys. Med. Biol*. **50** 1047–70

Dimbylow P 2005b Resonance behaviour of whole-body averaged specific energy absorption rate (SAR) in the female voxel model, NAOMI *Phys. Med. Biol*. **50** 4053–63

Dimbylow P 2006 Development of pregnant female, hybrid voxel-mathematical models and their application to the dosimetry of applied magnetic and electric fields at 50 Hz *Phys. Med. Biol*. **51** 2383–94

Dimbylow P, Bolch W and Lee C 2010 SAR calculations from 20 MHz to 6 GHz in the University of Florida newborn voxel phantom and their implications for dosimetry *Phys. Med. Biol*. **55** 1519–30

Ding A, Gu J, Trofimov A V and Xu X G 2010 Monte Carlo calculation of imaging doses from diagnostic multidetector CT and kilovoltage cone-beam CT as part of prostate treatment plans *Med. Phys*. **37** 6199–204

Ding A, Mille M M, Liu T, Caracappa P F and Xu X G 2012 Extension of RPI-adult male and female computational phantoms to obese patients and a Monte Carlo study on the effects on CT imaging dose *Phys. Med. Biol*. **57** 2441–59

Doerfel H and Heide B 2007 Calibration of a phoswich type partial body counter by Monte Carlo simulation of low-energy photon transport *Radiat. Prot. Dosim.* **123** 464–72

Eckerman K F 1985 Aspects of the dosimetry of radionuclides within the skeleton with particular emphasis on the active marrow *Proc. 4th Int. Radiopharmaceutical Dosimetry Symp*. ed A T Schlafke-Stelson and E E Watson (Oak Ridge, TN: Oak Ridge Associated Universities) pp 514–34

Eckerman K F and Stabin M G 2000 Electron absorbed fractions and dose conversion factors for marrow and bone by skeletal regions *Health Phys*. **78** 199–214

Eckerman K F, Poston J W Sr, Bolch W E and Xu X G 2010 The stylized computational phantoms developed at ORNL and elsewhere *Handbook of Anatomical Models for Radiation Dosimetry* (New York: Taylor & Francis) 43–64

Eom J, Xu X G, De S and Shi C 2010 Predictive modeling of lung motion over the entire respiratory cycle using measured pressure-volume data, 4DCT images, and finite element analysis *Med. Phys.* **37** 4389–400

Farah J, Broggio D and Franck D 2010a Creation and use of adjustable 3D phantoms: application for the lung monitoring of female workers *Health Phys.* **99** 649–61

Farah J, Broggio D and Franck D 2010b Female workers and *in vivo* lung monitoring: a simple model for morphological dependence of counting efficiency curves *Phys. Med. Biol.* **55** 7377–95

Farah J, Broggio D and Franck D 2011 Examples of Mesh and NURBS modelling for *in vivo* lung counting studies *Radiat. Prot. Dosim.* **144** 344–8

Ferrari A, Pelliccioni M and Pillon M 1997 Fluence to effective dose and effective dose equivalent conversion coefficients for electrons from 5 MeV to 10 GeV *Radiat. Prot. Dosim.* **69** 97–104

Ferrari P and Gualdrini G 2005 An improved MCNP version of the NORMAN voxel phantom for dosimetry studies *Phys. Med. Biol.* **50** 4299–316

Ferrari P 2010 Development of an integrated couple of anthropomorphic models for dosimetric studies *Radiat. Prot. Dosim.* **142** 191–200

Fill U A, Zankl M, Petoussi-Henss N, Siebert M and Regulla D 2004 Adult female voxel models of different stature and photon conversion coefficients for radiation protection *Health Phys.* **86** 253–72

Findlay R P and Dimbylow P J 2009 Spatial averaging of fields from half-wave dipole antennas and corresponding SAR calculations in the NORMAN human voxel model between 65 MHz and 2 GHz *Phys. Med. Biol.* **54** 2437–47

Findlay R P and Dimbylow P J 2010 SAR in a child voxel phantom from exposure to wireless computer networks (Wi-Fi) *Phys. Med. Biol.* **55** N405–11

Fisher H L J and Snyder W S 1966 Variation of dose delivered by 137Cs as a function of body size from infancy to adulthood *Health Physics Division Annual Progress Report for Period Ending July 31, 1966 Report ORNL-4007* (Oak Ridge, TN: Oak Ridge National Laboratory) 221–28

Fisher H L J and Snyder W S 1967 Distribution of dose in the body from a source of gamma rays distributed uniformly in an organ *Health Physics Division Annual Progress Report for Period Ending July 31, 1967 Report ORNL-4168* (Oak Ridge, TN: Oak Ridge National Laboratory)

Fung G S, Segars W P, Gullberg G T and Tsui B M 2011 Development of a model of the coronary arterial tree for the 4D XCAT phantom *Phys. Med. Biol.* **56** 5651–63

Gardumi A, Farah J and Desbrée A 2013 Creation of ORNL NURBS-based phantoms: evaluation of the voxel effect on absorbed doses from radiopharmaceuticals *Radiat. Prot. Dosim.* **153** 273–81

Geyer A M, O'Reilly S, Lee C, Long D J and Bolch W E 2014 The UF/NCI family of hybrid computational phantoms representing the current US population of male and female children and adolescents—applications to CT dosimetry *Phys. Med. Biol.* **59** 5225–42

Gibbs S J, Pujol A, Chen T S, Malcolm A W and James A E 1984 Patient risk from interproximal radiography *Oral Surg. Oral Med. O.* **58** 347–54

Gibbs SJ, Pujol A Jr, Chen T S, Carlton J C, Dosmann M A, Malcom A W and James A E Jr 1987 Radiation doses to sensitive organs from intraoral dental radiography *Dentomaxillofac Radiol.* **16** 67–77

Gjonaj E, Bartsch M, Clemens M, Schupp S and Weiland T 2002 High-resolution human anatomy models for advanced electromagnetic field computations *IEEE Trans. Magn.* **38** 357–60

Goorley J T *et al* 2013 Initial MCNP6 Release Overview—MCNP6 version *1.0 Report LA-UR-13-22934* (Los Alamos, NM: Los Alamos National Laboratory)

Gosselin M-C *et al* 2014 Development of a new generation of high-resolution anatomical models for medical device evaluation: the virtual population 3.0 *Phys. Med. Biol.* **59** 5287–303

Griffith R V, Dean P N, Anderson A L and Fisher J C 1978 Fabrication of a tissue-equivalent torso phantom for intercalibration of *in-vivo* transuranic-nuclide counting facilities *Proc. of Int. Symp. on Advances in Radiation Protection Monitoring* (Stockholm: International Atomic Energy Agency) also as Lawrence Livermore National Laboratory Report UCRL-80343

Gu J, Dorgu A and Xu X G 2008a Comparison of main software packages for CT dose reporting *Health Phys.* **95** S50

Gu J, Bednarz B, Xu X G and Jiang S B 2008b Assessment of patient organ doses and effective doses using the VIP-Man adult male phantom for selected cone-beam CT imaging procedures during image guided radiation therapy *Radiat. Prot. Dosimetry* **131** 431–43

Gu J, Bednarz B, Caracappa P F and Xu X G 2009 The development, validation and application of a multi-detector CT (MDCT) scanner model for assessing organ doses to the pregnant patient and the fetus using Monte Carlo simulations *Phys. Med. Biol.* **54** 2699–717

Gu J 2010 Development of CT scanner models for patient organ dose calculations using Monte Carlo methods *Ph D Dissertation* Rensselaer Polytechnic Institute

Gu S, Gupta R and Kyprianou I 2011 Computational high-resolution heart phantoms for medical imaging and dosimetry simulations *Phys. Med. Biol.* **56** 5845–64

Han B, Zhang J, Na Y H, Caracappa P F and Xu X G 2010 Modeling and Monte Carlo organ dose calculations for workers walking on ground contaminated with Cs-137 and Co-60 gamma sources *Radiation Prot. Dosimetry* **141** 299–304

Han B, Xu X G, Chen G T Y 2011 Proton radiography and fluoroscopy of lung tumors: a Monte Carlo study using patient-specific 4DCT phantoms *Med. Phys.* **38** 1903–11

Han M C, Kim C H, Jeong J H, Yeom Y S, Kim S, Wilson P H and Apostolakis J 2013 DagSolid: a new Geant4 solid class for fast simulation in polygon-mesh geometry *Phys. Med. Biol.* **58** 4595–4609

Hammersley J M and Handscomb D C 1964 *Monte Carlo Methods* (London: Metheun & Co)

Hegenbart L, Na Y H, Zhang J Y, Urban M and Xu X G 2008 A Monte Carlo study of lung counting efficiency for female workers of different breast sizes using deformable phantoms *Phys. Med. Biol.* **53** 5527–38

Hintenlang D, Moloney W and Winslow J 2010 Physical Phantoms for Experimental Radiation Dosimetry *Handbook of Anatomical Models for Radiation Dosimetry* (New York: Taylor & Francis)

Hirata A, Ito N, Fujiwara O, Nagaoka T and Watanabe S 2008 Conservative estimation of whole-body-averaged SARs in infants with a homogeneous and simple-shaped phantom in the GHz region *Phys. Med. Biol.* **53** 7215–23

Hough M, Johnson P, Rajon D, Jokisch D, Lee C and Bolch W 2011 An image-based skeletal dosimetry model for the ICRP reference adult male—internal electron sources *Phys. Med. Biol.* **56** 2309–46

Hubbell J H 1969 Photon cross sections, attenuation coefficients and energy absorption coefficients from 10 keV to 100 GeV *Report NSRDS-NBS 29* (Washington, DC: National Bureau of Standards)

Hwang J M L, Shoup R L and Poston J W 1976 Mathematical description of a newborn human for use in dosimetry calculations *Report ORNL/TM-5453* (Oak Ridge, TN: Oak Ridge National Laboratory)

ICRP 1959 *Report of Committee II on Permissible Dose for Internal Radiation* (Oxford, UK: Pergamon)

ICRP 1975 *Report of the Task Group on Reference Man ICRP Publication 23* (Oxford, UK: Pergamon)

ICRP 2002a *Basic anatomical and physiological data for use in radiological protection reference values ICRP Publication 89* (Oxford, UK: Pergamon)

ICRP 2002b *2002 Annual Report of the International Commission on Radiological Protection* www.icrp.org/docs/2002_ann_rep_52_429_03.pdf)

ICRP 2007 *Recommendations of the International Commission on Radiological Protection ICRP Publication 103* (Oxford, UK: Pergamon)

ICRP 2009 *Adult reference computational phantoms ICRP Publication 110* (Oxford, UK: Pergamon)

ICRU 1992 *Phantoms and computational models in therapy, diagnosis and protection ICRU Report 48* (Bethesda, MD: International Commission on Radiation Units and Measurements)

Jiang H, Wang B, Xu X G, Suit H D and Paganetti H 2005 Simulation of organ-specific patient effective dose due to secondary neutrons in proton radiation treatment *Phys. Med. Biol.* **50** 4337–53

Jin W, Lim Y-J, Xu X G, Singh T P and De S 2005 Improving the visual realism of virtual surgery *Proc. of Medicine Meets Virtual Reality 13: The Magical Next Becomes the Medical Now* ed J D Westood *et al* (Amsterdam: IOS) pp 227–33

Johnson P, Lee C, Johnson K, Siragusa D and Bolch W E 2009 The influence of patient size on dose conversion coefficients: a hybrid phantom study for adult cardiac catheterization *Phys. Med. Biol.* **54** 3613–29

Johnson P B, Bahadori A A, Eckerman K F, Lee C, and Bolch W E 2011 Response functions for computing absorbed dose to skeletal tissues from photon irradiation—an update *Phys. Med. Biol.* **56** 2347–66

Jones R M, Poston J W, Hwang J L, Jones T D and Warner G G 1976 The development and use of a fifteen-year-old equivalent mathematical phantom for internal dose calculations *Report ORNL/TM-5278* (Oak Ridge, TN: Oak Ridge National Laboratory)

Jones D G 1997 A realistic anthropomorphic phantom for calculating organ doses arising from external photon irradiation *Radiat. Prot. Dosimetry* **72** 21–9

Jones A K, Simon T A, Bolch W E, Holman M M and Hintenlang D E 2006 Tomographic physical phantom of the newborn child with real-time dosimetry I. Methods and techniques for construction *Med. Phys*. **33** 3274–82

Katagiri M, Hikoji M, Kitaichi M, Sawamura S and Aoki Y 2000 Effective dose and organ doses per unit fluence calculated for monoenergetic 0.1 MeV to 100 MeV electrons by the MIRD-5 phantom *Radiat. Prot. Dosim.* **90** 393–401

Kereiakes J G, Seltzer R A, Blackburn B and Saenger E L 1965 Radionuclide doses to infants and children: a plea for a standard child *Health Phys*. **11** 999–1004

Kim J I, Choi H, Lee B I, Lim Y K, Kim C S, Lee J K and Lee C 2006 Physical phantom of typical Korean male for radiation protection purpose *Radiat. Prot. Dosimetry* **118** 131–6

Kim C H, Choi S H, Jeong J H, Lee C and Chung M S 2008 HDRK-Man: a whole-body voxel model based on high-resolution color slice images of a Korean adult male cadaver *Phys. Med. Biol*. **53** 4093–106

Kim J H, Kim C S and Whang J H 2010a Assessment of radiation dose for surrounding organs and persons approaching implanted patients upon brachytherapy of prostate cancer with Iridium-192 *Radiat. Prot. Dosim.* **141** 283–8

Kim J S, Ha W H, Jeong J H, Cho K-W and Lee J K 2010b Use of photographic images to construct voxel phantoms for use in whole-body counting *Radiat. Prot. Dosim.* **138** 119–22

Kim C H, Jeong J H, Bolch W E, Cho K-W and Hwang S B 2011 A polygon-surface reference Korean male phantom (PSRK-Man) and its direct implementation in Geant4 Monte Carlo simulation *Phys. Med. Biol*. **56** 3137–61

Kramer R, Zankl M, Williams G and Drexler G 1982 The calculation of dose from external photon exposures using reference human phantoms and Monte Carlo methods: Part I. The male (ADAM) and female (EVA) adult mathematical phantoms *GSF-Report S-885* (Neuherberg: Institut fuer Strahlenschutz, GSF-Forschungszentrum fuer Umwelt und Gesundheit)

Kramer G H, Burns L and Noel L 1991 The BRMD BOMAB phantom family *Health Phys*. **61** 895–902

Kramer R, Vieira J W, Khoury H J, Lima F R A and Fuelle D 2003 All about MAX: a male adult voxel phantom for Monte Carlo calculations in radiation protection dosimetry *Phys. Med. Biol*. **48** 1239–62

Kramer R, Khoury H J, Vieira J W, Loureiro E C M, Lima V J M, Lima F R A and Hoff G 2004 All about FAX: a Female Adult voXel Phantom for Monte Carlo Calculation in Radiation Protection Dosimetry *Phys. Med. Biol*. **49** 5203–16

Kramer R, Khoury H J, Vieira J W and Lima V J M 2006 MAX06 and FAX06: update of two adult human phantoms for radiation protection dosimetry *Phys. Med. Biol*. **51** 3331–46

Kramer R, Cassola V F, Khoury H J, Vieira J W, Lima V J M and Brown K R 2010 FASH and MASH: female and male adult human phantoms based on polygon mesh surfaces: II *Dosimetric calculations* **55** 163–89

Kyoto Kagaku co., LTD 2013 *Patient Simulators, Imaging Phantoms for Skill Training* www.kyotokagaku.com/ (last access 02/28/14)

Lee C *et al* 2013 Computational lymphatic node models in pediatric and adult hybrid phantoms for radiation dosimetry *Phys. Med. Biol*. **58** N59

Lee C, Lee J and Lee C 2004 Korean adult male voxel model KORMAN segmented from magnetic resonance images *Med. Phys*. **31** 1017–22

Lee C, Williams J L, Lee C and Bolch W E 2005 The UF series of tomographic computational phantoms of pediatric patients *Med. Phys*. **32** 3537–48

Lee C, Lee C, Park S H, Lee J K 2006a Development of the two Korean adult tomographic computational phantoms for organ dosimetry *Med. Phys*. **33** 380–90

Lee C, Lee C, Williams J L and Bolch W E 2006b Whole-body voxel phantoms of paediatric patients—UF Series B *Phys. Med. Biol*. **51** 4649–61

Lee C, Nagaoka T and Lee J-K 2006c Implementation of Japanese male and female tomographic phantoms to multi-particle Monte Carlo mode for ionizing radiation dosimetry *J. Nucl. Sci. Technol*. **43** 937–45

Lee C, Lodwick D, Hasenauer D, Williams J L, Lee C and Bolch W E 2007 Hybrid computational phantoms of the male and female newborn patient: NURBS-based whole-body models *Phys. Med. Biol*. **52** 3309–33

Lee C, Lodwick D, Williams J L and Bolch W E 2008 Hybrid computational phantoms of the 15-year male and female adolescent: applications to CT organ dosimetry for patients of variable morphometry *Med. Phys*. **35** 2366–82

Lee C, Lodwick D, Hurtado J, Pafundi D, Williams J L, Bolch W E 2010 The UF family of reference hybrid phantoms for computational radiation dosimetry *Phys. Med. Biol*. **55** 339–63

Lee B *et al* 2011 Dose evaluation of selective collimation effect in cephalography by measurement and Monte Carlo simulation *Radiat. Prot. Dosim.* **148** 58–64

Leyton M 2001 *A Generative Theory of Shape* (Berlin: Springer)

Li J, Qiu R, Zhang Z, Liu L, Zeng Z, Bi L and Li W 2009 Organ dose conversion coefficients for external photon irradiation using the Chinese voxel phantom (CVP) *Radiat. Prot. Dosim.* **135** 33–42

Lim S M, DeNardo G L, DeNardo D A, Shen S, Yuan A, O'Donnell T O and DeNardo S J 1997 Prediction of myelotoxicity using radiation doses to marrow from body, blood, and marrow sources *J. Nucl. Med*. **38** 1374–8

Lima V J M, Cassola V F, Kramer R, Lira C A B O, Khoury H J and Vieira J W 2011 Development of 5- and 10-year-old pediatric phantoms based on polygon mesh surfaces *Med. Phys*. **38** 4723–36

Liu T *et al* 2014 ARCHER-CT, an extremely fast Monte Carlo code for patient-specific CT dose calculations using Nvidia GPU and Intel coprocessor technologies: part I—software development and testing *Phys. Med. Biol.* submitted

Loevinger R, Japha E M and Brownell G L 1965a Discrete radioisotope sources *Radiation Dosimetry* ed G J Hine and G L Brownell (New York: Academic) 693–799

Loevinger R, Hiolt J G and Hine G J 1965b Internally administered radionuclides *Radiation Dosimetry* ed G J Hine and G L Brownell (New York: Academic) 801–73

Loevinger R 1969 Distributed radionuclide sources *Radiation Dosimetry Volume III* 2nd edn ed F H Attix and Tochilin (New York: Academic) 51

Marinelli L D 1942 Dosage determination with radioactive isotopes *Am. J. Roentgenol. Rad. Therapy* **47** 210–6

Marinelli L D, Quimby E H and Hine G J 1948 Dosage determination with radioactive isotopes II. Practical considerations in therapy and protection *Am. J. Roentgenol. Rad. Therapy* **59** 260–81

Mason P A, Ziriax J M, Hurt W D, Walters T J, Ryan K L, Nelson D A, Smith K I and D'andrea J A 2000 Recent advancements in dosimetry measurements and modeling *Radio Frequency Radiation Dosimetry and Its Relationship to the Biological Effects of Electromagnetic Fields* ed B J Klauenberg and D Miklavčič (Dordrecht: Kluwer) pp 141–55

Maynard M R, Geyer J W, Aris J P, Shifrin R Y and Bolch W 2011 The UF family of hybrid phantoms of the developing human fetus for computational radiation dosimetry *Phys. Med. Biol*. **56** 4839–79

Mazzurana M, Sandrini L, Vaccari A, Malacarne C, Cristoforetti L and Pontalti R 2003 A semi-automatic method for developing an anthropomorphic numerical model of dielectric anatomy by MRI *Phys. Med. Biol*. **48** 3157–70

McGurk R, Seco J, Riboldi M, Wolfgang J, Segars P and Paganetti H 2010 Extension of the NCAT phantom for the investigation of intra-fraction respiratory motion in IMRT using 4D Monte Carlo *Phys. Med. Biol*. **55** 1475–90

Mille M and Xu X G 2008 Fabrication of human organs for realistic calibration phantoms by rapid prototyping *Health Phys*. **95** S11

Mille M, Xu X G and Rivard M 2010 Comparison of organ doses for patients undergoing balloon brachytherapy of the breast with HDR ^{192}Ir or electronic sources using Monte Carlo simulations in a heterogeneous human phantom *Med. Phys*. **37** 662–71

Mille M 2013 A study of shape-dependent partial volume correction in PET imaging using ellipsoidal phantoms fabricated via rapid prototyping *Ph D Dissertation* Rensselaer Polytechnic Institute

Mishra P, Li R, James S S, Mak R H, Williams C L, Yue Y, Berbeco R I and Lewis J H 2013 Evaluation of 3D fluoroscopic image generation from a single planar treatment image on patient data with a modified XCAT phantom *Phys. Med. Biol*. **58** 841–58

Mofrad F B, Zoroofi R A, Tehrani-Fard A A, Akhlahpoor S, Hori M, Chen Y W and Sato Y 2010 Statistical construction of a Japanese male liver phantom for internal radionuclide dosimetry *Radiat. Prot. Dosimetry* **141** 140–148.

Moignier A, Derreumaux S, Broggio D, Beurrier J, Chea M, Boisserie G, Franck D, Aubert B and Mazeron J J 2013 Potential of hybrid computational phantoms for retrospective heart dosimetry after breast radiation therapy: a feasibility study *Int. J. Radiat. Oncol. Biol. Phys*. **85** 492–9

Na Y H 2009 Deformable adult human phantoms for radiation protection dosimetry: methods for adjusting body and organ sizes to match population-based percentile data *Ph D Dissertation,* Rensselaer Polytechnic Institute

Na Y H, Zhang B, Zhang J Y, Caracappa P F and Xu X G 2010 Deformable adult human phantoms for radiation protection dosimetry: anthropometric data representing size distributions of adult worker populations and software algorithms *Phys. Med. Biol*. **55** 3789–811

Nagaoka T, Watanabe S, Sakurai K, Kunieda E, Watanabe S, Taki M and Yamanaka Y 2004 Development of realistic high-resolution whole-body voxel models of Japanese adult males and females of average height and weight, and application of models to radio-frequency electromagnetic-field dosimetry *Phys. Med. Biol*. **49** 1–15

Nagaoka T, Togashi T, Saito K, Takahashi M, Ito K, Ueda T, Osada H, Ito H and Watanabe S 2006 An anatomically realistic voxel model of the pregnant woman and numerical dosimetry for a whole-body exposure to RF electromagnetic fields *Conf. Proc. IEEE Eng. Med. Biol. Soc* **1** 5463–7

Nagaoka T, Togashi T, Saito K, Takahashi M, Ito K and Watanabe S 2007 An anatomically realistic whole-body pregnant-woman model and specific absorption rates for pregnant-woman exposure to electromagnetic plane waves from 10 MHz to 2 GHz *Phys. Med. Biol*. **52** 6731–45

Nagaoka T, Kunieda E, Watanabe S 2008 Proportion-corrected scaled voxel models for Japanese children and their application to the numerical dosimetry of specific absorption rate for frequencies from 30 MHz to 3 GHz *Phys. Med. Biol*. **53** 6695–711

NCRP 1985 The experimental basis for absorbed-dose calculations in medical uses of radionuclides *NCRP Report No.* 83 (Besthesda, MD: National Council on Radiation Protection and Measurements)

Nipper J C, Williams J L and Bolch W E 2002 Creation of two tomographic voxel models of paediatric patients in the first year of life *Phys. Med. Biol*. **47** 3143–64

Niu X, Yang Y, Jin M, Wernick M N and King M A 2010 Regularized fully 5D reconstruction of cardiac gated dynamic SPECT images *IEEE Trans. Nucl. Sci*. **57** 1085–95

NRC 2013 *EGSnrc* http://irs.inms.nrc.ca/software/egsnrc/

Pafundi D, Lee C, Watchman C, Bourke V, Aris J, Shagina N, Harrison J, Fell T and Bolch W 2009 An image-based skeletal tissue model for the ICRP reference newborn *Phys. Med. Biol*. **54** 4497–531

Pafundi D, Rajon D, Jokisch D, Lee C and Bolch W 2010 An image-based skeletal dosimetry model for the ICRP reference newborn—internal electron sources *Phys. Med. Biol*. **55** 1785–814

Park S, Lee J K and Lee C 2006 Development of a Korean adult male computational phantom for internal dosimetry calculation *Radiat. Prot. Dosim.* **121** 257–64

Patni H K, Nadar M Y, Akar D K, Bhati S and Sarkar P K 2011 Selected organ dose conversion coefficients for external photons calculated using ICRP adult voxel phantoms and Monte Carlo code Fluka *Radiat. Prot. Dosimetry* **147** 406–16

Pelowitz D B (ed) 2005 MCNPX User's Manual Version 2.5.0 *Report LA-CP-05-0369* (Los Alamos, NM: Los Alamos National Laboratory)

Petoussi-Henss N, Zankl M, Fill U and Regulla D 2002 The GSF family of voxel phantoms *Phys. Med. Biol*. **47** 89–106

Phantom Laboratory 2013 *RANDO Phantoms* www.phantomlab.com/rando.html

Pretorius P H, Xia W, King M A, Tsui B M, Pan T S and Villegas B J 1997 Evaluation of right and left ventricular volume and ejection fraction using a mathematical cardiac torso phantom *J. Nucl. Med*. **38** 1528–35

Pujol A and Gibbs S J 1982 A Monte Carlo method for patient dosimetry from dental x-ray *Dentomaxillofac Radiol*. **11** 25–33

Qiu R, Li J, Zhang Z, Wu Z, Zeng Z and Fan J 2008 Photon SAF calculation based on the Chinese mathematical phantom and comparison with the ORNL phantoms *Health Phys*. **95** 716–24

Quimby E H 1970 The development of radiation dosimetry in nuclear medicine medical radionuclides: radiation dose and effects ed R J Cloutier, C L Edwards and W S Snyder *Proc. of AEC Symp. Series 20 (CONF-691212)* (Washington, DC: U.S. Atomic Energy Commission) 7–15

Raeside D E 1976 Monte Carlo principles and applications *Phys. Med. Biol*. **21** 181–97

Reece W D, Poston J W Sr and Xu X G 1994 Determining the effective dose equivalent for external photon radiation: Calculational results for beam and point source geometries *Radiat. Prot. Dosimetry* **55** 5–21

Reece W D and Xu X G 1997 Determining the effective dose equivalent for external photon radiation: assessing effective dose equivalent from personal dosemeter readings *Radiat. Prot. Dosimetry* **69** 167–78

Rogers D W 2006 Fifty years of Monte Carlo simulations for medical physics *Phys. Med Biol*. **51** R287–R301

Sachse F B *et al* 1997 *MEET Man–Models for Simulation of Electromagnetic, Elastomechanic and Thermic Behavior of Man* (Karlsruhe: Universität Karlsruhe) www.ibt.kit.edu/english/973.php

Saito K, Wittmann A, Koga S, Ida Y, Kamei T, Funabiki J and Zankl M 2001 Construction of a computed tomographic phantom for a Japanese male adult and dose calculation system *Radiat. Environ. Biophys*. **40** 69–75

Saito K, Koga S, Ida Y, Kamei T and Funabiki J 2008 Construction of a voxel phantom based on CT data for a Japanese female adult and its use for calculation of organ doses from external electrons *Jpn. J. Health Phys*. **43** 122–30

Salvat F, Fernández-Varea J M and Sempau J 2003 *PENELOPE—a code system for Monte Carlo simulation of electron and photon transport* www2.cose.isu.edu/~tforest/Classes/NucSim/penelope-2003.pdf

Sato K, Noguchi H, Emoto Y, Koga S and Saito K 2007a Japanese adult male voxel phantom constructed on the basis of CT images *Radiat. Prot. Dosim.* **123** 337–44

Sato K, Noguchi H, Endo A, Emoto Y, Koga S and Saito K 2007b Development of a voxel phantom of Japanese adult male in upright posture. *Radiat. Prot. Dosim.* **127** 205–8

Sato K, Noguchi H, Emoto Y, Koga S, Saito K 2009 Development of a Japanese adult female voxel phantom *J. Nucl. Sci. Technol*. **46** 907–913

Schlattl H, Zankl M and Petoussi-Henss N 2007 Organ dose conversion coefficients for voxel models of the reference male and female from idealized photon exposures *Phys. Med. Biol*. **52** 2123–45

Schultz F W and Zoetelief J 1996 Organ and effective doses in the male phantom Adam exposed in AP direction to broad unidirectional beams of monoenergetic electrons *Health Phys*. **70** 498–504

Segars W P 2001 Development and application of the new dynamic NURBS-based cardiac-torso (NCAT) phantom *Ph D Dissertation* University of North Carolina

Segars W P, Tsui B M W, Frey EC, Johnson G A and Berr S S 2004 Development of a 4-D digital mouse phantom for molecular imaging research *Mol. Imaging Biol*. **6** 149–59

Segars W P and Tsui B 2007 4D MOBY and NCAT phantoms for medical imaging simulation of mice and men *J. Nucl. Med*. **48** 203P (Suppl. 2)

Segars W P, Lalush D S, Frey E C, Manocha D, King M and Tsui B M W 2009 Improved dynamic cardiac phantom based on 4D NURBS and tagged MRI *IEEE Trans. Nucl. Sci*. **56** 2728–38

Segars W P and Tsui B M W 2010 The MCAT, NCAT, XCAT, and MOBY computational human and mouse phantoms *Handbook of Anatomical Models for Radiation Dosimetry* ed X G Xu and K F Eckerman (Boca Raton, FL: Taylor & Francis) pp 105–134

Segars W P *et al* 2013 Population of anatomically variable 4D XCAT adult phantoms for imaging research and optimization *Med. Phys*. **40** 043701

Shi C Y 2004 Development and application of a tomographic model from CT images for calculating internal dose to a pregnant woman *Ph D Dissertation* Rensselaer Polytechnic Institute

Shi C and Xu X G 2004 Development of a 30-week-pregnant female tomographic model from computed tomography (CT) images for Monte Carlo organ dose calculations *Med. Phys*. **31** 2491–7

Shi C, Xu X G and Stabin M G 2008 SAF values for internal photon emitters calculated for the RPI-P pregnant-female models using Monte Carlo methods *Med. Phys*. **35** 3215–24

Sjögreen K, Ljungberg M, Wingårdh K, Erlandsson K and Strand S E 2001 Registration of emission and transmission whole-body scintillation-camera images *J. Nucl. Med*. **42** 1563–70

Smans K, Tapiovaara M, Cannie M, Struelens L, Vanhavere F, Smet M and Bosmans H 2008 Calculation of organ doses in x-ray examinations of premature babies *Med. Phys*. **35** 556–68

Smith T J, Petouissi N and Zankl M 2000 Comparison of internal radiation doses estimated by MIRD and voxel techniques for a 'family' of phantoms *Eur. J. Nucl. Med*. **27** 1387–98

Snyder W S 1967 Variation of dose in man from exposure to a point source of gamma rays Health Physics Division Annual Progress report for Period Ending July 31, 1967 *Report ORNL-4168* (Oak Ridge, TN: Oak Ridge National Laboratory) p 257

Snyder W S, Ford M R Warner G G, Fisher H L Jr 1969 Estimates of absorbed fractions for monoenergetic photon sources uniformly distributed in various organs of a heterogeneous phantom *J. Nucl. Med*. **10** 5–52 (Suppl 3)

Snyder W S, Ford M R and Warner G G 1978 Estimates of specific absorbed fractions for monoenergetic photon sources uniformly distributed in various organs of a heterogeneous phantom *MIRD Pamphlet 5, Revised* (Oak Ridge, TN: Oak Ridge National Laboratory)

Son I Y, Winslow M, Yazici B and Xu X G 2006 X-ray imaging optimization using virtual phantoms and computerized observer modelling *Phys. Med. Biol*. **51** 4289–310

Spitzer V M and Whitlock D G 1998 *Atlas of the Visible Human Male: Reverse Engineering of the Human Body* (Sudbury, MA: Jones and Bartlett)

Stabin M G, Watson E E, Cristy M, Ryman J C, Eckerman K F, Davis J L, Marshall D and Gehlen M K 1995 Mathematical models and specific absorbed fractions of photon energy in the nonpregnant adult female and at the end of each trimester of pregnancy *Report ORNL/TM-12907* (Oak Ridge, TN: Oak Ridge National Laboratory)

Stabin M, Emmons M A, Segars W P, Fernald M and Brill A B 2008 ICRP-89 based adult and pediatric phantom series *J. Nucl. Med*. **49** 14P (Supp. 1)

Stabin M G, Xu X G, Emmons M A, Segars W P, Shi C, Fernald M J. 2012 RADAR reference adult, pediatric and pregnant female phantom series for internal and external dosimetry *J. Nucl. Med*. **53** 1807–13

Staton R J, Kyle J A, Lee C, Hintenlang D E, Arreola M M, Williams J L and Bolch W E 2006 A tomographic physical phantom of the newborn child with real-time dosimetry II. Scaling factors for calculation of mean organ dose in pediatric radiography *Med. Phys*. **33** 3283-9

Storm L and Israel H I 1970 Photon cross sections from 1 keV to 100 MeV for elements Z=1 to Z=100 *Atomic Data and Nuclear Data Tables* **7** 565–681

Stovall M, Smith S A and Rosenstein M 1989 Tissue doses from radiotherapy of cancer of the uterine cervix *Med. Phys*. **16** 726–33

Stroud I 2006 *Boundary Representation Modeling Techniques* (London: Springer)

Su L, Han B and Xu X G 2012 Calculated organ doses for individuals in a sitting posture above a contaminated ground and a PET imaging room *Radiat. Prot. Dosimetry* **148** 439–43

Su L, Yang Y M, Bednarz B, Sterpin E, Du X, Liu T, Ji W and Xu X G 2014 ARCHER—a photon-electron coupled Monte Carlo dose computing engine for GPU: software development and application to helical tomotherapy *Med. Phys*. submitted

Sun W, Jia X, Xie T, Xu F and Liu Q 2013 Construction of boundary-surface-based Chinese female astronaut computational phantom and proton dose estimation *J. Radiat. Res*. **54** 383–97

Tabary J, Marache-Francisco S, Valette S, Segars W P and Lartizien C 2009 Realistic x-ray CT simulation of the XCAT phantom with SINDBAD *2009 IEEE Nuclear Science Symp. Conf. Record (NSS/MIC)* pp 3980–3

Taddei P J, Mirkovic D, Fontenot J D, Giebeler A, Zheng Y, Kornguth D, Mohan R and Newhauser W D 2009 Stray radiation dose and second cancer risk for a pediatric patient receiving craniospinal irradiation with proton beams *Phys. Med. Biol*. **54** 2259–75

Takahashi M, Kinase S, and Kramer R 2011 Evaluation of counting efficiencies of a whole-body counter using Monte Carlo simulation with voxel phantoms. *Radiat. Prot. Dosim.* **144** 407–10

Taranenko V and Xu X G 2009 Foetal dose conversion coefficients for ICRP-compliant pregnant models from idealised proton exposures *Radiat. Prot. Dosim.* **133** 65–72

Tinniswood A D, Furse C M and Gandhi O P 1998 Power deposition in the head and neck of an anatomically based human body model for plane wave exposures *Phys. Med. Biol*. **43** 2361–78

Tresser M A and Hintenlang D E 1999 Construction of a newborn dosimetry phantom for measurement of effective dose *Health Phys*. **76** S190

Tsui B M, Terry J A and Gullberg G T 1993 Evaluation of cardiac cone-beam single photon emission computed tomography using observer performance experiments and receiver operating characteristic analysis *Inv. Radiol*. **28** 1101–12

Tsui B M W, Zhao X D, Gregoriou G K, Lalush D S, Frey E C, Johnston R E and Mccartney W H 1994 Quantitative cardiac SPECT reconstruction with reduced image degradation due to patient anatomy *IEEE Trans. Nucl. Sci*. **41** 2838–44

Tung C J, Tsai S F, Tsai H Y and Chen I J 2011 Determination of voxel phantom for reference Taiwanese adult from CT image analyses *Radiat. Prot. Dosimetry* **146** 186–90

Turner J E, Wright H A and Hamm R N 1985 A Monte Carlo primer for health physicists *Health Phys*. **48** 717–33

Tward D J, Ceritoglu C, Sturgeon G, Segars W P, Miller M I and Ratnanather J T 2011 Generating patient-specific dosimetry phantoms with whole-body diffeomorphic image registration *2011 IEEE 37th Annual Northeast Bioengineering Conf. (NEBEC)* pp *1–2*

Uusitupa T, Laakso I, Ilvonen S, Nikoskinen K 2010 SAR variation study from 300 to 5000 MHz for 15 voxel models including different postures *Phys. Med. Biol*. **55** 1157–76

Vazquez J A, Ding A, Haley T, Caracappa P F, and Xu X G 2014a A dose reconstruction study of the 1997 Sarov criticality accident using animated dosimetry techniques *Health Phys*. **106** 571–82

Vazquez J A, Caracappa P F, and Xu X G 2014b Development of posture-specific computational phantoms using motion capture technology and application to radiation dose reconstruction for the 1999 Tokaimura Nuclear Criticality Accident *Phys. Med. Biol*. **59** 5277–86

Veress A I, Segars W P, Tsui B M W and Gullberg G T 2011 Incorporation of a left ventricle finite element model defining infarction into the XCAT imaging phantom. *IEEE Trans. Med. Imaging* **30** 915–27

Wang B, Xu X G and Kim C H 2004 A Monte Carlo CT model of the Rando Phantom *Trans. Am. Nucl. Soc*. **90** 473–4

Wang J, Fujiwara O, Watanabe S and Yamanaka Y 2004 Computation with a parallel FDTD system of human-body effect on electromagnetic absorption for portable telephones *IEEE Trans. Microw. Theory Tech*. **52** 53–8

Wang B, Xu X G, Goorley J T and Bozkurt A 2005a The use Of MCNP code for an extremely large voxel model VIP-Man *The Monte Carlo Method: Versatility Unbounded in a Dynamic Computing World Proc. of the Monte Carlo 2005 Topical Meeting on CD-ROM* (*Chattanooga, TN*, 17–21 April 2005) (LaGrange, Park IL: American Nuclear Society)

Wang B, Xu X G, Goldstein M and Sahoo N 2005b Adjoint Monte Carlo method for prostate external photon beam treatment planning: an application to 3-D patient anatomy *Phys. Med. Biol*. **50** 923–35

Williams G, Zankl M, Abmayr W, Veit R and Drexler G 1986 The calculation of dose from external photon exposures using reference and realistic human phantoms and Monte Carlo methods *Phys. Med. Biol*. **31** 449–52

Winslow M, Huda W, Xu X G, Chao T C, Shi CY, Ogden K M, and Scalzetti E M 2004 Use of the VIP-Man model to calculate energy imparted and effective dose for x-ray examinations *Health Phys*. **86** 174–82

Winslow M, Xu X G and Yazici B 2005 Development of a simulator for radiographic image optimization *Comput. Methods Programs Biomed*. **78** 179–90

Wu D, Shamsi S, Chen J and Kainz W 2006 Evaluations of specific absorption rate and temperature increase within pregnant female models in magnetic resonance imaging birdcage coils *IEEE Trans. Microw. Theory Tech*. **54** 4472–8

Xie T *et al* 2010 Comparison of absorbed fractions of electrons and photons using three kinds of computational phantoms of rat *App. Phys. Lett*. **97**

Xie T, Bolch W E, Lee C and Zaidi H 2013 Pediatric radiation dosimetry for positron-emitting radionuclides using anthropomorphic phantoms *Med. Phys*. **40** 102502–14

Xie T and Zaidi H 2014 Evaluation of radiation dose to anthropomorphic paediatric models from positron-emitting labelled tracers *Phys. Med. Biol*. **59** 1165–87

Xu X G, Reece W D and Poston J W 1995 A study of the angular dependence problem in effective dose equivalent assessment *Health Phys*. **68** 214–24

Xu X G and Reece W D 1996 Sex-specific tissue weighting factors for effective dose equivalent calculations *Health Phys*. **70** 81–6

Xu X G, Chao T C and Bozkurt A 2000 VIP-Man: an image-based whole-body adult male model constructed from color photographs of the Visible Human Project for multi-particle Monte Carlo calculations *Health Phys*. **78** 476–86

Xu X G, Chao T C, and Bozkurt A 2005 Comparison of effective doses from various monoenergetic particles based on the stylised and the VIP-Man tomographic models *Radiat. Prot. Dosimetry* **115** 530–5

Xu X G, Taranenko V, Zhang J and Shi C 2007 A boundary-representation method for designing whole-body radiation dosimetry models: pregnant females at the ends of three gestational periods—RPI-P3, -P6 and -P9 *Phys. Med. Biol*. **52** 7023-44

Xu X G and Eckerman K F 2010 *Handbook of Anatomical Models for Radiation Dosimetry* (Boca Raton, FL: Taylor & Francis)

Yeom Y S, Han M C, Kim C H and Jeong J H 2013 Conversion of ICRP male reference phantom to polygon-surface phantom *Phys. Med. Biol*. **58** 6985–7007

Zaidi H 1999 Relevance of accurate Monte Carlo modeling in nuclear medical imaging *Med. Phys*. **26** 574–608

Zaidi H and Sgouros G (ed) 2003 *Therapeutic Applications of Monte Carlo Calculations in Nuclear Medicine* (London: IOP Publishing)

Zaidi H and Xu X G 2007 Computational anthropomorphic models of the human anatomy: the path to realistic Monte Carlo modeling in radiological sciences *Annu. Rev. Biomed. Eng*. **9** 471–500

Zaidi H and Tsui B M W 2009 Review of computational anthropomorphic anatomical and physiological models *Proc. IEEE* **97** 1938–1953

Zankl M, Veit R, Williams G, Schneider K, Fendel H, Petoussi N and Drexler G 1988 The construction of computer tomographic phantoms and their application in radiology and radiation protection *Radiat. Environ. Biophys*. **27** 153–64

Zankl M, Fill U, Petoussi-Henss N and Regulla D 2002 Organ dose conversion coefficients for external photon irradiation of male and female voxel models *Phys. Med. Biol*. **47** 2367–85

Zankl M, Becker J, Fill U, Petoussi-Henss N and Eckerman K F 2005 GSF male and female adult voxel models representing ICRP Reference Man—the present status *The Monte Carlo Method: Versatility Unbounded in a Dynamic Computing World Proc. of the Monte Carlo 2005 Topical Meeting on CD-ROM* (*Chattanooga, TN*, 17–21 April 2005) (LaGrange, Park IL: American Nuclear Society)

Zeng Z, Li J and Qiu R 2006 Dose assessment for space radiation using a proton differential dose spectrum *J. of Tsinghua University (Science and Technology)* **46** 374–376

Zhang B, Ma J, Liu L and Cheng J 2007a CNMAN: a Chinese adult male voxel phantom constructed from color photographs of a visible anatomical data set *Radiat. Prot. Dosimetry* **124** 130–6

Zhang G, Liu Q and Luo Q 2007b Monte Carlo simulations for external neutron dosimetry based on the visible Chinese human phantom *Phys. Med. Biol*. **52** 7367-83

Zhang G, Liu Q, Zeng S and Luo Q 2008a Organ dose calculations by Monte Carlo modeling of the updated VCH adult male phantom against idealized external proton exposure *Phys. Med. Biol*. **53** 3697–722

Zhang G, Luo Q, Zeng S and Liu Q 2008b The development and application of the visible Chinese human model for Monte Carlo dose calculations *Health Phys*. **94** 118–25

Zhang J Y, Xu X G, Shi C and Fuss M 2008c Development of a geometry-based respiratory motion-simulating patient model for radiation treatment dosimetry *J. Appl. Clin. Med. Phys*. **9** 2700

Zhang B, Ma J, Zhang G, Liu Q, Qiu R and Li J 2010 The Chinese computational phantoms: CNMAN, VCH, and CVP *Handbook of Anatomical Models for Radiation Dosim.* ed X G Xu and K F Eckerman (Boca Raton, FL: Taylor & Francis) pp 279–304

Zhang J, Na Y H, Caracappa P F, Xu X G 2009 RPI-AM and RPI-AF, a pair of mesh-based, size-adjustable adult male and female computational phantoms using ICRP-89 parameters and their calculations for organ doses from monoenergetic photon beams. *Phys. Med. Biol*. **54** 5885–908

Zubal I G, Harrell C R, Smith E O, Rattner Z, Gindi G and Hoffer P B 1994 Computerized three-dimensional segmented human anatomy *Med. Phys*. **21** 299–302

IOP Publishing | Institute of Physics and Engineering in Medicine Physics in Medicine & Biology

Phys. Med. Biol. **60** (2015) 5601–5625 doi:10.1088/0031-9155/60/14/5601

VirtualDose: a software for reporting organ doses from CT for adult and pediatric patients

Aiping Ding[1], Yiming Gao[1], Haikuan Liu[1,2], Peter F Caracappa[1], Daniel J Long[3], Wesley E Bolch[3], Bob Liu[4] and X George Xu[1]

[1] Nuclear Engineering Program, Rensselaer Polytechnic Institute, Troy, NY 12180, USA
[2] Institute of Radiation Medicine, Fudan University, Shanghai 200032, People's Republic of China
[3] Department of Biomedical Engineering, University of Florida, Gainesville, FL 32611, USA
[4] Department of Radiology, Massachusetts General Hospital, Boston, MA 02114, USA

E-mail: xug2@rpi.edu

Received 8 September 2014, revised 2 May 2015
Accepted for publication 14 May 2015
Published 2 July 2015

Abstract

This paper describes the development and testing of *VirtualDose*—a software for reporting organ doses for adult and pediatric patients who undergo x-ray computed tomography (CT) examinations. The software is based on a comprehensive database of organ doses derived from Monte Carlo (MC) simulations involving a library of 25 anatomically realistic phantoms that represent patients of different ages, body sizes, body masses, and pregnant stages. Models of GE Lightspeed Pro 16 and Siemens SOMATOM Sensation 16 scanners were carefully validated for use in MC dose calculations. The software framework is designed with the 'software as a service (SaaS)' delivery concept under which multiple clients can access the web-based interface simultaneously from any computer without having to install software locally. The RESTful web service API also allows a third-party picture archiving and communication system software package to seamlessly integrate with *VirtualDose*'s functions. Software testing showed that *VirtualDose* was compatible with numerous operating systems including Windows, Linux, Apple OS X, and mobile and portable devices. The organ doses from *VirtualDose* were compared against those reported by CT-Expo and ImPACT—two dosimetry tools that were based on the stylized pediatric and adult patient models that were known to be anatomically simple. The

organ doses reported by *VirtualDose* differed from those reported by CT-Expo and ImPACT by as much as 300% in some of the patient models. These results confirm the conclusion from past studies that differences in anatomical realism offered by stylized and voxel phantoms have caused significant discrepancies in CT dose estimations.

Keywords: CT dosimetry, dose reporting, software as a service (SaaS)

(Some figures may appear in colour only in the online journal)

1. Introduction

X-ray computed tomography (CT) has experienced tremendous technological advances in recent years and is one of the most useful diagnostic imaging modalities today. Driven particularly by advanced multi-detector CT (MDCT) technologies, the number of CT scans performed each year in the United States had reached nearly 81.2 million in 2014(IMV's 2014 CT Market Outlook Report 2015). The potential radiation risk to the patient population, particularly children, has led to increasing attention from the radiology community in the past few years (Berrington de Gonzalez *et al* 2009, Sodickson *et al* 2009, Brenner 2010, Ding *et al* 2010, Boone *et al* 2012, Pearce *et al* 2012). For a long time, the as low as reasonably achievable (ALARA) principle (ICRP 1977) has been widely adopted in the radiation protection of patients undergoing diagnostic imaging including CT (Slovis 2003, Kalra *et al* 2004, McCollough *et al* 2009, Dougeni *et al* 2012). In its Publication 102, the international commission on radiological protection (ICRP) emphasized the importance of managing patient dose, particularly from repeated or multiple examinations (ICRP 2007b). Recently, several task groups from the american association of physicists in medicine (AAPM) developed methodologies for the evaluation of CT doses (AAPM 2008, 2010), including the size-specific dose algorithm for pediatric and adult CT examinations (AAPM 2011). Public campaigns such as the dose index registry (DIR) (ACR 2012), Image Wisely (Wisely 2013), and Image Gently (Gently 2013) have been initiated to engage the radiology community. In January of 2015, revised elements of performance (EPs) for organizations that provide diagnostic imaging services have been finalized by the Joint Commission and will go into effect on July 1, 2015(The Joint Commission 2015).

Presently, three types of dosimetric quantities are used in CT dosimetry (Tack and Gevenois 2007, Mahesh 2009, Seeram 2009): 1) weighted CT dose index ($CTDI_w$) and volume CT dose index ($CTDI_{vol}$), which provide an indication of the average absorbed dose to a cylindrical phantom in the scan region, 2) dose-length product (DLP), which integrates the dose along the length of the scan, and 3) effective dose (E), which is a risk-related method for comparing whole-body patient radiation doses across different imaging procedures. To respond to the increasing trend in CT dose, the States of California, Connecticut, and Texas in the United States have mandated the CT dose reporting in terms of $CTDI_{vol}$ and DLP. However, there are some concerns about the use of $CTDI_{vol}$ as a metric for patient dose, because it does not account for the size or anatomy of the patient (Brenner 2006, Dixon 2006, McCollough 2006, Boone 2007, McCollough *et al* 2011).

Radiation-induced health effects are correlated with the mean absorbed dose to organs and tissues. The absorbed dose is determined as the quotient of mean energy imparted from any type of radiation and the mass of any irradiated material of interest. To quantify the whole-body risk, the ICRP recommends the effective dose as a radiation protection quantity, which is based on the weighted sum of selected major radio-sensitive organs or tissues according to:

$$E = \sum_{T} w_T H_T = \sum_{T} w_T \sum_{R} w_R D_{T,R} \quad (1)$$

where $D_{T,R}$ is the average absorbed dose in tissue T from the radiation type R. w_R is a radiation weighting factor accounting for the relative biological damage of different types of radiation (and is always unity for x-rays), and w_T is a tissue weighting factor for T derived from that tissue's relative radio-sensitivity. The set of 'tissue weighting factors' has been revised periodically to reflect the latest epidemiological information, most recently in ICRP Publication 103(ICRP 2007a) which replaces the recommendations in IRCP Publication 60 (ICRP 1991). Although, the ICRP developed the concept of effective dose for the purpose of setting occupational dose limits for radiation protection, and stated that the effective dose concept should not be used to indicate risk for specific individuals, the quantity is still widely used by the radiology community to compare risk for patients who undergo x-ray imaging (McCollough and Schueler 2000, McNitt-Gray 2002, Brenner and Huda 2008). The effective dose is defined only for the ICRP reference adult models (ICRP 2009), but the methodology has been applied to other computational phantoms (Xu 2014).

Several CT organ dose calculation tools are currently available (Kalender *et al* 1999, Stamm and Nagel 2002, CT Dose 2008, Ban *et al* 2011, eXposure 2012, ImPACT 2012). Most these existing packages are based on stylized patient phantoms developed prior to the 1980s using overly simplified anatomies. Although stylized phantoms were utilized worldwide both for external and internal dosimetry studies, the stylized models had been found to result in significant dose errors when compared against anatomically realistic patient models (Zanki *et al* 2002, Liu *et al* 2010, Lee *et al* 2011, 2012, Xu 2014). Furthermore, most existing software packages do not consider patient populations other than averaged-sized adults, ignoring pediatric, pregnant, and obese patients.

This paper describes the development and testing of a new web-based software, called '*VirtualDose*', for reporting organ doses to patients who undergo diagnostic CT examinations. Funded by a grant from the national institute of biomedical imaging and bioengineering (NIBIB) for commercial development, *VirtualDose* is designed to improve upon existing software packages by considering validated CT scanner models and scanner-specific correction factors, latest ICRP recommendations, advanced 'software as a service (SaaS)' delivery mode, and a family of 25 anatomically realistic patient phantoms which includes a set of voxel phantoms covering median (50th percentile) adults, children at different ages, pregnant females at three gestational stages, and obese patients of different body mass.

2. Materials and methods

2.1. Twenty-five 'virtual patient' models

Computational phantoms can be divided into three generations with increasing anatomical realism and geometrical sophistication: 1) stylized phantoms developed prior to the 1980s, 2) voxel phantoms developed since the late 1980s, and 3) Boundary Representation (BREP) phantoms developed since the mid of 2000s (Xu 2014).This study took advantage of a total of 25 whole-body BREP phantoms that were previously developed at rensselaer polytechnic institute (RPI) and the university of florida (UF). These phantoms included reference adults representing the ICRP-89 50th percentile (median) of adults (named RPI-Adult-Male (RPI-AM) and RPI-Adult-Female (RPI-AF)) (Zhang *et al* 2009b, Na *et al* 2010), pediatric patients at different ages (newborn, 1-, 5-, 10-, and 15 year-old) (Bolch *et al* 2010), and pregnant females at three gestational stages (named RPI-Pregnant 3-,6-, and 9 month) (Xu *et al* 2007). A newly

developed set of phantoms representing overweight and obese patients (Ding *et al* 2012) were also adopted for the development of *VirtualDose*. Figure 1 depicts these phantoms which were originally designed in various BREP data formats that are easy to deform (Xu and Eckerman 2009). They were converted to voxel-based phantoms, as summarized in table 1, to perform MC organ dose calculations.

2.2. CT scanner models

Two CT scanner models (the GE LightSpeed Pro 16 and Siemens SOMATOM Sensation 16) were explicitly constructed in the Monte Carlo code, MCNPX v2.6 (Pelowitz 2005). The GE LightSpeed Pro 16 scanner (figure 2), operated at different tube voltages (i.e., 80, 100, 120, and 140 kVp) with different beam collimations (1.25, 5, 10, and 20 mm), was developed and validated using a previously validated method by Gu *et al* (2009) that was later refined by Ding (2012). The SOMATOM Sensation 16 was simulated by Lee *et al* (2011), operated at 80, 100, 120, and 140 kVp with two beam collimations of 10 and 24 mm.

It had been shown by Turner *et al* (2010) that organ doses normalized by $CTDI_{vol}$ were practically independent of the scanner type. Therefore, CT scanners other than the scanners validated in this study were corrected by the measured $CTDI_{vol}$ normalized to a tube current of 100 mAs, as described below in section 2.4. In this way, a small number of fully validated CT scanner models can be used to represent nearly any modern CT scanner.

2.3. Monte Carlo organ dose calculations

With detailed geometric and compositional information for dozens of well identified organs, a computational phantom contains necessary anatomical data for radiation dose calculations using a MC radiation transport code, such as MCNPX (Pelowitz 2005). Coupled with a model of the radiation produced by the CT scanner, a MC radiation simulation can produce a detailed distribution of radiation dose across various organs and tissues of the body.

For the purposes of reporting organ doses for a particular patient undergoing a specific CT scan, the scan range was first deconstructed into the individual tube rotations or slices of the scan. A series of separate axial scans from head to toe (as shown in figure 3), were successively simulated by using each specific tube voltage and each transverse beam width in the MCNPX code. For each slice simulated, the direct dose within the scan volume and the scattered radiation dose outside of the scan volume were calculated. The procedure was repeated for pediatric, pregnant female, and adult male/female phantoms, over a very large number of simulations. The MCNPX code can handle voxels efficiently using MCNPX's 'repeated structures' feature, therefore an in-house voxelization algorithm (Zhang *et al* 2009b) was developed to convert these BREP phantoms into a voxel-based data. The number of source photons was selected to ensure that the calculated organ doses had an acceptable level of statistical uncertainty—relative errors of <1% in most organs near the primary beam and <5% for organs with very small volumes or located at large distances from the primary beam. Dose to skin and also bone surfaces and red marrow were handled using the methods demonstrated in previous studies (Zhang *et al* 2009b, Johnson *et al* 2011).

The MC simulation results provided organ dose in units of MeV per gram per source particle and they must be adjusted according to the integrated x-ray tube current, which was expressed as the product of tube current (mA) and the exposure time (s). The proprietary nature of the x-ray tube and bowtie filter assembly makes it difficult to quantify the x-ray photon output directly. As a result, an empirical conversion factor (CF) was used to convert the tally output to absorbed dose per unit integrated tube current (in units of mGy/100 mAs).

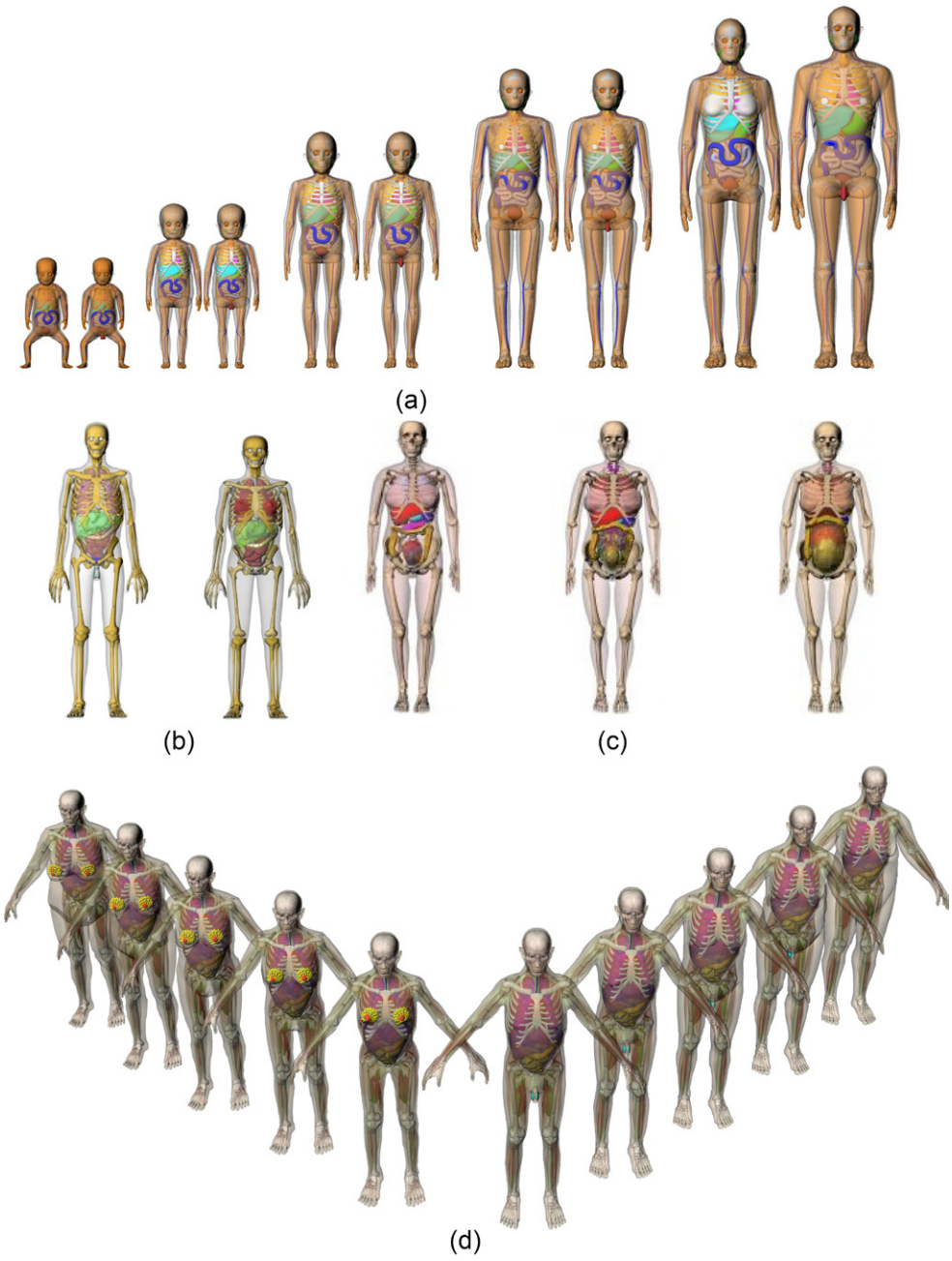

Figure 1. 3D rendering of whole-body BREP phantoms used in this study: (a) UF pediatric male and female patients at different ages (newborn, 1-, 5-, 10-, and 15 year-old), (b) RPI adult male and female patients matching with the 50th percentile of population, (c) RPI pregnant female patients at three gestational stages (3-,6-, and 9 month), and (d) RPI obese patients.

Table 1. Phantom parameters and body mass index (BMI) of the voxel-based 'Virtual Patient' models used in *VirutalDose*.

	Mass (kg)	Height (cm)	BMI ($kg\,m^{-2}$)	Voxel size (mm^3)
Pediatric patient models				
Newborn male	3.27	47.8	14.3	2 × 2 × 2
Newborn female	3.27	47.8	14.3	2 × 2 × 2
1 year male	9.39	76.6	16.0	3 × 3 × 3
1 year female	9.39	76.6	16.0	3 × 3 × 3
5 year male	16.45	110.4	13.5	3 × 3 × 3
5 year female	16.45	110.4	13.5	3 × 3 × 3
10 year male	30.16	140.1	15.4	3 × 3 × 3
10 year female	30.16	140.1	15.4	3 × 3 × 3
15 year male	53.13	166.5	19.2	3 × 3 × 3
15 year female	52.24	161.7	20.0	3 × 3 × 3
Pregnant female patient models				
3 month pregnant	61.9	163.2	23.2	3 × 3 × 3
6 month pregnant	66.6	163.5	24.9	3 × 3 × 3
9 month pregnant	72.4	163.5	27.1	3 × 3 × 3
Average adult patient models				
Average adult male	73	176	23.6	3 × 3 × 3
Average adult female	60.1	164	22.3	2.5 × 2.5 × 2.5
Obese patient models				
Normal body-weight male	72.7	176	23.5	3.5 × 3.5 × 3.5
Normal body-weight female	63.5	163	23.9	3.5 × 3.5 × 3.5
Over-weight male	85.7	176	27.7	3.5 × 3.5 × 3.5
Over-weight female	75.3	163	28.3	3.5 × 3.5 × 3.5
Obese level-I male	103.1	176	33.3	3.5 × 3.5 × 3.5
Obese level-I female	90.6	163	34.1	3.5 × 3.5 × 3.5
Obese level-II male	117.0	176	37.8	3.5 × 3.5 × 3.5
Obese level-II female	102.4	163	38.5	3.5 × 3.5 × 3.5
Morbidly-Obese male	139.4	176	45.0	3.5 × 3.5 × 3.5
Morbidly-Obese female	123.3	163	46.4	3.5 × 3.5 × 3.5

These CFs were unique to each combination of beam energy (E) and beam collimation (NT). A series of CFs were calculated using methods described in previous studies (DeMarco *et al* 2005, Gu *et al* 2009):

$$(CF)_{E,NT} = \frac{((CTDI_{100})^{Measured}_{in-air})_{E,NT}}{((CTDI_{100})^{Simulated}_{in-air})_{E,NT}} \quad (2)$$

where $((CTDI_{100})^{Measured}_{in-air})_{E,NT}$ is the measured air kerma $(CTDI_{100})_{in-air}$ values in units of mGy/100 mAs by using the ionization chamber in air at the CT scanner iso-center for a single axial scan; $((CTDI_{100})^{Simulated}_{in-air})_{E,NT}$ is the corresponding air kerma values in units of MeV per gram per source parcel acquired by simulating the ionization chamber in the MCNPX code under the same CT scan scenario. The units of $(CF)_{E,NT}$ are expressed as in units of (mGy·gram·source particle)/ (MeV·100 mAs). The $CTDI_{vol}$, which includes the effect of the

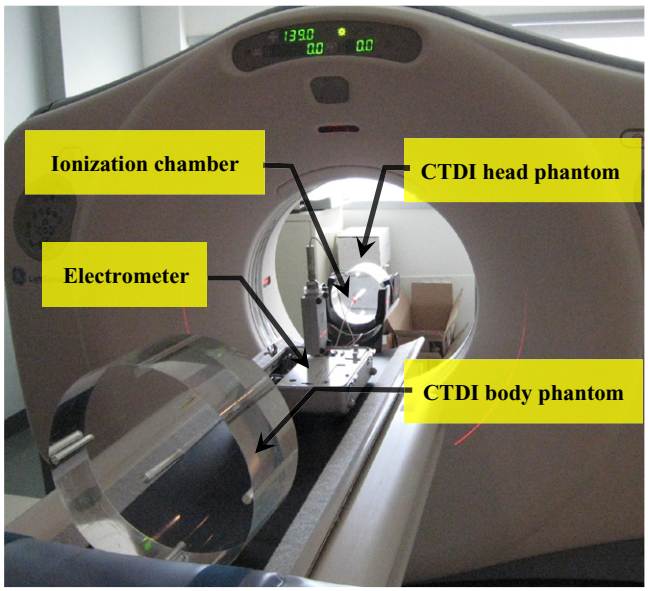

Figure 2. Typical equipment used in CTDI measurements including electrometer, ionization chamber, and a CTDI phantom (CTDI head or body phantom). The measured CTDI values were used to validate the CT scanner model in MCNPX code by comparing with the simulated results (photo taken at Massachusetts General Hospital, Boston, MA).

bowtie filter at 'off-center' positions, was used to scale the organ doses for different scanners as mentioned in section 2.4.

By using these CFs, the simulated results from the MCNPX code can be easily converted to the absorbed dose according to the following conversion equation:

$$(D_{\text{absolute}})_{\text{E,NT}}(\text{in unit of mGy}) = (D_{\text{Simulated}})_{\text{E,NT}} \times (\text{CF})_{\text{E,NT}} \times \left(\frac{\text{Total mAs}}{100}\right) \tag{3}$$

where $(D_{\text{absolute}})_{\text{E,NT}}$ is the absorbed dose in unit of mGy, $(D_{\text{Simulated}})_{\text{E,NT}}$ is the MCNPX simulation results in the units of MeV per gram per source particle, and $(\text{CF})_{\text{E,NT}}$ is the conversion factor for the beam energy E and beam collimation NT.

Effective dose (E) was first calculated as a weighted average of the equivalent doses to selected body organs or tissues using the tissue weighting factors specified by the ICRP-60 (ICRP 1991) according to the equation (1). In addition, we adopted the latest ICRP-103 (ICRP 2007a) definition of E as being a sex-averaged value calculated from the averaged equivalent doses of the male and female phantoms using the equation:

$$E = \sum_{\text{T}} w_{\text{T}} \left[\frac{H_{\text{T}}^{\text{F}} + H_{\text{T}}^{\text{M}}}{2}\right] = \sum_{\text{T}} w_{\text{T}} \left[\frac{\sum_{\text{R}} w_{\text{R}}^{\text{F}} D_{\text{T,R}}^{\text{F}} + \sum_{\text{R}} w_{\text{R}}^{\text{M}} D_{\text{T,R}}^{\text{M}}}{2}\right] \tag{4}$$

where H_{T}^{F} and H_{T}^{M} are the equivalent doses for organ or tissue T of the female and male phantoms, respectively. w_{T} is the updated tissue weighting factor for T provided in ICRP Publication 103. $D_{\text{T,R}}^{\text{F/M}}$ is the average absorbed dose in tissue T of the female or male phantoms from the radiation type R. w_{R} is a radiation weighting factor.

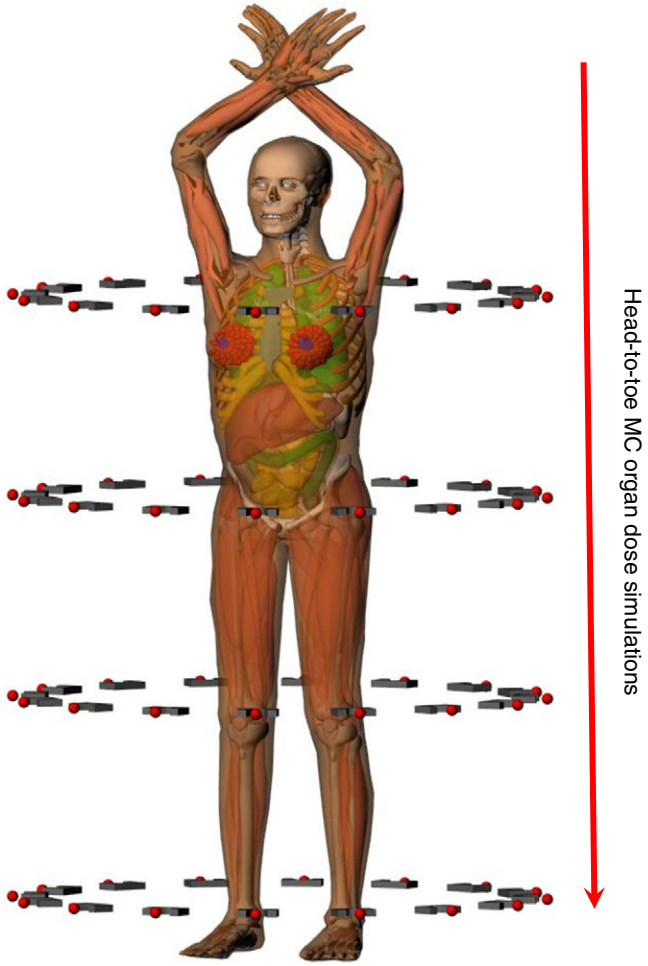

Figure 3. Scheme of the contiguous axial MC organ dose simulations on the patient phantom using a validated CT scanner model: a MC simulation mimics a series of continuous axial scans covering a phantom from the head to toe.

2.4. Organ dose reporting algorithms in virtualdose

Once the axial slice-by-slice dose database has been established, organ doses from a contiguous axial scan corresponding to a specific protocol can be obtained by directly summing the corresponding single axial slices in the scan range. When no-integer number of slices appears in the dose accumulation, a linear interpolation algorithm (based on the scan covered anatomy length among one piece axial scan distance) was applied to interpolate the data at the starting and ending places. In the helical scan mode, the dose calculation depends upon the 'pitch' of the scan, which was the ratio of the patient shift (table movement) during one rotation to the width of the beam. For a helical scan covering the same scan length and a pitch of 1, approximately the same radiation dose results as for a contiguous axial scan resulted in approximately the same radiation dose with the same technique factor (McNitt-Gray *et al* 1999). For non-contiguous (pitch $>$ 1) or overlapping (pitch $<$ 1) helical scans, radiation dose is inversely proportionally to the pitch value if all other scan parameters remain unchanged.

To correct for the use of CT scanners other than the scanners validated in this study, the organ radiation dose D_{H} can be estimated by:

$$D_{\mathrm{H}} = D_{\mathrm{c}} \times \frac{((\mathrm{CTDI_{vol}})_{\mathrm{E,NT}})_{\mathrm{Scanner}}}{((\mathrm{CTDI_{vol}})_{\mathrm{E,NT}})_{\mathrm{VirtualDose}}} \times \frac{\text{Total mAs}}{100} \tag{5}$$

where D_{C} is the organ dose from CT scans as reported by the scanners in *VirtualDose*, in unit of mGy, $((\mathrm{CTDI_{vol}})_{\mathrm{E,NT}})_{\mathrm{Scanner}}$ is the $\mathrm{CTDI_{vol}}$ value of the scanner being used in practice for a specific tube voltage (E) and beam collimation width (NT), $((\mathrm{CTDI_{vol}})_{\mathrm{E,NT}})_{\mathrm{VirtualDose}}$ is the $\mathrm{CTDI_{vol}}$ value used in *VirtualDose* for the same tube voltage and beam collimation width. Because the organ dose in the final slice-by-slice dose database was given per 100 mAs tube current time, the final dose result will be multiplied by the ratio of total mAs to 100 mAs.

In helical CT scans, additional rotations at the starting and ending points of the scan area of interest along the *Z*-axis were always needed, called *Z*-over scanning, for the purpose of image reconstruction of the first and last slices (Mahesh 2009, Seeram 2009, Tack and Gevenois 2007). The additional x-ray tube rotations must be included in the scan length and total integrated dose. To account for the *z*-over scanning, the total radiation dose D'_{H} is calculated in *VirtualDose* as:

$$D'_{\mathrm{H}} = D_{\mathrm{H}} + (D_{\mathrm{os}})_{\mathrm{Z_+}} + (D_{\mathrm{os}})_{\mathrm{Z_-}} \tag{6}$$

where $(D_{\mathrm{os}})_{\mathrm{Z_+}}$ and $(D_{\mathrm{os}})_{\mathrm{Z_-}}$ represent the radiation dose from the over scan length as specified by the user (due to the variability of over-scan length with different protocols, techniques, and scanner features).

As a method to reduce the total applied radiation dose, automatic exposure control (AEC) had become commonplace on modern MDCT scanners. AEC used tube current modulation (TCM) to automatically adjust the tube current according to the size and attenuation characteristics of the patient body region (McCollough *et al* 2006). To determine dose from CT scans using AEC technologies, the average tube current per rotation is used, such that:

$$D'_{\mathrm{H,AEC}} = \sum_{i\,=\,\text{first slice}}^{\text{last slice}} D_i \times w_i \tag{7}$$

where D_i is the organ dose result (in units of mGy /100 mAs) calculated from the axial MC simulations for the *i*-th slice in user specified scan region, w_i is the tube current weighting factor (the actual mAs in the *i*-th image divided by 100 mAs). The slice-averaged tube current, along with CT output (e.g. CTDI, DLP), CT scanner setting parameters (e.g. kVp, mAs, scan protocol) and patient information (weight, height, age, and gender) information may be extracted from the CT digital imaging and communications in medicine (DICOM) files and be imported automatically into *VirtualDose* to calculate the organ dose. If patient height and weight information is not available, *VirtualDose* will automatically select an adult phantom as default. Only the data necessary for the calculation need be extracted, so no protected patient information is transmitted to the *VirtualDose*.

2.5. SaaS architecture and web services interface design

SaaS is a modern software distribution method that hosts all its associated data and up-to-date resources centrally on a remote computer server (SaaS 2012). Different from the traditional software distribution model that requires a user to install and configure the application first, SaaS does not require any installation on user's computers. Using a license pre-assigned by

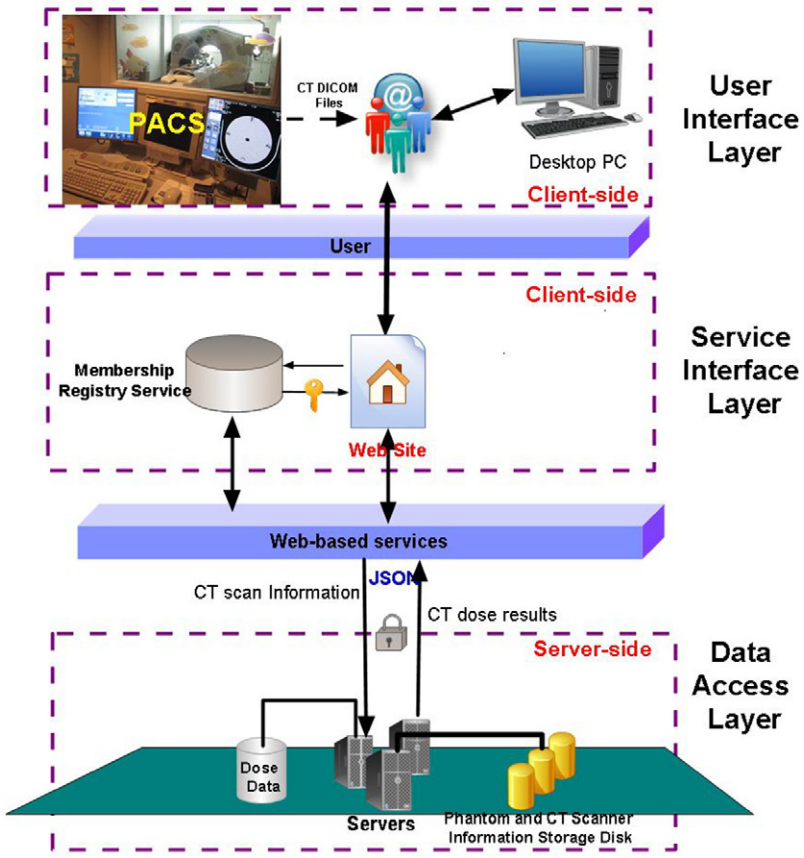

Figure 4. Schematic diagram of the SOA architecture for *VirtualDose* which includes 3 interface layers: the user, the service, and the data. Web-based interface uses javascript object notation (JSON) to send user's request and interpret the response messages from the remote server.

an SaaS provider, users can remotely access the software application, typically through an internet browser on demand at any time from any computer that is connected to the internet.

In this study, *VirtualDose* was designed as an SaaS application to allow multiple users to simultaneously access the software functions via the Internet. To implement this, a 'service-orientated architecture (SOA)' design was adopted (Erl 2005). As illustrated in figure 4, the SOA architecture in *VirtualDose* includes 3 different interface layers: the user, the service, and the data. Two main parts of the software design are needed: the client-side and the server-side. The client-side provides an interactive graphical user interface (GUI) within which visitors can provide the necessary scan parameters. The server-side hosts all the data and web service functions. After a user input is specified, the organ dose and effective dose can be calculated and tabulated instantly on the data grid panel embedded on the client-side GUI.

Using the SaaS platform, *VirtualDose* consists of many functional modules that were developed using several programming languages or technologies, including C-sharp (C#), JavaScript, hypertext markup language (HTML) specification, and cascading style sheets (CSS). For the client-side scripting, the HTML specification was used to define the content elements used in the web page; CSS was used to control the appearance and formatting of

marked-up contents when presented to the front-end user. JavaScript was used to manipulate the contents of HTML content elements and receive/respond to the user interaction, which can be embedded directly into the HTML web page. For the server-side scripting, C# was used as the primary programming language and all the service-side codes are implemented in C#. Each data model or object on the server-side was mapped directly to an individual HTML tag on the client-side and the entire web page was treated as a tree of HTML document object model (DOM) objects. JavaScript and HTML DOM are both used in the programming to better monitor and handle client-side events, such as when a user clicks a control, changes the value in an input control, moves the mouse over or away from a control button. As all the programming codes are stored and executed on a remote website host server but are invoked by users in the client side, the active server pages (ASP).NET model-view-controller (MVC) pattern was selected as the main development framework (Microsoft 2012b).

Another benefit of adopting the ASP.NET MVC is its high security for data protection. When programming under the ASP.NET MVC framework, the client-side code is prevented from directly reading a file or fetching data from a database hosted on the remote host server. Instead, when executing a web service hosted on the remote server-side, the client-side code sends a request message over the hypertext transfer protocol (HTTP) connection to the server. The request is a unique uniform resource locator (URL) for a web service hosted on the remote server-side which was essentially the endpoint of the user's HTTP request connection. This endpoint contains all information about the service function (Pathak 2011). A javascript object notation (JSON) request-response interaction pattern was used as a shortcut method for obtaining data from the remote server asynchronously (Richardson and Ruby 2008, Richardson *et al* 2013). JSON provides a compact way to either serialize or de-serialize the data from a remote host server to the client-side web page. In this way, the requested data can be loaded quickly from the remote server-side asynchronously to the client-side web page and rendered within the same browser without a visible page refresh.

In *VirtualDose,* all the detailed distributions of radiation doses to different organ/tissues are derived from a large MC-simulated organ dose database. To efficiently handle this database into *VirtualDose*, an 'entity framework' (EF) technology in the.NET development environment (Microsoft 2012a) was used to create various types of entity data models (e.g. patient phantoms, dose for each different beam thickness).

In this study, Microsoft Visual Studio 2010 Professional was used as the development tool for the designs of client- and server-side interfaces and functions developments. Microsoft SQL Server 2008 was used to process and compile the organ dose data.

2.6. Testing of virtualdose for routine CT scans

A testing of the CT radiation dose reporting functions in *VirtualDose* was also performed. Organ dose and effective dose reports were generated for four routine CT scan protocols of the head, chest, abdomen–pelvis (AP), and chest–abdomen–pelvis (CAP). The technical parameter settings for each of these sample scans were 120 kVp tube voltage, 100 mAs integrated tube current, head (for head scan) and body (for chest, AP, and CAP scans) bowtie filters, 10 mm collimation, and a pitch of 1. The scan ranges of these protocols were obtained from AAPM CT scan protocols collections (www.aapm.org/pubs/CTProtocols) and summarized in table 2.

2.7. Comparison of organ dose data in virtualdose with other existing data

CT scans use low x-ray energies and the resultant CT scan doses are sensitive to small anatomical details in the phantom. CT dose software packages such as the ImPACT CT patient

Table 2. Definition of anatomical boundaries using AAPM CT protocols.

Name of the CT protocol	Anatomic coverage
Head	From top of C1 lamina through top of calvarium
Chest	From top of lungs through the bottom of lungs
Abdomen–Pelvis	From top of liver to the pubic symphysis
Chest–Abdomen–Pelvis	From top of lungs to the pubic symphysis

dosimetry calculator (here inafter referred to as 'ImPACT') and CT-Expo (Stamm and Nagel 2002) are based on stylized patient phantoms with overly simplified anatomical information. A previous study has found that these stylized models could present significant dose discrepancies, particularly for low-energy x-rays, when compared against anatomically realistic patient models (Liu *et al* 2010). To further demonstrate the CT radiation dose reporting functions in *VirtualDose*, in this study we extended the comparison with the CT-Expo and ImPACT software by considering pediatric, adult, and pregnant patients.

3. Results and discussion

3.1. Monte Carlo organ dose database

Table 3 summarizes the comprehensive organ dose database that was based on extensive MC simulations of a total of 25 voxel phantoms covering pediatric, pregnant female, adult, and obese patients. Each CT scan of the phantom required a separate MC simulation, leading to more than 60 000 MC simulations to cover these phantoms involving different beam thicknesses and tube voltages in the MCNPX code. Results from each set of MC simulations were processed to generate a datasheet showing organ names and corresponding dose results for the axial continuous slice-by-slice scans. The datasheets were then integrated into a comprehensive organ dose database which was compiled using Microsoft SQL server 2008, as illustrated in figure 5.

3.2. VirtualDose

3.2.1. A Platform-independent CT dose reporting SaaS. *VirtualDose* was designed as an SaaS for CT dose reporting and it involved a web-based dynamic GUI compatible with numerous operating systems. The SaaS deliver mode can also be accessed from portable or mobile devices to be useful to users away from the office environment.

The main interface consists of parameter selection panel, a patient model/scan range display, and a dose result display. The parameter selection panel provides the options for a user to specify the operating conditions of a particular CT scan. Table 4 summarizes the available input features in *VirtualDose*. When the patient model is selected from a drop-down list of 25 phantoms, an image of that phantom appears on the patient model/scan range display window, with default coverage of the selected CT protocol superimposed on the phantom. The default scan length/position can be accepted, or the boundaries can be adjusted with click-and-drag controllers. To assist in the selection of the proper scan boundaries, transverse pseudo-CT slices of the anatomy for the scan range are also displayed.

Based on the user-specified scan parameters, *VirtualDose* fetches and calculates the patient-specific organ dose data from the remote server-side database. The results are then displayed as a table and a figure, as illustrated in figure 6. In addition to the manual entry of scan parameters, *VirtualDose* has the option to read the parameters from the DICOM

Table 3. Summary of patient phantoms and CT scan parameters used in the slice-by-slice MC simulations.

	Bowtie Filter	Beam Collimation (mm)	kVp	CT scanner
Pediatric patient models				
Newborn male Newborn female 1 year male 1 year female 5 year male 5 year female 10 year male 10 year female 15 year male 15 year female	Head	24	80,100,120	Siemens SOMATOM Sensation 16
		10	80,100,120	
	Body	24	80,100,120,140	
		10	80,100,120,140	
Pregnant patient models				
3 month pregnant 6 month pregnant 9 month pregnant	Head	20	80,100,120,140	GE LightSpeed Pro 16
		10	80,100,120,140	
		5	80,100,120,140	
		1.25	80,100,120,140	
	Body	20	80,100,120,140	
		10	80,100,120,140	
		5	80,100,120,140	
Average adult patient models				
Average adult male Average adult female	Head	20	80,100,120,140	GE LightSpeed Pro 16
		10	80,100,120,140	
		5	80,100,120,140	
		1.25	80,100,120,140	
	Body	20	80,100,120,140	
		10	80,100,120,140	
		5	80,100,120,140	
Obese patient models				
Normal body-weight male Normal body-weight female Over-weight male Over-weight female Obese level-I male Obese level-I female Obese level-II male Obese level-II female Morbidly-Obese male Morbidly-Obese female	Head	20	80,100,120,140	GE LightSpeed Pro 16
		10	80,100,120,140	
		5	80,100,120,140	
		1.25	80,100,120,140	
	Body	20	80,100,120,140	
		10	80,100,120,140	
		5	80,100,120,140	

file header, followed by the similar steps as the above to generate the dose report as above. In cases when some parameters are not available from a DICOM file, some default parameters will be selected automatically and users are also allowed to change them later on the interface.

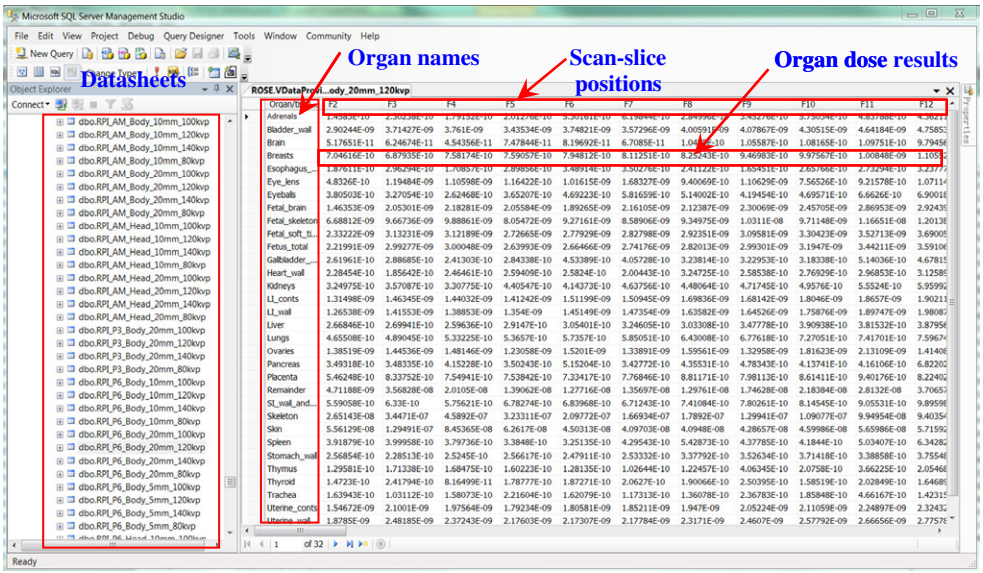

Figure 5. An example of how the slice-by-slice organ dose datasheets retrieved from MC simulations were incorporated into a comprehensive dose database compiled using Microsoft SQL Server 2008. In each datasheet, each data column was for one of axial continuous slice-by-slice scans that covered from head to toe for each phantom.

3.2.2. RESTful web service API available for third-party application integration. As a web-based SaaS, *VirtualDose* offers the representational state transfer (REST) web service using the JSON (Richardson and Ruby 2008, Richardson *et al* 2013) data exchange interface. This RESTful feature allows *VirtualDose* to be integrated seamlessly in a third-party software using an application programming interface (API). To retrieve the CT dosimetric metadata from *VirtualDose* server, a user can send a HTTP *POST* request including the necessary input parameters (e.g. patient gender, height, weight, kVp, pitch, mAs, TCM data, etc) to the target RESTful link via Internet connection. The remote server can then fetch asynchronously the parameters from user's request message and then return the requested CT dose results through the JSON data communication. In this way, the client software simply parses the contents of the HTTP response and creates its own dosimetric object before continuing processing.

3.3. CT doses reporting for routine CT scans using virtualDose

To demonstrate the CT dose reporting capabilities for different individual populations (small, average, and large patients), 3 pairs of male and female phantoms (1 year-old, median adult, and morbidly-obese) in the phantom library of *VirtualDose* were selected for four routine CT scan protocols of the head, chest, AP, and CAP. For each CT examination type, organ dose results for the small (1 year-old), average (adult), and large (morbidly-obese) males and females were reported by *VirtualDose* in tables 5–8. As $CTDI_{vol}$ was an effective parameter for the comparison between different MDCT scanners (Turner *et al* 2010), all the reported CT organ doses in tables 5–8 were normalized by the corresponding $CTDI_{vol}$ of the CT scanner validated in this study.

For head scans, as shown in table 5, brain and salivary glands received considerably higher radiation doses as compared to other organs. The brain was fully included in the head scan

Table 4. Parameter selection features available in *VirtualDose*.

Features and functions defined in *VirtualDose*
1. Patient phantom library
2. CT scanner manufacturer and model
3. A list of pre-defined CT scan protocols
4. X-ray tube voltage (kVp)
5. Bowtie filter type
6. Beam collimation
7. 2D whole-body cross-section landmark
8. Scan mAs
9. $CTDI_w$ specification, with default value provided
10. Pitch specification
11. Z-over beaming length specification
12. DICOM file reader
13. ICRP organ weighting scheme

region and the CT radiation doses per tube current to the brain in the small, average, and large patient phantoms were found to be very close. However, the doses to the salivary gland increased slightly with increasing patient size. As the salivary gland was not fully covered within the scan region, these increasing doses mostly resulted from the increasing covered portion of the salivary gland in the CT scans of the larger patients. The organ dose results from chest scans were tabulated in table 6 and it was found that, for the constant scan settings, the CT radiation dose per tube current to most organs in the small patient phantoms, particularly to those fully covered in the scan region (e.g. the breast, esophagus, lungs, etc) were significantly higher than those in the average and large patient phantoms. For example, a 54–110% decrease in the lung dose in the male phantoms and a 50–105% decrease in the lung dose in the female phantoms were observed with increasing patient size. As for abdomen–pelvis scans in table 7, these doses were found to decrease even more significantly as a function of size. For the colon, the results showed a decrease of 74–291% in the male phantoms and 61–288% in the female phantoms. For the stomach, these dose differences were even larger, ranging from 158–431% in the male phantoms and 171–408% in the female phantoms, mostly due to the fact that the stomach was highly shielded by adipose tissues abundant in the large patient phantoms. It was also interesting to observe that the doses to the ovaries in the 1 year-old female phantom were notably higher (up to six-fold) than observed for the larger phantoms. This was most likely due to body size and shape of this organ in the 1 year-old female phantom. Similar trends of dose per tube current versus patient size were found in most organs (e.g. breast, colon, liver, lung, stomach, gonadal, and so on) for chest–abdomen–pelvis scan, as shown in table 8. In summary, results showed that under the constant CT scan settings, smaller patient phantoms received considerably higher radiation dose, particularly for those organs within the CT scan region. This test illustrates how *VirtualDose* was used to evaluate patient organ doses for a given CT protocol.

3.4. Comparison of organ dose data in virtualdose with CT-Expo and ImPACT

3.4.1. Adults and children patients. A series of CT scans with the same CT scan parameters—120 kVp, 100 mAs, head (children) and body (adult) scan mode, 10 mm collimation and a pitch of 1—were performed using *VirtualDose,* CT-Expo (v2.3), and ImPACT (v1.0). In *VirtualDose,* 6 pairs of male and female phantoms (New-born, 1 year-old, 5 year-old,

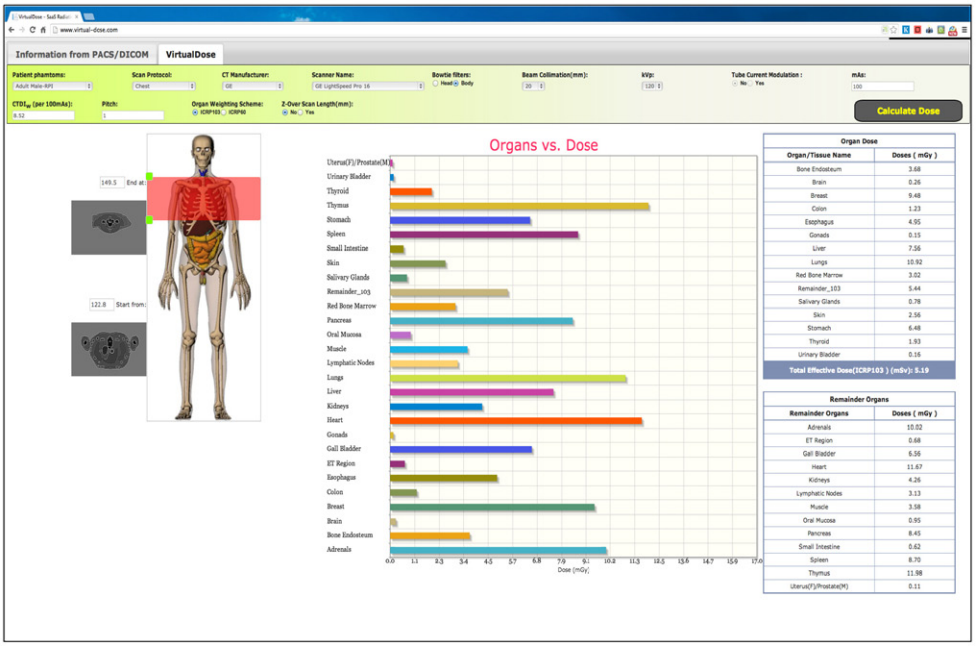

Figure 6. The results of organ doses were tabulated and plotted in the web-based GUI.

Table 5. Normalized organ doses in units of mGy per 100 mAs per $CTDI_{vol}$ reported by *VirtualDose* for the small, average, and large males and females for head examinations.

Patient size	Small patients		Average patients		Large patients	
Patient phantom	1 year-M	1 year-F	Adult-M	Adult-F	Morbidly-obese-M	Morbidly-obese-F
Scan length (cm)	11.2	11.2	12.7	12.2	12.7	12.2
Bone Surface	0.34	0.34	0.07	0.13	0.11	0.15
Brain	0.96	0.96	0.83	0.87	0.83	0.85
Breast	0.01	0.01	0.01	0.01	0.01	0
Colon	0	0	0	0	0	0
Esophagus	0.05	0.05	0.01	0.02	0.02	0.02
Gonads	0	0	0	0	0	0
Liver	0.01	0.01	0	0	0	0
Lungs	0.02	0.02	0.01	0.01	0.01	0.01
Red Bone Marrow	0.25	0.26	0.05	0.09	0.08	0.11
Salivary Glands	0.18	0.17	0.15	0.39	0.47	0.48
Skin	0.17	0.18	0.05	0.06	0.04	0.04
Stomach	0.01	0.01	0	0	0	0
Thyroid	0.07	0.07	0.02	0.04	0.03	0.04
Urinary Bladder	0	0	0	0	0	0

10 year-old, normal weight and morbidly-obese) and 1 pregnant female phantom (3 month) were selected to generate a comprehensive set of organ dose data for the comparison. In CT-Expo, 3 pairs of male and female phantoms (baby, child, and adult) were used to generate the organ dose data for pediatric and adult patients. In ImPACT, the only available hermaphroditic stylized phantom was used. As previously illustrated by Lee *et al* (2012), it would be very

Table 6. Normalized organ doses in units of mGy per 100 mAs per $CTDI_{vol}$ reported by *VirtualDose* for the small, average, and large males and females for chest examinations.

Patient size	Small patients		Average patients		Large patients	
Patient phantom	1 year-M	1 year-F	Adult-M	Adult-F	Morbidly-obese-M	Morbidly-obese-F
Scan length (cm)	9.9	9.9	26.7	24.8	27	24.8
Bone Surface	0.52	0.52	0.45	0.46	0.38	0.38
Brain	0.04	0.04	0.04	0.04	0.05	0.05
Breast	1.83	1.88	1.16	1.12	0.94	0.8
Colon	0.07	0.08	0.08	0.1	0.05	0.05
Esophagus	1.33	1.34	0.81	0.94	0.47	0.57
Gonads	0.01	0.03	0.02	0.02	0.01	0.01
Liver	0.66	0.67	0.53	0.55	0.29	0.3
Lungs	2.04	2.05	1.32	1.36	0.97	1
Red Bone Marrow	0.53	0.54	0.37	0.37	0.29	0.29
Salivary Glands	0.18	0.18	0.13	0.1	0.09	0.09
Skin	0.36	0.36	0.3	0.31	0.26	0.28
Stomach	0.63	0.63	0.54	0.64	0.4	0.4
Thyroid	0.65	0.66	0.37	0.34	0.28	0.34
Urinary Bladder	0.02	0.02	0.02	0.02	0.01	0.01

Table 7. Normalized organ doses in units of mGy per 100 mAs per $CTDI_{vol}$ reported by *VirtualDose* for the small, average, and large males and females for abdomen–pelvis examinations.

Patient size	Small patients		Average patients		Large patients	
Patient phantom	1 year-M	1 year-F	Adult-M	Adult-F	Morbidly-obese-M	Morbidly-obese-F
Scan length (cm)	19.7	19.7	32.7	30.3	32.9	30.2
Bone Surface	0.48	0.49	0.47	0.54	0.25	0.28
Brain	0.01	0.01	0.01	0.02	0.01	0.02
Breast	0.13	0.14	0.08	0.09	0.14	0.19
Colon	2.23	2.25	1.28	1.4	0.57	0.58
Esophagus	0.25	0.25	0.04	0.05	0.03	0.05
Gonads	0.72	2.16	0.2	1.18	0.12	0.34
Liver	1.98	2	0.98	1.06	0.68	0.76
Lungs	0.45	0.46	0.15	0.16	0.14	0.17
Red Bone Marrow	0.52	0.52	0.41	0.47	0.2	0.22
Salivary Glands	0.04	0.04	0.03	0.02	0.02	0.02
Skin	0.73	0.74	0.37	0.38	0.31	0.32
Stomach	1.91	1.93	0.74	0.71	0.36	0.38
Thyroid	0.1	0.1	0.04	0.04	0.03	0.03
Urinary Bladder	2.11	2.14	0.96	1.16	0.37	0.36

difficult to define scan ranges in the pediatric phantoms of CT-Expo using anatomical landmarks. Therefore, to eliminate the errors caused by the definition of scan ranges, a series of whole-body scans were successively performed using CT-Expo, ImPACT, and *VirtualDose* on the selected phantoms. All the reported CT organ doses were normalized by their corresponding $CTDI_{vol}$ values of the CT scanner used in this study. Since only one hermaphroditic stylized phantom is available in ImPACT, for the purpose of comparison, the organ doses to adult phantoms reported by CT-Expo and *VirtualDose* were all averaged to obtain the sex-averaged

Table 8. Normalized organ doses in units of mGy per 100 mAs per $CTDI_{vol}$ reported by *VirtualDose* for the small, average, and large males and females for chest–abdomen–pelvis examinations.

Patient size	Small patients		Average patients		Large patients	
Patient phantom	1 year-M	1 year-F	Adult-M	Adult-F	Morbidly-obese-M	Morbidly-obese-F
Scan length (cm)	28.4	28.4	57.6	53.4	57.4	53.4
Bone Surface	0.95	0.95	0.89	0.98	0.61	0.65
Brain	0.04	0.04	0.05	0.06	0.06	0.06
Breast	1.93	1.98	1.22	1.2	1.04	0.96
Colon	2.28	2.31	1.34	1.48	0.61	0.62
Esophagus	1.51	1.53	0.84	0.98	0.49	0.61
Gonads	0.72	2.18	0.21	1.2	0.12	0.35
Liver	2.35	2.37	1.36	1.44	0.89	0.98
Lungs	2.34	2.36	1.44	1.49	1.06	1.12
Red Bone Marrow	1	1.01	0.76	0.82	0.48	0.5
Salivary Glands	0.21	0.2	0.15	0.12	0.11	0.11
Skin	1.05	1.05	0.65	0.67	0.54	0.58
Stomach	2.29	2.32	1.18	1.26	0.69	0.72
Thyroid	0.73	0.74	0.4	0.37	0.3	0.36
Urinary Bladder	2.12	2.15	0.98	1.18	0.38	0.37

values (except for the case of the pregnant female phantoms, as there is no corresponding male phantoms). Those sex-averaged organ doses from *VirtualDose* were then normalized to those reported by the ImPACT and CT-Expo.

Figures 7 and 8 summarized the comparative organ dose values for a whole-body scan involving each pair of pediatric (New-born, 1 year-old, 5 year-old, and 10 year-old) and adult (normal weight and morbidly obese) phantoms from *VirtualDose* with the CT-Expo (baby, child, and adult) and ImPACT (adult) stylized phantoms. Figures 7(a) and (b) showed that most organ doses from CT-Expo in the whole body scan for the baby and child phantoms agreed with the values for the pediatric phantoms from *VirtualDose* within 34%. However, significant discrepancies were observed between the dose values for bone surface and breast from CT-Expo and *VirtualDose* pediatric phantoms. For example, in figures 7(a) and (b), doses for the bone surface in the baby and child phantoms in CT-Expo were 3-fold greater than those for the pediatric phantoms in *VirtualDose*. Figure 7(a) also showed that the breasts of the baby and child male phantoms receives 100% less dose than those for the pediatric male phantoms in *VirtualDose*, which was the reason why CT-Expo did not provide breast dose values for the male pediatric phantoms.

Figure 8 showed results for adult phantoms from CT-Expo, ImPACT, and *VirtualDose*. When compared to those of the stylized phantom in CT-Expo and ImPACT, most organ doses from *VirtualDose* were found to differ by −45 to 58% for the normal weight adult phantom. The differences were found to be significantly in the morbidly obese phantom for the same scan settings. For example, *VirtualDose* reported a reduction of 91 and 96% in the colon dose, 104 and 105% in the stomach dose, and 128 and 145% in the urinary bladder dose, when compared with those reported by CT-Expo and ImPACT, due to the shielding effect of the extra adipose tissues in morbidly obese phantoms used in the *VirtualDose*.

As three separate series of whole-body scans were independently performed on the patient phantoms in CT-Expo, ImPACT, and *VirtualDose* using the same CT scan settings, organs

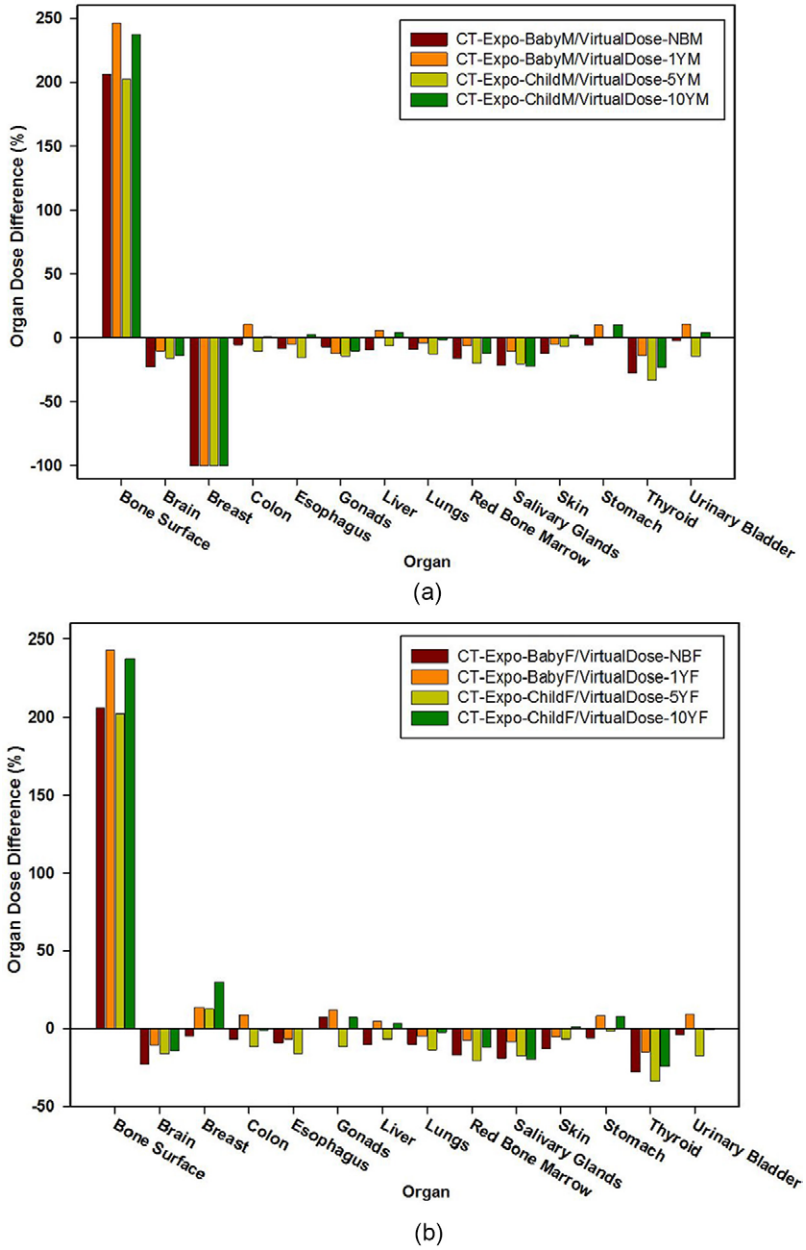

Figure 7. Plots of the organ dose differences reported by CT-Expo and *VirtualDose* for the whole-body CT scan on the pediatric (a) male and (b) female phantoms. The organ dose results for 'Baby' and 'Child' phantoms reported by *CT-Expo* were compared with those for newborn, 1 year-old, 5 year-old, and 10 year-old phantoms reported by *VirtualDose* by using the formula of $(\text{Dose}_{\text{CT-Expo}} - \text{Dose}_{\textit{VirtualDose}})/\ \text{Dose}_{\textit{VirtualDose}} * 100\%$.

in both the stylized phantom and voxel-based phantoms were entirely covered in the scan region. Thus, these dose discrepancies can be attributed mostly to the anatomical variations. These results confirm those were reported previously by Liu *et al* (2010) and Lee *et al* (2011,

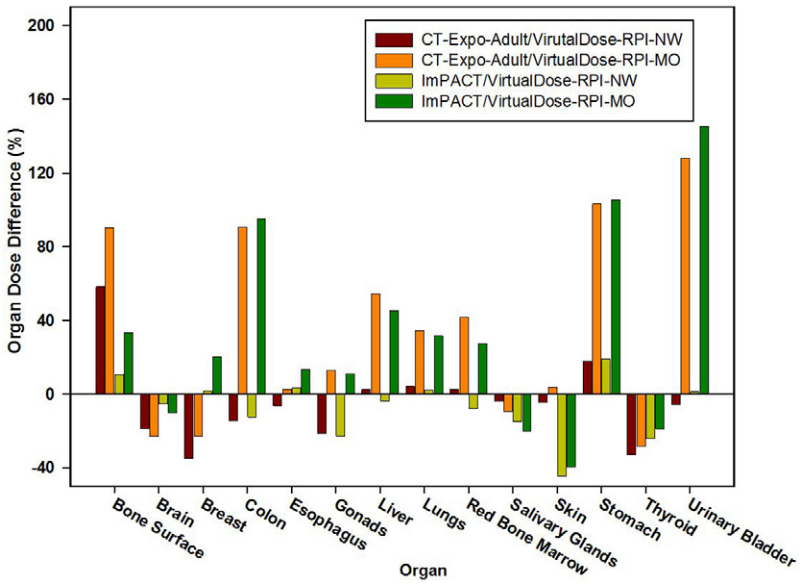

Figure 8. Plot of the sex-averaged organ dose differences reported by CT-Expo, ImPACT, and *VirtualDose* for the whole-body scan on the stylized and voxel-based adult normal weight (NW) and morbidly obese (MO) phantoms by using the formula of $(\text{Dose}_{\text{CT-Expo/ImPACT}} - \text{Dose}_{VirtualDose})/\ \text{Dose}_{VirtualDose} * 100\%$.

Table 9. Normalized fetal organ (mGy per 100 mAs per CTDI_{vol}) reported by ImPACT and *VirtualDose* for pregnant patients from abdomen–pelvis examinations.

Organs	ImPACT	*VirtualDose*-P3
Fetal_Brain	NA[a]	1.09
Fetal_Skeleton	NA[a]	NA[b]
Fetal_Soft_Tissue	NA[a]	1.14
Fetus_Total	1.3	1.13

[a] ImPACT does not report fetal organ dose.
[b] *VirtualDose*-P3 does not contain fetal skeleton.

2012) who concluded that the lack of realism offered by stylized phantoms caused significant discrepancies in reported CT dose results.

3.4.2. Pregnant patients. For pregnant patients, the primary focus of the comparison for pregnant patients was on CT radiation dose to fetus which was either partially or fully covered in the scan region. As no fetal organs were available in the ImPACT software, ImPACT used the uterus as a surrogate to estimate the fetal dose, as is done in similar situations (Angel *et al* 2008, Gu *et al* 2013). In *VirtualDose*, the CT radiation doses to the fetal brain, fetal skeleton, fetal soft tissues, and fetus total can be reported. The CT dose results from 2 routine CT scan protocols of the chest, and abdomen–pelvis from ImPACT and *VirtualDose* were tabulated in tables 9 and 10, respectively. As shown in table 9 for abdomen–pelvis scans, when the fetus is fully covered (for medical reasons) in the scan range, the CT radiation dose to the fetus reported by ImPACT was found to be 15% larger than that reported by *VirtualDose* for the voxel-based pregnant female at three-month gestational stage. However, for chest CT scans

Table 10. Normalized fetal organ (mGy per 100 mAs per $CTDI_{vol}$) reported by ImPACT and *VirtualDose* for pregnant patients from chest examinations.

Organs	ImPACT	*VirtualDose*-P3
Fetal_Brain	NA[a]	0.02
Fetal_Skeleton	NA[a]	NA[b]
Fetal_Soft_Tissue	NA[a]	0.03
Fetus_Total	0.002	0.03

[a] ImPACT does not report fetal dose.
[b] *VirtualDose*-P3 does not contain fetal skeleton.

when the fetus was only partially covered, the results in table 10 show that the dose to the fetus reported by ImPACT can be even smaller (~15 times) compared to the value reported by *VirtualDose*. These dose differences were mostly due to the fact that the stylized phantom in ImPACT does not contain a representation of the fetus, using only a surrogate organ. The size and position of the uterus in the stylized phantom introduce significant overestimating or underestimating of the fetal radiation dose. Furthermore, the CT radiation doses to other fetal organs (e.g. brain, skeleton, and soft tissues) were not available in ImPACT. The developing fetus is very sensitive to radiation and the risk of developing leukemia varies with the gestational age (Chatterson *et al* 2011). For this reason, the fetal dose information provided by *VirtualDose* can be helpful to the physicians and pregnant patients.

In summary, for relatively low x-ray energies, CT doses depend on organ shape, size and position. Therefore, *VirtualDose*, which is based on the latest patient phantoms, can be used to significantly improve data for organ doses to patients undergoing CT examinations.

3.5. Limitations of this work

Although the *VirtualDose* software represents a significant improvement on realism and accuracy of patient modeling and Monte Carlo dose calculations, there are several remaining technological limitations that may introduce uncertainty in the calculation organ dose for a specific patient undergoing CT scans. First, the MC dose calculations performed were based on a limited number of validated CT source term models, namely, the GE LightSpeed Pro 16 and Siemens SOMATOM Sensation 16. Applications of the correction factor techniques to extend to other scanners, while yielded reasonably good agreements with those reported in the literature, may introduce an uncertainty in the estimated organ doses (Turner *et al* 2010, Li *et al* 2011, Lee *et al* 2012, Sahbaee *et al* 2014). Second, the software does not currently support tube current modulation employed by a modern CT scanner, but an interface is being developed that will address the limitation in the near future. When projecting through different body part of the patient, the tube current value can vary in the *x*–*y* axis (angular modulation), *z*-axis (longitudinal modulation), or both. However, the angle-specific tube current information is not currently captured in the scan record, and only the slice-averaged tube current data are available in the DICOM file. When such slice-averaged information is used to compute organ dose, some uncertainties can be introduced, particularly for organs with highly asymmetric placement in the body, although the effect was found to be small in most cases (Khatonabadi *et al* 2012). Third, the contiguous axial scans with a specific pitch value were used to approximate the radiation dose for a helical scan covering the same scan length. This axial scan approximation method may introduce an uncertainty due to the surface dose variation effect when a low pitch value is used (Zhang *et al* 2009a). An ideal solution is to simulate real-time helical scans in a Monte Carlo code instead of using the pre-calculated axial scan

data. A fast Monte Carlo code for CT dose calculation is being developed to address this issue (Xu *et al* 2014). Finally, the software assumes the patient's arms are in the overhead position for scans of the body which may introduce an uncertainty in usual CT scans where the arms are inside the scan range (such as for patients in the emergency situations that are sedated, or that are unable to hold their arms above the head). The effects of arm positioning have been discussed else (Liu *et al* 2015).

4. Conclusions

Based on an extensive and latest library of 25 patient phantoms of both genders and various ages, *VirtualDose* has been shown in this study to be fully functional in reporting organ doses for a variety of patient types. When compared against the CT-Expo and ImPACT software that are based on anatomically simplified models, *VirtualDose* is found to be more accurate owing to anatomically realistic geometries. These results confirm those were reported previously by Liu *et al* (2010) and Lee *et al* (2011, 2012) who concluded that the lack of realism offered by stylized phantoms caused significant discrepancies in CT dose estimations. The development of *VirtualDose* as an SaaS platform allows multiple users to access the software simultaneously via Internet without having to install the software locally. The web-based GUI design and reporting features of *VirtualDose* are designed to cover a large list of CT manufacturers and scanner types and current ICRP recommendations. The SaaS framework and object-oriented programming methods can provide the necessary flexibility to generate accurate dose estimates for arbitrary scan protocols defined by a user. Furthermore, with innovative software engineering features such as the RESTful web service API, *VirtualDose* permits seamless integration with a third-party picture archiving and communication system (PACS) software package. Effort is on-going to continue to improve both the accuracy and usability in reporting CT doses for more than 50 current users worldwide. More information about *VirtualDose* is available from www.virtual-dose.com.

Acknowledgments

The development of *VirtualDose (*www.virtul-dose.com) as a commercial software was supported by an STTR grant to Virtual Phantoms, Inc. (www.virtualphantoms.com) from the national institute of biomedical imaging and bioengineering (NIBIB) (1R42EB010404). Patient phantoms used in *VirtualDose* were developed previously by grants to Rensselaer Polytechnic Institute from the national cancer institute (NCI) (R01CA116743) and the national library of medicine (NLM) (R01LM009362; R01LM009362-03S1) and a grant to the University of Florida from NIBIB (R01EB00267).

References

AAPM 2008 American Association of Physicists in Medicine AAPM report No.96: The Measurement, Reporting, and Management of Radiation Dose in CT. AAPM Report No. 96. Report of AAPM Task Group 23 of the Diagnostic Imaging Council CT Committee (www.aapm.org/pubs/reports/RPT_96.pdf)

AAPM 2010 American Association of Physicists in Medicine AAPM report No.111: Comprehensive Methodology for the Evaluation of Radiation Dose in X-Ray Computed Tomography: Report of AAPM Task Group 111: The Future of CT Dosimetry (www.aapm.org/pubs/reports/RPT_111.pdf)

AAPM 2011 American Association of Physicists in Medicine AAPM report No.204: Size-Specific Dose Estimates (SSDE) in Pediatric and Adult Body CT Examinations (www.aapm.org/pubs/reports/RPT_204.pdf)

ACR 2012 Dose index registry https://nrdr.acr.org/Portal/DIR/Main/page.aspx

Angel E *et al* 2008 Radiation dose to the fetus for pregnant patients undergoing multidetector CT imaging: Monte Carlo simulations estimating fetal dose for a range of gestational age and patient size *Radiology* **249** 220–7

Ban N, Takahashi F, Sato K, Endo A, Ono K, Hasegawa T, Yoshitake T, Katsunuma Y and Kai M 2011 Development of a web-based CT dose calculator: waza-Ari *Radiat. Prot. Dosim.* **147** 333–7

Berrington de Gonzalez A, Mahesh M, Kim K P, Bhargavan M, Lewis R, Mettler F and Land C 2009 Projected cancer risks from computed tomographic scans performed in the United States in 2007 *Arch. Intern. Med.* **169** 2071–7

Bolch W, Lee C, Wayson M and Johnson P 2010 Hybrid computational phantoms for medical dose reconstruction *Radiat. Environ. Biophys.* **49** 155–68

Boone J M 2007 The trouble with CTDI100 *Med. Phys.* **34** 1364–71

Boone J M, Hendee W R, McNitt-Gray M F and Seltzer S E 2012 Radiation exposure from CT scans: how to close our knowledge gaps, monitor and safeguard exposure—proceedings and recommendations of the radiation dose summit, sponsored by NIBIB, February 24–25, 2011 *Radiology* **265** 544–54

Brenner D J 2006 It is time to retire the computed tomography dose index (CTDI) for CT quality assurance and dose optimization. For the proposition *Med. Phys.* **33** 1189–90

Brenner D J 2010 Should we be concerned about the rapid increase in CT usage? *Rev. Environ. Health* **25** 63–8

Brenner D and Huda W 2008 Effective dose: a useful concept in diagnostic radiology *Radiat. Prot. Dosim.* **128** 503–8

Chatterson L C, Leswick D A, Fladeland D A, Hunt M M and Webster S T 2011 Lead versus bismuth–antimony shield for fetal dose reduction at different gestational ages at CT pulmonary angiography *Radiology* **260** 560–7

Dose C T 2008 The CT Dose calculation program (www.mta.au.dk/ctdose/index.htm)

DeMarco J J, Cagnon C H, Cody D D, Stevens D M, McCollough C H, O'Daniel J and McNitt-Gray M F 2005 A Monte Carlo based method to estimate radiation dose from multidetector CT (MDCT): cylindrical and anthropomorphic phantoms *Phys. Med. Biol.* **50** 3989–4004

Ding A P 2012 Development of a radiation dose reporting software for x-ray computed tomography (CT) *PhD Thesis* Rensselaer Polytechnic Institute

Ding A P, Gu J W, Trofimov A V and Xu X G 2010 Monte Carlo calculation of imaging doses from diagnostic multidetector CT and kilovoltage cone-beam CT as part of prostate cancer treatment plans *Med. Phys.* **37** 6199–204

Ding A P, Mille M M, Liu T Y, Caracappa P F and Xu X G 2012 Extension of RPI-adult male and female computational phantoms to obese patients and a Monte Carlo study of the effect on CT imaging dose *Phys. Med. Biol.* **57** 2441–59

Dixon R L 2006 Restructuring CT dosimetry—a realistic strategy for the future Requiem for the pencil chamber *Med. Phys.* **33** 3973–6

Dougeni E, Faulkner K and Panayiotakis G 2012 A review of patient dose and optimisation methods in adult and paediatric CT scanning *Eur. J. Radiol.* **81** E665–E83

Erl T 2005 *Service-Oriented Architecture: Concepts, Technology, and Design* (Upper Saddle River, NJ: Prentice Hall)

eXposure 2012 (www.radimetrics.com)

Gently I 2013 Image gently, (www.pedrad.org/associations/5364/ig)

Gu J, Bednarz B, Caracappa P F and Xu X G 2009 The development, validation and application of a multi-detector CT (MDCT) scanner model for assessing organ doses to the pregnant patient and the fetus using Monte Carlo simulations *Phys. Med. Biol.* **54** 2699–717

Gu J W, Xu X G, Caracappa P F and Liu B 2013 Fetal doses to pregnant patients from CT with tube current modulation calculated using Monte Carlo simulations and realistic phantoms *Radiat. Prot. Dosim.* **155** 64–72

ICRP 1977 Recommendations of the ICRP. ICRP Publication 26 *Ann. ICRP* 1 (Oxford: Pergamon)

ICRP 1991 1990 Recommendations of the International Commission on Radiological Protection. ICRP Publication 60 *Ann. ICRP* 21 (Oxford: Pergamon)

ICRP 2007a The 2007 Recommendations of the International Commission on Radiological Protection. ICRP Publication 103 *Ann. ICRP* 37 (Oxford: Pergamon)

ICRP 2007b Managing patient dose in multi-detector computed tomography (MDCT). ICRP Publication 102 *Ann. ICRP* 37 (Oxford: Pergamon)
ICRP 2009 Adult reference computational phantoms. ICRP Publication 110 *Ann. ICRP* 39 (Oxford: Pergamon)
ImPACT 2012 ImPACT's ct dosimetry tool (www.impactscan.org/ctdosimetry.htm)
IMV's 2014 CT Market Outlook Report 2015 IMV's 2014 CT Market Outlook Report (www.imvinfo.com/index.aspx?sec=ct&sub=dis&itemid=200081)
Johnson P B, Bahadori A A, Eckerman K F, Lee C and Bolch W E 2011 Response functions for computing absorbed dose to skeletal tissues from photon irradiation—an update *Phys. Med. Biol.* **56** 2347–65
Kalender W A, Schmidt B, Zankl M and Schmidt M 1999 A PC program for estimating organ dose and effective dose values in computed tomography *Eur. Radiol.* **9** 555–62
Kalra M K, Maher M M, Toth T L, Hamberg L M, Blake M A, Shepard J A and Saini S 2004 Strategies for CT radiation dose optimization *Radiology* **230** 619–28
Khatonabadi M, Zhang D, Mathieu K, Kim H J, Lu P Y, Cody D, DeMarco J J, Cagnon C H and McNitt-Gray M F 2012 A comparison of methods to estimate organ doses in CT when utilizing approximations to the tube current modulation function *Med. Phys.* **39** 5212–28
Lee C, Kim K P, Long D J and Bolch W E 2012 Organ doses for reference pediatric and adolescent patients undergoing computed tomography estimated by Monte Carlo simulation *Med. Phys.* **39** 2129–46
Lee C, Kim K P, Long D, Fisher R, Tien C, Simon S L, Bouville A and Bolch W E 2011 Organ doses for reference adult male and female undergoing computed tomography estimated by Monte Carlo simulations *Med. Phys.* **38** 1196–206
Li X, Samei E, Segars W P, Sturgeon G M, Colsher J G, Toncheva G, Yoshizumi T T and Frush D P 2011 Patient-specific radiation dose and cancer risk estimation in CT: part II. Application to patients *Med. Phys.* **38** 408–19
Liu H, Gao Y, Ding A, Caracappa P F and Xu X G 2015 The profound effects of patient arm positioning on organ doses from CT procedures calculated using Monte Carlo simulations and deformable phantoms *Radiat. Prot. Dosim.* **164** 368–75
Liu H, Gu J, Caracappa P F and Xu X G 2010 Comparison of two types of adult phantoms in terms of organ doses from diagnostic CT procedures *Phys. Med. Biol.* **55** 1441–51
Mahesh M 2009 *MDCT Physics: The Basics—Technology, Image Quality and Radiation Dose* (Philadelphia, PA: Lippincott Williams and Wilkins)
McCollough C H 2006 It is time to retire the computed tomography dose index (CTDI) for CT quality assurance and dose optimization. Against the proposition *Med. Phys.* **33** 1190–1 (PMID: 16752553)
McCollough C H, Bruesewitz M R and Kofler J M Jr 2006 CT dose reduction and dose management tools: overview of available options *Radiographics* **26** 503–12
McCollough C H, Leng S, Yu L, Cody D D, Boone J M and McNitt-Gray M F 2011 CT dose index and patient dose: they are not the same thing *Radiology* **259** 311–6
McCollough C H, Primak A N, Braun N, Kofler J, Yu L and Christner J 2009 Strategies for reducing radiation dose in CT *Radiol. Clin. North Am.* **47** 27–40
McCollough C H and Schueler B A 2000 Calculation of effective dose *Med. Phys.* **27** 828–37
McNitt-Gray M F 2002 AAPM/RSNA physics tutorial for residents: topics in CT—radiation dose in CT1 *Radiographics* **22** 1541–53
McNitt-Gray M F, Cagnon C H, Solberg T D and Chetty I 1999 Radiation dose in spiral CT: the relative effects of collimation and pitch *Med. Phys.* **26** 409–14
Microsoft 2012a The ADO.NET Entity Framework Overview (http://msdn.microsoft.com/en-us/library/aa697427(v=vs.80).aspx)
Microsoft 2012b NET Framework Conceptual Overview (http://msdn.microsoft.com/library/zw4w595w.aspx)
Na Y H, Zhang B, Zhang J, Caracappa P F and Xu X G 2010 Deformable adult human phantoms for radiation protection dosimetry: anthropometric data representing size distributions of adult worker populations and software algorithms *Phys. Med. Biol.* **55** 3789–811
Pathak N 2011 *Pro WCF 4: Practical Microsoft SOA Implementation* (New York: Apress)
Pearce M S *et al* 2012 Radiation exposure from CT scans in childhood and subsequent risk of leukaemia and brain tumours: a retrospective cohort study *Lancet* **380** 499–505
Pelowitz D B 2005 *Mcnpx User's Manual* (Los Alamos, NM: Los Alamos National Laboratory)
Richardson L, Amundsen M and Ruby S 2013 *RESTful Web APIs* (Sebastopol, CA: O'Reilly Media)
Richardson L and Ruby S 2008 *RESTful Web Services* (Sebastopol, CA: O'Reilly Media)

SaaS 2012 Software as a service (http://en.wikipedia.org/wiki/Software_as_a_service)
Sahbaee P, Segars W P and Samei E 2014 Patient-based estimation of organ dose for a population of 58 adult patients across 13 protocol categories *Med. Phys.* **41** 072104
Seeram E 2009 *Computed Tomography: Physical Principles, Clinical Applications, and Quality Control* (St. Louis, MO: Saunders/Elsevier)
Slovis T L 2003 Children, computed tomography radiation dose, and the as low as reasonably achievable (ALARA) concept *Pediatrics* **112** 971–2
Sodickson A, Baeyens P F, Andriole K P, Prevedello L M, Nawfel R D, Hanson R and Khorasani R 2009 Recurrent CT, cumulative radiation exposure, and associated radiation-induced cancer risks from CT of adults *Radiology* **251** 175–84
Stamm G and Nagel H D 2002 CT-Expo—ein neuartiges Programm zur Dosisevaluierung in der CT *Fortschr Röntgenstr* **174** 1570–6
Tack D and Gevenois P A 2007 *Radiation Dose from Adult and Pediatric Multidetector Computed Tomography* (Berlin: Springer)
The Joint Commission 2015 The joint commission. Revised requirements for diagnostic imaging services (www.jointcommission.org/assets/1/6/HAP-CAH_DiagImag_Prepub_July2015release_20150105.pdf)
Turner A C, Zankl M, DeMarco J J, Cagnon C H, Zhang D, Angel E, Cody D D, Stevens D M, McCollough C H and McNitt-Gray M F 2010 The feasibility of a scanner-independent technique to estimate organ dose from MDCT scans: using CTDIvol to account for differences between scanners *Med. Phys.* **37** 1816–25
Wisely I 2013 Image wisely (www.imagewisely.org/)
Xu X G 2014 An exponential growth of computational phantom research in radiation protection, imaging, and radiotherapy: a review of the fifty-year history *Phys. Med. Biol.* **59** R233–302
Xu X G *et al* 2014 ARCHER, a new Monte Carlo software tool for emerging heterogeneous computing environments *Ann. Nucl. Energy* at press (doi:10.1016/j.anucene.2014.08.062)
Xu X G and Eckerman K F 2009 *Handbook of Anatomical Models for Radiation Dosimetry* (Boca Raton, FL: CRC/Taylor and Francis Group)
Xu X G, Taranenko V, Zhang J and Shi C 2007 A boundary-representation method for designing whole-body radiation dosimetry models: pregnant females at the ends of three gestational periods—RPI-P3, -P6 and -P9 *Phys. Med. Biol.* **52** 7023–44
Zanki M, Fill U, Petoussi-Henss N and Regulla D 2002 Organ dose conversion coefficients for external photon irradiation of male and female voxel models *Phys. Med. Biol.* **47** 2367–85
Zhang D *et al* 2009a Variability of surface and center position radiation dose in MDCT: Monte Carlo simulations using CTDI and anthropomorphic phantoms *Med. Phys.* **36** 1025–38
Zhang J, Na Y H, Caracappa P F and Xu X G 2009b RPI-AM and RPI-AF, a pair of mesh-based, size-adjustable adult male and female computational phantoms using ICRP-89 parameters and their calculations for organ doses from monoenergetic photon beams *Phys. Med. Biol.* **54** 5885–908

New capabilities of the Monte Carlo dose engine ARCHER-RT: Clinical validation of the Varian TrueBeam machine for VMAT external beam radiotherapy

David P. Adam
Medical Physics, University of Wisconsin Madison, 1111 Highland Avenue, Madison, WI 53705, USA

Tianyu Liu
Nuclear Engineering Rensselaer Polytechnic Institute, 110 8th Street, Troy, NY 12180, USA

Peter F. Caracappa
Virtual Phantoms, Inc, Albany, NY 12205, USA

Bryan P. Bednarz
Medical Physics, University of Wisconsin Madison, 1111 Highland Avenue, Madison, WI 53705, USA

Xie George Xu[a)]
Nuclear Engineering Rensselaer Polytechnic Institute, 110 8th Street, Troy, NY 12180, USA

(Received 24 June 2019; revised 3 February 2020; accepted for publication 10 February 2020; published 13 April 2020)

Purpose: The Monte Carlo radiation transport method is considered the most accurate approach for absorbed dose calculations in external beam radiation therapy. In this study, an efficient and accurate source model of the Varian TrueBeam 6X STx Linac is developed and integrated with a fast Monte Carlo photon-electron transport absorbed dose engine, ARCHER-RT, which is capable of being executed on CPUs, NVIDIA GPUs, and AMD GPUs. This capability of fast yet accurate radiation dose calculation is essential for clinical utility of this new technology. This paper describes the software and algorithmic developments made to the ARCHER-RT absorbed dose engine.
Methods: AMD's Heterogeneous-Compute Interface for Portability (HIP) was implemented in ARCHER-RT to allow for device independent execution on NVIDIA and AMD GPUs. Architecture-specific atomic-add algorithms have been identified and both more accurate single-precision and double-precision computational absorbed dose calculation methods have been added to ARCHER-RT and validated through a test case to evaluate the accuracy and performance of the algorithms. The validity of the source model and the radiation transport physics were benchmarked against Monte Carlo simulations performed with EGSnrc. Secondary dose-check physics plans, and a clinical prostate treatment plan were calculated to demonstrate the applicability of the platform for clinical use. Absorbed dose difference maps and gamma analyses were conducted to establish the accuracy and consistency between the two Monte Carlo models. Timing studies were conducted on a CPU, an NVIDIA GPU, and an AMD GPU to evaluate the computational speed of ARCHER-RT.
Results: Percent depth doses were computed for different field sizes ranging from 1.5 cm^2 × 1.5 cm^2 to 22 cm^2 × 40cm^2 and the two codes agreed for all points outside high gradient regions within 3%. Axial profiles computed for a 10 cm^2 × 10 cm^2 field for multiple depths agreed for all points outside high gradient regions within 2%. The test case investigating the impact of native single-precision compared to double-precision showed differences in voxels as large as 71.47% and the implementation of KAS single-precision reduced the difference to less than 0.01%. The 3%/3mm gamma pass rates for an MPPG5a multileaf collimator (MLC) test case and a clinical VMAT prostate plan were 94.2% and 98.4% respectively. Timing studies demonstrated the calculation of a VMAT plan was completed in 50.3, 187.9, and 216.8 s on an NVIDIA GPU, AMD GPU, and Intel CPU, respectively.
Conclusion: ARCHER-RT is capable of patient-specific VMAT external beam photon absorbed dose calculations and its potential has been demonstrated by benchmarking against a well validated EGSnrc model of a Varian TrueBeam. Additionally, the implementation of AMD's HIP has shown the flexibility of the ARCHER-RT platform for device independent calculations. This work demonstrates the significant addition of functionality added to ARCHER-RT framework which has marked utility for both research and clinical applications and demonstrates further that Monte Carlo-based absorbed dose engines like ARCHER-RT have the potential for widespread clinical implementation.
 [https://doi.org/10.1002/mp.14143]

Key words: dose calculation, GPU, Monte Carlo, radiation therapy, software

1. INTRODUCTION

External beam radiotherapy (EBRT) has remained an essential modality in the armamentarium of oncologists over the last several decades. Over 50% of all cancer patients receive EBRT for curative or palliative purposes.[1] EBRT requires accurate absorbed dose computation to safely and effectively deliver radiation treatment regimens to patients. Monte Carlo methods are regarded as the "gold standard" for performing these absorbed dose calculations.[2] Thoroughly benchmarked general-purpose Monte Carlo codes have been used for decades to support research efforts related to EBRT including EGSnrc,[3,4] MCNP,[5–7] PENELOPE,[8,9] and GEANT4.[10,11] Although highly accurate, Monte Carlo-based absorbed dose calculation engines require a large amount of computational resources. To this end, several CPU-based Monte Carlo codes that utilize algorithmic approximations and modifications have been developed to improve run-time efficiency including DPM,[12] VMC++,[13] and MCDOSE.[14] Additionally, several groups have demonstrated significant performance gains in comparison to CPU-based MC codes for EBRT Monte Carlo simulations on graphics processing units (GPUs).[15–20]

While GPU-accelerated Monte Carlo codes exhibit desirable performance characteristics, the accuracy of these codes can be compromised by GPU architecture-specific optimization considerations, mainly, (a) the necessity of atomic-add operations to accurately tally absorbed dose and (b) the utilization of single vs double-precision floating point representation of real numbers. For Monte Carlo radiotherapy absorbed dose calculations, a single array shared by all threads is implemented to accumulate tally data because GPU thread-specific memory is usually not large enough to hold an entire local tally array. Atomic-add operations are required to avoid race conditions where two threads try to update the same memory location.

There are also trade-offs in accuracy vs performance when utilizing single-precision vs double-precision. Using single-precision generally results in better performance (at least twice as fast[21]) at the expense of accuracy, whereas using double-precision results in better accuracy at the expense of performance. To date, single-precision has been widely adopted in various other studies of GPU-accelerated Monte Carlo absorbed dose calculation due to better performance and the lack of support of double-precision numbers on several GPU architectures. Specifically, NVIDIA GPUs prior to the Pascal generation and all AMD GPUs do not offer the same hardware level atomic-add operation support for double-precision numbers and suboptimal software emulation can be prohibitively slow. One major drawback of using native implementations of single-precision atomic-add operations is that round-off errors can occur in highly absorbed dose regions, where small absorbed dose increments are added to counters with large absorbed dose values. The lower digits of the absorbed dose increments may be truncated, resulting in an underestimate of the absorbed dose. Magnoux et al. found in voxel-based absorbed dose calculations that single-precision calculations can differ from double-precision calculations by over 40%.[21] Liu et al. found that in CT scan absorbed dose calculations the lung dose can be underestimated by as much as 20% using single-precision calculation methods.[22]

Additionally, the majority of the aforementioned GPU codes all rely on the CUDA architecture, which is not desirable in terms of portability. Tian et al. utilized OpenCL to promote an architecture independent simulation platform,[23,24] but computational speeds for this OpenCL platform were slightly slower than its CUDA counterpart and as of 2018, OpenCL is deprecated on MacOS.

This work builds upon our previously published ARCHER-RT work[25] and seeks to address these pitfalls by (a) describing and demonstrating the implementation of a single-precision Kahan summation-based atomic-add algorithm to ensure dosimetric accuracy for all GPU architectures, (b) describing architecture-specific optimal atomic-add algorithms to provide older NVIDIA GPUs software emulation of double-precision atomic-add methods to ensure accurate absorbed dose calculations, (c) implementing ARCHER-RT on AMD's Heterogeneous-Compute Interface for Portability (HIP), a C++ Application Programming Interface (API) which allows for device-independent execution on NVIDIA and AMD GPUs, and (d) adding VMAT capable source modeling by utilizing patient-independent phase spaces as input and performing radiation transport simulations through patient-dependent collimators into patient geometries. We demonstrate this through the modeling and benchmarking of a flattened photon 6 MV Varian TrueBeam linear accelerator in the ARCHER-RT framework.

2. METHODS

2.A. ARCHER-RT description

The following section describes both the software design and the underlying physics models used in absorbed dose calculation engine called ARCHER-RT (Accelerated Radiation-transport Computations in Heterogeneous EnviRonments).

2.A.1. Software design for GPU and multithread CPU codes

ARCHER-RT is designed and optimized for both CPU and GPU processors.[26–28] The CPU code uses open multiprocessing (OpenMP) API for parallel computing, whereas the GPU code uses HIP) — a new C++ API developed by AMD.[29] The advantage of choosing HIP is portability and simplicity. HIP allows the same source code to be compiled into different binaries to run on AMD and NVIDIA GPUs respectively. On AMD's platform, the HIP functions are compiled into the Instruction Set Architecture (ISA) of AMD GPUs using the hcc compiler, whereas on NVIDIA's, they are wrappers of their CUDA counterparts (for instance, hipMalloc calls cudaMalloc) and are compiled into NVIDIA GPUs' ISA using the nvcc compiler driver. In ARCHER-RT,

there are only a few cases where HIP cannot directly provide a uniform interface, due to architectural differences between AMD and NVIDIA GPUs, and platform-dependent code becomes necessary. For example, a warp consists of 32 threads on NVIDIA GPUs but 64 on AMD's. Consequently, in our highly-optimized absorbed dose accumulation functions, the intrinsic function __popc (requiring a 32-bit integer parameter, each bit representing the status of a lane in a warp) should be exclusively applied to NVIDIA GPUs and __popcll (requiring a 64-bit integer parameter) to AMD GPUs.[30] HIP also provides an element of simplicity. HIP is a high-level API designed to closely resemble the syntax of CUDA runtime API, the use of which has dominated NVIDIA GPU-accelerated applications. HIP significantly reduces the amount of boilerplate code required by some alternative GPU computing APIs such as OpenCL or CUDA driver API.

ARCHER-RT is written in C++11, with a strong emphasis on both performance (achieved by low-level optimizations) and maintainability (using object-oriented design). All computationally intensive components are GPU accelerated (i.e. phase space particle coordinate transforms, particle transport in the Linac source model, and particle transport in the patient). Meanwhile, the multithreaded CPU fallbacks are available, serving two purposes: to allow fair CPU-GPU performance comparison, where both codes are sufficiently parallelized and optimized, and to allow code verification, where the developed GPU code is constantly verified with the CPU code in a variety of unit tests. The absorbed dose engine in ARCHER-RT supports both single-precision and double-precision formats implemented by a C++ template. In general, the GPU results are expected to have 10–15 identical digits with the CPU result for double-precision, and 4–7 for single-precision.

2.A.2. Architecture-specific atomic-add methods for single and double-precision

ARCHER-RT is now designed to operate in either single or double-precision modes depending upon the needs and constraints of the end-user. In each of these modes atomic-add algorithms are implemented to provide optimal performance when used for GPU-accelerated absorbed dose computation.[30]

Although double-precision is significantly more reliable than native single-precision for absorbed dose accumulation calculations, NVIDIA GPUs prior to the Pascal generation and all existing AMD GPUs do not directly support double-precision "atomic-add" operations at the hardware level. GPU implementation of "compare-and-swap" (CAS) is a commonly used algorithm for the software emulation of double-precision "atomic-add" operations but can be prohibitively slow. In the CAS algorithm, a calling thread adds the absorbed dose increment to a memory location using a do-while loop structure. Specifically, the calling thread repeatedly executes instructions in the do-while loop until no other thread in the same warp has meanwhile updated the same memory location. This takes indefinite number of steps to complete. The root cause of CAS low performance lies in GPU's nominal SIMT (single instruction, multiple threads) architecture where threads in a warp execute the same instruction at nearly the same time. If several threads in a warp attempt to update the same memory location, contention arises and each thread tend to repeat the do-while loop indefinitely many times before succeeding.

ARCHER-RT addresses the limitation of CAS by implementing the Warp-aggregated method (WAG) algorithm to eliminate intra-warp thread contention on supportive architectures. The WAG reduces intra-warp contention by utilizing GPU warp shuffle methods.[31,32] The general idea behind WAG is that threads of a warp attempting to update the same memory location are put into the same subgroup. In each subgroup, a leader thread sums all absorbed dose increments from its peer threads and singly updates the memory location without contention. It is worth pointing out that theoretically inter-warp thread contention exists as well but happens significantly less frequently,whereas GPUs implement SIMT for threads within the same warp, threads from different warps are not synchronized on the GPU grid level by design. This means that the inter-warp thread contention in the WAG algorithm theoretically exists but only occurs by chance and is significantly less likely than the intra-warp thread contention in the CAS algorithm caused by GPU's SIMT design.

ARCHER-RT supports hardware-level double-precision atomic-add operations for NVIDIA GPUs following the Pascal generation. While recent iterations of NVIDIA GPUs enable double-precision atomic-add operations at the hardware level, the problem of thread contention, despite being less severe than the software counterpart, still inevitably exists, where threads in a warp updating the same memory location are serialized by the hardware. In ARCHER, WAG is used again to have the leader threads alone update the memory locations and avoid serialization.

For architectures that do not support double-precision, single-precision must be used. Bossler et al.[33] and Liu et al.[30] have performed studies to identify appropriate single-precision atomic-add algorithms that retain accuracy at only a small performance penalty. Based on these results, the Kahan summation algorithm (KAS) has been implemented in ARCHER-RT to allow for both fast and accurate absorbed dose accumulation computations. The algorithm has been historically used in sequential code to reduce numerical rounding errors for single-precision summation but it has been adopted in ARCHER-RT for parallel GPU computations to accumulate 64-bit absorbed dose values (32-bit absorbed dose increment and 32-bit numerical error) while using the same techniques as in WAG to eliminate intra-warp thread contention.[30,34]

2.A.3. ARCHER-RT workflow

ARCHER-RT is designed using the general workflow depicted in Fig. 1 using the unified modeling language activity diagram for radiation therapy applications. The white blocks indicate code run on the host system, and the shaded blocks on the GPUs (with CPU fallbacks).

The host system initializes several key modules of ARCHER-RT, including Linac source modeling, phase space file I/O, DICOM, and radiation transport in patient. The Linac source module transports particles in X/Y jaws and multileaf collimator (MLCs). The phase space file I/O module reads phase-space-1 files from the disk and allocates/deallocates the memory for particle data storage. The DICOM module parses CT images, RT plan, RT dose, and RT structure files, sets up radiotherapy simulation parameters, and generates patient-specific phantoms. The transport in patient module simulates photon-electron transport inside the patient body. For each beam in an IMRT plan, ARCHER-RT passes one or more (customizable) batches of phase-space-1 files to the Linac source module that tracks particles through the rotated collimator comprised of the X/Y jaws and MLCs until they reach the phase-space-2 plane. ARCHER-RT then applies the geometry transformation to the particles according to the gantry angle and couch angle before saving them to phase-space-2 particle container. For a VMAT plan, the DICOM module implicitly converts the control point sequence into beam sequence, so that ARCHER-RT is capable of simulating VMAT plans in the same way as IMRT. Once phase-space-2 particles from all beams are obtained, ARCHER-RT proceeds to photon-electron coupled transport inside the patient, using the batch simulation scheme. Because this process is usually more computationally intensive, multi-GPU support is provided based on dynamic scheduling, where each GPU, if idle, retrieves one batch of particles to simulate. After all batches are finished, the voxel absorbed dose and the relative standard deviation arrays are stored.

2.A.4. Source modeling

Source modeling, in the context of Monte Carlo absorbed dose engine, refers to a method that calculates information about particles passing through linear accelerator beamline components. In the method that uses phase space information collected from treatment head simulations,[35] source particles originated from the target are transported through the detailed geometric model of the treatment head, in which the energy,

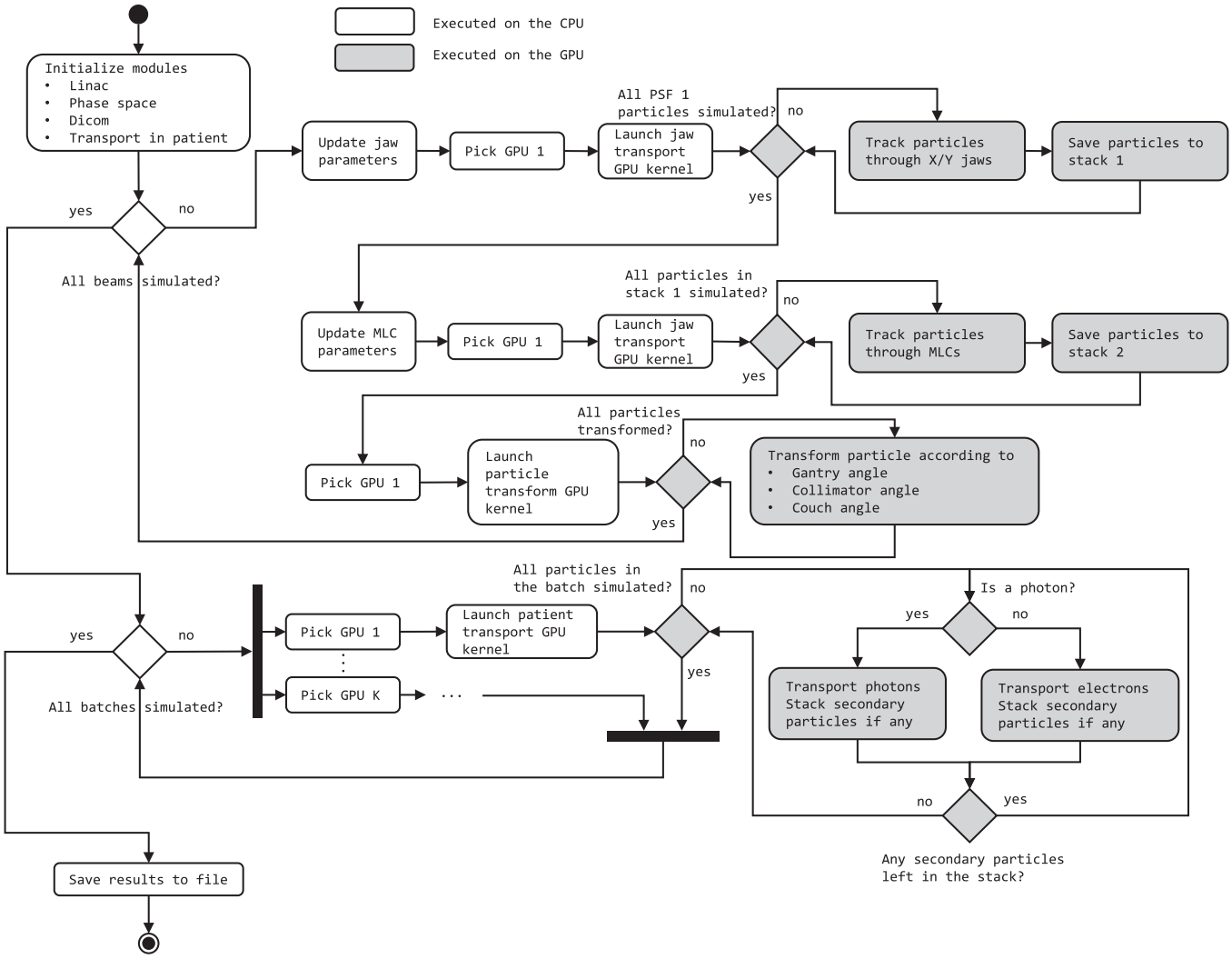

FIG. 1. Unified modeling language activity diagram of ARCHER-RT for radiation therapy applications. The white blocks illustrate the tasks of the sequential code executed on the CPU and the shaded blocks illustrate the tasks of the parallel code on the GPU.

position, direction and statistical weight information of a particle are recorded. With the correct setup of geometry parameters and energy spectrum of the linear accelerator, this method provides the most accurate source model.[35]

The source modeling is initiated at the patient-independent phase space directly below the primary collimators but just above the secondary X/Y collimator of the Varian TrueBeam. These patient-independent phase spaces are generated by GEANT4 simulations performed and validated by Constantin et al.[36] As such, the task of source modeling for ARCHER-RT is narrowed down to modeling of secondary X/Y jaws and MLC, and efficient sampling of particles through these components.

To balance the accuracy of source term representation and sampling efficiency, a First-Compton-based approximate transport method[37,38] was used for the particle transport through the secondary X/Y jaws and MLC in ARCHER-RT. ARCHER-RT only transports photons in the beam collimation routines. Only the Compton scattering effect is considered in the source modeling method because any electron generated is assumed to be absorbed locally for both photoelectric interactions and Compton scattering interactions. Pair production is ignored because of the low interaction probability for any photon less than 5 MeV. As photons traverse through the secondary jaws or the MLC, the interaction site is sampled over the slab thickness assuming an exponential attenuation of incident photons. The probability of Compton scattering is evaluated by the ratio of the Compton and total attenuation coefficients and the energy and angle of Compton scattered photons are determined according to the Klein-Nishina formula.[39] In accordance with the methods outlined by Keall et al.,[37] an interacting particle's weight is modified based on scattered photons' energy and direction, while the emerged Compton electron histories are terminated.[38] The remaining thickness after the interaction and the corresponding attenuation coefficient of the Compton scattered photons are then used to attenuate the photon as they exit the secondary jaws/MLC leaves.

In this work, we modeled the jaws and specifically the Varian HDMLC using the Siebers-Keall method.[37,38] The Varian HDMLC is a multileaf collimator consisting of two banks of 60 tungsten-alloy leaves with 32 $cm^2 \times 0.25$ cm^2 wide (projected at isocenter) leaves in the central 8 cm of the field and 28 $cm^2 \times 0.50$ cm^2 leaves on the outer 14 cm of the field. MLC-specific parameters that were modeled include intraleaf thickness, interleaf leakage, leaf tip radius and thickness, tongue-and-groove effects, and leaf-edge effects. Physical dimensions and material composition of both the jaws and HDMLC leaves were obtained from the proprietary Varian Monte Carlo data package. The MLC is modeled in a method similar to that described by Bergman et al.[40] The leaf geometry for ARCHER-RT is specified in two input files that account for the distance from the upper surface of an MLC region from the source, the leaf number, and the leaf thickness. In a separate file, the physical density of the tungsten alloy, the leaf tip radius of curvature, the leaf tip 'tip angle,' the maximum thickness of the leaf tip, and the physical leaf offset between closed leaf pairs are specified.[40]

2.A.5. Coupled electron-photon transport

The coupled electron-photon transport kernel in ARCHER-RT is based on the DPM open-source code.[12] Photon transport is explicitly modeled, that is, all particle interactions including those of secondary particles generated along the particle tracks are explicit and independently simulated until they reach the cutoff energy or leave the geometry. In the photon transport module, ARCHER-RT takes photoelectric effect, Compton scattering, and pair production into account. Rayleigh scattering is safely neglected since it has very little impacts on absorbed dose distributions considering the energy range used for radiation therapy (keV to 20 MeV).[12]

A Class II condensed history method is employed in ARCHER-RT for electron simulations. Class II condensed history method basically divides electron simulations into two categories: (a) Hard collisions which are simulated explicitly since they can lead to significant changes in the direction or kinetic energy of the electron, and (b) Soft collisions which are frequent interactions resulting in an energy loss below a predefined threshold and are modeled using the Continuously Slowing Down Approximation. Energy loss for soft collisions is calculated using restricted stopping powers and the direction change is calculated using the Multiple Scattering methods.[39] In this study, the energy threshold is set to 200 keV (the default value in DPM) since the range of MeV electrons being transported in soft tissues is about 1.0 mm — a typical voxel size of a patient phantom.

2.A.6. Patient modeling

ARCHER-RT consists of a DICOM processing module to parse CT images, RT plan, RT dose, and RT structure files, built on top of the DCMTK API.[41] Conversion of CT images into a patient-specific phantom is implemented according to a simplistic, four-material scheme originating from EGSnrc's "ctcreate" program which maps the Hounsfield Units (HU) of each image pixel to a density value and a material type (dry air, lung, soft tissue, or compact bone). Absolute absorbed dose calibration was performed for ARCHER-RT according to a simplified dose conversion factor expression of Popescu which ignores chamber backscatter.[40,42]

2.B. EGSnrc description

The dosimetric accuracy of ARCHER-RT was evaluated using a validated model of a flattened 6X Varian TrueBeam implemented using a coupled EGSnrc simulation using BEAMnrc "Source 21" for source modeling and DOSXYZnrc "Source 20" for in-phantom particle transport. The source models implemented in both BEAMnrc/DOSXYZnrc allow for time-dependent beam configurations. Similar to

ARCHER-RT, a patient-independent phase space generated by Constantin et al. is used as input for the BEAMnrc source model.[36] The component modules "SYNCJAWS" and "SYNCHDMLC" were used to model the jaws and HDMLC respectively. MLC-specific parameters are input into the "SYNCHDMLC" component module using data obtained from the proprietary Varian Monte Carlo data package. A workflow for extracting patient specific beam parameters was developed using the "pycom" utilities developed by Lixin Zhan.[43] This suite of utilities is specifically designed to automatically populate the BEAMnrc/DOSXYZnrc input files. EGSPHANT phantoms used in DOSXYZnrc simulations were generated using modified Computational Environment for Radiotherapy Research scripts.[44] The CT calibration curves used in the phantom generation scripts matched those input for ARCHER-RT. Absolute absorbed dose calibration was separately performed for the EGSnrc beam model according to a simplified dose conversion factor expression of Popescu which ignores chamber backscatter.[40,42]

2.C. Test cases

2.C.1. Single vs double-precision test case

Supplementing the work of Liu et al.,[30] a test case was conducted in line with Magnoux et al.[21] to compare the impact of native single-precision vs double-precision on the computational accuracy and the effectiveness of the Kahan-summation method as implemented in ARCHER-RT GPU code. A 1-MeV monoenergetic electron volumetric source (a cube of 2mm sides) was placed directly above a 10 cm^3 × 10 cm^3 × 10 cm^3 with a voxel size of 1 mm^3 × 1 mm^3 × 1 mm^3. Electrons were chosen as the simulated particle in order to isolate the electron transport in the photon–electron transport. The number of histories that was run included 7e8 particles. Absorbed dose was tallied to the phantom using three different algorithms, (a) native single-precision, (b) double-precision, and (c) single-precision utilizing the KAS algorithm. Absorbed dose differences were computed to assess the agreement between the three algorithms and timing studies were conducted to assess the performance of each algorithm. double-precision calculations were taken as the gold standard. The calculations were performed on an NVIDIA GTX 1080Ti GPU which is capable of computing all three algorithms at the hardware level; for example, software emulation of the algorithms was not conducted. The NVIDIA GTX 1080Ti is capable of 1134 GFLOPS (giga-floating point operations) in single-precision computations and 354.4 GFLOPS in double-precision computations.

2.C.2. PDD and Axial profiles

Percent depth dose (PDD) curves and lateral absorbed dose profiles in a cubic water phantom were calculated in both ARCHER-RT and EGSnrc codes. The phantom was a 40 cm^3 × 40 cm^3 × 40 cm^3 water phantom with a voxel size of 0.1 cm^3 × 0.1 cm^3 × 0.1 cm^3. The source-to-surface distance was set to 100.0 cm. For the PDD verification, open field sizes of 1.5 cm^2 x 1.5 cm^2, 3 cm^2 × 3 cm^2, 6 cm^2 × 6 cm^2, 10 cm^2 × 10 cm^2, 20 cm^2 × 20 cm^2, and 22 cm^2 x 40 cm^2 were simulated, and the absorbed dose distributions were scored using a voxel size of 0.2 cm^3 × 0.2 cm^3 × 0.2 cm^3. The lateral absorbed dose verification was performed with the open field size of 10 cm^2 × 10 cm^2 and the absorbed dose distributions are scored at different depths including 1.5, 5.0, 10.0, and 20.0 cm. The absorbed dose distributions are scored using a voxel size of 0.2 cm^3 × 0.2 cm^3 × 0.2 cm^3.

2.C.3. Picket fence test

To verify the accuracy of the HD120 MLC model, a picket fence MLC pattern was simulated in ARCHER-RT and compared against absorbed dose distributions calculated by EGSnrc. The phantom was 10 cm^3 × 10 cm^3 × 10cm^3 with a voxel size of 0.2 cm^3 × 0.2 cm^3 × 0.2 cm^3 with an SSD of 90 cm. Leaves were moved in the cross-plane direction from -5 to 5 cm in 1 cm intervals. Results were normalized to the same voxel index for both the EGS and ARCHER-RT dose grid in a region near d_{max} (e.g., voxel exposed to fluence).

2.C.4. MPPG5a test case

As an additional check to verify the accuracy of the MLC model, a static MLC pattern recommended by MPPG5a[45] for treatment planning system commissioning was simulated in ARCHER-RT and compared against absorbed dose distributions calculated by EGSnrc. The phantom was 10 cm^3 × 10 cm^3 × 10 cm^3 with a voxel size of 0.2 cm^3 × 0.2 cm^3 × 0.2 cm^3. To quantify the differences, an absolute absorbed dose difference and 3D gamma test were calculated.

2.C.5. VMAT

A clinical prostate VMAT treatment plan was calculated in ARCHER-RT, and EGSnrc to evaluate ARCHER-RT capability of clinical treatment plan absorbed dose calculations. The voxel size used in the simulation was 0.25 cm^3 × 0.25 cm^3 × 0.25cm^3. Sufficient histories were simulated to ensure the relative standard deviation of critical regions, that is, the uncertainty for voxels with absorbed dose greater than 20% was under 1.7% in ARCHER-RT. Absorbed dose difference and 3D gamma tests were performed to evaluate the dosimetric accuracy of ARCHER-RT.

2.D. VMAT efficiency studies

Timing studies were conducted to evaluate the relative speed of ARCHER-RT being executed under three different

hardware architectures: (a) an Intel i7-8700K CPU with six cores (12 hardware threads), (b) an NVIDIA 1080Ti GPU with 28 streaming multiprocessors and 11GB GDDR5X memory, and (c) an AMD Vega 56 GPU with 56 compute units and 8GB HBM2 memory. The host system has 16GB DDR4 memory and a solid-state drive (SSD). Timing of different modules in ARCHER-RT (i.e., time to read the phase space file, time for source modeling execution, and time for particle transport in the patient) was also investigated. Timing studies were also conducted on the VMAT plan to compare the relative speed of the computation conducted in native single-precision, KAS single-precision, and double-precision.

3. RESULTS

3.A. Single vs double-precision test case

Figure 2(a) depicts the absorbed dose distribution of the test case executed in double-precision, Fig. 2(b) depicts the difference between the test case executed in native single-precision vs double-precision, and Fig. 2(c) depicts the difference between the test case executed utilizing the KAS single-precision algorithm vs double-precision. The results of the test case in Fig. 2 are presented for a 20 mm^2 × 20 mm^2 subsection of the phantom for a slice 2mm from the source. The results presented are for voxels that are close to the source and as expected, these voxels will be accessed and written to most, thus creating a scenario to highlight numerical truncation errors. A maximum difference of 71.73% between the native single and double-precision case was calculated. In the second case where KAS was implemented, the maximum difference between KAS and double-precision was less than 0.01%. The native single-precision, KAS single-precision, and double-precision took 39, 55, and 70 s, respectively to calculate. The results both confirm the findings of Liu[30] and Magnoux[21] and proffer a solution to the inaccuracies of the native single-precision atomic-add method through the implementation of the KAS atomic-add algorithm.

3.B. PDD and Axial profiles

Figure 3 compares relative depth dose and lateral dose profiles for ARCHER-RT and EGSnrc. Absorbed doses are normalized to the maximum absorbed dose of the 10 cm^2 × 10 cm^2 PDD field on the central axis. Outside the buildup region for the PDDs, there was less than 3% difference between the two codes for all points. Similarly, outside the penumbra region there was less than 2% difference for all points in the axial profiles. The large difference between the two codes in the buildup region of the PDDs could be that ARCHER-RT transports only photons in the beam collimation routines (Note: ARCHERRT transports both photons and electrons inside the patient), whereas EGSnrc transports both photons and electrons in beam collimation routines. It is also possible that the buildup region of the PDD, a region with a large gradient, contain large local absolute differences. Either of these are plausible explanations for the underestimation of the absorbed dose in the buildup region for static beam configurations as demonstrated in the PDDs. The latter reason is certainly applicable for the differences noted in the axial profiles; large differences are only seen in the penumbra region.

3.C. Picket fence test

Figure 4 depicts the calculated cross-plane dose profile on the central axis of the in-plane direction and at a depth of 5 cm for the picket fence test demonstrating good agreement in the MLC model between ARCHER-RT and EGSnrc. Slight differences in the in-field scatter are likely attributable to the difference fluence models each code uses; EGSnrc models the MLC geometry explicitly while ARCHER-RT uses an approximate form of the MLC. Slight differences in the out-of-field scatter are likely attributable to ARCHER-RT's use of the first Compton scatter approximation for MLC photon transport.

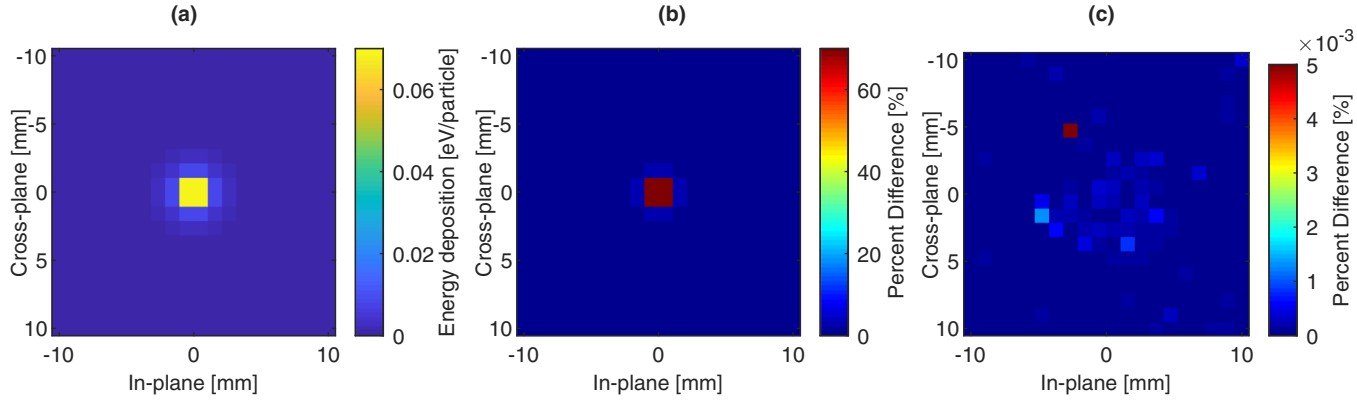

FIG. 2. Results from the test case (a) absorbed dose distribution of the case run in double-precision, (b) relative difference (data shown in percent difference) between native single-precision and double-precision and (c) the relative difference between KAS single-precision and double-precision. The figure is displaying data in a slice 2mm from the surface of the phantom. Note the scales for the relative difference between (b) and (c) are dramatically different to highlight differences. [Color figure can be viewed at wileyonlinelibrary.com]

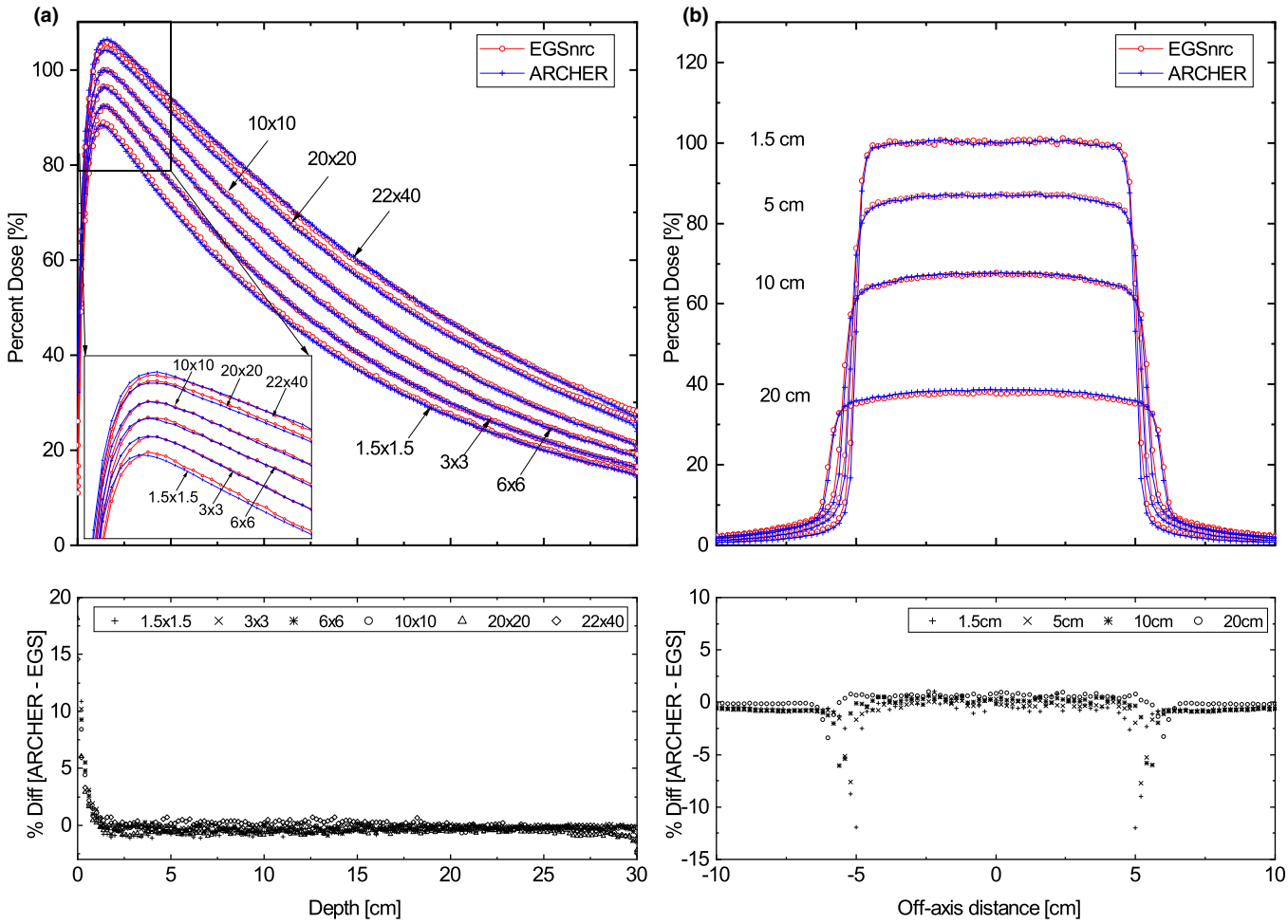

FIG. 3. Comparison of percent depth dose and lateral dose profiles for ARCHER-RT and EGSnrc. (a) percent depth dose and calculated differences and (b) axial profiles and calculated differences for a 10 cm^2 × 10 cm^2 field at depths of 1.5, 5, 10, and 20 cm. [Color figure can be viewed at wileyonlinelibrary.com]

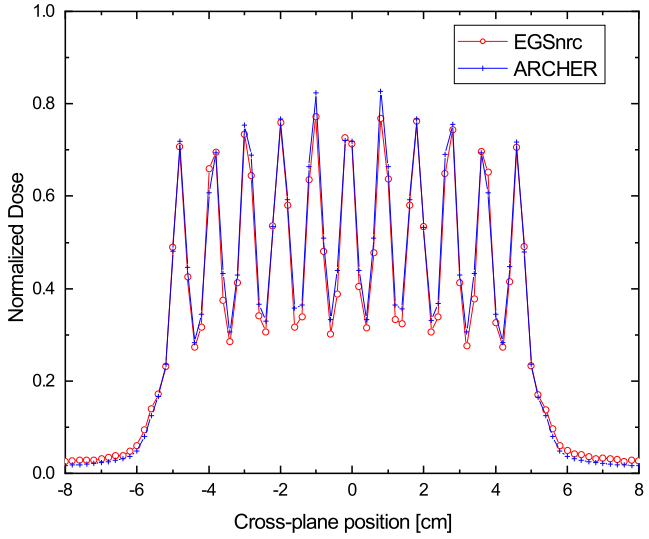

FIG. 4. Comparison of the picket-fence test for ARCHER-RT and EGSnrc. [Color figure can be viewed at wileyonlinelibrary.com]

3.D. MPPG5a test case

Figure 5 depicts the calculated absorbed dose for the MPPG5a clinical test plan for (a)–(c) ARCHER-RT, and (d)–(f) the absolute difference between the two (EGSnrc-ARCHER-RT), demonstrating good qualitative agreement between ARCHER-RT and EGSnrc. A gamma index test is performed for voxels equal to or greater than 20% of the maximum absorbed dose to quantitatively evaluate the agreement between the two codes. The passing rate is found to be 94.2% for 3%/3 mm criterion and 86.4% for 2%/2 mm, thus further confirming the agreement of these two codes and the accuracy of the HD120 MLC model. Similar to that for the PDDs, the difference between the two codes near the surface of the phantom in the electron contamination region could be that ARCHER-RT transports only photons in the beam collimation routines, whereas EGSnrc transports both photons and electrons in all media and the buildup region is a region with a large gradient. Either of these are plausible explanations for the underestimation of the absorbed dose in the surface contamination region for static beam configurations by ARCHER-RT as shown in Figs. 5(e) and 5(f).

3.E. VMAT

Figure 6 depicts the calculated absorbed dose for the clinical VMAT plan for (a)–(c) ARCHER-RT, and (d)–(f) the absolute difference between the two (EGSnrc- ARCHER-RT). From these visual inspections, it is clear that ARCHER-RT and EGSnrc agree well. A gamma index test was performed for voxels equal to or greater than 20% of the maximum absorbed dose to quantitatively evaluate the agreement between the two codes. The passing rate was 98.35% for 3%/3mm criterion, suggesting that the accuracy of ARCHER-RT is satisfactory. Furthermore, Fig. 7 depicts the dose volume histogram (DVH) for the VMAT prostate case including the PTV, and organs at risk including the bladder, rectum, femoral heads, and penile bulb. It can be seen that these two codes agree with each other very well. The penile bulb showed the most notable difference between the two codes, likely because the volume of the ROI is quite small and thus will manifest in exaggerated differences on a DVH plot.

3.F. VMAT efficiency studies

A comparison of the total wall time and execution time of different modules in ARCHER-RT for the Intel CPU, NVIDIA GPU, and AMD GPU conducted on the clinical VMAT prostate plan are presented in Table I. ARCHER-RT was compiled with the fast-math flag and executed using single-precision atomic-add methods for the timing studies presented. While these two options may theoretically limit the accuracy of the absorbed dose accumulation, the agreement to EGSnrc indicated the computational approximations were valid. Statistical uncertainties are kept under 1.7% for critical absorbed dose regions, that is, for voxels with absorbed dose greater than or equal to 20% of D_{max}. The NVIDIA 1080Ti card executed the fastest and completed the absorbed dose calculation in 50.3 s. This time was 4.3x faster than the i7-8700K CPU and 3.7x faster than the AMD Vega 56 GPU. In theory, the AMD GPU has competitive computing power with NVIDIA GPU, but it seriously underperformed in our analysis primarily due to identified deficiencies within the compiler. Specifically, the AMD hcc compiler generates a hanging kernel code for particle transport in patient. A workaround was utilized by combining several C++ classes in the kernel into one large class, but the GPU register spill resulted in a side effect causing remarkable performance degradation. Overall, the most time-consuming part was the Monte Carlo particle transport in the patient, which is expected considering the heterogeneities and dimension of the patient phantom.

There were no voxel level dosimetric differences in excess of 0.01% between native single-precision, KAS single-precision, and double-precision; however, there were differences in the timing studies. The major difference in timing between the three cases was the patient transport time; the other routines took approximately the same amount of time. The patient transport time for the native single-precision case took 25.6 s and was 3.04x faster than that for double-precision, which took 77.9 s, whereas the KAS single-precision case took

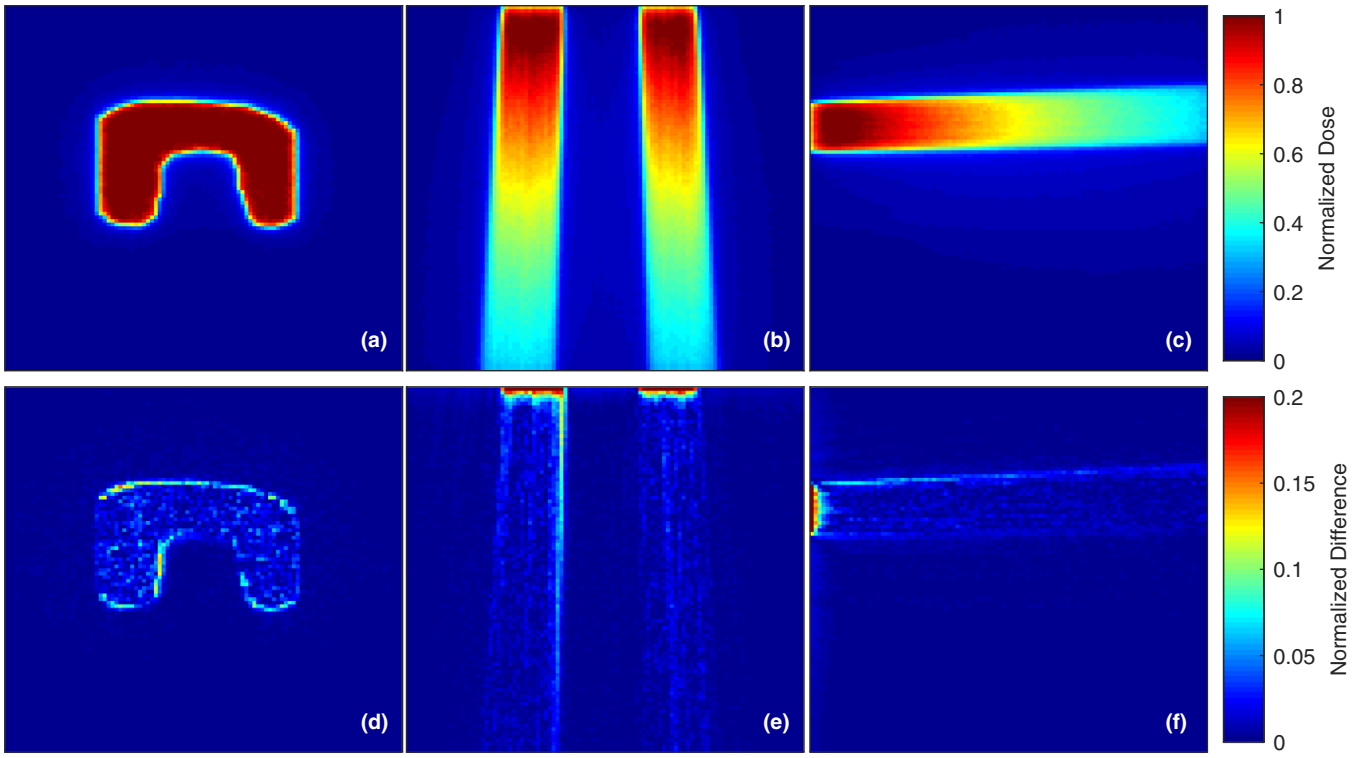

FIG. 5. Visual inspection of absorbed dose distributions of two codes for the MPPG5a test plan showing excellent agreement. (a)–(c) ARCHER-RT, and (d)–(f) absolute difference (EGSnrc-ARCHER-RT). [Color figure can be viewed at wileyonlinelibrary.com]

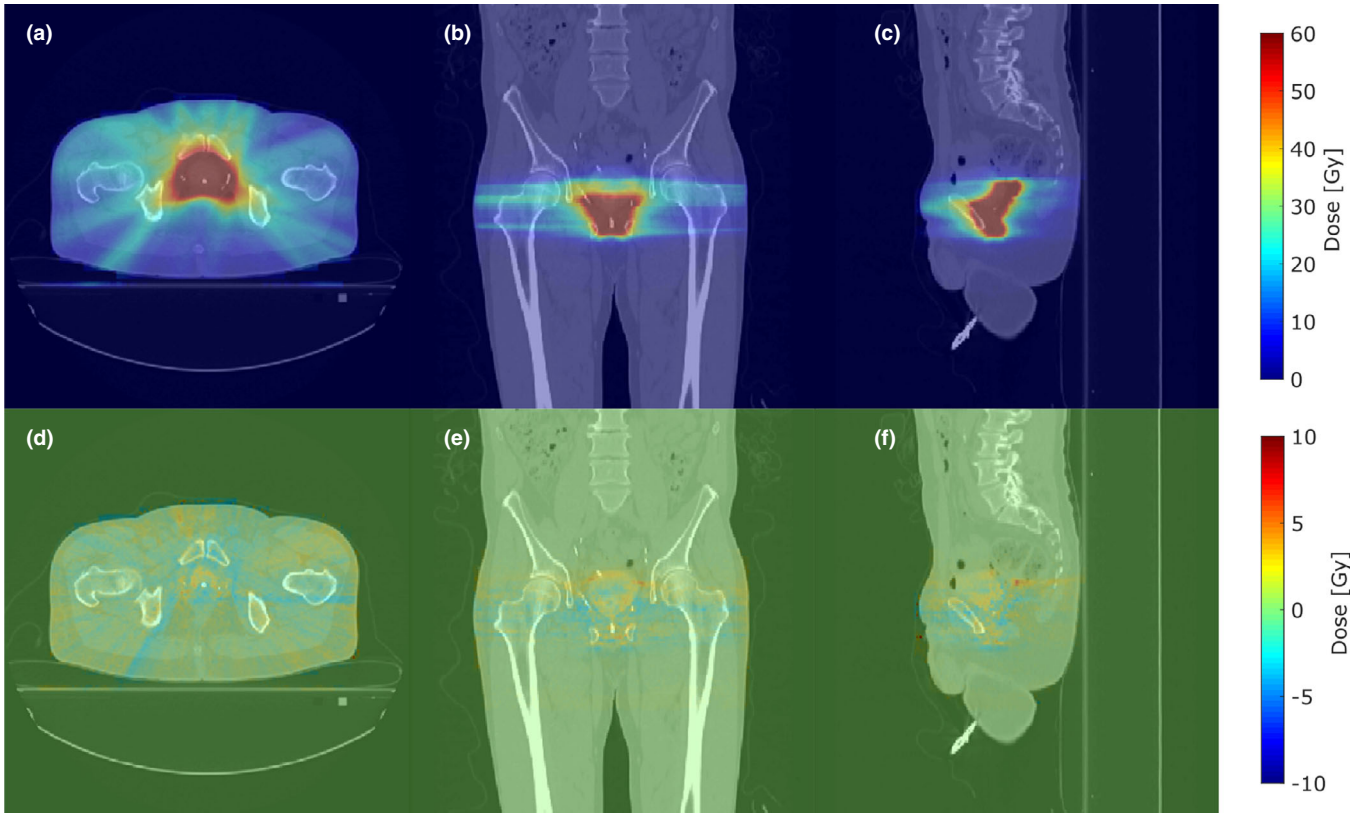

FIG. 6. Clinical VMAT prostate calculated absorbed dose distributions showing excellent agreement of two codes. (a)–(c) ARCHER-RT, and (d)–(f) absolute difference (EGSnrc-ARCHER-RT). [Color figure can be viewed at wileyonlinelibrary.com]

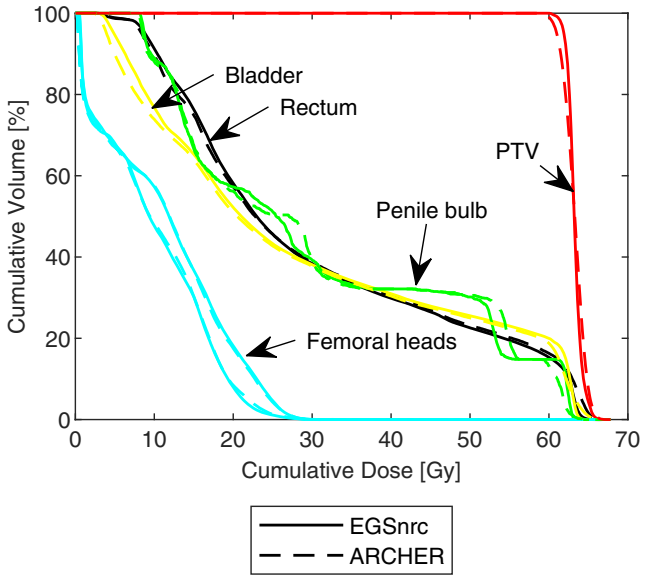

FIG. 7. Dose volume histogram comparison between ARCHER-RT and EGSnrc for the VMAT prostate case showing excellent agreement between the two MC codes. [Color figure can be viewed at wileyonlinelibrary.com]

30.1 s and thus was 2.59x faster than the double-precision case. The results indicate there is a small performance penalty in the use of the KAS single-precision algorithm but in accordance with the results of the test case, ensures there is computational accuracy.

TABLE I. Architecture timing results for the ARCHER-RT simulation of the VMAT prostate plan.

Architecture	Total wall time (s)	PSF reading time (s)	Linac transport time (s)	Patient transport time (s)
Intel i7-8700K CPU	216.8	3.1	100.8	108.2
NVIDIA 1080Ti GPU	50.3	3.4	16.8	25.6
AMD Vega 56 GPU	187.9	3.3	28.0	151.6

4. DISCUSSION

This work demonstrates that ARCHER-RT is a versatile, cross-platform Monte Carlo absorbed dose calculation engine and is compatible with multiple hardware architectures in the clinical setting. We have benchmarked ARCHER-RT by comparing calculated absorbed dose distributions to results from EGSnrc. With an NVIDIA GPU, we demonstrated that a clinical VMAT prostate case can be executed in less than 51 s and dosimetrically verified its results against well-benchmarked codes. Source modeling has been implemented in ARCHER-RT in which patient-independent phase spaces are used as input for transporting particles through secondary X/Y jaws and MLCs. The Siebers-Keall first Compton-based approximate transport method is used to balance the accuracy of source term representation and sampling efficiency. The

results reported in this work indicate that the source modeling implementation is accurate and reproducible.

Cross platform compatibility is an important feature for clinical deployment onto different computing architectures. Previous groups have implemented OpenCL to employ cross-platform compatibility; however, OpenCL is currently deprecated on MacOS. We implemented HIP for cross platform compatibility so that that ARCHER-RT can run on CPUs, and both AMD and NVIDIA GPUs. While HIP allows for cross-GPU compatibility, the AMD GPU implementation seriously underperformed because of two unresolved inadequacies currently residing in the HIP compiler. Specifically, the compiler cannot correctly handle a C++ "aggregation" class where, for instance, class A references external objects B, C, D by pointers. The compiled binary crashes upon execution. A workaround is to switch the design to a C++ "composition" class where objects B, C, D are instantiated inside of A as a data member. The downside of this workaround is that the size of class A is inflated by a large degree, causing register spills, a common culprit for GPU performance degradation. The second shortcoming of the compiler we have found is that the HIP compiler cannot correctly handle in branch code the warp vote functions, which constitute the centerpiece of our WAG and KAS algorithms for fast atomic-add tallies.[30] The only viable workaround is to switch back to the slow, default CAS algorithm for absorbed dose accumulation. These slower execution times on AMD GPUs are similar to other studies in which HIP was utilized.[46] While we have successfully implemented a cross-platform code, further performance increases will come from architecture-specific algorithmic development and HIP API maturation.

The motivation behind the test case comparing the accuracy and performance of native single-precision, double-precision, and KAS single-precision was to proffer a better solution to that offered by Magnoux than the software emulation of double-precision computational methods. The test case is indeed an idealized case enacted to demonstrate a scenario in which native single-precision is inadequate and large dosimetric differences are present. The reason there are greater voxel-level discrepancies between atomic-add methods in the test electron case is simply because there is a greater frequency of voxel-specific interactions (voxels near the source) thus leading to more opportunity for voxel specific truncation errors. This is in contrast to the VMAT case in which the spatial distribution of interacting photons is much more diffuse. While there was little dosimetric difference between the different algorithms in the VMAT case, the identification and implementation of algorithms to ensure computational accuracy are an important consideration in the software development of a Monte Carlo absorbed dose engine such as ARCHER-RT and there could be clinical scenarios in which this may be important. Additionally, the implementation of KAS is important to preserve the accuracy on all NVIDIA and AMD devices, some of which do not support double-precision calculations at the hardware level. The timing results of each algorithm showed there is some penalty in performance utilizing KAS over native single-precision, but it is a small price compared to the software emulation of double-precision as described by Magnoux. There was a smaller performance penalty in utilizing KAS over single-precision for the VMAT case in comparison to the test electron case. Theoretically the penalty should be the same for every dose accumulation event, but this discrepancy between the two cases is simply because the electron case only transported electrons, whereas the VMAT case included coupled photon–electron transport and thus the dose deposition (electron transport) was only a portion of the particle transport in the VMAT case.

ARCHER-RT was validated by comparing against a validated EGSnrc TrueBeam model. Benchmarking tests included PDD and axial profiles, an MPPG5a MLC test shape, and a clinical prostate VMAT plan. The agreement was quantitatively evaluated using absorbed dose differences and gamma tests. PDD's for both ARCHER-RT and EGSnrc was found to match within 3%. Slight differences between ARCHER-RT and EGSnrc in the MPPG5a static beam case are attributable to how the MLC geometry is specified in each code package and because ARCHER-RT does not include the source modeling of electrons. EGSnrc explicitly models the HDMLC in entirety including small features like tongue and groove, whereas ARCHER-RT's MLC model is based upon that described by Siebers and Keall and represents the complexity of the MLC's geometry by breaking down the MLC into simple geometrical regions.[37] The rationale for using the MLC representation described by Siebers and Keall was to simplify the radiation transport calculation for complex IMRT beam delivery; small differences in individual beamlets effectively "wash-out" in evaluating full IMRT deliveries because the average interaction probability is determined by evaluating the probability of an incident particle in the MLC multiple times. This lends itself to systemic MLC collimator edge differences between ARCHER-RT and EGSnrc as depicted in Figs. 5(d)–5(f). Considering these slight deficiencies, they were shown to be acceptable approximations. As demonstrated in the clinical VMAT plan results, individual beamlet differences do effectively cancel each other out and patient surface absorbed dose differences are not appreciable.

There are known limitations of utilizing the gamma test to compare Monte Carlo dose distributions. These limitations are generally influenced by the presence of statistical noise, especially in low dose gradient regions.[47,48] We have run enough particles for each scenario in which the gamma test is used such that we can be confident the gamma test is an accurate representation of the agreement between the two codes.[49]

5. CONCLUSIONS

ARCHER-RT's capabilities have been dramatically extended from the previous publication to include newer modalities, and, with these improvements, the accuracy, speed, and computational precision have been demonstrated in this work through the modeling and benchmarking of a flattened photon 6 MV Varian TrueBeam. ARCHER-RT

fulfills the clinical requirements of fast yet accurate radiation dose calculation that are essential for absorbed dose engines to be introduced into clinical workflows. There are examples today for how a Monte Carlo absorbed dose engine like ARCHER-RT can be adapted into the clinical workflow as part of the Monte Carlo-based treatment planning system. Under this auspice, this work demonstrates the significant addition of functionality to ARCHER-RT framework which has marked utility for both research and clinical applications.

ACKNOWLEDGMENTS

This project was supported by NIH/NIBIB (R42EB019265-01A1) and NIH SPORE CA196513-01. We would like to thank the anonymous reviewers and associate editor for carrying out an extremely thorough review that has helped improve the quality and impact of this manuscript.

CONFLICT OF INTEREST

X. George Xu is a cofounder of Virtual Phantoms, Inc (Albany, New York) that commercializes software technologies—VirtualDose™ for medical CT dose reporting and ARCHER™ for real-time Monte Carlo dose computing.

[a)]Author to whom correspondence should be addressed. Electronic mail: xug2@rpi.edu

REFERENCES

1. Delaney G, Jacob S, Featherstone C, Barton M. The role of radiotherapy in cancer treatment: estimating optimal utilization from a review of evidence-based clinical guidelines. *Cancer*. 2005;104:1129–1137.
2. Rogers DWO. Fifty years of Monte Carlo simulations for medical physics. *Phys Med Biol*. 2006;51:R287–R301.
3. Kawrakow I.The EGSnrc Code System, Monte Carlo simulation of electron and photon transport. NRCC Rep. PIRS-701, 2001.
4. Kawrakow I, Walters BRB. Efficient photon beam dose calculations using DOSXYZnrc with BEAMnrc. *Med Phys*. 2006;33:3046–3056.
5. Forster RA, et al. MCNP™ Version 5. *Nucl Instrum Methods Phys Res Sect B Beam Interact Mater Atoms*. 2004;213:82–86.
6. Lewis RD, Ryde SJS, Hancock DA, Evans CJ. An MCNP-based model of a linear accelerator x-ray beam. *Phys Med Biol*. 1999;44:1219–1230.
7. Mesbahi A, Reilly AJ, Thwaites DI. Development and commissioning of a Monte Carlo photon beam model for Varian Clinac 2100EX linear accelerator. *Appl Radiat Isot*. 2006;64:656–662.
8. Baró J, Sempau J, Fernández-Varea JM, Salvat F. PENELOPE: An algorithm for Monte Carlo simulation of the penetration and energy loss of electrons and positrons in matter. *Nucl Instrum Methods Phys Res Sect B Beam Interact Mater Atoms*. 1995;100:31–46.
9. Sempau J, Badal A, Brualla L. A PENELOPE -based system for the automated Monte Carlo simulation of clinacs and voxelized geometries-application to far-from-axis fields. *Med Phys*. 2011;38:5887–5895.
10. Agostinelli S, et al. Geant4—a simulation toolkit. *Nucl Instrum Methods Phys Res Sect A Accel Spectrom Detect Assoc Equip*. 2003;506:250–303.
11. Grevillot L, Frisson T, Maneval D, Zahra N, Badel J-N, Sarrut D. Simulation of a 6 MV Elekta Precise Linac photon beam using GATE/GEANT4. *Phys Med Biol*. 2011;56:903–918.
12. Sempau J, Wilderman SJ, Bielajew AF. DPM, a fast, accurate Monte Carlo code optimized for photon and electron radiotherapy treatment planning dose calculations. *Phys Med Biol*. 2000;45:2263–2291.
13. Kawrakow I. VMC++, Electron and Photon Monte Carlo Calculations Optimized for Radiation Treatment Planning, In *Advanced Monte Carlo for Radiation Physics, Particle Transport Simulation and Applications*. Berlin, Heidelberg: Springer Berlin Heidelberg. 2001;pp. 229–236.
14. Ma C-M, et al. A Monte Carlo dose calculation tool for radiotherapy treatment planning. *Phys Med Biol*. 2002;47:305.
15. Jia X, Gu X, Graves YJ, Folkerts M, Jiang SB. GPU-based fast Monte Carlo simulation for radiotherapy dose calculation. *Phys Med Biol*. 2011;56:7017–7031.
16. Jia X, Ziegenhein P, Jiang SB. GPU-based high-performance computing for radiation therapy. *Phys Med Biol*. 2014;59:R151–R182.
17. Jahnke L, Fleckenstein J, Wenz F, Hesser J. GMC: a GPU implementation of a Monte Carlo dose calculation based on Geant4. *Phys Med Biol*. 2012;57:1217–1229.
18. Hissoiny S, Ozell B, Bouchard H, Després P. GPUMCD: a new GPU-oriented Monte Carlo dose calculation platform. *Med Phys*. 2011;38:754–764.
19. Townson RW, Jia X, Tian Z, Graves YJ, Zavgorodni S, Jiang SB. GPU-based Monte Carlo radiotherapy dose calculation using phase-space sources. *Phys Med Biol*. 2013;58:4341–4356.
20. Tian Z, Graves YJ, Jia X, Jiang SB. Automatic commissioning of a GPU-based Monte Carlo radiation dose calculation code for photon radiotherapy. *Phys Med Biol*. 2014;59:6467–6486.
21. Magnoux V, Ozell B, Bonenfant É, Després P. A study of potential numerical pitfalls in GPU-based Monte Carlo dose calculation. *Phys Med Biol*. 2015;60:5007–5018.
22. Liu T, Xu XG, Carothers CD. Comparison of two accelerators for Monte Carlo radiation transport calculations, Nvidia Tesla M2090 GPU and Intel Xeon Phi 5110p coprocessor: a case study for X-ray CT imaging dose calculation. *Ann Nucl Energy*. 2015;82:230–239.
23. Tian Z, Shi F, Folkerts M, Qin N, Jiang SB, Jia X. A GPU OpenCL based cross-platform Monte Carlo dose calculation engine (goMC). *Phys Med Biol*. 2015;60:7419–7435.
24. Tian Z, Li Y, Hassan-Rezaeian N, Jiang SB, Jia X. Moving GPU-OpenCL-based Monte Carlo dose calculation toward clinical use: Automatic beam commissioning and source sampling for treatment plan dose calculation. *J Appl Clin Med Phys*. 2017;18:69–84.
25. Su L, Yang Y, Bednarz B, et al. ARCHERRT- A GPU-based and photon-electron coupled Monte Carlo dose computing engine for radiation therapy: software development and application to helical tomotherapy. *Med Phys*. 2014;41:1–13.
26. Liu T. Development of ARCHER — a Parallel Monte Carlo Radiation Transport Code — for X-Ray CT Dose Calculations Using GPU and Coprocessor Technologies. Rensselaer Polytechnic Institute. 2014.
27. Su L. Development and application of a GPU-based fast electron-photon coupled monte carlo code for radiation therapy by major subject: nuclear engineering. Rensselaer Polytechnic Institute. 2014.
28. Lin H. GPU-Based Monte Carlo Source Modeling and Simulation for Radiation Therapy Involving Varian TrueBeam LINAC. Rensselaer Polytechnic Institute. 2018.
29. AMD. HIP Programming Guide. 2019. Available: https://rocm-documentation.readthedocs.io/en/latest/Programming_Guides/HIP-GUIDE.html Accessed: 28-Apr-2019.
30. Liu T, Wolfe N, Lin H, Carothers CD, Xu XG. Performance study of atomic tally methods for GPU-accelerated Monte Carlo dose calculation. in 20th Topical Meeting of the Radiation Protection and Shielding Division of the American Nuclear Society. 2018.
31. Adinets A. "CUDA Pro Tip: optimized Filtering with Warp-Aggregated Atomics", 2014. [Online]. Available: https://devblogs.nvidia.com/cuda-pro-tip-optimized-filtering-warp-aggregated-atomics/ [Accessed: 16-Sep-2019].
32. Westphal E. "Voting and Shuffling to Optimize Atomic Operations", 2015. [Online]. Available: https://devblogs.nvidia.com/voting-and-shuffling-optimize-atomic-operations/ [Accessed: 16-Sep-2019].
33. Bossler KL. "Methods for Computing Monte Carlo Tallies on the Gpu", PHYSOR 2018 React. Phys. Paving W. Towar. More Effic. Syst., pp. 166–177, 2018.
34. Kahan W. Pracniques: further remarks on reducing truncation errors. *Commun ACM*. 1965;8:40.
35. Chetty IJ, Curran B, Cygler JE, et al. Report of the AAPM Task Group No. 105: issues associated with clinical implementation of Monte Carlo-

based photon and electron external beam treatment planning. *Med Phys*. 2007;34:4818–4853.
36. Constantin M, Perl J, LoSasso T, et al. Modeling the TrueBeam linac using a CAD to Geant4 geometry implementation: dose and IAEA-compliant phase space calculations. *Med Phys*. 2011;38:4018–4024.
37. Siebers JV, Keall PJ, Kim JO, Mohan R. A method for photon beam Monte Carlo multileaf collimator particle transport. *Phys Med Biol*. 2002;47:3225–3249.
38. Keall PJ, Siebers JV, Arnfield M, Kim JO, Mohan R. Monte Carlo dose calculations for dynamic IMRT treatments. *Phys Med Biol*. 2001;46:929–941.
39. Turner JE. *Atoms, Radiation, and Radiation Protection*. Hoboken, NJ: Wiley; 2007.
40. Bergman AM, Gete E, Duzenli C, Teke T. Monte Carlo modeling of HD120 multileaf collimator on Varian TrueBeam linear accelerator for verification of 6X and 6X FFF VMAT SABR treatment plans. *J Appl Clin Med Phys*. 2014;15:148–163.
41. Eichelberg M, Riesmeier J, Wilkens T, Hewett AJ, Barth A, Jensch P. Ten years of medical imaging standardization and prototypical implementation: the DICOM standard and the OFFIS DICOM toolkit (DCMTK). *Med Imaging*. 2004;5371:57.
42. Popescu IA, Shaw CP, Zavgorodni SF, Beckham WA. Absolute dose calculations for Monte Carlo simulations of radiotherapy beams. *Phys Med Biol*. 2005;50:3375–3392.
43. Zhan L. pycom –- Python DICOM Processing Toolkit. 2013.
44. Deasy JO, Blanco AI, Clark VH. CERR: a computational environment for radiotherapy research. *Med Phys*. 2003;30:979–985.
45. Jacqmin DJ, Bredfeldt JS, Frigo SP, Smilowitz JB. Implementation of the validation testing in MPPG 5.a 'Commissioning and QA of treatment planning dose calculations–megavoltage photon and electron beams'. *J Appl Clin Med Phys*. 2017;18:115–127.
46. Dong T, Haidar A, Tomov S, Dongarra J. Accelerating the SVD bi-diagonalization of a batch of small matrices using GPUs. *J Comput Sci*. 2018;26:237–245.
47. Low DA. Gamma dose distribution evaluation tool. *J Phys Conf. Ser.* 2010;250:349–359.
48. Low DA, Dempsey JF. Evaluation of the gamma dose distribution comparison method. *Med Phys*. 2003;30:2455–2464.
49. Graves YJ, Jia X, Jiang SB. Effect of statistical fluctuation in Monte Carlo based photon beam dose calculation on gamma index evaluation. *Phys Med Biol*. 2013;58:1839–1853.

A method of rapid quantification of patient-specific organ doses for CT using deep-learning-based multi-organ segmentation and GPU-accelerated Monte Carlo dose computing

Zhao Peng
Department of Engineering and Applied Physics, University of Science and Technology of China, Hefei, Anhui 230026, China

Xi Fang, Pingkun Yan and Hongming Shan
Department of Biomedical Engineering, Rensselaer Polytechnic Institute, Troy, NY 12180, USA

Tianyu Liu
Department of Mechanical, Aerospace and Nuclear Engineering, Rensselaer Polytechnic Institute, Troy, NY 12180, USA

Xi Pei
Department of Engineering and Applied Physics, University of Science and Technology of China, Hefei, Anhui 230026, China
Anhui Wisdom Technology Company Limited, Hefei, Anhui 238000, China

Ge Wang
Department of Biomedical Engineering, Rensselaer Polytechnic Institute, Troy, NY 12180, USA

Bob Liu and Mannudeep K. Kalra
Department of Radiology, Massachusetts General Hospital, Boston, MA 02114, USA

X. George Xu[a)]
Department of Biomedical Engineering, Rensselaer Polytechnic Institute, Troy, NY 12180, USA
Department of Mechanical, Aerospace and Nuclear Engineering, Rensselaer Polytechnic Institute, Troy, NY 12180, USA

(Received 1 October 2019; revised 6 February 2020; accepted for publication 29 February 2020; published 3 April 2020)

Purpose: One technical barrier to patient-specific computed tomography (CT) dosimetry has been the lack of computational tools for the automatic patient-specific multi-organ segmentation of CT images and rapid organ dose quantification. When previous CT images are available for the same body region of the patient, the ability to obtain patient-specific organ doses for CT — in a similar manner as radiation therapy treatment planning — will open the door to personalized and prospective CT scan protocols. This study aims to demonstrate the feasibility of combining deep-learning algorithms for automatic segmentation of multiple radiosensitive organs from CT images with the GPU-based Monte Carlo rapid organ dose calculation.

Methods: A deep convolutional neural network (CNN) based on the U-Net for organ segmentation is developed and trained to automatically delineate multiple radiosensitive organs from CT images. Two databases are used: The lung CT segmentation challenge 2017 (LCTSC) dataset that contains 60 thoracic CT scan patients, each consisting of five segmented organs, and the Pancreas-CT (PCT) dataset, which contains 43 abdominal CT scan patients each consisting of eight segmented organs. A fivefold cross-validation method is performed on both sets of data. Dice similarity coefficients (DSCs) are used to evaluate the segmentation performance against the ground truth. A GPU-based Monte Carlo dose code, ARCHER, is used to calculate patient-specific CT organ doses. The proposed method is evaluated in terms of relative dose errors (RDEs). To demonstrate the potential improvement of the new method, organ dose results are compared against those obtained for population-average patient phantoms used in an off-line dose reporting software, VirtualDose, at Massachusetts General Hospital.

Results: The median DSCs are found to be 0.97 (right lung), 0.96 (left lung), 0.92 (heart), 0.86 (spinal cord), 0.76 (esophagus) for the LCTSC dataset, along with 0.96 (spleen), 0.96 (liver), 0.95 (left kidney), 0.90 (stomach), 0.87 (gall bladder), 0.80 (pancreas), 0.75 (esophagus), and 0.61 (duodenum) for the PCT dataset. Comparing with organ dose results from population-averaged phantoms, the new patient-specific method achieved smaller absolute RDEs (mean ± standard deviation) for all organs: 1.8% ± 1.4% (vs 16.0% ± 11.8%) for the lung, 0.8% ± 0.7% (vs 34.0% ± 31.1%) for the heart, 1.6% ± 1.7% (vs 45.7% ± 29.3%) for the esophagus, 0.6% ± 1.2% (vs 15.8% ± 12.7%) for the spleen, 1.2% ± 1.0% (vs 18.1% ± 15.7%) for the pancreas, 0.9% ± 0.6% (vs 20.0% ± 15.2%) for the left kidney, 1.7% ± 3.1% (vs 19.1% ± 9.8%) for the gallbladder, 0.3% ± 0.3% (vs 24.2% ± 18.7%) for the liver, and 1.6% ± 1.7% (vs 19.3% ± 13.6%) for the stomach. The trained automatic segmentation tool takes <5 s per patient for all 103 patients in the dataset. The Monte Carlo radiation dose calculations performed in parallel to the segmentation process using the

GPU-accelerated ARCHER code take <4 s per patient to achieve <0.5% statistical uncertainty in all organ doses for all 103 patients in the database.
Conclusion: This work shows the feasibility to perform combined automatic patient-specific multi-organ segmentation of CT images and rapid GPU-based Monte Carlo dose quantification with clinically acceptable accuracy and efficiency. © *2020 American Association of Physicists in Medicine* [https://doi.org/10.1002/mp.14131]

Key words: convolutional neural network, CT organ dose, Monte Carlo, multi-organ segmentation, patient-specific

1. INTRODUCTION

In the United States, the number of computed tomography (CT) examinations increased drastically between the 1980s and 2010s due to rapid improvements in multidetector CT (MDCT) technologies.[1–3] In 2018, about 88.7 million CT examinations were performed in the United States alone, which represented a substantial increase from 21 million exams in 1995.[4] The abdomen and chest regions represent the most frequently scanned body regions, accounting for more than a third of all CT examinations. Given the rising use of CT and concerns over associated radiation risks, the American College of Radiology (ACR) has called for more research and development in patient-specific dose quantification, scanner optimization, and protocol comparison.[1]

Computed tomography dose index volume (CTDIvol) and dose length product (DLP) are technical dose descriptors and do not represent or take into account patient body habitus (size or shape), attenuation, scanned anatomy, age, gender, or actually absorbed radiation doses.[5] Although CTDIvol and DLP provide a good way to compare scanners and scan protocols, they cannot be used to compare, monitor, or assess patient-specific radiation doses from CT. For this reason, size-specific dose estimates (SSDE) have been recommended as an improved approach that take into account patient body habitus.[6] Many methods of generating organ-specific CT dose databases have been reported.[7–15] These methods require Monte Carlo simulations of CT scanner components as well as radiation interactions with whole-body computational phantoms that contain organs/tissues explicitly defined in tiny voxels in accordance with the "Reference-Man" concept — population-averaged anatomical parameters originally defined for radiation protection purposes.[16] However, the process that is required to create such whole-body phantoms is prohibitively complex for routine analysis of patient-specific images. As a result, most clinical end users can only perform CT organ dose assessment using "off-line" software tools, such as VirtualDose,[15] which are based on databases precalculated from a library of population-averaged phantoms. In contrast, in radiation treatment planning, we routinely delineate the target volume and adjacent healthy organs at risk (OARs) using patient-specific images, before performing rapid dose calculation and inverse treatment plan optimization to minimize normal tissue complication probability (NTCP).[17–19] Patient-specific organ dose computing methods already exist. Recently, GPU-based Monte Carlo dose computing codes, including ARCHER,[20,21] for example, have achieved clinically acceptable speeds for both patient CT imaging dose assessment and for treatment planning.

Rising CT utilization has also heightened the concern that patients accrue large cumulative doses from recurrent CT imaging. Sodickson et al. performed a cohort study of 31 462 patients who underwent diagnostic CT in 2007 and had undergone 190 712 CT examinations over the prior 22 yr.[22] The authors discovered that 33% of patients underwent five or more lifetime CT examinations and that 5% of patients underwent between 22 and 132 examinations, leading to the conclusion of the study that, while most patients accrue low radiation-induced cancer risks, a subgroup is potentially at higher risk due to recurrent CT imaging. A recent survey performed in 2019 on 90 146 CT patients at Massachusetts General Hospital found that about 63% of chest scan patients have received at least one previous CT scan between 2014 and 2019.[23] The percentage for recurrent abdomen/pelvis scan patients is 50% and is 40% for head-scan patients. Approximately 50% of patients in the US undergoing CT scan have prior CT images. To take advantage of prior CT scans of the same patient, CT dose optimization will require the current "retrospective dosimetry" paradigm to be replaced by the "prospective dosimetry" paradigm, in which organ dose information is used to guide subsequent CT scans of that patient.

A prospective patient-specific organ dose method will be a game changer in CT dosimetry and can help extend the existing tube current modulation techniques by taking full advantage of organ localization and distribution of organ doses. It can also help imaging physicians make informed and prospective decisions regarding the delivery of doses based on the clinical question, expected disease distribution, and organ dose distribution. Such prospective decisions regarding radiation dose delivery from CT can help usher in personalized scan protocols with truly organ dose-modulated techniques. Among the current technical barriers are the lack of clinically acceptable organ segmentation and rapid organ dose computing tools for CT.

Organ dose quantification for a set of radiosensitive organs in every patient undergoing CT scans is important for radiation protection purposes (instead of cancer treatment planning purposes). Segmentation of radiosensitive organ volumes from CT images has long been a challenging task to the medical physics community.[24] Manual organ segmentation is labor intensive and user dependent, making the

approach impractical for clinical applications involving patient-specific images. Until recently, methods of automatic segmentation of organs relied on low-level image features that require strong prior knowledge about the anatomical structures, both of which are insufficient for clinical use.[25] The advent of deep learning methods involving convolutional neural network (CNN) has brought an unprecedented level of innovation to the field of image segmentation.[26–29] The state-of-the-art models in organ segmentation are variants of encoder–decoder architecture such as the fully convolutional networks (FCNs)[30] and U-Net.[31] However, these models are usually trained for specific organs and cannot be easily extended to multi-organ segmentation needed for CT organ dosimetry. Recently, Trullo et al.[32] used a modified two-dimensional FCN to segment four OARs from CT images and apply conditional random fields to further improve the segmentation performance. Gibson et al.[33] applied a three-dimensional (3D) Dense V-Network to segment eight organs from CT images for navigation purposes in endoscopic pancreatic and biliary procedures. However, these studies did not perform organ dose calculations for patients who receive the CT scans. Recent studies by other groups that did consider CT organs dose evaluations employed traditional organ segmentation algorithm such as feature-based or atlas-based methods.[34,35] Finally, without the necessary accuracy and efficiency, patient-specific dosimetry tools would not become a viable part of the clinical workflow.

This study[36] aims to demonstrate the feasibility of a streamlined fast patient-specific CT organ dose assessment method that performs segmentation of multiple organs from patient-specific CT images using deep CNN algorithms and GPU-accelerated Monte Carlo dose calculations using the ARCHER code in a parallel computational workflow as illustrated in Fig. 1. This is the first study to combine these two tools to achieve the computational accuracy and efficiency required for routine clinical applications. In subsequent sections, we describe steps and methods, summarize results, and discuss limitations before drawing conclusions.

2. MATERIALS AND METHODS

2.A. Organ segmentation

2.A.1. Datasets and image preprocessing

In this study, two publicly available datasets were used: (a) The 2017 lung CT segmentation challenge (LCTSC),[37–39] which contains 60 thoracic CT scan patients with five segmented organs (left lung, right lung, heart, spinal cord, and esophagus), and (b) Pancreas-CT (PCT), which contains 43 abdominal contrast enhanced CT scan patients with eight segmented organs (the spleen, left kidney, gallbladder, esophagus, liver, stomach, pancreas, and duodenum).[28,33,39,40] For each patient in these two datasets, the Hounsfield Unit (HU) values were processed using a minimum threshold of −200 and a maximum threshold of 300 prior to being normalized to yield values between 0 to 1. In order to focus on organs and suppress the background information, we cropped and reserved the regions of interest according to the body contour in the original CT images and used it as training data. Finally, to circumvent the computer memory limitation, data resampling was performed using linear interpolation for CT images and using nearest interpolation for the labels. The interpolation operations are standard routine implementations in common image processing software. In our implementation, we used a python package called scipy.[41] In the linear interpolation, the value of a pixel after resampling is computed as the weighted average of its surrounding pixels, where the weights are calculated based on the distances to the target location. In the nearest-neighbor interpolation, the value of the nearest pixel around the target location is assigned to the target pixel after resampling.[42] For the LCTSC dataset, the original slice resolution is from 1.0 mm × 1.0 mm to 1.4 mm × 1.4 mm and the slice thickness is from 1.0 to 3.0 mm. The resulting resolution after resampling is 2.0 mm × 2.0 mm × 2.5 mm. For the PCT dataset, the original slice resolution is from 0.7 mm × 0.7 mm to 1.0 mm × 1.0 mm, and the original slice thickness is 1.0 mm. Here, we followed the

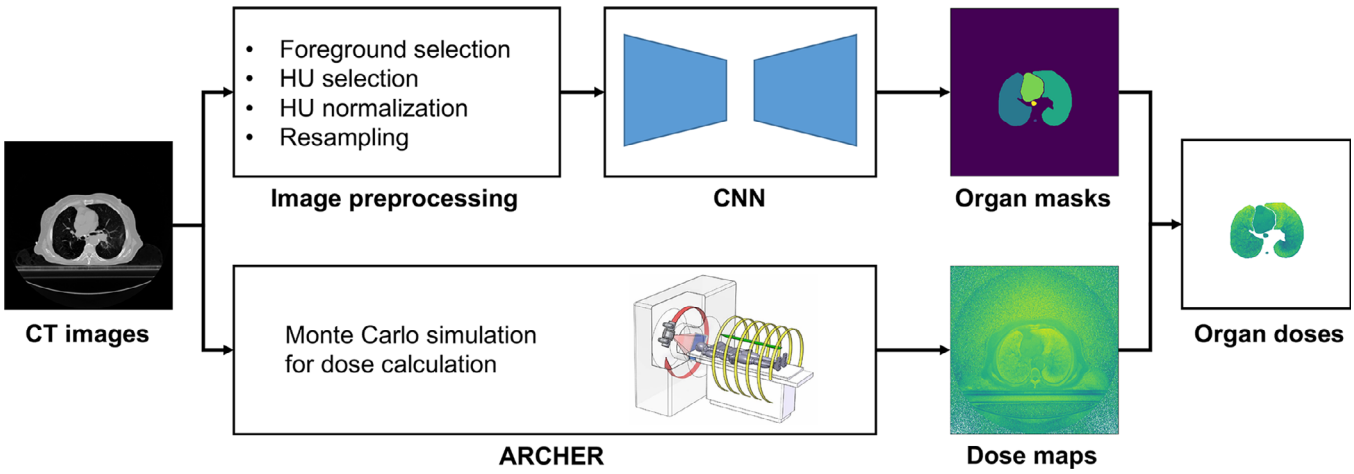

FIG. 1. The overall parallel computational process of the method of patient-specific organ dose assessment for computed tomography combining convolutional neural network-based multi-organ segmentation and a GPU-based Monte Carlo dose engine, ARCHER. [Color figure can be viewed at wileyonlinelibrary.com]

methods described by Gibson et al.,[33] and the size of CT images was resampled to 144 × 144 × 144 pixels. So after resampling, the resolution for each patient is different; specifically, the slice resolution is from 1.8 mm × 1.4 mm to 2.5 mm × 2.1 mm, and the slice thickness is from 1.1 to 1.6 mm.

2.A.2. Network architecture

The proposed network in this study is based on the 3D U-Net.[43] As shown in Fig. 2, the network consists of an encoder and a decoder. The role of the decoder network is to map the low resolution encoder feature maps to full input resolution feature maps for pixel-wise classification.[44] The encoder contains four repeated residual blocks. Each block consists of four convolutional modules and each convolutional module is composed by a convolution layer with the kernel of 3 × 3 × 3, an instance normalization, and a leaky rectified linear unit. For each residual block, the stride of convolution layer in the convolutional modules is 1 × 1 × 1 except for the last convolutional module in which the stride is 2 × 2 × 2 to achieve the purpose of downsampling, and there is a spatial dropout layer between the early two convolutional modules to prevent the network from overfitting. The decoder contains four repeated segmentation blocks. Each block consists of two convolutional modules and one deconvolutional module. Four dashed arrows in the figure indicate four skipping connections that copy and reuse early feature maps as the input to later layers that have the same feature map size by a concatenation operation to preserve high-resolution features. In the final three segmentation blocks, a 1 × 1 × 1 convolution layer is used to map the feature tensor to the probability tensor with the channels of the desired number of classes, n, before all results are merged by the upsampling operation to enhance the precision of segmentation results. Finally, a SoftMax activation is used to output a probability of each class for every voxel.[45]

2.A.3. Training and validation

The fivefold cross-validation method was adopted for this work.[46] The entire dataset is randomly split, using the "random.shuffle()" function in Python, into five non-overlapping subsets for training, validation, and testing in the ratio of 3:1:1 (i.e., three subsets for training, one subset for validation, and one subset for testing). Specifically, for the LCTSC dataset, a total of 60 patients are divided into five subsets (each having 12 patients). For the PCT dataset, a total of 43 patients are divided into five subsets (each having eight or nine patients). The validation process is used to monitor the training process and to prevent overfitting. To reduce potential bias, randomly split five subsets are rotated five times to report the average performance over these five different hold-out testing subsets, as illustrated in Fig. 3. The fivefold cross validation strategy is key to ensuring the independence of the testing data, that is, each sample is used in the testing subsets only once.

At the training stage, patches are first randomly extracted from the resampled CT images to achieve data diversity and to prevent overfitting. The patch size is 96 × 96 × 96 in LCTSC and 128 × 128 × 128 in PCT. Figure 4 shows an example of such patches from LCTSC used in the training in terms of axial, sagittal, and coronal views. The patch-based training method addresses the problem of different sizes of CT images as well as the requirement of data augmentation. An advantage is that it enhances the robustness of the network model. The limitation is that it may negatively impact the predicted performance due to the lack of global information when the patch size is too small. The network can be aware of the Z location of the patches implicitly because the patch image in the different Z location is different, and the patches in any Z location are trained. The orientation of all patches is the same, so the right lung and left lung have different positions, and they have different shapes in the patch. Therefore, the right and left lungs can be differentiated by their position and shape although they have a similar pixel value.

Then, the network is trained by the patch and its corresponding labels. The loss function is defined as the weighted dice similarity coefficient as:

$$\text{Loss} = -\frac{1}{N \times K}\sum_{i=1}^{N}\sum_{k=1}^{K}\frac{2 \times \sum_{v=1}^{V}\left(p_{i,k,v} \times y_{i.k.v}\right) + \varepsilon}{\sum_{v=1}^{V} p_{i,k,v} + \sum_{v=1}^{V} y_{i,k,v} + \varepsilon},$$

where $p_{i,k,v}$ is the predicted probability of the voxel v of the sample i belonging to the class k, $y_{i,k,v}$ is the ground truth label (0 or 1), N is the number of samples, K is the number of classes, V is the number of voxels in one sample, and ε is a smooth factor (set to be 1 in this study). The initial learning rate is 0.0005, and the Adam algorithm[47] is used to update the parameters of the network. The validation loss is calculated for every epoch, and the learning rate is halved when the validation loss no longer decreases after 30 consecutive epochs. To prevent overfitting, the training process is terminated when the validation loss on longer decreases after 50 consecutive epochs.

2.A.4. Testing

In the testing stage, patches are first extracted from each CT images with a moving window with the size of 96 × 96 × 96 in LCTSC and 128 × 128 × 128 in PCT. The stride is 48 in LCTSC and eight in PCT. In other words, multiple patches are extracted from one patient and fed into the network. The output of the network is a probability tensor for each patch. Then, all probability tensors are merged from the same patient with a mean operator in the overlapping area to obtain the final probability tensor. Next, the class of each voxel is determined by the largest probability, which is the preliminary results of organ segmentation, and the value of each voxel is the class number. Last, using the nearest-neighbor interpolation, the preliminary segmentation results are resampled to the size of original CT images to obtain the final organ segmentation results.

All experiments described above were performed on a Linux computer system. Keras with TensorFlow as the

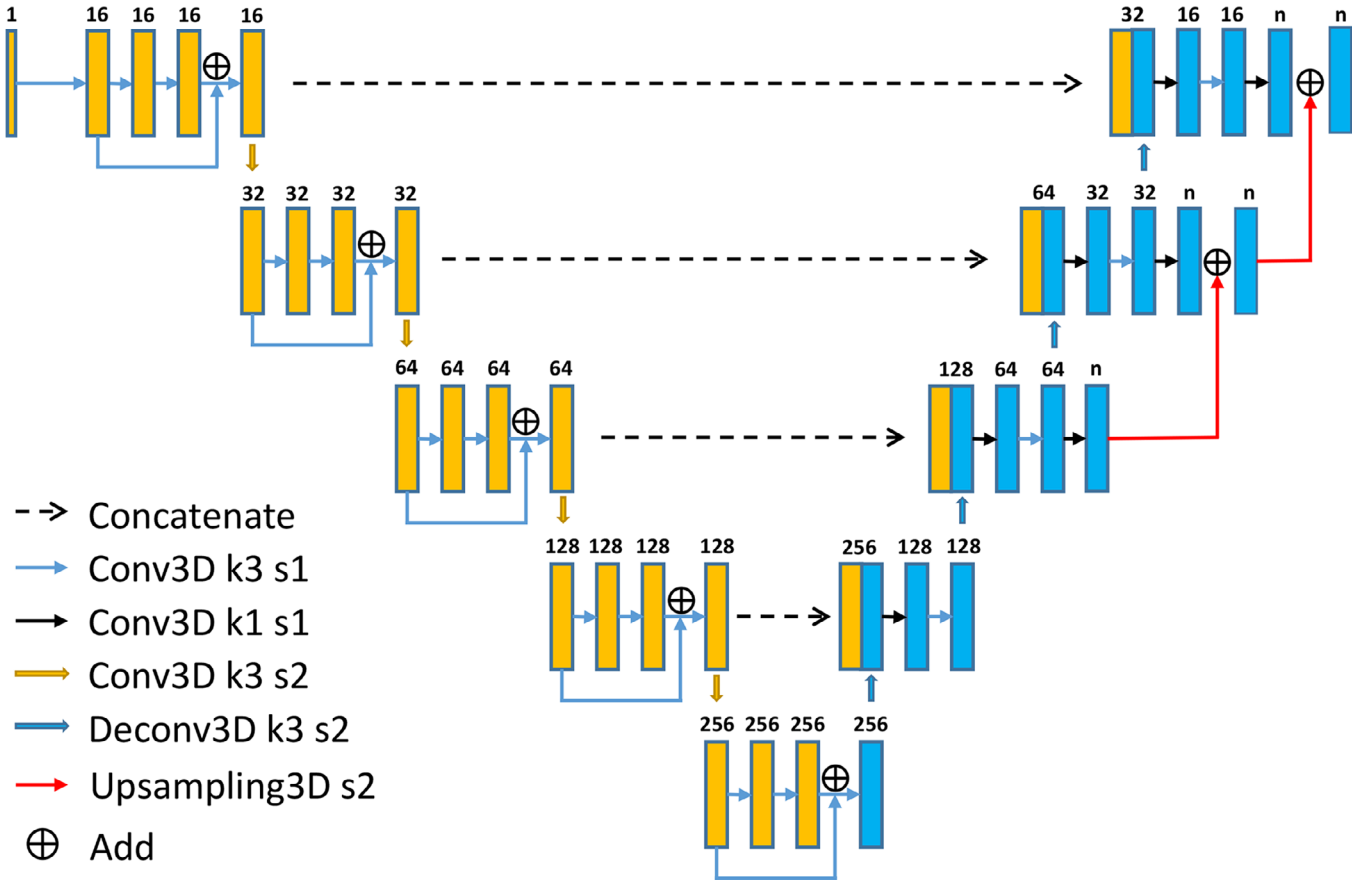

FIG. 2. The network architecture. [Color figure can be viewed at wileyonlinelibrary.com]

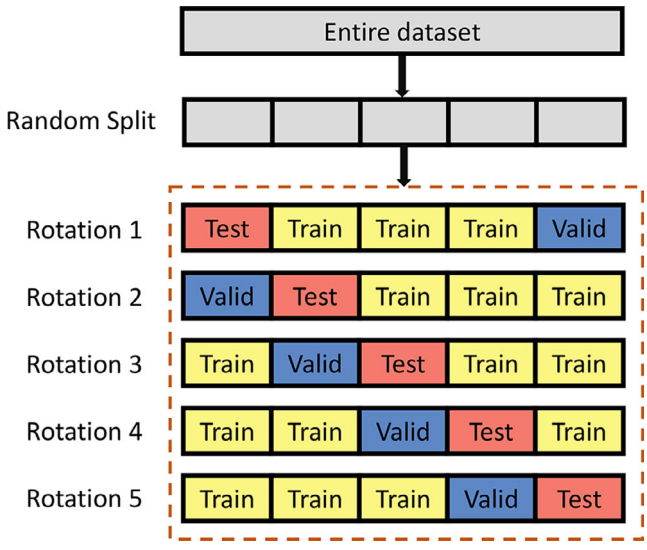

FIG. 3. Example of splitting and rotation using the fivefold cross-validation method for the dataset involving five subsets. [Color figure can be viewed at wileyonlinelibrary.com]

backend was used as the platform for designing and training the neural network.[48] The hardware includes: (a) GPU — Nvidia GeForce Titan X Graphics Card with 12 GB memories, and (b) CPU — Intel Xeon Processor X5650 with 16 GB memories.

2.B. Organ dose calculations

A GPU-accelerated Monte Carlo code, ARCHER, previously developed by members of this group was used in this study to calculate organ doses.[20–21,49] ARCHER simulates the transport of low-energy x-ray photons in heterogeneous media defined by the patient CT images where photoelectric effect, Compton scattering, and Rayleigh scattering can take place. Computed tomography scan protocols are predefined for ARCHER including a combination of scan mode (helical or axial), beam collimation (5, 10, or 20 mm), and kVp (80, 100, 120, or 140). Figure 5 illustrates the simulation model involving a patient and a CT scanner.

This study considers a scanner model representing a GE Lightspeed Pro 16 MDCT that has been validated in our previous studies,[50,51] although a newer scanner model can be similarly created when needed in the future. The scanning protocol includes 120 kVp, 20-mm beam collimation, axial body scan at a constant 100 mAs. A CT scanner's continuous rotational motion is simulated using the step-and-shoot pattern, with each rotation approximated by 16 discrete positions.[50] As shown earlier in Fig. 1, the average absorbed dose for each organ of interest is derived by combining the newly segmented organ masks and voxel-wise dose maps calculated by ARCHER for a specific patient — as is done in radiation treatment planning. The computational speed is evaluated to make sure it is acceptable as part of the clinical workflow.

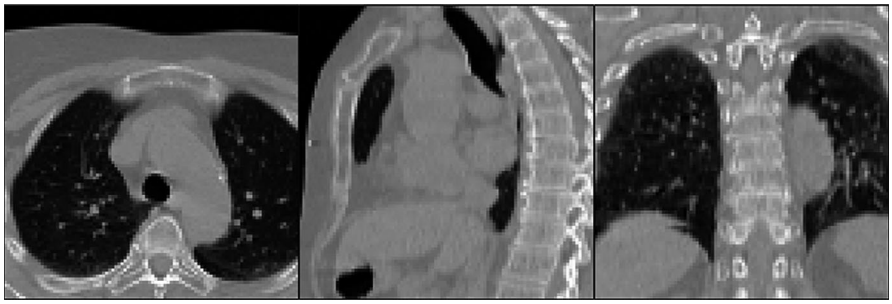

FIG. 4. An example to illustrate patches from lung computed tomography segmentation challenge the database used in the training in terms of axial, sagittal, and coronal views.

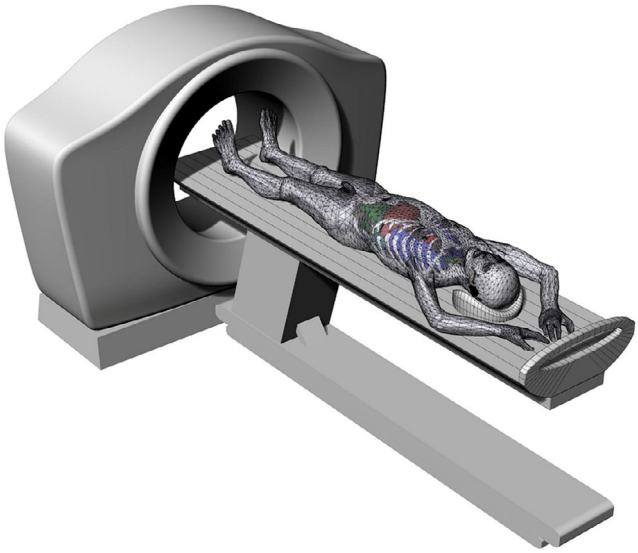

FIG. 5. Computed tomography (CT) dose simulation model of a patient undergoing a CT scan. [Color figure can be viewed at wileyonlinelibrary.com]

To show the potential clinical impact of the new method, patient-specific organ dose results are compared against organ doses derived from population-average phantoms used in the VirtualDose software.[45,52] Figure 6 shows the RPI-Adult Male (73 kg in weight and 176 cm in height) and RPI-Adult Female (60 kg in weight and 163 cm in height) phantoms that were designed in accordance with anatomical parameters for the 50th percentile of the population.[52] When the weight and height of an adult patient are unspecified, the clinical organ dose assessment procedure at Massachusetts General Hospital usually picks these standard adult phantoms from the VirtualDose software to represent that patient.

2.C. Segmentation and organ dose evaluation criteria

The Dice Similarity Coefficient (DSC) is used to evaluate the performance of organ segmentation[53]:

$$DSC = \frac{2|A \cap B|}{|A| + |B|}$$

where A is the manually segmented organ (i.e., the ground truth) and B is the automatically segmented organ by the network. The DSC ranges from 0 to 1 with the latter indicating a perfect performance. The relative dose error (RDE) was used to evaluate the accuracy of dose calculation for each organ:

$$RDE = \frac{D - D_r}{D_r} \times 100\%$$

where D is the organ dose calculated by ARCHER using either automatically segmented organs in the patient-specific phantom (i.e., our method) or organs in the population-average phantom, and D_r is the reference organ dose calculated by ARCHER using manually segmented organs in the patient-specific phantom.

3. RESULTS

3.A. Organs segmentation

The performance of our network in organ segmentation is evaluated in terms of the DSC. As shown in Fig. 7, the segmentation results of all organs are summarized in these two box plots. For 60 patients from LCTSC, we achieved median DSCs of 0.97 (right lung), 0.96 (left lung), 0.92 (heart), 0.86 (spinal cord), and 0.76 (esophagus), which can be seen in Fig. 7(a). For 43 patients from PCT, we achieved median DSCs of 0.96 (spleen), 0.96 (liver), 0.95 (left kidney), 0.90 (stomach), 0.87 (gall bladder), 0.80 (pancreas), 0.75 (esophagus), and 0.61 (duodenum), which can be seen in Fig. 7(b). Figures 8(a) and 8(b) show visual comparison of manual and automatic multi-organ segmentation results from both LCTSC and PCT, respectively, in axial, sagittal, coronal, and 3D views.

3.B. Organ dose calculations

The accuracy of organ dose calculations is evaluated in terms of RDE for the purposes of CT organ dosimetry, where 10% is generally considered excellent. In the dataset from LCTSC for a total of 60 patients, organs doses are calculated for organs including the lung, heart, and esophagus. The left lung and right lung are treated as one organ, and the RDE of the spinal cord is not considered because it is not segmented

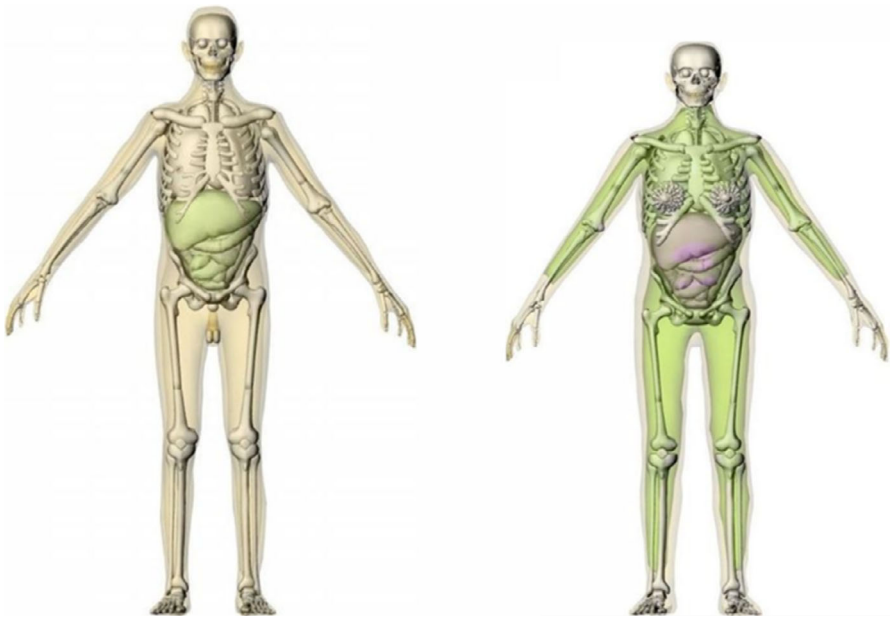

FIG. 6. RPI-Adult Male (left) and RPI-Adult Female (right) phantoms in the VirtualDose software that were designed in accordance with anatomical parameters for the 50th percentile of the population, thus bringing errors when compared with patient-specific organ doses.[52] [Color figure can be viewed at wileyonlinelibrary.com]

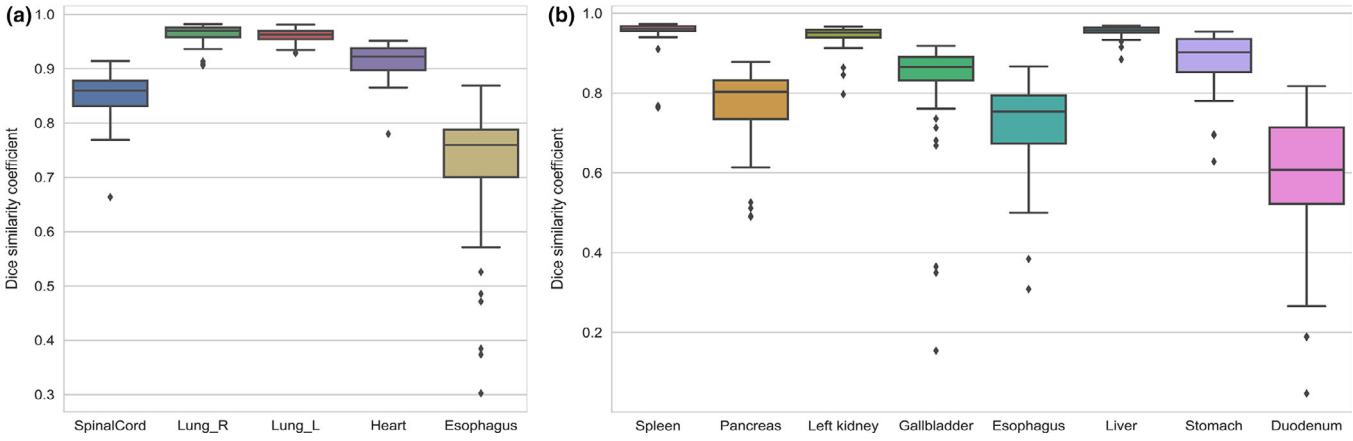

FIG. 7. Evaluation of organ segmentation performance in terms of dice similarity coefficients. (a) Data based on 60 patients from the lung computed tomography segmentation challenge database. (b) Data based on 43 patients from the pancreas-CT database. [Color figure can be viewed at wileyonlinelibrary.com]

in the population-average phantom. In the dataset from PCT for a total of 43 patients, organs doses are calculated for organs including the spleen, left kidney, gallbladder, liver, stomach, and pancreas. The duodenum is not segmented in the population-average phantom, and the esophagus in the specific patient is incomplete in the abdominal CT scanning, so the RDEs are not considered for the duodenum and esophagus. The results are summarized in Table I and further visually compared in Figs. 9(a) and 9(b) using box plots of RDEs for each organ in these two datasets. The ground-truth reference organ doses are calculated for the specific patient using ground-truth segmentation data from the original database. The "proposed method" represents the RDE between organ doses from our automatic segmentation and the reference organ doses, and the "phantom-based method" represents the RDE between organ doses from the population-average phantom and reference organ doses. Comparing with the population-average phantom-based method, our proposed patient-specific method achieved much smaller RDE values. In a CT scan, the height, weight, and organ topology of a patient can influence organ dose values. There is no doubt that it introduces some errors using population-average phantoms to replace a specific patient for organ dose calculation. In the case of dose to the heart, the current method of using population-average phantom in the VirtualDose software is found to have the error range (−15.4%–124.6%) due to the anatomical differences between the phantom and a real patient. The patient-specific method has much smaller errors with the range of −2.9% to 2.6% for the heart due to difference in organ segmentation between the CNN-based method and the

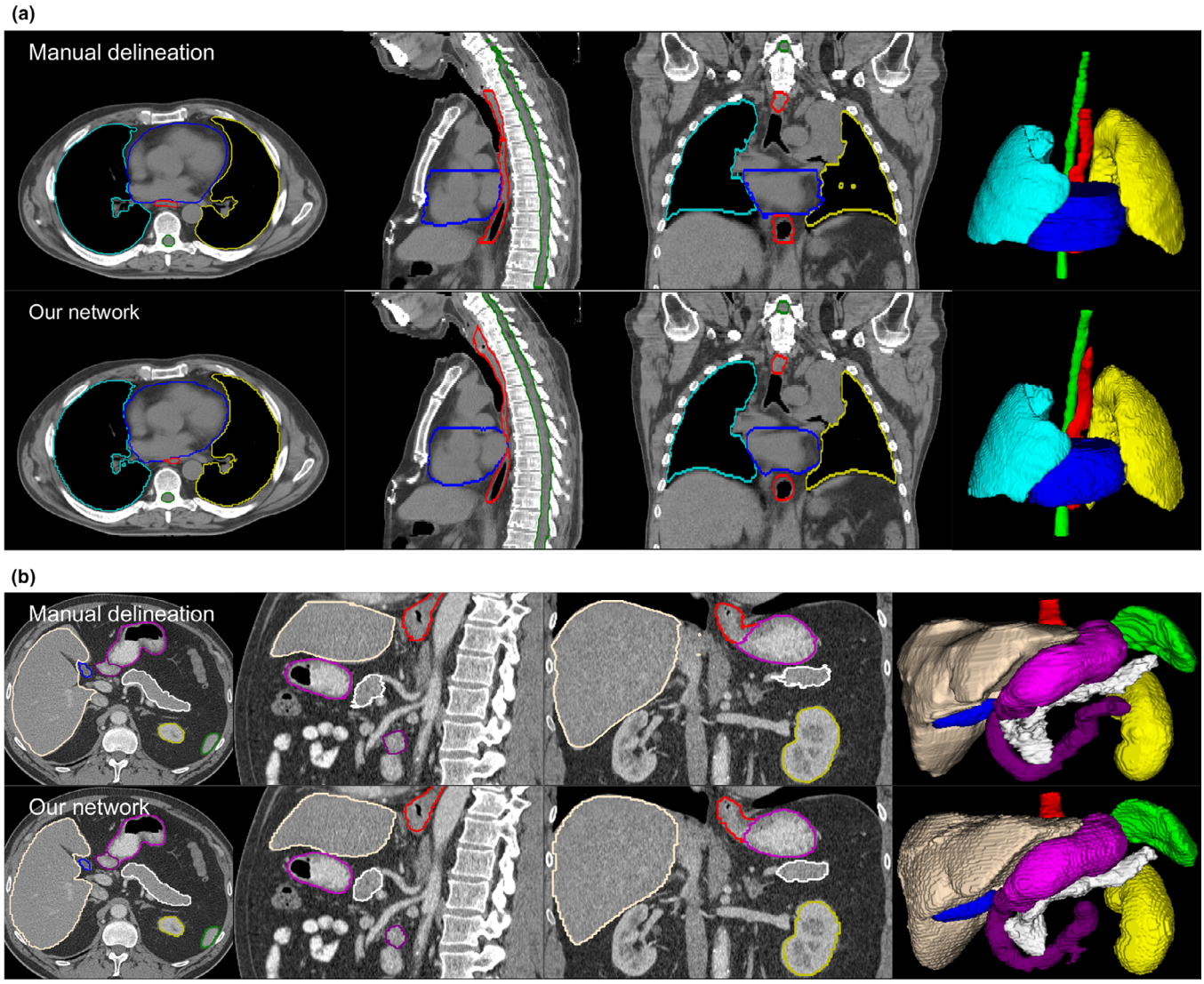

FIG. 8. Examples for visual comparison of organ segmentation between manual methods from lung computed tomography segmentation challenge (LCTSC) or pancreas-CT (PCT) database (showed in the upper row in each panel) and our automatic method (showed in the upper row in each panel), in terms of axial, sagittal, coronal, and 3D views (from left to right). (a) LCTSC database showing left lung (yellow), right lung (cyan), heart (blue), spinal cord (green), and esophagus (red). (b) PCT database showing spleen (green), pancreas (white), left kidney (yellow), gallbladder (blue), esophagus (red), liver (bisque), stomach (magenta), and duodenum (purple). [Color figure can be viewed at wileyonlinelibrary.com]

ground truth. These results suggest that the patient-specific method can bring significant (in the case of dose to the heart, 125/3 times) improvement to the current CT organ dose assessment method that is based on population-average phantoms.

3.C. Computational efficiency

The computing time in our method includes two processes performed in parallel as illustrated previously in Fig. 1. The time for automatic multi-organ segmentation for each patient is <5 s for all 103 patient cases considered in the study. The time to calculate a total of 1×10^8 photons for each patient (for a maximum organ dose statistical uncertainty of 0.5%) using ARCHER code running on an Nvidia Titan RTX GPU card with 24 GB memory is less than 4 s for all 103 patient cases. From our experiences, such computational accuracy and efficiency are expected to be acceptable as part of the routine clinical workflow.

4. DISCUSSION

In this study, we designed a 3D CNN model to automatically segment thoracic and abdominal organs in patient-specific CT images using two publicly available databases. For the duodenum or esophagus, the segmentation performance of our network was found to be relatively poor because the organ and its surrounding tissues have similar pixel values in CT image, making the boundary difficult to detect by the CNN model. Nevertheless, results from this study have clearly demonstrated the accuracy and efficiency of the CNN model in performing the automatic multi-organ segmentation

TABLE I. Comparison of relative dose errors (RDE) of organ doses calculated by the proposed patient-specific method and the population-averaged phantom method.

		Proposed patient-specific method			Population-averaged phantom method		
			Absolute RDE (%)			Absolute RDE (%)	
	Organs	RDE range (%)	Mean	Standard deviation	RDE range (%)	Mean	Standard deviation
Thorax	Lung	−7.5–2.2	1.8	1.4	−21.1–46.4	16.0	11.8
	Heart	−2.9–2.6	0.8	0.7	−15.4–124.6	34.0	31.1
	Esophagus	−9.4–5.0	1.6	1.7	−10.5–125.6	45.7	29.3
Abdomen	Spleen	−7.9–1.0	0.6	1.2	−20.1–57.1	15.8	12.7
	pancreas	−3.4–4.6	1.2	1.0	−20.2–61.1	18.1	15.7
	Left kidney	−2.0–1.9	0.9	0.6	−39.0–70.8	20.0	15.2
	Gallbladder	−15.0–3.9	1.7	3.1	−40.1–14.0	19.1	9.8
	Liver	−0.8–1.3	0.3	0.3	−30.0–72.7	24.2	18.7
	Stomach	−4.6–8.1	1.6	1.7	−47.7–20.8	19.3	13.6

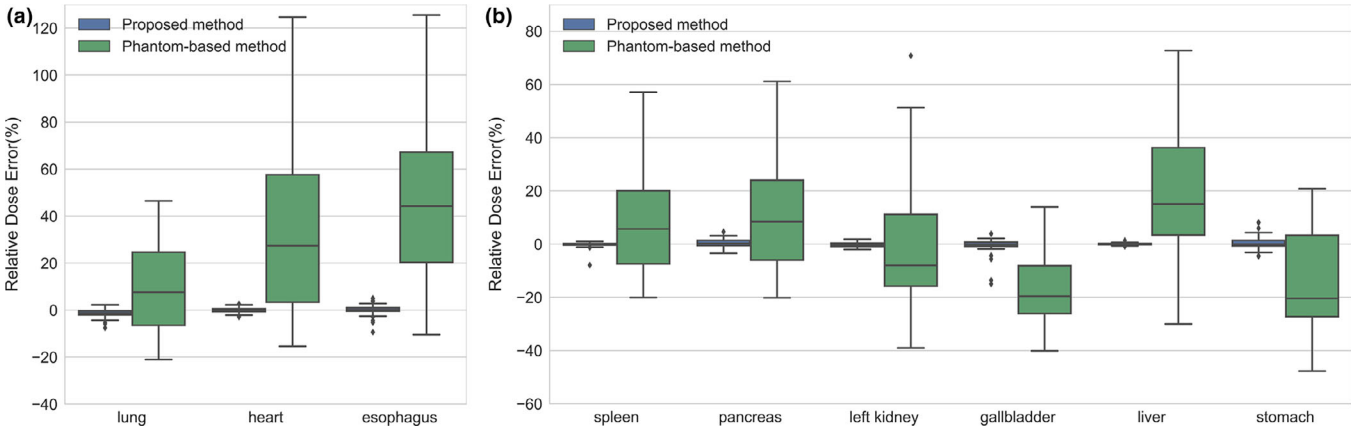

FIG. 9. The box plots of relative dose errors showing that the proposed patient-specific method has much smaller errors than the population-averaged phantom method when evaluated against the ground truth data. (a) For 60 patients from lung computed tomography segmentation challenge and (b) for 43 patients from pancreas-CT. [Color figure can be viewed at wileyonlinelibrary.com]

task for the purposes of assessing patient organ doses. Implementation of the proposed method can lead to significant improvement in the accuracy of organ dose calculation based on the population-average phantoms.

As evidenced in the 2017 AAPM Thoracic Auto-Segmentation Challenge, start-of-the-art automatic segmentation methods, DL-based or atlas-based, can already achieve impressive performances.[38] Therefore, the objective of this study was not to invent a new and better organs segmentation method. Instead, the significance of this study is that, for the first time, we have demonstrated that it is feasible to combine DL-based automatic multi-organ segmentation tool with the GPU-based rapid Monte Carlo dose calculation code in a streamlined process that takes <5 s for each patient. With this newly demonstrated capability of "patient-specific" organ dose assessment, future CT scanners can take advantage of patient- and scan-specific features in a new paradigm — the "prospective" design of tube voltage and current modulation, beam collimation and filtering, and gantry angle — leading to the ultimate goal of achieving low-dose and optimized CT imaging.

There are several limitations in the current study. The variable and somewhat less accurate performance of our approach for segmenting narrow and long structures with poor soft-tissue contrast such as the esophagus and duodenum may be related to the relatively small size of training data in the databases causing irregularities in CT attenuation and position of these structures. Another limitation is that we did not assess the effect of major abnormalities on the organ segmentation — an issue already recognized by organizers of the 2017 lung CT segmentation challenge.[38] Likewise, diffuse abnormalities and paucity of intra-abdominal fat can have a negative effect on the ability of our segmentation algorithm. Further studies should consider larger patient data sizes, covering children and including additional radiosensitive organs in the head and neck regions. One set of unique data already available from MGH is the annotated cadaver CT images that are ideal for testing of DL-based image analysis and dosimetry algorithms.[54–56]

Finally, it is worth noting that, with the patient-specific organ dose information, one can derive the so-called "effective dose" — a quantity that the American Association of

Physicists in Medicine (AAPM) believes to bear significant uncertainty and therefore should be used only for prospective radiologic protection purposes and to help patients understand medical radiation dose in perspective.[57]

5. CONCLUSIONS

In this study, an automatic multi-organ segmentation method has been developed using a CNN model that was trained with two publicly available CT databases involving a total of 103 patients. The method takes <5 s to perform automatic multi-organ segmentation for one patient and, for purposes of CT organ dosimetry, has achieved good segmentation accuracy for the testing cases considered in this study. The organ dose calculation method takes <4 s for a total of 1×10^8 photons using the GPU-based rapid Monte Carlo code, ARCHER, to achieve the organ dose statistical uncertainty of better than 0.5%. These results demonstrate, for the first time, the excellent accuracy and efficiency of a streamlined patient-specific organ dosimetry computational tool. Implementation of such methods as part of the clinical workflow can yield considerable improvement over the current CT organ dose methods that are based on population-average phantoms, thus opening the door to prospective patient-specific optimization features in the future.

ACKNOWLEDGMENTS

Zhao Peng was a visiting Ph.D. student at RPI whose work was supported by a grant from the University of Science and Technology of China and by an International Training Grant from the American Association of Physicists in Medicine (AAPM). Co-authors were supported in part by various grants: NIH/NIBIB (R42EB019265-01A1, U01EB017140, R01EB026646), NIH/NCI (R01CA233888 and R01CA237267), and National Natural Science Foundation of China (11575180).

CONFLICT OF INTEREST

X. George Xu is a co-founder of Virtual Phantoms, Inc (Albany, New York) that commercializes software technologies — VirtualDose™ for medical CT dose reporting and ARCHER™ for real-time Monte Carlo dose computing.

[a]Author to whom correspondence should be addressed. Electronic mail: xug2@rpi.edu; Telephone: 518-276-4014.

REFERENCES

1. Amis ES Jr., Butler PF, Applegate KE, et al. American College of Radiology white paper on radiation dose in medicine. *J Am Coll Radiol*. 2007;4:272–284.
2. de Gonzalez AB, Darby S. Risk of cancer from diagnostic X-rays: estimates for the UK and 14 other countries. *Lancet*. 2004;363:345–351.
3. Brenner DJ, Hall EJ. Computed tomography—an increasing source of radiation exposure. *N Engl J Med*. 2007;357:2277–2284.
4. IMV Medical Information Division, Inc.IMV Benchmark Report for CT; 2018.
5. Shope TB, Gagne RM, Johnson GC. A method for describing the doses delivered by transmission x-ray computed tomography. *Med Phys*. 1981;8:488–495.
6. Newman B, Ganguly A, Kim JE, et al. Comparison of different methods of calculating CT radiation effective dose in children. *Am J Roentgenol*. 2012;199:W232–W239.
7. Deak P, van Straten M, Shrimpton PC, et al. Validation of a Monte Carlo tool for patient-specific dose simulations in multi-slice computed tomography. *Eur Radiol*. 2008;18:759–772.
8. Jarry G, DeMarco JJ, Beifuss U, et al. A Monte Carlo-based method to estimate radiation dose from spiral CT: from phantom testing to patient-specific models. *Phys Med Biol*. 2003;48:2645–2663.
9. Angel E, Yaghmai N, Jude CM, et al. Monte Carlo simulations to assess the effects of tube current modulation on breast dose for multidetector CT. *Phys Med Biol*. 2009;54:497–511.
10. Tian XY, Li X, Segars WP, et al. Pediatric chest and abdominopelvic CT: organ dose estimation based on 42 patient models. *Radiology*. 2014;270:535–547.
11. Lee C, Kim KP, Long DJ, et al. Organ doses for reference pediatric and adolescent patients undergoing computed tomography estimated by Monte Carlo simulation. *Med Phys*. 2012;39:2129–2146.
12. Turner AC, Zhang D, Khatonabadi M, et al. The feasibility of patient size-corrected, scanner-independent organ dose estimates for abdominal CT exams. *Med Phys*. 2011;38:820–829.
13. Li XA, Samei E, Segars WP, et al. Patient-specific radiation dose and cancer risk estimation in CT: part I. Development and validation of a Monte Carlo program. *Med Phys*. 2011;38:397–407.
14. Lee C, Kim KP, Bolch WE, et al. NCICT: a computational solution to estimate organ doses for pediatric and adult patients undergoing CT scans. *J Radiol Protect Off J Soc Radiol Protect*. 2015;35:891–909.
15. Ding A, Gao Y, Liu H, et al. VirtualDose: a software for reporting organ doses from CT for adult and pediatric patients. *Phys Med Biol*. 2015;60:5601.
16. Xu XG. An exponential growth of computational phantom research in radiation protection, imaging, and radiotherapy: a review of the fifty-year history. *Phys Med Biol*. 2014;59:R233.
17. Emami B, Lyman J, Brown A, et al. Tolerance of normal tissue to therapeutic irradiation. *Int J Radiat Oncol*. 1991;21:109–122.
18. Bentzen SM, Constine LS, Deasy JO, et al. Quantitative analyses of normal tissue effects in the clinic (Quantec): an introduction to the scientific issues. *Int J Radiat Oncol*. 2010;76:S3–S9.
19. Emami B. Tolerance of normal tissue to therapeutic radiation. *Rep Radiother Oncol*. 2013;1:123–127.
20. Liu T, Xu XG, Carothers CD. Comparison of two accelerators for Monte Carlo radiation transport calculations, Nvidia Tesla M2090 GPU and Intel Xeon Phi 5110p coprocessor: a case study for X-ray CT imaging dose calculation. *Ann Nucl Energy*. 2015;82:230–239.
21. Su L, Yang Y, Bednarz B, et al. ARCHERRT—a photon-electron coupled Monte Carlo dose computing engine for GPU: software development and application to helical tomotherapy. *Med Phys*. 2014;41:071709.
22. Sodickson A, Baeyens PF, Andriole KP, et al. Recurrent CT, cumulative radiation exposure, and associated radiation-induced cancer risks from CT of adults. *Radiology*. 2009;251:175–184.
23. Xu XG. Personnal Communications. 2019.
24. Sharp G, Fritscher KD, Pekar V, et al. Vision 20/20: perspectives on automated image segmentation for radiotherapy. *Med Phys*. 2014;41:050902.
25. Han M, Ma J, Li Y, et al. Segmentation of organs at risk in CT volumes of head, thorax, abdomen, and pelvis. Medical Imaging 2015: Image Processing: International Society for Optics and Photonics. 2015;94133J.
26. Chen X, Zhang R, Yan P. Feature Fusion Encoder Decoder Network For Automatic Liver Lesion Segmentation. arXiv preprint arXiv:190311834; 2019.
27. Christ PF, Elshaer MEA, Ettlinger F, et al. Automatic liver and lesion segmentation in CT using cascaded fully convolutional neural networks and 3D conditional random fields. In: *International Conference on Medical Image Computing and Computer-Assisted Intervention*. Berlin: Springer; 2016:415–423.
28. Roth HR, Lu L, Farag A, et al. Deeporgan: multi-level deep convolutional networks for automated pancreas segmentation. In: *International*

Conference on Medical Image Computing and Computer-Assisted Intervention. Berlin: Springer; 2015:556–564.
29. Dou Q, Chen H, Jin Y, et al. 3D deeply supervised network for automatic liver segmentation from CT volumes. In: *International Conference on Medical Image Computing and Computer-Assisted Intervention*. Berlin: Springer; 2016:149–157.
30. Long J, Shelhamer E, Darrell T. Fully convolutional networks for semantic segmentation. Proceedings of the IEEE conference on computer vision and pattern recognition; 2015:3431–3440.
31. Ronneberger O, Fischer P, Brox T. U-net: Convolutional networks for biomedical image segmentation. In: *International Conference on Medical image Computing and Computer-Assisted Intervention*. Berlin: Springer; 2015:234–241.
32. Trullo R, Petitjean C, Ruan S, et al. Segmentation of organs at risk in thoracic CT images using a sharpmask architecture and conditional random fields. 2017 IEEE 14th International Symposium on Biomedical Imaging (ISBI 2017): IEEE; 2017:1003–1006.
33. Gibson E, Giganti F, Hu Y, et al. Automatic multi-organ segmentation on abdominal CT with dense v-networks. *IEEE Trans Med Imaging*. 2018;37:1822–1834.
34. Schmidt TG, Wang AS, Coradi T, et al. Accuracy of patient-specific organ dose estimates obtained using an automated image segmentation algorithm. *J Med Imaging*. 2016;3:043502.
35. Fu W, Segars W, Abadi E, et al. From patient-informed to patient-specific organ dose estimation in clinical computed tomography. Conference on Medical Imaging - Physics of Medical Imaging. Houston, TX; 2018.
36. Peng Z, Fang X, Yan P, et al. A method of rapid quantification of patient-specific organ dose for CT using coupled deep multi-organ segmentation algorithms and GPU-accelerated Monte Carlo dose computing code. arXiv:190800360v2; 2019.
37. Yang J, Sharp G, Veeraraghavan H, et al. Data from lung CT segmentation challenge. The Cancer Imaging Archive; 2017.
38. Yang J, Veeraraghavan H, Armato SG III, et al. Autosegmentation for thoracic radiation treatment planning: a grand challenge at AAPM 2017. *Med Phys*. 2018;45:4568–4581.
39. Clark K, Vendt B, Smith K, et al. The Cancer Imaging Archive (TCIA): maintaining and operating a public information repository. *J Digit Imaging*. 2013;26:1045–1057.
40. Roth HR, Farag A, Turkbey E, et al. Data from Pancreas-CT. The cancer imaging archive;2016.
41. https://docs.scipy.org/doc/scipy/reference/generated/scipy.ndimage.zoom.html
42. Thévenaz P, Blu T, Unser M. 25 - Image interpolation and resampling. In: Bankman IN, ed. *Handbook of Medical Imaging*. San Diego: Academic Press; 2000:393–420.
43. Çiçek Ö, Abdulkadir A, Lienkamp SS, et al. 3D U-Net: Learning Dense Volumetric Segmentation from Sparse Annotation. International Conference on Medical Image Computing and Computer-Assisted Intervention; 2016.
44. Badrinarayanan V, Kendall A, Cipolla R. SegNet: a deep convolutional encoder-decoder architecture for image segmentation. *IEEE Trans Pattern Anal*. 2017;39:2481–2495.
45. Bishop CM. *Pattern Recognition and Machine Learning*. Berlin: Springer; 2006.
46. Arlot S, Celisse A. A survey of cross validation procedures for model selection. *Statistics Surveys*. 2009;4:40–79.
47. Kingma DP, Ba J. Adam: A method for stochastic optimization. arXiv preprint arXiv:14126980; 2014.
48. Abadi M, Barham P, Chen J, et al. Tensorflow: a system for large-scale machine learning. 12th USENIX Symposium on Operating Systems Design and Implementation (OSDI; 2016;16:265–283.
49. Chen LC, Yang Y, Wang J, et al. Attention to scale: scale-aware semantic image segmentation. *IEEE Conf Comput Vis Pattern Recogn*. 2016;2016:3640–3649.
50. Gu J, Bednarz B, Caracappa P, et al. The development, validation and application of a multi-detector CT (MDCT) scanner model for assessing organ doses to the pregnant patient and the fetus using Monte Carlo simulations. *Phys Med Biol*. 2009;54:2699.
51. Ding A. Development of a radiation dose reporting software for X-ray computed tomography (CT). Rensselaer Polytechnic Institute; 2012.
52. Ding A, Mille MM, Liu T, et al. Extension of RPI-adult male and female computational phantoms to obese patients and a Monte Carlo study of the effect on CT imaging dose. *Phys Med Biol*. 2012;57:2441.
53. Dice LR. Measures of the amount of ecologic association between species. *Ecology*. 1945;26:297–302.
54. Zhang D, Padole A, Li XH, et al. In vitro dose measurements in a human cadaver with abdomen/pelvis CT scans. *Med Phys*. 2014;41:091911.
55. Li XH, Shi JQ, Zhang D, et al. A new technique to characterize CT scanner bow-tie filter attenuation and applications in human cadaver dosimetry simulations. *Med Phys*. 2015;42:6274–6282.
56. Padole A, Khawaja RDA, Otrakji A, et al. Comparison of measured and estimated CT organ doses for modulated and fixed tube current: a human cadaver study. *Acad Radiol*. 2016;23:634–642.
57. Mccollough C, Cody D, Edyvean S. The measurement, reporting, and management of radiation dose in CT. *Clin Transl Sci*. 2008;8:330–333.